IM-20
89789
p.198

NASA Contractor Report 187207

THRUST CHAMBER MATERIAL TECHNOLOGY PROGRAM

FINAL REPORT

J. S. Andrus and R. G. Bordeau
Pratt & Whitney
Government Engines & Space Propulsion
P.O. Box 109600
West Palm Beach, FL 33410-9600

March 1989

NASA
National Aeronautics and
Space Administration
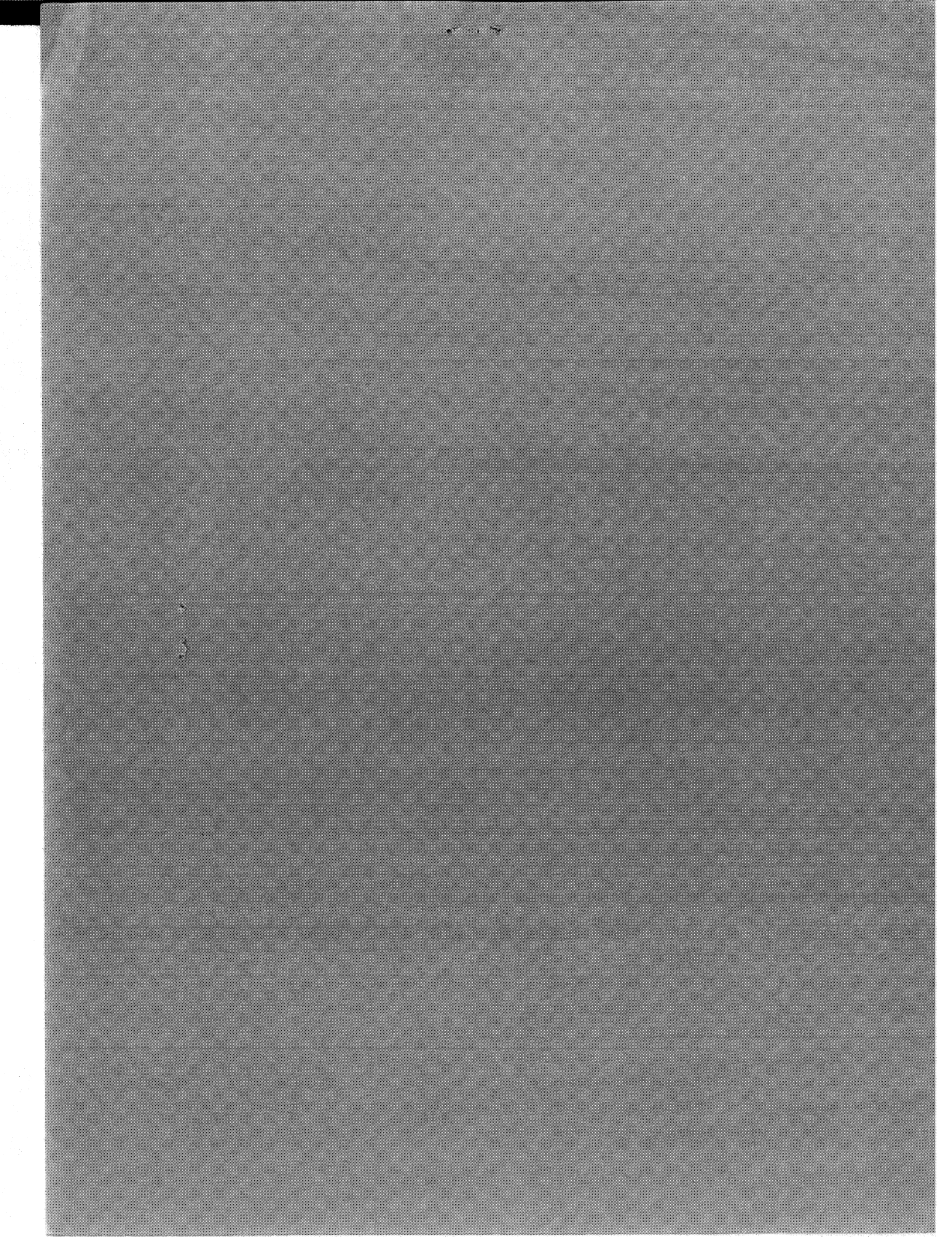
FOREWORD

This report describes development of copper-based materials for use in cooled rocket engine thrust chambers of an advanced Orbital Transfer Vehicle (OTV). The work was conducted by Pratt & Whitney (P&W) Government Engine Business (GEB) for the National Aeronautics and Space Administration-Lewis Research Center (NASA-LeRC) under contract NAS3-23858 Task C.I, with Mr. John M. Kazaroff as Task Order Manager.

Included as Appendix C of this report is a material variation study previously issued as P&W report FR-19440-1.

i

CONTENTS

CONTENTS (Continued)

ILLUSTRATIONS

ILLUSTRATIONS (Continued)

ILLUSTRATIONS (Continued)

ILLUSTRATIONS (Continued)

ILLUSTRATIONS (Continued)

TABLES

TABLES (Continued)

SUMMARY

This report covers work performed at Pratt & Whitney (P&W) on development of copper-based materials for long-life, reuseable, regeneratively cooled rocket engine thrust chambers. The work was performed to support development of a P&W expander cycle liquid hydrogen/liquid oxygen-fueled rocket engine for orbital transfer vehicle propulsion. The engine had a planned life of 300 cycles, so with safety factors, the thrust chamber material needed a life capability of 1200 cycles, which is greater than the life capabilities of either NASA-Z or Amzirc under similar conditions.

The program approached the goal of enhanced cyclic life through the application of rapid solidification to alloy development. Rapid solidification was used to introduce fine dispersions of stable compounds that would strengthen and stabilize the alloys at elevated temperatures. Such compounds included copper-base intermetallics, copper-free high-temperature intermetallics, borides, and silicides. Rapid solidification also allowed the refinement and control of microstructures.

Candidate alloy systems were screened in subscale by the use of small arc-cast ingots. Electron beam passes were made on these ingots to produce small subscale samples of rapidly solidified material for evaluation.

Copper alloys based on additions of chromium, cobalt, hafnium, silver, titanium, and zirconium, in various combinations, showed the most promise in the screening effort and were processed by rapid solidification in bulk quantities. Promising alloy compositions were atomized in the P&W rapid solidification rate (RSR) device to produce rapidly solidified powder. These powders were consolidated to bar stock, which was further processed and evaluated. Those alloys and conditions that exhibited the best phase stabilities and softening resistances were tensile tested at elevated temperature. Those alloys with favorable tensile properties were further characterized by additional tensile testing, thermal conductivity testing, and elevated-temperature, low-cycle fatigue (LCF) testing.

The characterization effort indicated that, of the alloys studied, rapid-solidification-processed Cu-1.1%Hf exhibited the greatest potential as an improved-life thrust chamber material. This alloy exhibited LCF life about four times that of NASA-Z at 705°C (1300°F). The alloy exhibited higher elevated-temperature tensile strengths and slightly lower thermal conductivities than NASA-Z.

Other alloys exhibited promise for use in this application. They were rapid-solidification-processed Cu-0.6%Zr and Cu-0.6%Zr-1.0%Cr. The former alloy exhibited higher thermal conductivities and LCF life than NASA-Z, but slightly lower tensile strengths. The latter alloy exhibited very high tensile strengths and thermal conductivities comparable to those of NASA-Z, but low LCF life. It seemed apparent that further work with these systems might allow the development of another well-balanced system superior to NASA-Z, providing material options in addition to the copper-hafnium alloy noted above.

SECTION I
INTRODUCTION

The objective of the Thrust Chamber Material Exploratory Technology Program was to develop a copper alloy that would provide longer lives than NASA-Z or Amzirc in an Orbital Transfer Vehicle engine (OTVE) thrust chamber application.

The Pratt & Whitney (P&W) OTVE concept envisioned high expander cycle performance resulting from the use of high thrust chamber wall temperatures. The maximum hot-wall temperature would be about 705°C (1300°F). This would result in maximum cyclic strain range of 3 percent. These constraints would be coupled with a conductivity requirement equivalent to that of Amzirc and a life capability of 1200 cycles.

These requirements exceeded the properties available from either Amzirc or NARloy-Z™ (trademark of Rocketdyne — called NASA-Z when made by NASA), commonly used for thrust chambers. Using half-hard + aged Amzirc, which exhibited the best low-cycle fatigue (LCF) properties, it was calculated that the proposed chamber would last 760 cycles, only 63 percent of the desired life. This analysis applied 540°C (1000°F) data to 705°C (1300°F) use, so the life may be even shorter.

This program was undertaken to develop a copper-based alloy that could support the envisioned thrust chamber as currently available alloys were not capable of doing so. This report describes the program and its results.

1. BACKGROUND

The P&W OTVE uses a milled-channel copper alloy regeneratively cooled thrust chamber. This concept came into use for high-pressure rocket engines in the late 1960s (1) and is used in the Space Shuttle Main Engine (SSME). The chamber is spun from a copper alloy, then machined to size on the outside diameter (OD) and inside diameter (ID). Longitudinal cooling channels are cut on the OD, as shown in Figure 1. These channels are filled with conductive wax, then the entire OD and wax are plated with copper. The OD is then covered with a thick structural electroformed layer of nickel, and machined to size (Figure 2). The wax is cleaned out of the channels, then the gas manifolds are attached.

Three copper alloys have been used for thrust chambers: Oxygen-Free High-Conductivity (OFHC) copper, Amzirc, and NARloy-Z™ (NASA-Z). Original test chambers were made of OFHC copper (1). This alloy was adequate to prove the design concept, but did not provide sufficient life for reuseable engines. Therefore, the other alloys were tested, in several comparative studies. The first study was done by Rocketdyne (2). They found that NARloy-Z™ (their alloy) exhibited longer LCF and actual chamber lives than Amzirc. They also found that commercial Amzirc exhibited more inclusions than NARloy-Z™ and was more difficult to process to a fine-grained condition.

The National Aeronautics and Space Administration-Lewis Research Center (NASA-LeRC) LCF tested a number of copper alloys and found half-hard + aged Amzirc to be most promising, exhibiting LCF lives longer than even NARloy-Z™ (3-6). They tested several NARloy-Z™ (and NASA-Z, the same alloy) chambers, one half-hard + aged Amzirc chamber, and several half-hard unaged Amzirc chambers (7,8,9). The half-hard + aged Amzirc chamber exhibited a longer life than the NARloy-Z™ (NASA-Z) chambers, which themselves exhibited longer lives than the unaged Amzirc chambers. NASA-Z and NARloy-Z™ have remained the alloys of choice for thrust chambers.

1
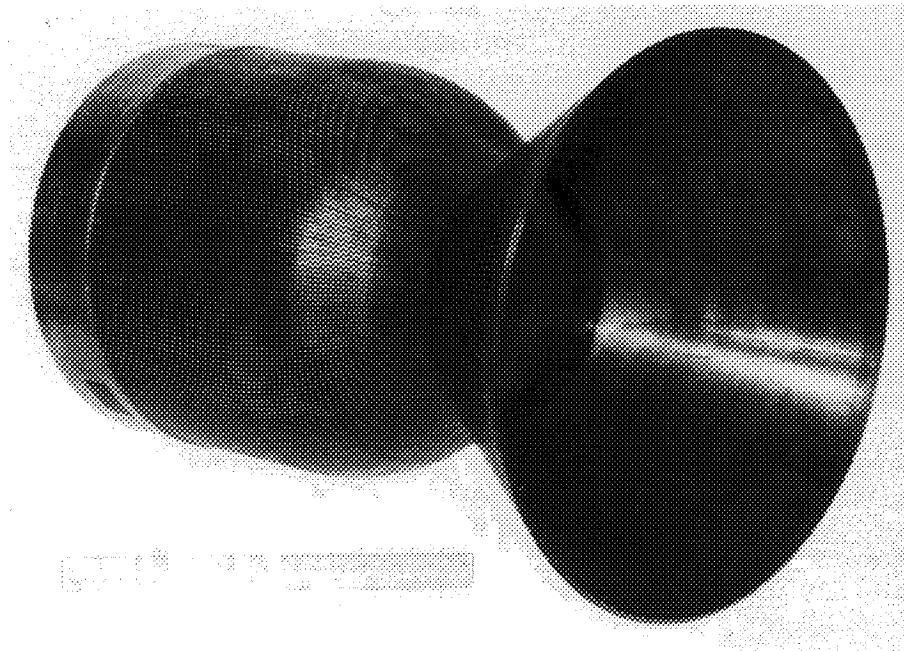
Figure 1. XLR 129 Chamber With Passages Machined
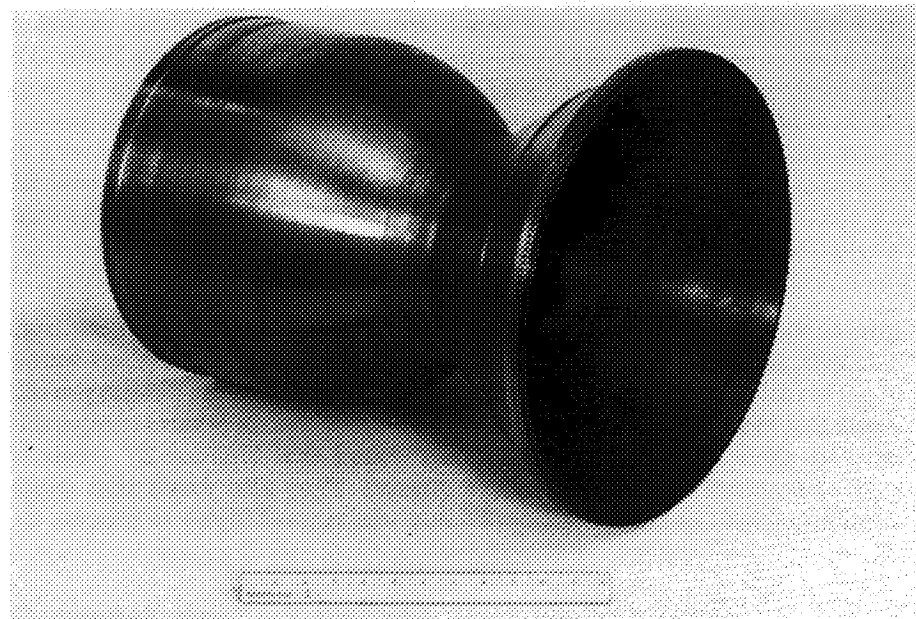
Figure 2. XLR 129 Chamber After Electroforming and Machining

P&W has made one regenerative copper alloy chamber, of Amzirc, and tested it in the XLR-129 engine (10). Tested 16 cycles, the chamber performed well, but failed at gross machining defects.

Copper alloy thrust chambers have been found to degrade or fail by four mechanisms: orange peel surface roughening, blanching, cracking at inclusions, and channel wall thinning.

Orange peel roughening was observed in Rocketdyne and NASA chamber tests (2,8). Such phenomena are commonly a result of the deformation of large-grain-size metals, as was the case in those tests.

Blanching is a surface degradation condition which has been described in numerous studies of failed NARloy-Z™ chambers (9). It usually occurs at hot spots on the chamber walls, and usually precedes channel wall thinning and failure. Descriptions of the phenomena are unclear. Suitable explanations have not been advanced. Rocketdyne has published reports that explain the phenomenon as a result of cyclic oxidation/reduction of the chamber surface (11,12).

Cracking at inclusions have been observed in both Rocketdyne and NASA tests (2,7,9). These are associated with either zirconia or copper-zirconium intermetallic inclusions. Little yielding of the surrounding matrix is observed at these failures.

The most troublesome, common, and insidious failure mechanism for copper alloy thrust chambers is channel wall thinning and rupture. First documented by NASA (7,8,9), this is characterized by the gradual deformation of the channel wall profile from the as-machined rectangle, Figure 3a, to a dog-house profile, Figure 3b, to a dog-house shape with a thinned wall, Figure 3c, and finally to rupture, Figure 3d. Although initial examinations of failures give the impression that the wall has thinned and lost material, careful measurement has revealed that no material has been lost (9,12,13). Instead, material has migrated from the mid-channel wall to the web region. In every case, this failure occurs at injector hot spots on the chamber (9).

Thinning and failure are accompanied by significant changes in microstructure (present work and 8). For NASA-Z, thinning is accompanied by recrystallization, as shown in Figure 4. Grains in the web are unaffected. Moving outward along the web, grains near the web/wall juncture experience some recrystallization, primarily along grain boundaries. At mid-span, the microstructure is completely recrystallized and reworked, with grain sizes of 20 um, and is beginning to recrystallize again. Microhardness has not been found to vary significantly through such a region in NASA-Z (8,9). However, this could be rationalized by the hardening effect of the silver in the alloy.

Samples of thinning in Amzirc were not available. This is unfortunate since, as will later be discussed, the silver-free copper-zirconium alloys do not appear to be as susceptible as NASA-Z to recrystallization — presumably due to the lower work-hardening rate produced by the absence of dissolved silver. Hardness losses were observed in the thinned areas of half hard + aged Amzirc chambers (9), however; indicating that recrystallization may occur also with that alloy.

The structural failure mechanism producing wall thinning and failure has been the subject of much study and controversy (2,7,8,9,12,13). Several names have been applied to the mechanisms: creep ratcheting, cyclic creep, low-cycle fatigue, thermal fatigue, and cyclic yielding. Several studies have been presented to account for the phenomenon. The most complete to date has been one by Rocketdyne (13) that seems to predict the observed changes in wall geometry through a series of chamber firings. This study finds that when an SSME chamber segment is operated at its design temperature of 540°C to 595°C (1000°F to 1100°F), no channel deformation should occur, which has been found in practice to be the case. However, when injector hot spots of up to 815°C (1500°F) are studied (here they believe creep to be a factor), the model predicts the observed channel wall deformation and thinning. As the wall thins, the biaxial ductility of the material is exhausted and the wall fails.

3

Hot Side

Wall

Web Channel

Closeout

a. Original Channels

b. Dog House Profiles

c. Thinned Dog House Profiles

d. Rupture of Channel Wall
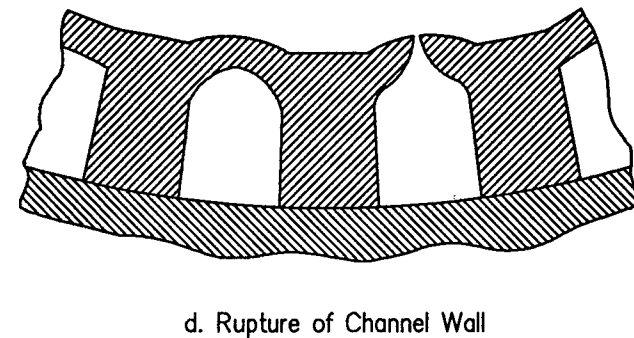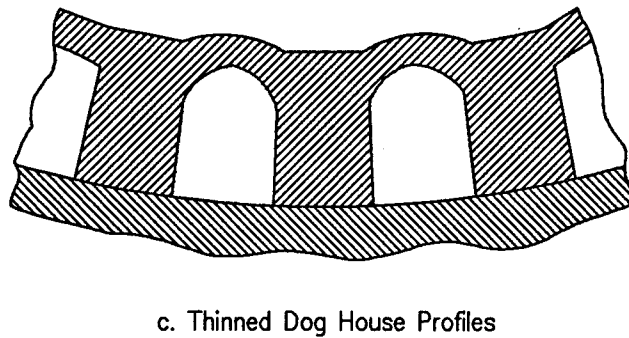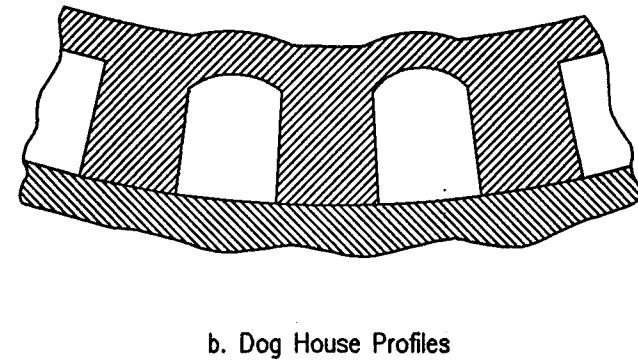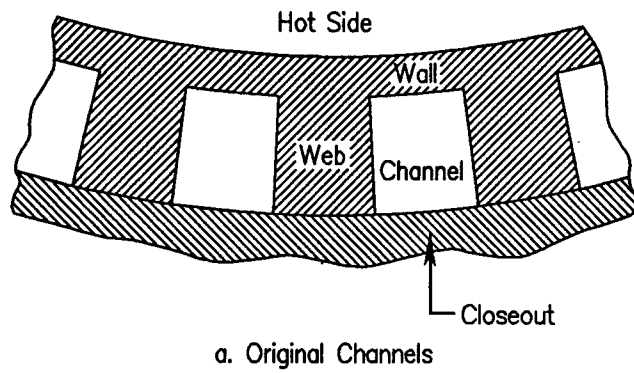
Figure 3. Channel Wall Thinning
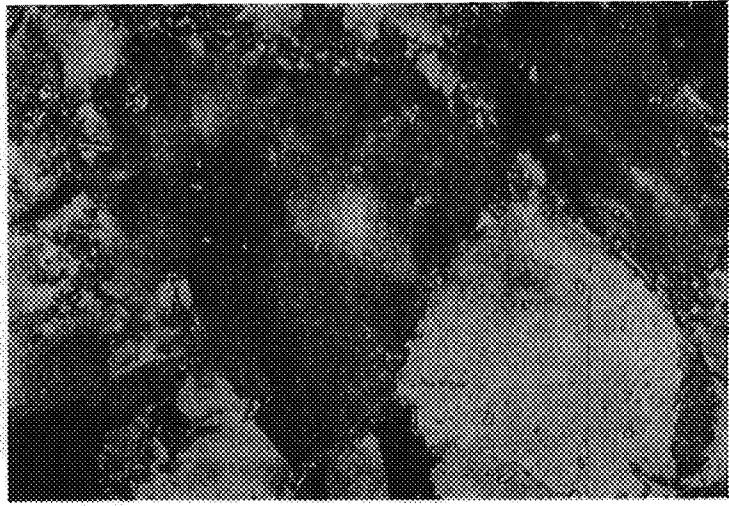
Figure 4. Microstructures in NASA-Z Test Chamber

Added to this model is the belief by investigators at NASA-LeRC that the softer local hot spots absorb the circumferential strains of the remainder of the chamber (9). This process could increase cyclic strains in the hot spot region to a level of about 10 percent, which is far above any design allowances.

2. PROGRAM PLAN

The goal of this program was to develop a copper alloy that would allow the use of the envisioned P&W OTVE thrust chamber within the envisioned operating parameters. This was believed to require enhancement of low cycle fatigue/thermal mechanical fatigue (LCF/TMF) capability, strength, and probably creep resistance. In addition, a thermal and structural analysis was performed to identify more-detailed property requirements, determine allowable property tradeoffs, and define specific mechanical testing parameters.

The alloy development effort encompassed several complementary approaches. Life capability improvements were attempted through the study of stable strengthening precipitates (solutionable), the introduction of stable strengthening dispersions through rapid solidification, and the reduction of segregation and defects through the use of rapidly solidified powder metallurgy. Life capability improvements were also sought through the use of oxide dispersion strengthening in work done under a subcontract to Professor N. Grant at the Massachusetts Institute of Technology (MIT). Retention of high thermal conductivity was to be attained through the use of low-solubility alloying additions.

The program was structured into the following tasks and subtasks.

Task 1:

1.1 Literature Survey and MIT Subcontract

A survey of the available literature was performed to gather background information on previous copper thrust chamber work and high-conductivity copper alloy development. Some candidate alloy systems were chosen based on this prior work. The results of the literature survey were presented as P&W FR-18383-1 (14).

A subcontract was issued to Prof. N. Grant of MIT to study various oxide-dispersion-strengthened copper alloy systems for possible use in thrust chambers.

1.2 Structural Analysis

Thermal and structural analyses were performed on the OTVE thrust chamber design to establish allowable tradeoffs between material properties and to identify property requirements. Results are presented in Appendix C.

1.3 Alloy Screening

Subscale laboratory alloy screening was performed to allow evaluation of candidate alloy systems prior to selection of alloys for atomization to powder, consolidation, and testing. Screening alloys were melted and cast into small buttons, worked, heat treated, annealed, and evaluated for softening resistance and microstructural stability. To assess the applicability of the alloys to rapid solidification, screening alloys were resolidified by narrow electron-beam passes, which remelted the alloys and allowed them

6

to solidify at a high rate, being quenched by the substrate. The electron-beam passes and substrates were subjected to cold rolling and anneals to allow assessment of the stabilities of the rapid solidification structures. Finally, rapidly solidified melt-spun ribbons were made of selected copper-metal-boride alloys to allow assessment of the processability of such alloys.

Task 2:

2.1 Power Production

Alloys selected for atomization to powder for further evaluation and testing were melted and atomized in a P&W 7-foot-diameter rotary powder atomization device.

2.2 Powder Processing and Evaluation

Powder alloys were consolidated by extrusion to bar stock and subjected to thermomechanical processing to allow evaluation of microstructural stability and softening resistance, and to provide bar stock for test specimens. Preliminary tensile tests were conducted to allow selection of alloys for property characterization.

Task 3:

3.1 Characterization

The most promising powder metal (PM) alloys were characterized by elevated temperature, tensile, creep, LCF/TMF, and thermal conductivity testing. Testing was conducted at conditions believed to adequately match those found in actual thrust chamber use.

The work was performed iteratively, with results of the screening efforts and PM alloy evaluations being used to guide further screening alloy and PM alloy selections. The logic steps are shown in Figure 5.

Two general iterations were made, resulting in two batches of powder alloys.

Screening alloy systems were chosen on the basis of the literature survey and previous experience at P&W on other alloy systems. Several types of alloy systems were chosen.

One system consisted of alloys that could be expected to form precipitates or dispersions, based on the alloy addition's solubility in solid copper. These included precipitation hardening systems found in the literature survey. These systems were also screened as dispersion systems by increasing the alloy content above the solid solubility limit and using rapid solidification to finely disperse the excess primary solidification precipitates. Being above the solid solubility limit, these dispersions could never be completely dissolved; if dimensionally stable, they could act as effective hardeners.

Another type of screening alloy system investigated encompassed additions that might form compounds so stable at high temperature (high melting point or free energy of formation) that if dispersed effectively in copper, they should remain well dispersed at high temperatures and stabilize the microstructure. These systems were comprised of borides, silicides, and high-temperature intermetallic compounds.

7

The last type of alloy system investigated here was a class of alloys that was expected to produce precipitates/dispersions having low lattice mismatch with the copper matrix. A low mismatch would be expected to minimize precipitate/dispersion coarsening at high temperatures. In most cases, low-solubility alloying additions were used.

The specific systems tried are listed, by type, in Table 1.

The screening alloys were evaluated in the cast + wrought form and in the rapidly solidified (+ wrought) forms. The latter were used to assess the effects of rapid solidification. Cast + wrought alloys were solution-treated, cold-worked (optional), aged, and then stability tested by a 12-hour, 650°C (1200°F) anneal (650°C was used to approximate the maximum use temperature without going so high as to rule out systems that were almost sufficiently stable). This allowed assessment of age-hardenability, cold-work hardenability, and softening resistance, giving a baseline view of the alloy characteristics. Rapidly solidified (electron-beam-processed) alloys were cold-worked (optional) and stability tested (650°C/12-hour anneal) to assess the stability of the dispersion and its effect on microstructure and softening resistance. Electron-beam processing was used to effect rapid solidification because it was simple, effective, and provided samples in a convenient form for further mechanical working and annealing.

From the results of the screening studies, powder alloys were formulated, processed, and evaluated. Powder metallurgy alloys were evaluated after extrusion consolidation, and various post-consolidation wrought and thermal treatments. Again, the intention was to assess the stability of precipitates/dispersions and microstructure after deformation and thermal extrusions. The 650°C/12-hour stability test anneal was used here also.

Mechanical and physical property testing was conducted under conditions expected to simulate thrust chamber conditions. All testing was conducted under argon or vacuum (thermal conductivity) to avoid oxidation effects. Testing was conducted in the range of room temperature to 705°C (1300°F), which is the expected maximum hot-wall temperature. Mechanical tests were conducted at the high end of the temperature range, since that was where the significant effects were expected. Mechanical tests were conducted at strain rates expected to be present in the hardware, since some alloys might be more strain rate sensitive than others. Creep testing was conducted at the yield stress, since the high strains existing in the part cause any holds to occur after it has yielded. LCF testing was conducted under conditions as closely approximating actual service as present testing capability would permit.

8
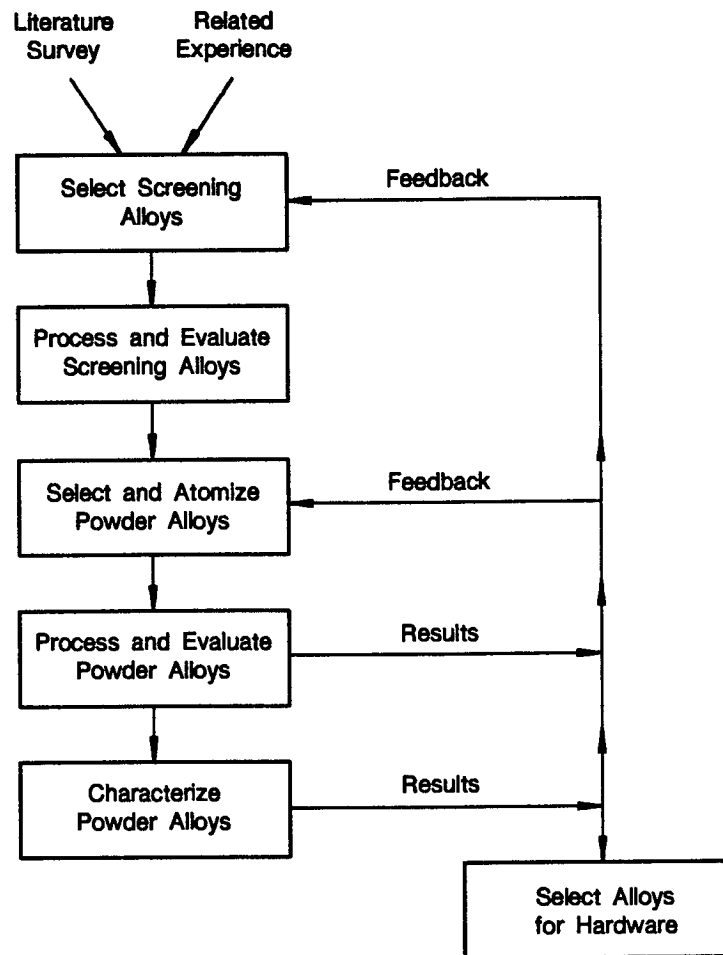
Figure 5. Program Logic

TABLE 1. — SCREENING ALLOY SYSTEMS AND EXPECTED STRENGTHENING PHASES

Conventional Systems		High-Temperature Dispersions	
Cu-Zr	(Cu$_5$Zr)	Borides (1-2 at.%)	
Cu-Cr	(Cr)		
Cu-Ag	(Ag)	Cu-Zr-B	(ZrB$_2$)
Cu-Hf	(Cu$_5$Hf)	Cu-Hf-B	(HfB$_2$)
Cu-Nb	(Nb)	Cu-Ti-B	(TiB$_2$)
Cu-V	(V)	Cu-MM-B	(MMB$_6$)
Cu-MM	(Cu$_6$MM)	Cu-Y-B	(YB$_6$)
Cu-Y	(Cu$_6$Y)	Cu-V-B	(VB$_2$)
Cu-Mo	(Mo)	Cu-Cr-B	(CrB$_2$)
Cu-Zr-Cr	(Cu$_5$Zr, Cr)	Cu-Nb-B	(NbB$_2$)
Cu-Zr-Ag	(Cu$_5$Zr, Ag)	Cu-Mo-B	(MoB)
Cu-Zr-Hf	(Cu$_5$Zr, Cu$_5$Hf)	Cu-Al-B	(AlB$_{12}$)
Cu-Zr-Nb	(Cu$_5$Zr, Nb)	Cu-Si-B	(SiB)
Cu-Zr-V	(Cu$_5$Zr, V)	Cu-Ni-B	(NiB$_2$)
Cu-Zr-MM	(Cu$_5$Zr, Cu$_6$MM)	Cu-Fe-B	(FeB)
Cu-Zr-Y	(Cu$_5$Zr, Cu$_6$Y)	Cu-Co-B	(Co$_2$B)
Cu-Zr-Mo	(Cu$_5$Zr, Mo)	Ci-Zr-B-Ag	(ZrB$_2$)
Cu-Zr-Ti	(Cu$_5$Zr, Cu$_x$Ti)	Cu-Ti-B-Ag	(TiB$_2$)
Cu-Zr-Cr-Ag	(Cu$_5$Zr, Cr, Ag)	Cu-MM-B-Ag	(MMB$_6$)
Cu-Cr-Ti	(Cr, Cu$_x$Ti)	Cu-Ti-B-Cr	(TiB$_2$, Cr)
Cu-Cr-Y	(Cr, Cu$_6$Y)		
Cu-Cr-MM	(Cr, Cu$_6$MM)	Silicides (2 at.%)	
Cu-Cr-V	(Cr, V)		
Cu-Cr-Nb	(Cr, Nb)	Cu-Nb-Si	(Nb$_5$Si$_3$)
Cu-Cr-Hf	(Cr, Cu$_5$Hf)	Cu-Cr-Si	(Cr$_3$Si)
Cu-Cr-Ag	(Cr, Ag)	Cu-Hf-Si	(Hf$_3$Si$_2$)
Cu-Cr-Hf-Ag	(Cr, Cu$_5$Hf, Ag)	Cu-Ti-Si	(Ti$_5$Si$_3$)
Cu-Hf-Ag	(CU$_5$Hf, Ag)	Cu-Zr-Si	(Zr$_3$Si$_2$)
Cu-Ti-Ag	(Cu$_x$Ti, Ag)	Cu-Y-Si	(YSi$_2$)
Cu-Ti-Hf	(Cu$_x$Ti, Cu$_5$Hf)		

Low-Mismatch Compounds, (misfit) (2 at.%)		Intermetallics (2 at.%)	
		Cu-Hf-Fe	(HfFe$_2$)
Cu-Cr-Fe	(Cr w/Fe, <2.2%**)	Cu-Hf-Mn	(HfMn$_2$)
Cu-Cr-Co	(Cr w/Co, <2.2%**)	Cu-Hf-Ni	(HfNi$_2$)
Cu-Al-Ni	(Ni$_3$Al, 1.1%)	Cu-Hf-Co	(HfCo$_2$)
Cu-Zr-Al	(Zr$_3$Al, 21%)	Cu-Fe-Ti	(Fe$_2$Ti)
Cu-Co-V	(Co$_3$V, 1.5%	Cu-Fe-Nb	(Fe$_2$Nb)
Cu-Ni-Si	(Ni$_3$Si, 3.0%)	Cu-Fe-Zr	(Fe$_2$Zr)
Cu-Ag-Y	(AgY, 0.1%)	Cu-Ni-Zr	(Ni$_4$Zr)
Cu-Cr-Hf	(Cr$_2$Hf, 2.5%*)	Cu-Ti-Al	(Ti$_3$Al)
Cu-Fe-Y	(Fe$_2$Y, 1.7%*)		
Cu-Co-Y	(Co$_2$Y, 0.1%)		

MM = mischmetal
* Based on 2x copper lattice (2a=7.23Å)
** Kurdjemov-Sachs, along Cu <110> and Cr <111>

SECTION II
EXPERIMENTAL PROCEDURE

1. SCREENING EFFORT

Screening alloys having the compositions listed in Table 2 were melted, processed via the flowsheets in Figures 6 through 8, and evaluated as described below.

a. Screening Alloy Melting

Screening alloys were arc-melted under argon with a nonconsumable tungsten electrode in a water-cooled copper hearth and cast in-situ, producing button castings weighing 100 to 400 grams. Arc melting was performed in a device (Figure 9) that incorporated a 1200-amp power supply. The procedure for arc melting was:

1. Charge hearth with elemental additions (C10100 copper was used. Cu-15%Cr and Cu-30%Zr master alloys were used in applicable alloys after CB-43).

2. Close device, pump down to 10 millitorr or less (by thermocouple gauge), backfill with Ar, pump down to 2 millitorr or less, backfill with Ar to 28 kPa (4 psig.)

3. Arc melt and mix with arc for 1 to 1-1/2 minutes. Let cool.

4. Open chamber, flip button, repeat steps 2 and 3, remove button.

b. Screening Alloy Processing

Buttons were cut up and processed by conventional wrought processing and rapid solidification processing according to Table 2 and the flow sheets in Figures 6 - 8.

Conventional processing consisted of heat treatments and rolling. Solution and age-heat treatments were performed in air-atmosphere electric furnaces. The 650°C (1200°F) stability test anneals were performed in a vacuum furnace, operating at over 10^{-4} microns vacuum, and employing a heatup rate of about 550°C/hr (1000°F/hr) and a cooldown rate of about 330°C/hr (600°F/hr). Rolling was accomplished on a 2-high rolling mill with 10-inch-diameter rolls. Soaks prior to hot rolling lasted about 30 minutes, and reheats about 5-10 minutes. Reductions per pass were about 20-25 percent for hot rolling, 10 percent for cold rolling. No intermediate anneals were used in cold rolling.

Rapidly solidified samples of screening alloys were prepared by traversing a 3mm (1/8-inch) thick slice of the cast or hot-rolled alloy with an electron beam. Several beam passes were made on each alloy slice, spaced about 3mm (1/8-inch) apart. Beam pass parameters were: 100-kV beam voltage, 10-mA beam current, and 90 inches/minute beam traverse speed. Part of the sample was cut off for as-solidified evaluation, another was cut off for the 650°C stability test (optional: see flowcharts), and the remainder was clad in a piece of copper tube. This was cold-rolled (see flowcharts for reductions), and a portion of the cold-rolled sample was subjected to the 650°C stability test.

11

TABLE 2. — SCREENING ALLOYS

Button No.	Aim Composition (wt.%)	Solution Temperature		EB Process	Remarks
		°C	°F		
CB-1	Cu-1.0Ag	790	1450		
CB-2	Cu-3.0Ag	790	1450		
CB-3	Cu-5.0Ag	790	1450		
CB-4	Cu-0.5Zr-3.0Ag	925	1700	Yes	NASA-Z equivalent
CB-5	Cu-0.2Zr	925	1700		Amzirc equivalent
CB-6	Cu-0.4Zr	925	1700	Yes	
CB-7	Cu-1.0Zr	925	1700	Yes	
CB-16	Cu-0.2Zr-1.5Ag	925	1700		NASA 1.1 equivalent
CB-17	Cu-1.1Zr-0.3B	925	1700	Yes	ZrB_2
CB-18	Cu-2.2Hf-0.3B	925	1700	Yes	HfB_2
CB-19	Cu-0.7Ti-0.3B	925	1700	Yes	TiB_2
CB-20	Cu-0.8MM-0.4B	870	1600	Yes	MMB_6
CB-21	Cu-0.4Cr	925	1700		
CB-22	Cu-1.0Cr-0.8Zr	925	1700	Yes	Undissolved Cr
CB-23	Cu-1.0Cr	925	1700	Yes	Undissolved Cr
CB-24	Cu-0.2Zr-1.5Ag	925	1700		
CB-25	Cu-0.4Cr-0.2Zr	925	1700		
CB-26	Cr-0.6Zr-0.13B	NA		Yes	ZrB_2
CB-27	Cu-1.0Zr-0.13B	NA		Yes	ZrB_2+Zr
CB-28	Cr-0.6Zr-0.25B	NA		Yes	ZrB_2+B
CB-29	Cu-0.35Ti-0.16B	NA		Yes	TiB_2
CB-30	Cu-0.50Ti-0.16B	NA		Yes	TiB_2+Ti
CB-31	Cu-0.35Ti-0.30B	NA		Yes	TiB_2+B
CB-32	Cu-0.4V-0.13B	925	1700	Yes	VB_2
CB-33	Cu-0.55Zr-0.16B-1.0Ag	925	1700	Yes	ZrB_2+Ag
CB-34	Cu-0.8Hf	925	1700		
CB-35	Cu-1.3Hf	925	1700	Yes	
CB-36	Cu-0.2Zr-0.8Hf	925	1700		
CB-37	Cu-0.8Zr-1.3Hf	925	1700	Yes	
CB-43	Cu-1.0Cr	1000	1830	Yes	
CB-44	Cu-0.5Cr	1000	1830		
CB-45	Cu-0.2Cr	1000	1830		
CB-46	Cu-1.0Cr-0.8Zr	955	1750	Yes	
CB-47	Cu-0.4Cr-0.8Zr	955	1750	Yes	
CB-48	Cu-0.4Cr-0.2Zr	955	1750	Yes	
CB-49	Cu-0.5V	1040	1900		
CB-50	Cu-0.2Zr-0.5Hf	955	1750	Yes	
CB-51	Cu-0.6Zr-0.5Hf	955	1750	Yes	
CB-52	Cu-0.6Zr-1.2Hf	955	1750	Yes	
CB-53	Cu-0.7MM-0.3B	845	1550	Yes	MMB_6
CB-54	Cu-0.7MM-0.4B	845	1550	Yes	MMB_6
CB-56	Cu-0.4Y-0.3B	870	1600	Yes	YB_6
CB-57	Cu-0.6V-0.2B	1050	1920	Yes	VB_2
CB-58	Cu-0.6Cr-0.2B	1000	1830	Yes	CrB_2
CB-59	Cu-1.0Nb-0.2B	1050	1920	Yes	NbB_2
CB-60	Cu-1.5Mo	NA			
CB-61	Cu-1.5Mo-0.2B	NA		Yes	MoB
CB-62	Cu-0.1Al-0.3B	1050	1920	Yes	AlB_{12}
CB-63	Cu-0.4Si0.2B	1000	1830	Yes	SiB
CB-64	Cu-0.2Cr-0.8Zr	955	1750	Yes	
CB-65	Cu-2.0Cr-2.0Zr	955	1750	Yes	
CB-66	Cu-0.2Y	870	1600	Yes	
CB-67	Cu-0.4Y	870	1600	Yes	
CB-68	Cu-1.0Y	870	1600	Yes	

TABLE 2. — SCREENING ALLOYS (CONTINUED)

Button No.	Aim Composition (wt.%)	Solution Temperature °C	Solution Temperature °F	EB Process	Remarks
CB-69	Cu-0.4MM	845	1550	Yes	
CB-70	Cu-1.0MM	845	1550	Yes	
CB-71	Cu-0.8Zr-0.4Y	870	1600	Yes	
CB-72	Cu-0.8Zr-1.0Y	870	1600	Yes	
CB-73	Cu-0.8Zr-0.4MM	845	1550	Yes	
CB-74	Cu-0.8Zr-1.0MM	845	1550	Yes	
CB-75	Cu-0.4Cr-0.4Y	870	1600	Yes	
CB-76	Cu-1.0Cr-1.0Y	870	1600	Yes	
CB-77	Cu-0.4Cr-0.4MM	845	1550	Yes	
CB-78	Cu-1.0Cr-1.0MM	845	1550	Yes	
CB-79	Cu-0.4Mo	1050	1920	Yes	
CB-80	Cu-0.4Zr-0.4Mo	955	1750	Yes	
CB-81	Cu-1.8Nb-0.3Si	1000	1830	Yes	
CB-82	Cu-1.2Cr-0.2Si	1000	1830	Yes	
CB-83	Cu-3.3Hf-0.4Si	955	1750	Yes	
CB-84	Cu-1.0Ti-0.3Si	955	1750	Yes	
CB-85	Cu-1.7Zr-0.4Si	955	1750	Yes	
CB-86	Cu-0.9Y-0.6Si	870	1600	Yes	
CB-87	Cu-0.7Nb	1040	1900	Yes	
CB-88	Cu-1.3Nb	1040	1900	Yes	
CB-91	Cu-1.0Cr-1.0Nb	1000	1830	Yes	
CB-92	Cu-2.0Cr-2.0Nb	1000	1830	Yes	
CB-93	Cu-1.2V	1050	1920	Yes	
CB-94	Cu-0.2Zr-0.5V	955	1750	Yes	
CB-95	Cu-0.8Zr-1.0V	955	1750	Yes	
CB-96	Cu-0.4Cr-0.5V	1000	1830	Yes	
CB-97	Cu-1.0Cr-1.0V	1000	1830	Yes	
CB-98	Cu-0.4Cr-0.8Zr-1.0Ag	955	1750	Yes	
CB-99	Cu-0.4Cr-1.0Ag	1000	1830	Yes	
CB-100	Cu-0.7Ti-0.3B-1.0Ag	955	1750	Yes	TiB_2+Ag
CB-101	Cu-0.8MM-0.4B-1.0Ag	845	1550	Yes	MMB_6+Ag
CB-102	Cu-1.0Cr-0.7Ti-0.3B	955	1750	Yes	TiB_2+Cr
CB-104	Cu-0.2Zr-0.7Nb	955	1750	Yes	
CB-105	Cu-0.8Zr-1.3Nb	955	1750	Yes	
CB-107	Cu-2.2Zr-0.2Al	955	1750		Zr_3Al
CB-108	Cu-1.1Ti-0.2Al	955	1750		Ti_3Al
CB-109	Cu-1.4Co-0.4V	1020	1870	Yes	Co_3V
CB-110	Cu-1.4Ni-0.2Si	955	1750		Ni_3Si
CB-111	Cu-1.6Ag-1.4Y	870	1600		AgY
CB-112	Cu-1.0Cr-2.0Hf	955	1750		Cr_2Hf
CB-113	Cu-1.1Fe-1.0Y	870	1600		Fe_2Y
CB-114	Cu-1.2Co-1.0Y	870	1600		Co_2Y
CB-115	Cu-1.4Ni-0.2Al	1020	1870		Ni_3Al
CB-116	Cu-0.6Cr-3.0Ag	1000	1830		
CB-117	Cu-0.8Hf-3.0Ag	940	1725		
CB-118	Cu-0.6Cr-0.8Hf	940	1725	Yes	
CB-119	Cu-0.6Cr-0.6Zr-3.0Ag	940	1725		
CB-120	Cu-0.6Cr-0.8Hf-3.0Ag	940	1725		
CB-121	Cu-0.6Cr-0.7Ti	940	1725		
CB-122	Cu-0.6Zr-0.7Ti	940	1725		
CB-123	Cu-0.8Hf-0.7Ti	940	1725	Yes	
CB-124	Cu-1.0Ti-3.0Ag	900	1650		
CB-125	Cu-0.6Cr-0.2Fe	1000	1830		(CrFe)

TABLE 2. — SCREENING ALLOYS (CONTINUED)

Button No.	Aim Composition (wt.%)	Solution Temperature °C	Solution Temperature °F	EB Process	Remarks
CB-126	Cu-0.6Cr-0.2Co	1000	1830	Yes	(CrCo)
CB-127	Cu-0.6Ni-0.2B	1025	1880	Yes	NiB_2
CB-128	Cu-0.9Fe-0.2B	1025	1880	Yes	FeB
CB-129	Cu-1.2Co-0.2B	1025	1880	Yes	Co_2B
CB-130	Cu-1.9Hf-1.1Fe	940	1725	Yes	$HfFe_2$
CB-131	Cu-1.9Hf-1.1Mn	940	1725	Yes	$HfMn_2$
CB-132	Cu-1.9Hf-1.2Ni	940	1725	Yes	$HfNi_2$
CB-133	Cu-1.9Hf-1.2Co	940	1725	Yes	$HfCo_2$
CB-134	Cu-1.1Fe-0.5Ti	940	1725	Yes	Fe_2Ti
CB-135	Cu-1.1Fe-1.0Nb	1025	1880	Yes	Fe_2Nb
CB-136	Cu-1.1Fe-1.0Zr	940	1725	Yes	Fe_2Zr
CB-137	Cu-1.5Ni-0.6Zr	940	1725	Yes	Ni_4Zr
CB-138	Cu-0.4Y-0.3B	NA			Check for YB_6
CB-139	Cu-1.0Nb-0.2B	NA			Check for NbB_2
CB-140	Cu-0.6Al- 0.3B	NA			Check for AlB_{12}
CB-144	Cu-0.05Ti-0.01Hf-0.2Al	940	1725		
Amzirc	Cu-0.15Zr	925	1700		Commercial material
NASA-Z	Cu-0.5Zr-3.0Ag	925	1700	Yes	NASA LeRC material

Material origins:
   CB-1 — CB-6: P&W Materials Engineering Research Lab., E. Hartford, CT
   CB-7 — CB-37: United Technologies Research Center, E. Hartford, CT
   CB-43 — CB-144: P&W Florida; used Cu-15%Cr and Cu-30%Zr master Alloys.
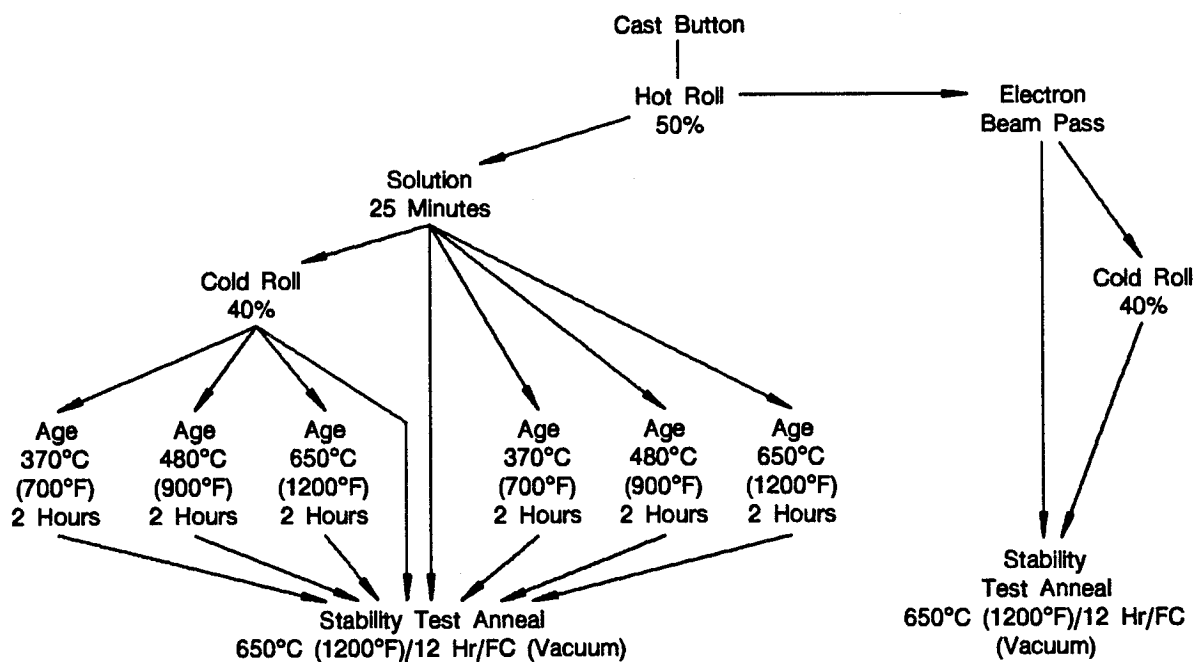
Figure 6. Screening Flow Chart: Alloys CB-1 Through CB-25 and CB-34 Through CB-37

14
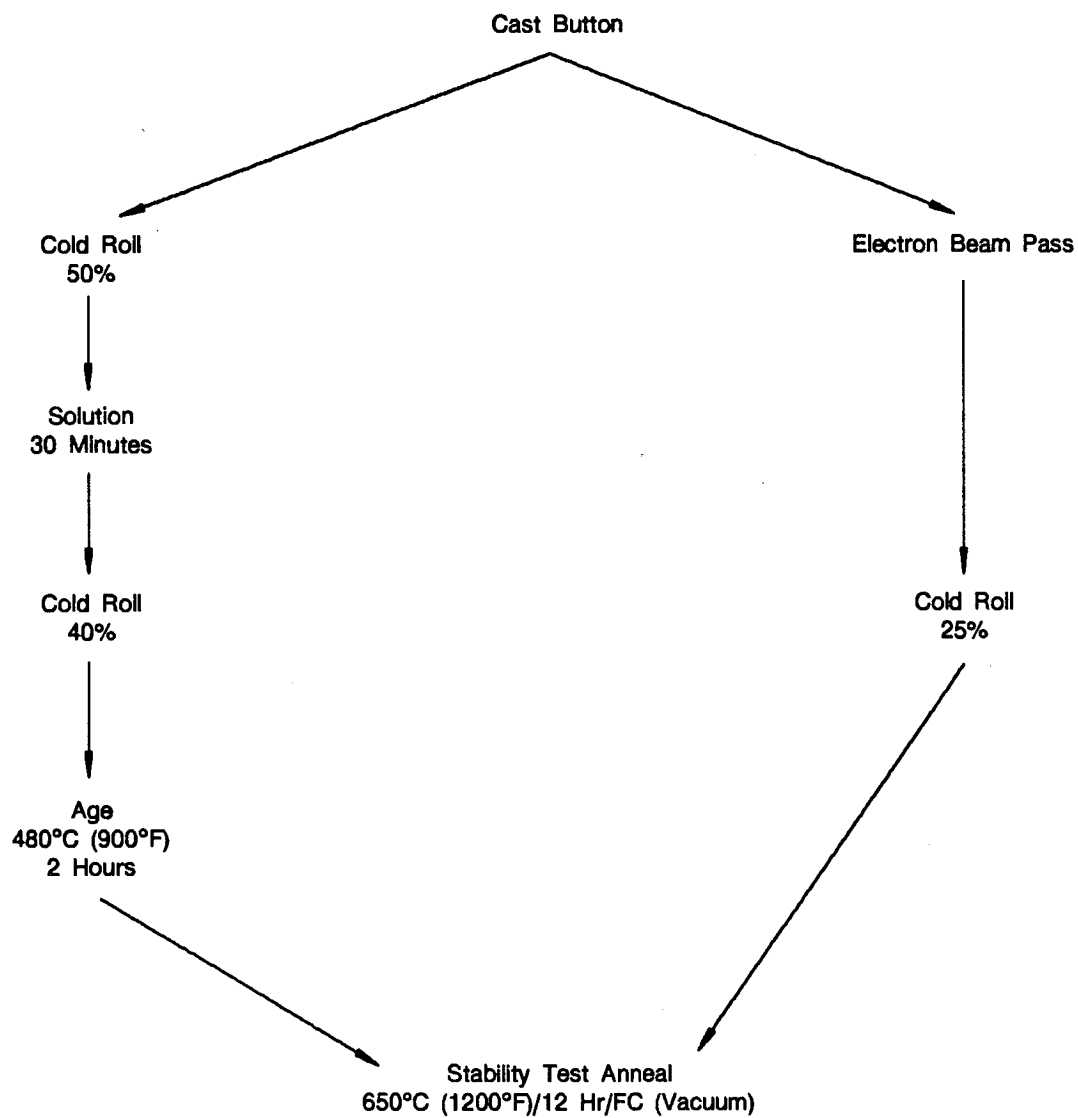
Figure 7. Screening Flow Chart: Alloys CB-43 through CB-107, CB-109 through CB-120, CB-125, CB-126, and CB-138 through CB-144
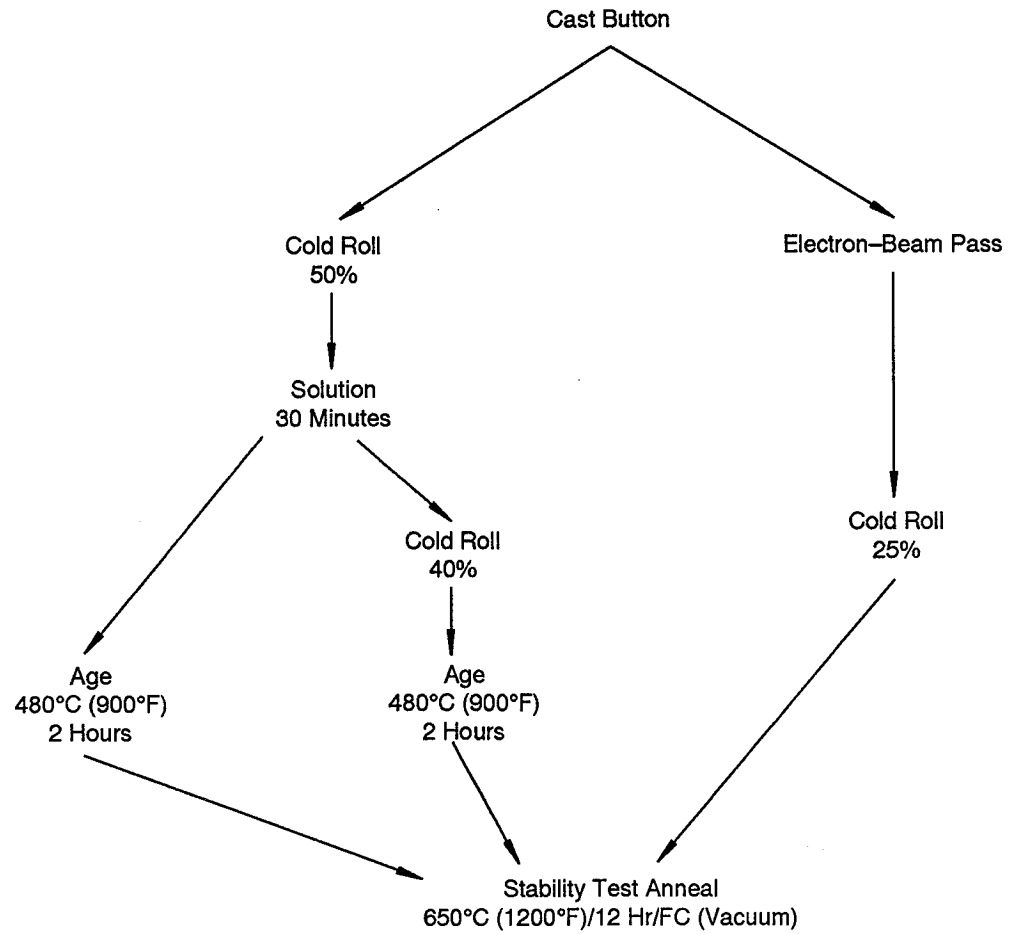
Figure 8. Screening Flow Chart: CB-108, CB-121 through CB-124, and CB-127 through CB-137
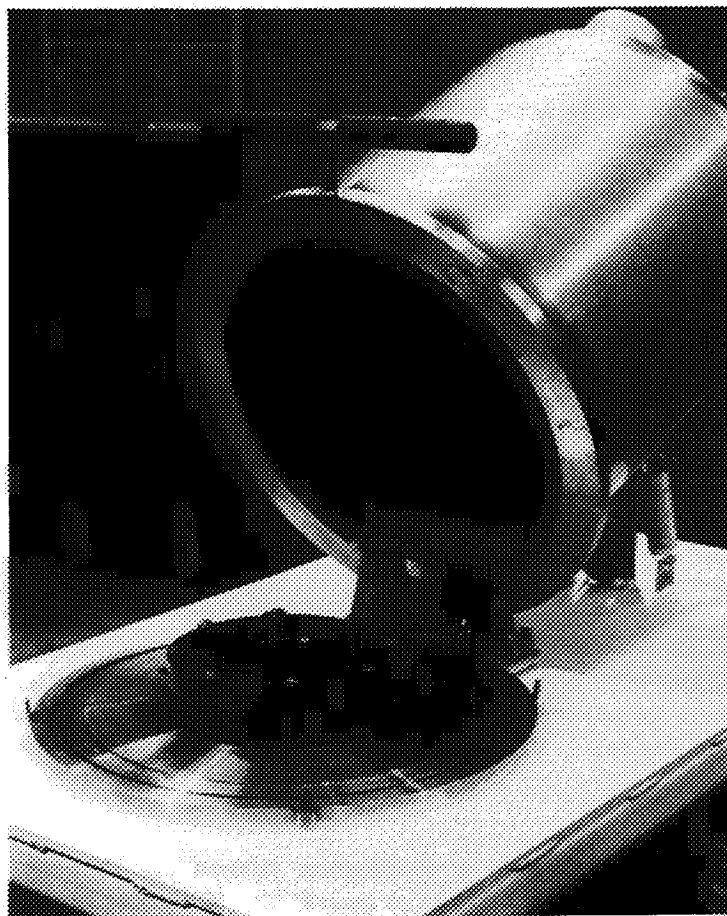
Figure 9.   P&W Arc Button Melter

Rapidly solidified samples of copper-zirconium-boron alloys were also prepared on a P&W-built melt spinner, shown schematically in Figure 10. This jet-type spinner employed a 200 mm-(8-inch)-diameter by 25 mm-(1-inch)-thick copper wheel driven directly by a variable-speed motor. Wheel speed was monitored by a digital tachometer employing a magnetic pickup. The alloy, generally cut from an arc-melted button, was melted in a 1/2-inch-diameter tubular quartz crucible coated on the inside with a fired Al_2O_3 coating (Taycor 341 slurry, applied, dried at 100°C (210°F), fired 500°C (930°F)/2 hr + 600°C (1110 °F)/6 hr). The crucible had a 1-mm orifice at the bottom. Heat was supplied by a 9 1/2-turn induction coil (4.7 mm or 3/16 inch OD tube) powered by a variable-power, high-frequency supply. The crucible top was covered with a fitting employing a viewport at the end and a helium inlet port for jet pressurization. At times, an Ircon 2-color pyrometer was sighted through the viewport to monitor melt temperature. The entire device was enclosed in a drybox with a vacuum pump and attendant plumbing to allow inert operation. The melt spinning process entailed:

1.   Set up with charge in quartz tube.

2.   Pump out drybox 30 minutes. Backfill box with helium to positive pressure.

3.   Turn on wheel motor and adjust speed.

4.   Turn on induction furnace, adjust power until desired melt temperature is reached.

17

5. Turn on jet gas to force melt through crucible orifice onto wheel, where it solidifies before being flung off.

6. Turn off furnace, motor. Open drybox and collect ribbon.

Ribbons were spun using the parameters in Table 3 and evaluated as-solidified.

c. Screening Alloy Evaluation

Cast + wrought screening alloys were evaluated by optical microscopy, scanning electron microscopy, electron microprobe, microhardness, and x-ray diffraction. The rapidly solidified materials were evaluated by optical microscopy, scanning electron microscopy, transmission electron microscopy of extraction replicas, electron microprobe, and microhardness. Melt-spun ribbon was evaluated by optical microscopy and electron microbprobe. Details of these methods are discussed later.

2. POWDER PRODUCTION

The compositions atomized and general atomization parameters are listed in Tables 4 - 6. Atomized alloys were formulated from elemental charges, late elemental additions, and master alloys, as shown in the table. Assays of the constituents used are shown in Table 7.

a. Master Alloy Production

Master alloys were melted in a 45-kilogram (100-pound) capacity vacuum-induction melting furnace, using a silica-stabilized alumina crucible (10 percent silica) and copper or steel molds. Elemental additions were used and were added to the molten copper. Vacuum melting parameters are shown in Table 8.

b. Powder Production

Copper-based powders were atomized in the P&W 2-meter (7-foot)-diameter RSR device. The device is shown in Figures 11 and 12. This device incorporates a 140-kilogram (300-pound)-capacity induction melting furnace with late addition capability. Below the furnace is an induction-heated tundish and metering nozzle system that directs a stream of molten copper alloy on to the center of the atomizer. The atomizer is a horizontal 100-mm (4-inch)-diameter disk that spins at 35,000 rpm (turbine driven). The molten metal is accelerated off of the disk in the form of fine droplets that are then quenched and solidified by a curtain of flowing helium gas. The resulting powder falls to the bottom of the chamber and into a collector can. The helium flows past the collector can, into a cyclone separator where airborne particles are removed, and into a system of coolers and a blower to return to the atomizer device for reuse. The device is fully instrumented with thermocouples, pyrometers, speed transducers, pressure gauges, closed-circuit television with video recorders, and high-speed movie cameras. Alumina-10% silica crucibles and tundishes are used.

RSR device operation entails the following steps.

1. Charge is melted under a vacuum of about 100 microns. About 3 minutes before atomization begins, any late additions are added.

2. The system is filled with gaseous helium, to 14 kPa (2 psig).

3. The turbine and atomizer disk are brought up to speed and the helium recirculator blower is turned on.

4. The metal is poured from the melt furnace into the tundish, from which it pours onto the atomizer disk. Atomization commences. Atomization continues, while parameters and data are monitored.

5. When the melt is exhausted, the turbine is turned off, the furnace power is shut off, and the recirculator blower is shut off.

6. The lower head is blown out with helium to flush settled powder into the collector can. Then a ball valve at the top of the collector can is closed and the sealed can is removed from the device.

7. The device is then disassembled, cleaned, and set up for reuse.

Run parameters for the copper alloys are listed in Tables 4 - 6.

c. Powder Handling

After atomization, the powder is transferred via the sealed collector can to a helium-filled glove box. The can is attached to the glove box and emptied into it. The powder is screened into the desired size fractions inside the box, using 200 mm-(8-inch)-diameter Tyler screens. Powder not used immediately is stored under helium in glass Ball-type canning jars.

d. Powder Evaluation

Atomized powder was evaluated by optical and scanning electron microscopy, electron microprobe, x-ray diffraction, water analysis, oil analysis, oxygen analysis, carbon analysis, and chemical analysis by inductively coupled plasma emission spectrophotometry.

3. POWDER PROCESSING

a. Vacuum Hot Compaction Consolidation

Samples of copper alloy powders were hot vacuum consolidated for cleanliness evaluation. This was performed in a P&W vacuum hot compaction/diffusion bonding press, which is essentially a small vacuum isothermal forging press. Powder samples were poured into a 90 mm long × 45 mm-diameter × 1.2 mm wall thickness (3.5-inch × 1.75-inch × 0.05 inch) austenitic stainless steel closed-bottom cylindrical can (in air). Multiple samples were separated with sheets of nickel foil. The top of the powder was covered with a 0.07-inch-thick stainless steel disk, and the entire assembly was coated with a boron nitride parting compound, placed in a TZM molybdenum die, and covered with a TZM molybdenum punch. The assembly was placed in the vacuum hot press and instrumented with thermocouples. The press was closed, pumped out to better than 5×10^{-5} microns, heated for 1.5 hours to 760°C (1400°F), and held at temperature another 2 hours. Next, compaction pressure of 200 MPa (30 ksi) was applied gradually over 30 minutes and held another 2 hours at a temperature of 760°C (1400°F). The compaction force was then removed, the unit cooled (12 hours) and backfilled, and the part removed. Powder alloy samples of Alloy 992, 993, 994, 995, 996, 997, 998, and 999 were compacted in this manner.

Glass View Port

Stainless Tubes

Argon for Spray

Hose

Clamp

Alumina-Coated
Quartz Crucible

Coil Leads

Induction Coil

Wheel Wiper

Gap = 1.5 mm

Copper
Wheel

Rotation

Bearing

Support

4 cm
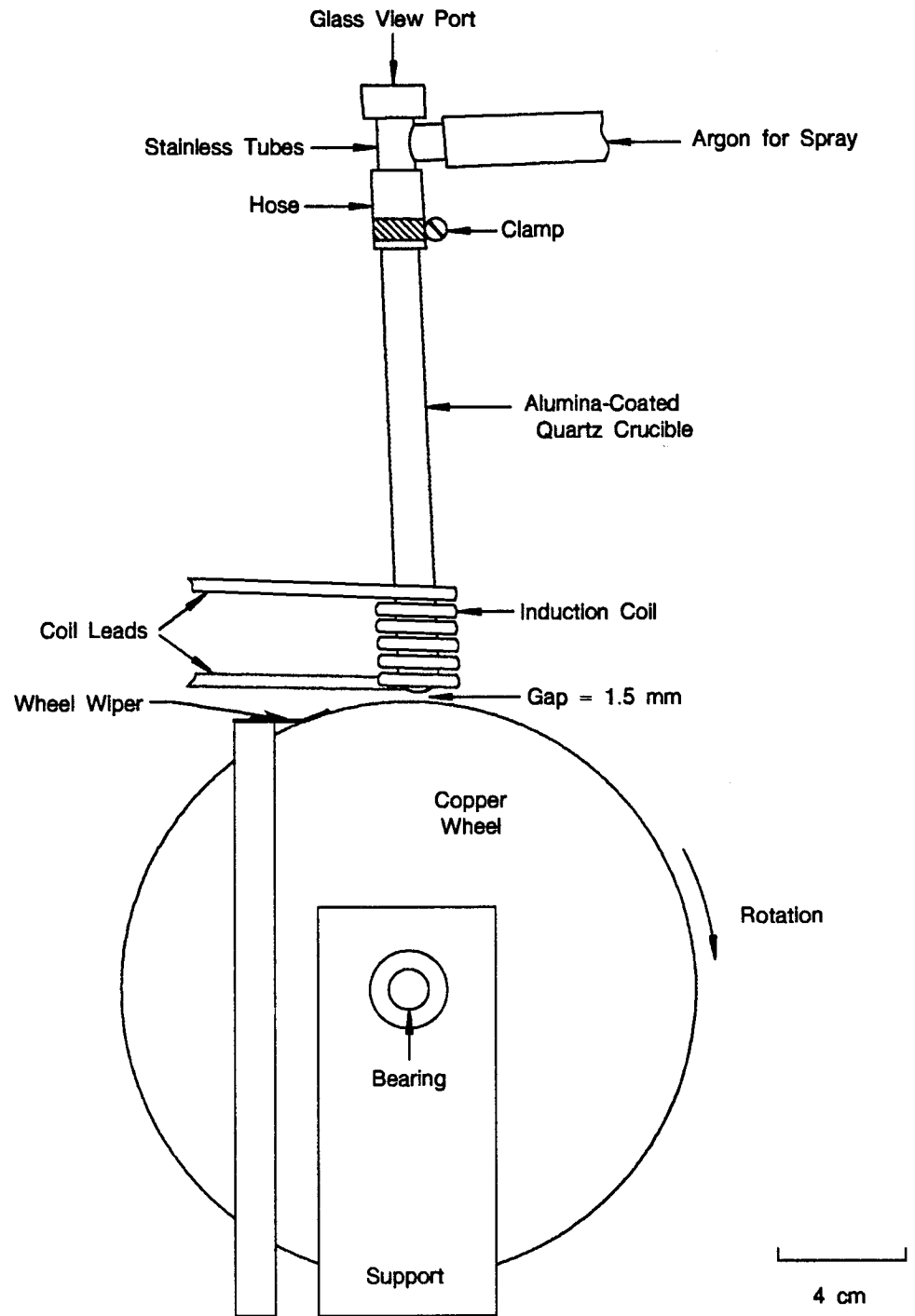
Figure 10.   P&W Florida ME&T Melt Spin Rig

20

TABLE 3. — MELT SPINNING PARAMETERS

Run	Alloy	Temperature °C	°F	Wheel Speed (rpm)	Gas Pressure kPa	psig	Comments
1	CB-26	Melt		2400	69	10	
2	CB-26	1420	2600	2400	69	10	
3	CB-26	1370	2500	2500	76	11	Hold melt one minute
4	CB-26	1540	2800	2500	76	11	
5	CB-26	1370	2500	3000	83	12	Small nozzle
6	CB-26	1650	3000	2500	83	12	

TABLE 4. — ATOMIZATION MELTS

Run	Alloy Composition (wt.%)	Total Charge Weight (kg)	Crucible Charge*	Late Additions
992	Cu-1.1Zr-0.34B	70	Copper bar, B	Zr
993	Cu-1.1Hf	69	Copper bar	Hf
994	Cu-0.8Zr	110	Copper bar, Zr	
995	Cu-0.6Zr	68	Cu bar, VM Cu-Zr (1733)	
996	Cu-0.5Zr-3.0Ag	68	Cu bar, Ag	Zr
997	Cu-0.55Zr-0.05B	69	Cu bar, B	Zr
998	Cu-0.65Zr	68	Cu bar	Zr
999	Cu-0.5Zr-3.0Ag	70	Cu bar, Ag	Zr
1032	Cu-0.8Hf-0.7Ti	74	Cu bar	Ti, Hf
1033	Cu-0.6Cr-0.2Co	76	Cu bar, VM Cu-Cr-Co (1834)	
1034	Cu-1.4Co-0.4V	72	VM Cu-Co-V (1835, 1839)	
1035	Cu-1.0Cr-0.6Zr	73	VM Cu-Cr (1840, 1841)	Zr
1036	Cu-0.6Zr-1.1Hf	74	Cu bar	Zr, Hf
1037	Cu-1.0Cr-0.6Zr-3.0Ag	76	Cu bar, VM Cu-Cr (1843)	Zr, Ag
1038	Cu-1.0Cr-0.6Zr-3.0Ag	70	Run 1037 heel	Zr, Ag
1039	Cu-1.0Cr-3.0Ag	73	Cu bar,VM Cu-Cr-Ag (1846)	
1040	Cu-0.6Zr-1.1Hf	74	Cu bar	Zr, Hf
1041	Cu-0.6Zr-1.1Hf	80	Run 1040 heel	Zr, Hf
1042	Cu-1.4Co-0.4V	71	VM Cu-Co-V(1848, 1849)	
1043	Cu-1.0Cr-3Ag	72	VM Cu-Cr-Ag (1864, 1865)	

* VM =Vacuum-induction-melted master Alloy

TABLE 5. — SELECTED ATOMIZATION PARAMETERS

Run	Alloy Composition (wt.%)	Charge Weight (kg)	Melt Vacuum	O_2 in He (ppm)	Nozzle Dia. (mm)	Metal Flow Rate (kg/min.)	Atomizer Speed (krpm)	Comments
992	Cu-1.1Zr-0.34B	70	295 µm	20	4.3	NA	35	Chucked skulls – abort.
993	Cr-1.1Hf	69	200 µm	–	4.3	14.2	33	
994	Cu-0.8Zr	110	500 µm	20	4.3	6.4	35	Slag; skulls – abort.
995	Cu-0.6Zr	68	500 µm	25	4.3	13.4	35	Slag
996	Cu-0.5Zr-3.0Ag	68	500 µm	20	4.3	15.5	35	
997	Cu-0.55Zr-0.05B	69	700 µm	30	4.0	12.0	35	
998	Cu-0.65Zr	68	800 µm H_2	20	4.0	13.4	35	H_2; skulls – abort.
999	Cu-0.5Zr-3.0Ag	70	800 µm H_2	20	4.3	13.3	35	H_2; graphite tundish.
1032	Cu-0.8Hf-0.7Ti	74	3 mm Ar	20	4.3	15.1	35	
1033	Cu-0.6Cr-0.2Co	76	3 mm Ar	25	4.3	15.1	35	
1034	Cu-1.4Co-0.4V	72	3 mm Ar	25	4.3	18.1	35	
1035	Cu-1.0Cr-0.6Zr	73	3 mm Ar	25	4.3	16.4	35-28	
1036	Cu-0.6Zr-1.1Hf	74	3 mm Ar	30	4.3	16.2	35	
1037	Cu-1.0Cr-0.6Zr-3.0Ag	76	3 mm Ar	30	4.3	0.0	35	Blocked nozzle – abort.
1038	Cu-1.0Cr-0.6Zr-3.0Ag	70	3 mm Ar	25	4.3	15.5	35	
1039	Cu-1.0Cr-3.0Ag	73	4 mm Ar	30	4.3	16.4	35	Oil leak, powder ruined.
1040	Cu-0.6Zr-1.1Hf	74	3 mm Ar	–	4.3	0.0	35	Blocked nozzle – abort.
1041	Cu-0.6Zr-1.1Hf	80	3 mm Ar	30	4.3	15.8	35	
1042	Cu-1.4Co-0.4V	71	3 mm Ar	–	4.3	15.1	34-35	
1043	Cu-1.0Cr-3.0Ag	72	3 mm Ar	–	4.3	16.5	35	

TABLE 6. — ATOMIZATION PARAMETERS (METAL TEMPERATURES)

Run	Alloy Composition (wt.%)	Melt Temp at Pour (°C)	Tundish Temp Pour (°C)	Tundish Temp End (°C)	Nozzle Temp Pour (°C)	Nozzle Temp End (°C)	Comments
992	Cu-1.1Zr-0.34B	1045	1340	1325	NA	NA	Chucked skulls – abort.
993	Cu-1.1Hf	1180	1250	1100	NA	NA	
994	Cu-0.8Zr	1220	1225	1225	1115	1070	Skulls – abort.
995	Cu-0.6Zr	1205	1220	1175	1080	1055	
996	Cu-0.5Zr-3.0Ag	1170	1240	1150	1070	1060	
997	Cu-0.55Zr-0.05B	1500	1470	1405	1240	1220	
998	Cu-0.65Zr	1150	1205	1175	1050	1040	Skulls – abort.
999	Cu-0.5Zr-3.0Ag	1240	1370	1125	1010	1030	
1032	Cu-0.8Hf-0.7Ti	1175	1165	1150	1350	> 1355	
1033	Cu-0.6Cr-0.2Co	1180	1245	1150	1345	> 1355	
1034	Cu-1.4Co-0.4V	1240	1315	1215	> 1355	> 1355	
1035	Cu-1.0Cr-0.6Zr	1175	1280	1175	1275	1320	
1036	Cu-0.6Zr-1.1Hf	1165	1255	1150	1290	1270	
1037	Cu-1.0Cr-0.6Zr-3.0Ag	1120	1270	1270	1225	NA	Blocked nozzle – abort.
1038	Cu-1.0Cr-0.6Zr-3.0Ag	1120	1150	1120	1205	1150	
1039	Cu-1.0Cr-3.0Ag	1120	1095	1095	1105	1095	
1040	Cu-0.6Zr-1.1Hf	1120	1120	NA	1260	NA	Blocked nozzle – abort.
1041	Cu-0.6Zr-1.1Hf	1140	1150	1100	1250	1240	
1042	Cu-1.4Co-0.4V	1240	1265	1220	> 1355	NA	
1043	Cu-1.0Cr-3.0Ag	1120	1115	1115	1315	1245	

TABLE 7. — MELT STOCK USED IN POWDER MAKING

Element	Melt Stock
Boron	99.8% B, granules
Chromium	99.4% Cr, aluminothermic
Cobalt	99.9% Co, electrolytic
Copper	C10100, oxygen-free electronic, 99.99% Cu, bar
Hafnium	99.7% Hf (including ≤1.5% Zr), chips
Silver	99.9% Ag, pellets
Titanium	99% Ti, chopped sheet
Vanadium	99.7% V, chips
Zirconium	99.7% Zr (including ≤1.5% Hf), chips

TABLE 8. — VACUUM MELTING PARAMETERS

VIM No.	Type	Total Melt Weight (kg)	Crucible Charge	Late Additions	Vacuum (Microns)	Mix Temp/Time (°C/min)	Pour Temp. (°C)
1733	Cu-Zr master	15	Cu bar	Zr	60	1260/30	1150
1834	Cu-Cr-Co master	39	Cu bar, Co	Cr	170	1260/30	1205
1835	Cu-Co-V master	39	Cu Bar, Co	V	170	1290/50	1315
1839	Cu-Co-V master	39	Cu Bar, Co	V	160	1370/50	1345
1840	Cu-Cr master	39	Cu bar	Cr	100	1290/35	1195
1841	Cu-Cr master	38	Cu bar	Cr	30	1260/15	1195
1843	Cu-Cr master	36	Cu bar	Cr	150	1290/20	1275
1846	Cu-Cr-Ag master	40	Cu bar	Cr, Ag	250	1250/20	1230
1848	Cu-Co-V master	37	Cu bar, Co	V	950	1345/20	1315
1849	Cu-Co-V master	37	Cu bar	V, Co	110	1260/15	1260
1864	Cu-Cr-Ag master	38	Cu bar	Cr, Ag	400	1345/30	1150
1865	Cu-Cr-Ag master	38	Cu bar	Cr, Ag	100	1415/20	1095
1866	NASA-Z	38	Cu bar	Zr, Ag	100	NA	NA

Continuous Helium
Recirculation System

Inert Powder
Production System

He In

He Out.
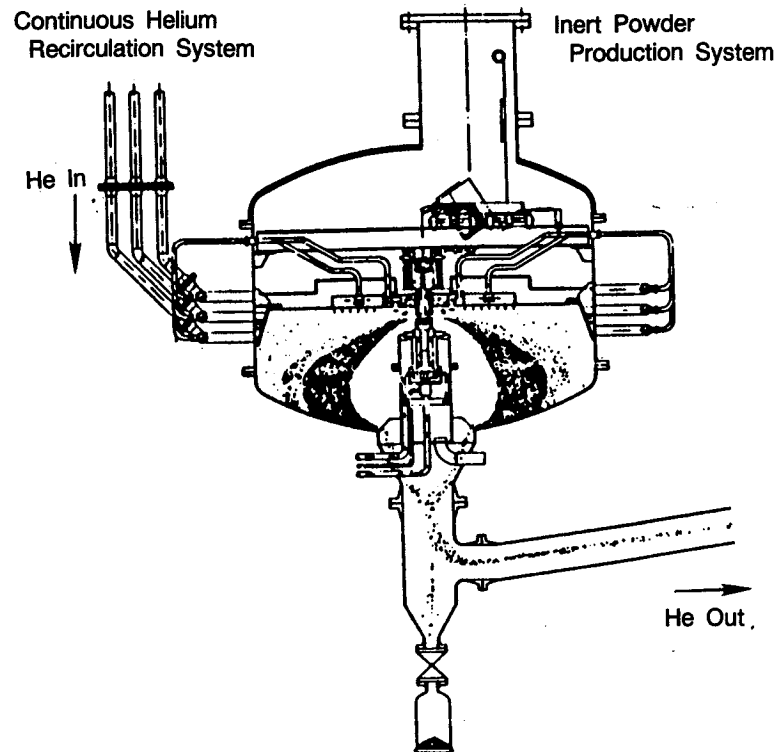
Figure 11.   P&W RSR Atomizer
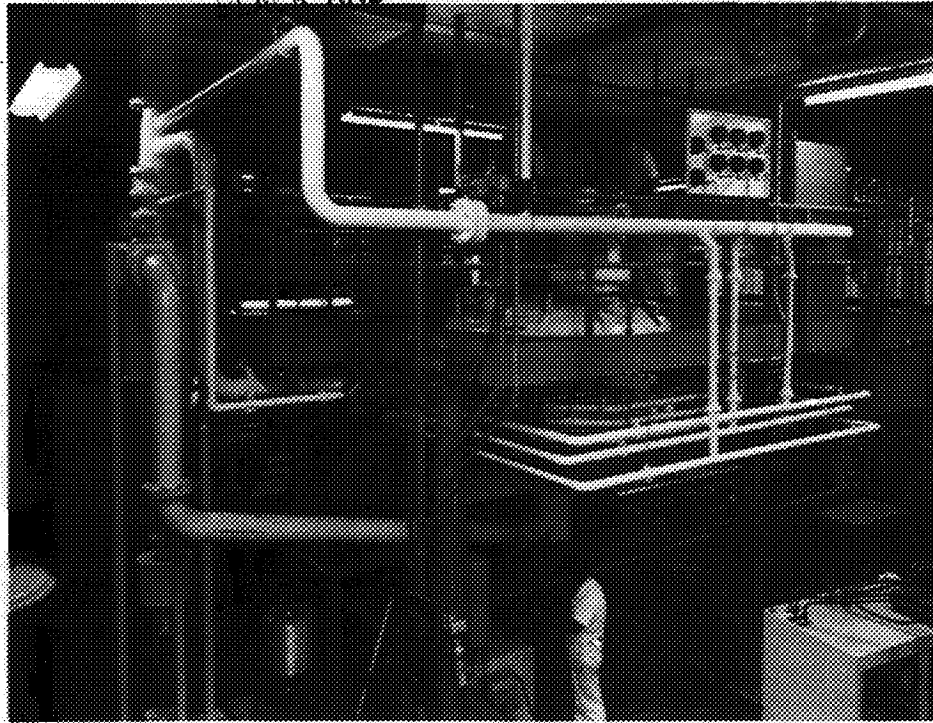
Figure 12. P&W RSR Atomizer

b. Canning for Extrusion Consolidation

Powder was canned in nominal 3-inch-diameter extrusion cans for extrusion consolidation. Can configuration is shown in Figure 13. Cans were welded from either deoxidized copper (C10100 and C12200 with AWS RCu wire) or plain low-carbon steel (see Table 9 for can applications). Cans were leak tested with helium mass spectrometer leak detectors to leak rates better than 10^{-8} cm^8/second. (About one third of the copper cans were made and tested at P&W, the remainder were made and tested at ZAK Co., Troy, NY.)

Cans were filled and outgassed in three ways. See Table 9 for applications, alloys canned, and size fractions used.

(1) Can Filling via Outgasser

The outgasser used is shown in Figure 14. It is a system comprised of a heatable vertical tube through which powder is poured from a transfer can into the extrusion can, all under vacuum produced by the attached pumps. The procedure for copper alloys was:

1. With the transfer can unattached and the metering valve closed, an extrusion can was attached and the system pumped down and leak checked.

2. The transfer can was filled with 540 ml of powder in the drybox and the isolation valve was closed.

3. The transfer can was attached to the outgasser, tipped (via a hose attachment), and allowed to pump out through the isolation and metering valves for 15 minutes.

25

4. The transfer can was righted and the metering valve adjusted for a powder flow of 0.5 kg/min through the outgasser.

5. After the extrusion can was full, it was pumped out for another 30 minutes.

6. The filler tube was crimped 3 times and severed from the outgasser at the center crimp. The end was sealed further with a gas-tungsten-arc weld.

Throughout the process, system vacuum was maintained below 5×10^{-5} microns. Outgassing was done at room temperature.
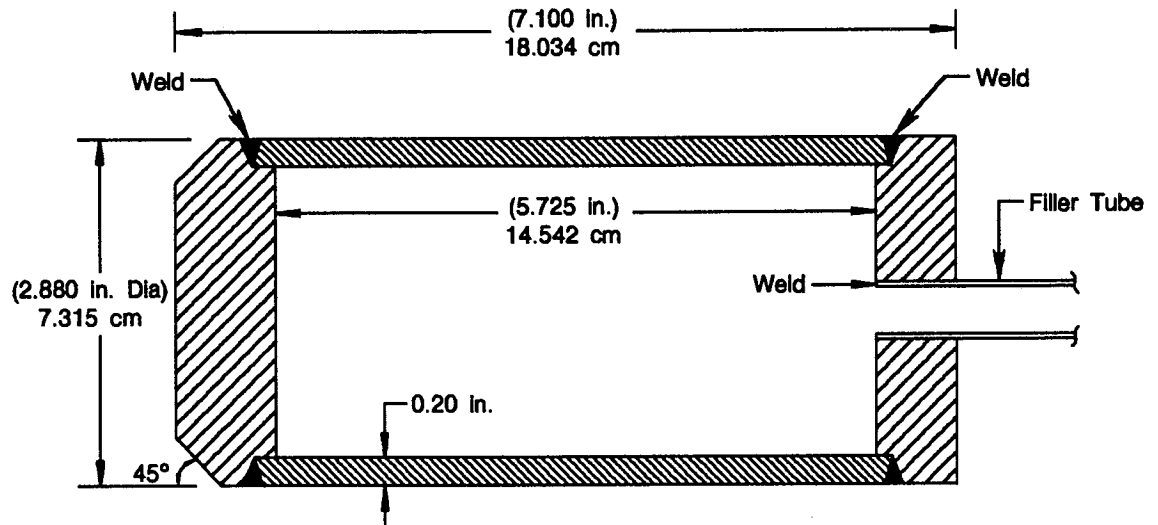
Figure 13. P&W Extrusion Can Assembly

(2) Can Filling via Cold Pumpdown

For this method, the can was filled in the drybox and pumped out, using the outgasser as a vacuum source, as follows.

1. An extrusion can was filled in the drybox under argon; an isolation valve was attached to the can and closed. The assembly was attached to the outgasser.

2. The outgasser was pumped down, the isolation valve was opened, and the can was pumped out for 1 hour. System vacuum was maintained below 5×10^{-5} microns.

3. The can was sealed as above.

Powder Reservoir

Isolation Valve

Metering Valve

Vacuum
Gauge

Roughing Valve

Tube Furnace

High Vac
Valve

Diffusion
Pump

Vacuum Pump
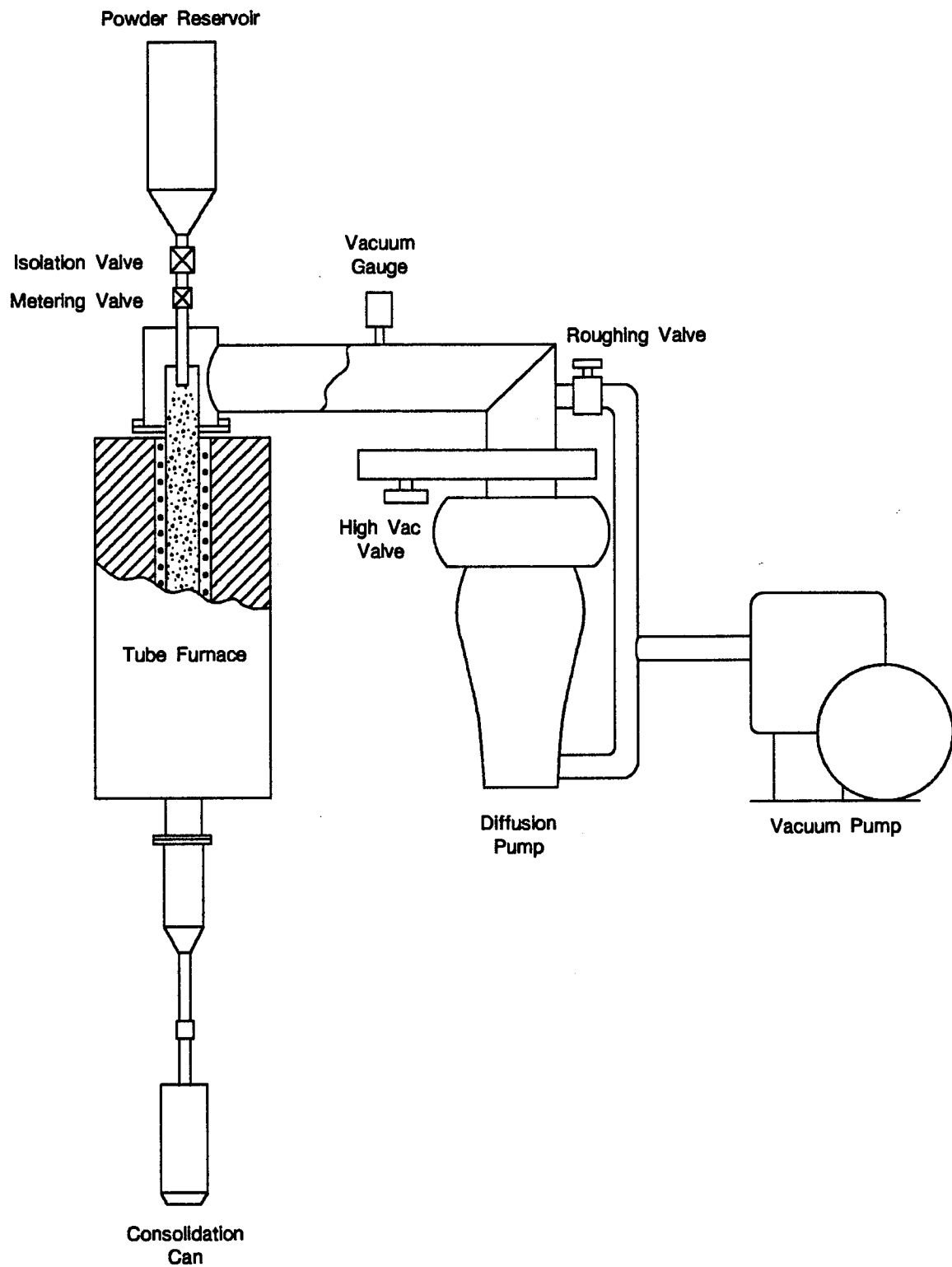
Consolidation
Can

Figure 14. P&W Powder Outgasser

27

c. Extrusion Consolidation

Powder alloys were consolidated into barstock via hot extrusion from the P&W 700-ton Lombard press (Figure 15). Both direct extrusions and extrusions preceded by hot blank die compactions were made. Alloys extruded, extrusion temperatures, application of precompactions, extrusion ratios, press loads, and other variable data are summarized in Table 9. Other nonvariable parameters are listed below:

- Billet preparation: Grit blast, then coat with DAG137 lube.
- Soak furnace: air.
- Liner: 80 mm (3.18-inch) diameter, heated to 250°C (500°F), Fiske 604 liner lube (graphite/grease).
- Die: Round conical, H-12 tool steel coated with zirconia, Polygraph lube (graphite/grease)
- Compaction Conditions: Hold 60 seconds at 600 tons.
- Furnace-to-press transfer time: less than 15 seconds.

d. Processing of Extrusions

Extruded powder alloys were subjected to various thermomechanical processing treatments for alloy evaluation. The processing schedules are shown in Figures 16 through 19. Air furnaces were used for the solution and age treatments. A vacuum furnace was used for the 650°C (1200°F) stability tests: vacuum levels were better than 10^{-4} microns, the heatup rate was 500°C/hr (1000°F/hr) and the cooling rate was 330°C/hr (600°F/hr). Swaging was performed in a Fenn 4F two-die swaging machine, using a die set having increments of 13 percent reduction in area.
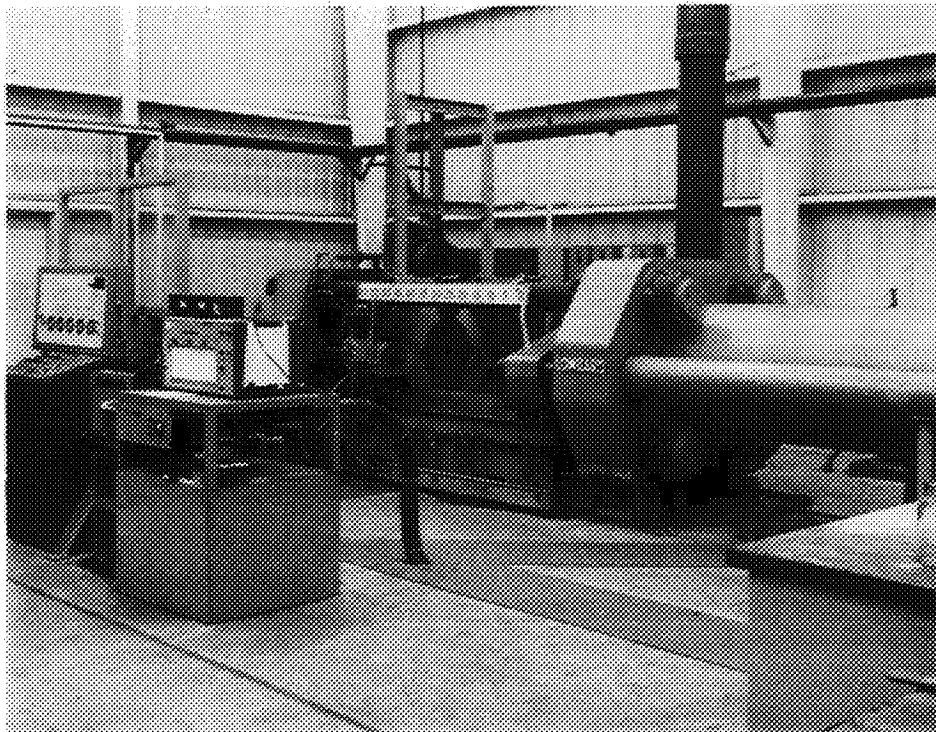
Figure 15. P&W Extrusion Press

TABLE 9. — COPPER ALLOY EXTRUSION CONDITIONS

Alloy-Bar No.	Composition (wt.%)	Powder Fraction (mesh)	Compaction Soak (3) (°C/hr)	Extrusion Soak (°C/hr)	Extrusion Ratio	Extrusion Diameter (mm)	Load (Metric Tons) (6) B/T	Load (Metric Tons) (6) RUN
993-1	Cu-1.1Hf	-230	650/2	650/2	8:1	28	315	255
993-2	Cu-1.1Hf	-230	No comp.	650/2	12:1	23	371	318
993-3	Cu-1.1Hf (4,5,7)	-80+230	No comp.	650/2	20:1	18	637	512
993-4	Cu-1.1Hf	-230	650/2	650/2	10:1	25	354	328
993-5	Cu-1.1Hf	-230	650/2	650/2	10:1	25	308	265
993-6	Cu-1.1Hf (7)	-80+230	No comp.	650/2	20:1	17	NA	NA
995-1	Cu-0.6Zr	-230	650/2	650/2	8:1	28	339	325
995-2	Cu-0.6Zr	-230	No comp.	650/2	12:1	23	339	311
995-3	Cu-0.6Zr	-230	No comp.	650/2	20:1	18	425	403
995-4	Cu-0.6Zr	-230	No comp.	650/2	20:1	18	460	439
996-1	Cu-0.5Zr-3.0Ag	-230	650/2	650/2	8:1	28	403	347
996-2	Cu-0.5Zr-3.0Ag	-230	No comp.	650/2	12:1	23	407	371
997-1	Cu-0.55Zr-0.05B	-230	No comp.	650/2	12:1	23	350	325
997-2	Cu-0.55Zr-0.05B	-230	650/2	650/2	8:1	28	311	276
998-1	Cu-0.65Zr (7)	-80	No comp.	650/2	12:1	23	364	325
999-1	Cu-0.5Zr-3.0Ag	-230	650/2	650/2	8:1	28	389	364
999-2	Cu-0.5Zr-3.0Ag	-230	No comp.	650/2	12:1	23	410	371
1032-1	Cu-0.8Hf-0.7Ti	-230	650/2	650/2	10:1	25	371	311
1032-1	Cu-0.8Hf-0.7Ti	-230	No comp.	650/2	20:1	18	523	474
1033-1	Cu-0.6Cr-0.2Co	-230	650/2	650/2	10:1	25	283	255
1033-2	Cu-0.6Cr-0.2Co	-230	No comp.	650/2	20:1	18	442	389
1035-1	Cu-1.0Cr-0.6Zr	-230	650/2	650/2	10:1	25	354	308
1035-2	Cu-1.0Cr-0.6Zr	-230	No comp.	650/2	20:1	18	495	474
1036-1	Cu-0.6Zr-1.1Hf	-230	650/2	650/2	10:1	25	332	NA
1036-2	Cu-0.6Zr-1.1Hf	-230	No comp.	650/2	20:1	18	425	389
1038-1	Cu-1.0Cr-0.6Zr-3.0Ag	-230	650/2	650/2	10:1	25	460	379
1038-2	Cu-1.0Cr-0.6Zr-3.0Ag	-230	No comp.	650/2	20:1	18	523	478
1042-1	Cu-1.4Co-0.4V	-230	650/2	650/2	10:1	25	318	268
1042-2	Cu-1.4Co-0.4V	-230	No comp.	650/2	20:1	18	425	375
1043-1	Cu-1.0Cr-3.0Ag	-230	650/2	650/2	10:1	25	382	308
1043-2	Cu-1.0Cr-3.0Ag	-230	No comp.	650/2	20:1	18	530	460
MIT-4	Cu-1.1Hf (1,4,7)	NA	No comp.	700/2	20:1	18	371	347
MIT-5	Cu-1.1Hf+Oxygen (1,2,4,7)	NA	No comp.	700/2	20:1	18	347	328
PWNASZ-1	Cu-0.5Zr-3.0Ag	ingot	No comp.	840/2	22:1	16	453	396

1. Hydrogen reduced
2. Attrited powder
3. "No comp." means no compaction – a direct extrusion
4. 993-3, MIT-4, MIT-5 sent to MIT
5. Steel can
6. B/T means breakthrough force
7. Pumpdown fills. All others through outgaser.

e. Additional Process Work

Additional processing investigations were conducted on Alloys 993 and 999. Both alloys were hot-swaged to a 50 percent reduction in area at 870°C (1600°F), then solution-treated at 925°C (1700°F) for 30 minutes and water quenched, then cold swaged to a 50 percent reduction in area, then aged at 480°C (900°F) for 2 hours and air cooled. Evaluation was by optical microscopy.

Extrude 12:1/650°C (1200°F)

Solution 925°C (1700°F)/30 Min/WQ

Age 480°C (900°F)/2 Hr/AC

Age 480°C (900°F)/2 Hr/AC

Stability Test Anneal
650°C (1200°F)/12 Hr
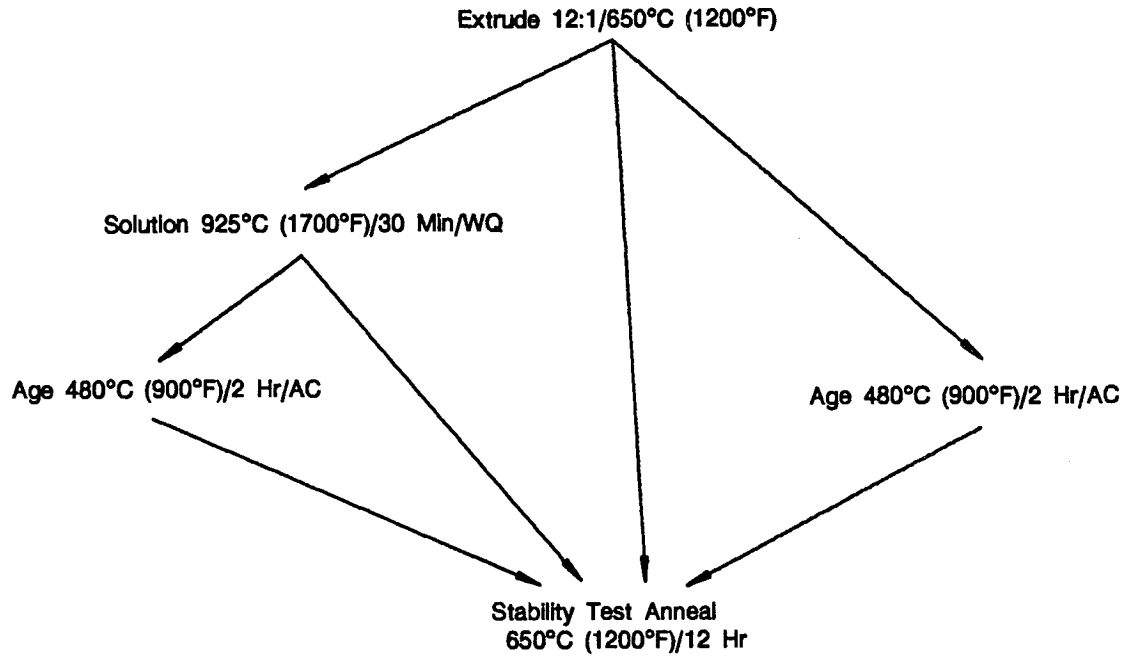
Figure 16. *Powder Processing Flow Chart: Alloys 993 Through 999 (Small Extrusions)*

Hot Compact 650°C (1200°F)
Extrude 8:1/650°C (1200°F)

Solution 925°C (1700°F)/30 Min/WQ

Cold Swage 35% RA

Cold Swage 35% RA

Age 480°C (900°F)/2 Hr/AC

Age 480°C (900°F)/2 Hr/AC

Stability Test Anneal
650°C (1200°)/12 Hr
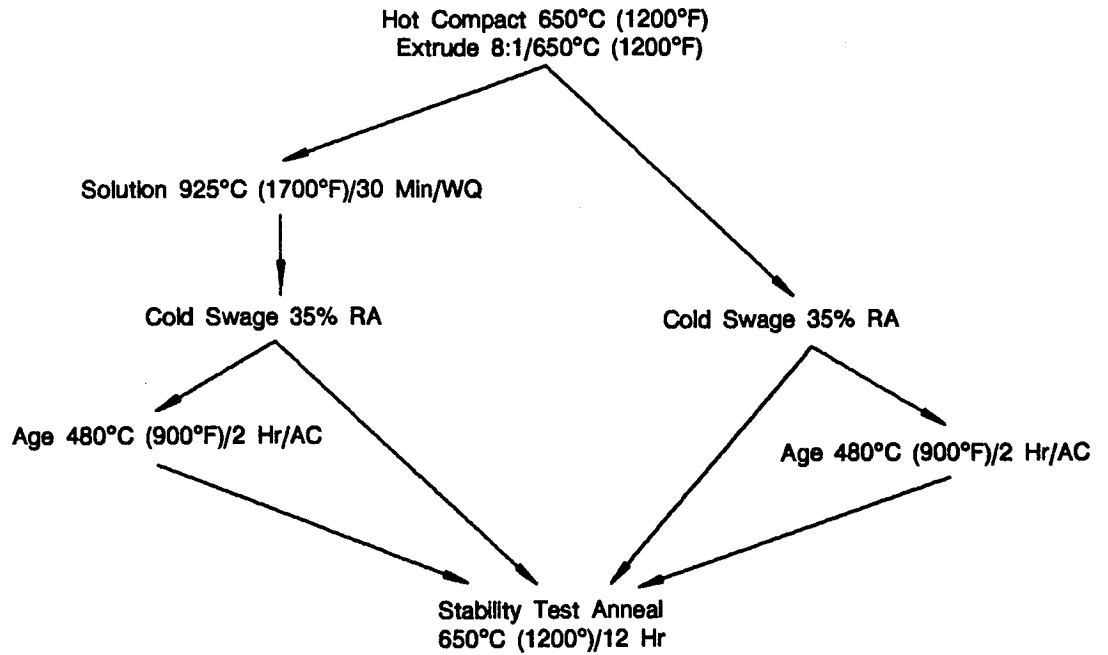
Figure 17. *Powder Processing Flow Chart: Alloys 993 Through 999 (Large Extrusions)*

30

Extrude 19:1/650°C (1200°F)

Solution (H) 925°C (1700°F)/30 Min/WQ

Age (H) 480°C (900°F)/2 Hr/AC

Stability Test Anneal
650°C (1200°F)/12 Hr/FC
(Vacuum)
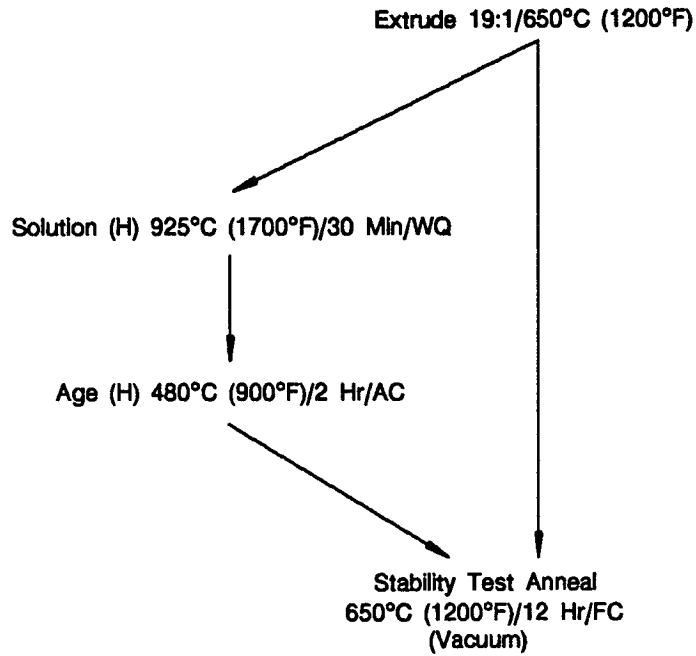
Figure 18. Powder Processing Flow Chart: Alloys 1032 Through 1043 (Small Extrusions)

Hot Compact 650°C (1200°F)
Extrude 10:1/650°C (1200°F)

Solution (H) 925°C (1700°F)/30 Min/WQ

Cold Swage (H) 35% RA   Cold Swage (H) 35% RA

Age (H) 480°C (900°F)/2 Hr/AC

Stability Test Anneal
650°C (1200°F)/12 Hr/FC
(Vacuum)
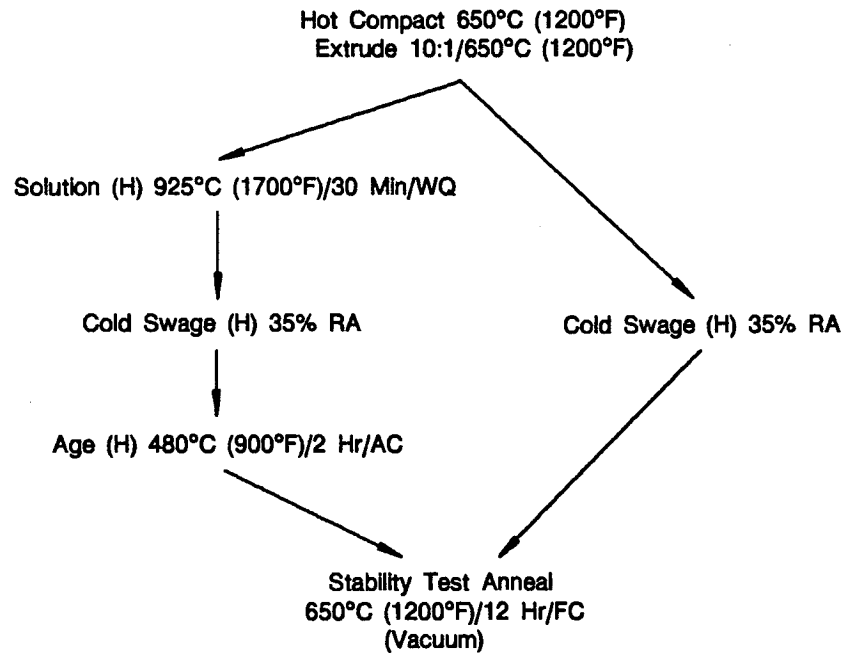
Figure 19. Powder Processing Flow Chart: Alloys 1032 Through 1043 (Large Extrusions)

f. Processing of Materials for Testing

Materials for mechanical and physical property tests were processed according to the schedules in Table 10, using techniques described earlier. Processed materials were evaluated by optical microscopy prior to specimen machining.

TABLE 10. — PROCESSING SCHEDULES FOR TEST MATERIALS

Alloy	Serial No. (Condition)	Source Extrusion	Processing Description*
NASA-Z	1, 2	NA	Two hollow cylinders, as received, NASA LeRC
NASA-Z	3, 4, 5	NA	Three pancake sections, as received, NASA LeRC
NASA-Z	TC	NA	NASA-Z1 + H.T. 705°C (1300°F)/1 hr/air cool
993	AE	993-2	As-extruded
993	SCWA-211	993-2	925°C (1700°F)/30 min/WQ + CSW 30% RA + 480°C (900°F)/2 hr/AC
993	HWSCWA	993-1	HSW 870°C (1600°F)/50% RA + 925°C (1700°F)/1 hr/WQ + CSW 50% RA + 480°C (900°F)/2 hr/AC
993	HWSA	993-1	HSW 870°C (1600°F)/50% RA + 925°C (1700°F)/1 hr/WQ + 480°C (900°F)/2 hr/AC
993	CWCAR-1, 2, 3	993-4	HSW 870°C (1600°F)/24% RA + 940°C (1725°F)/1 hr/WQ + CSW 30% RA + 480°C (900°F)/2 hr/AC
993	TC	993-1	705°C (1300°F)/1 hr/AC
995	AE-2	995-2	As-extruded
995	AE-3, AE-4	995-3, 995-4	As-extruded
995	SCWA-211	995-2	925°C (1700°F)/30 min/WQ + CSW 30% RA + 480°C (900°F)/2 hr/AC
995	EC	995-1	CSW 50%
995	TC	995-2	705°C (1300°F)/1 hr/AC
996	AE	996-2	As-extruded
997	AE	997-1	As-extruded
997	SCWA-111	997-1	925°C (1700°F)/30 min/WQ + CSW 30% RA + 480°C (900°F)/2 hr/AC
999	SA	999-2	925°C (1700°F)/30 min/WQ + 480°C (900°F)/4 hr/AC
999	SCWA-211	999-2	925°C (1700°F)/30 min/WQ + CSW 30% RA + 480°C (900°F)/2 hr/AC
999	HW	999-1	HSW 870°C (1600°F)/50% RA
999	HWSA	999-1	HSW 870°C (1600°F)/50% RA + 925°C (1700°F)/30 min/WQ + 480°C (900°F)/4 hr/AC
1032	AE	1032-2	As-extruded
1032	SCWA-1, -2	1032-1	925°C (1700°F)/30 min/WQ + CSW 50% RA + 480°C (900°F)/2 hr/AC
1032	TC	1032-2	705°C (1300°F)/1 hr/AC
1035	AE	1035-2	As-extruded
1035	EC	1035-1	CSW 50% RA
1035	TC	1035-2	705°C (1300°)/1 hr/AC
1036	AE	1036-2	As-extruded
1038	AE	1038-2	As-extruded
1038	SA	1038-2	925°C (1700°F)/30 min/WQ + 480°C (900°F)/2 hr/AC
1042	AE	1042-2	As-extruded
1043	AE	1043-2	As-extruded
1043	SCWA	1043-1	980°C (1800°F)/30 min/WQ + CSW 50% RA + 480°C (900°F)/2 hr/AC

* WQ = water quench, CSW = cold swage, RA = reduction in area, AC = air cool, HSW = hot swage

g. Evaluation of Powder Metallurgy Copper Alloys

Wrought powder metallurgy copper alloys were evaluated by optical microscopy, scanning electron microscopy, transmission electron microscopy, electron microprobe, x-ray diffraction analysis, Rockwell B and F hardness, hot tensile tests, and hot compression tests.

4. TEST AND CHARACTERIZATION METHODS

Wrought powder alloys were conditioned and subjected to tests as detailed in Table 11.

a. Tensile Testing

Tensile testing was carried out in argon at elevated temperature and generally at high strain rates. Early tests were performed using a Tinius Olsen hydraulic tensile machine and used a deflectometer on the crosshead to obtain yield data. Later tests were conducted on an MTS servohydraulic machine using extensometers on the specimen to collect strain data. Applications of the test types are listed in Table 11.

Early tests were conducted on a conventional hydraulic tensile testing machine equipped with a retort to encapsulate the specimen and grips in argon, and a clamshell furnace to heat the retort and specimen within. The specimen (Figure 20a) was installed on the grips and instrumented with thermocouples. The assembly was installed in the retort, which was then purged with argon for 30 minutes. Then the retort was installed on the tensile tester and heated with a clamshell furnace. The specimen was heated to 705°C (1300°F), held at that temperature for at least 30 minutes, and then pulled at a crosshead speed of 4 inches/minute, giving an initial strain rate of 0.06/second. A deflectometer connected to the crosshead was used to obtain strain data. Yield strength (0.2 percent), ultimate tensile strength, percent elongation in 2.5 cm (specimens were scribed), and percent reduction in area were reported.

Later tensile tests were conducted on an MTS servohydraulic programmable tensile tester, equipped with an extensometer-capable retort to facilitate collection of stress-strain data. The specimen (Figure 20b), was installed in the grips, LVDT-type extensometers were attached at the holes shown on Figure 20b, and thermocouples were attached. The assembly was inserted into the retort, which was attached to the MTS machine and purged 10 minutes with argon. Next the retort was heated in a clamshell furnace, heating the specimen to the testing temperature of 540°C (1000°F) or 705°C (1300°F). The specimen was held 30 minutes at temperature and then pulled at strain rates of either 0.1/second or 0.0005/second. Force and strain data were collected on an X-Y plotter. Yield strength (0.2 percent), ultimate tensile strength, percent elongation in 1.8 cm (four diameters), and percent reduction in area were reported. On occasion, engineering stress-strain curves were plotted.

Failed specimens were examined by optical, scanning electron, and transmission electron microscopy.

b. Creep Testing

Some of the alloys were subjected to high-stress creep testing at 705°C (1300°F) in argon. Stress levels were equivalent to the slow-strain-rate proportional limits for the respective alloys, which were determined through tensile testing as above.

TABLE 11. — TEST APPLICATIONS/TESTS PERFORMED

Alloy	Condition	705°C Tensile at 0.05%/Sec	705°C Tensile at 6% Sec*	705°C Tensile at 10%/Sec	540°C Tensile at 10%/Sec	705°C Creep	Thermal Conductivity	Low-Cycle Fatigue
NASA-Z	1, 2, 3, 4, 5	1	2	3	2	2		4
NASA-Z	TC						1	
993	TC						1	
993	AE		2					
993	SCWA-211		2					
993	HWSA			1				
993	HWSCWA			1				
993	CWCAR 1, 2, 3			2	5			4
995	TC						1	
995	AE	1	2	2	2	2		6
995	SCWA 211		2					
996	AE		2					
996	HWSA							3
997	AE		2					
997	SCWA 111		2					
999	SA		3					
999	SCWA 211		3					
999	HW			1				
999	HWSA			1				
1032	TC						1	
1032	AE			3				
1032	SCWA			3				3
1035	TC						1	
1035	AE			3	2			3
1035	EC			3				
1036	AE			2				
1038	AE			3				
1038	SA			3				
1042	AE			2				
1043	AE			2				
1043	SCWA			2				

* Simple tensile specimen. All other tensile and creep tests used stress-strain specimen.

6.4

6.4

Chamfer
Both Ends

15.1

27

15.1

0.500 in.
13 UNJC Thread

70

Tensile Specimen (a)

Remove First Half of Thread at
Both Ends

Drill

1.57 (Both Sides)

3/8 in.
16 UNJC Thread

15.9

4.8

4.8

22

38

83
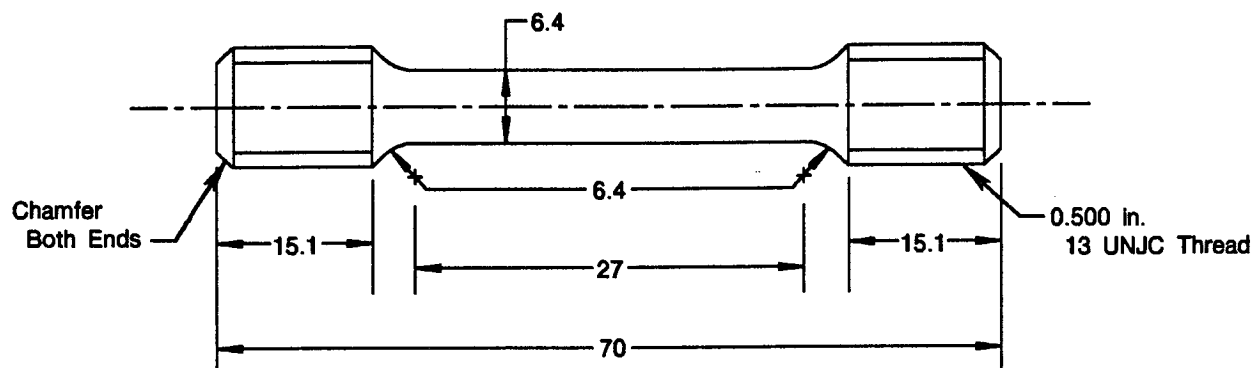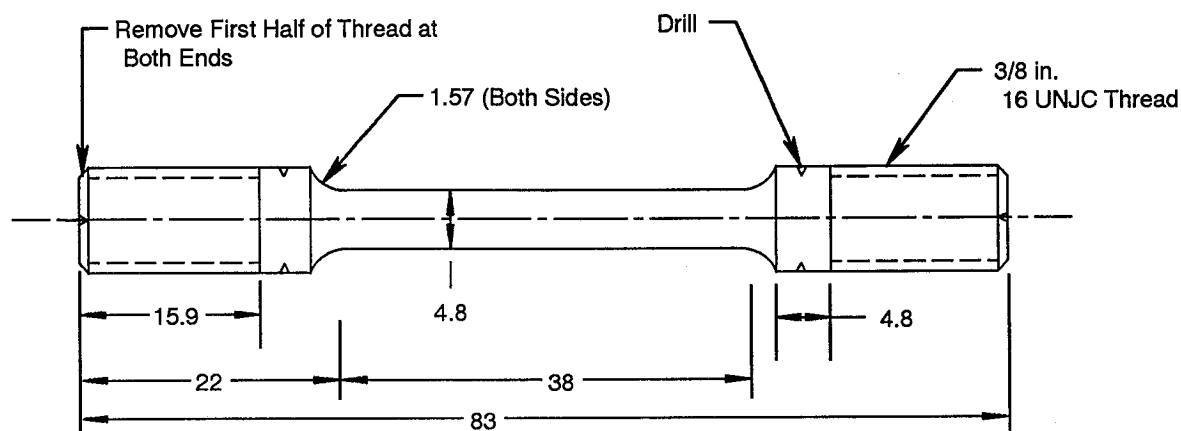
Stress–Strain Specimen (b)

Figure 20. Tensile Specimens (Dimensions in mm, Except Threads)

Creep tests were conducted on an MTS servohydraulic programmable tensile tester, equipped with an extensometer-capable retort to facilitate collection of stress-strain data. The specimen (Figure 20b) was installed in the grips, LVDT-type extensometers were attached at the holes shown in Figure 20b, and thermocouples were attached. The assembly was inserted into the retort, which was attached to the MTS machine and purged 10 minutes with argon. Next the retort was heated in a clamshell furnace, heating the specimen to 705°C (1300°F). The specimen was held 30 minutes at temperature and then pulled at a strain rate of 0.1/second to the creep test load. Load was then held constant until the specimen failed or the extensometry bottomed

out. Time and strain data were collected on an X-Y plotter. Percent creep versus-time plots were made. Time to failure, percent elongation in 0.75 inches (specimens were lightly punched), and percent reduction in area were also reported. Failed specimens were examined by optical microscopy.

c. Thermal Conductivity Testing

Thermal conductivity characterization was performed by the Purdue University Thermophysical Properties Laboratories. Conductivities were measured indirectly, by way of flash thermal diffusivity, specific heat, and bulk density. Conductivities were determined at 21, 99, 199, 299, 399, 499, 599, and 699°C, (70, 210, 390, 570, 750, 930, 1110, and 1290°F).

Thermal diffusivity was measured using a pulsed Korad K2 laser. A specimen 13 mm (0.5-inch) in diameter by 6.4 mm (0.25-inch) thick was placed in a small resistance furnace inside a vacuum chamber. A pulsed laser was aimed through a glass port of the vacuum chamber at the front side of the specimen. The chamber was evacuated. The sample was then heated to the test temperature, allowed to stabilize for 5 minutes, and exposed to a laser pulse. A thermocouple or infrared detector was used to measure the rear face temperature rise after the laser pulse. From this, the diffusivity was calculated by the controlling minicomputer.

Specific heat was measured at Purdue using a Perkin-Elmer doped silicon carbide (DSC)-2 differential scanning calorimeter with a sapphire reference. Specimens measured 6.4 mm (0.25-inch) diameter by 1.2 mm (0.5-inch) thick. Specific heats were plotted as a function of temperature from 22°C to 700°C (70°F to 1290°F).

Density was measured at P&W, using the buoyancy method. The sample was weighed. Then it was hung on a wire from a scale and weighed in water. Then the wire without the sample was weighed in water (immersed to the same depth as with the sample). The density was calculated:

$$d = \frac{a}{a - (b - w)}$$

where: d = density
        a = dry sample
        b = weight of sample and wire in water
        w = weight of wire in water

Thermal conductivity was calculated for each temperature using:

$$\lambda = \alpha c_p d$$

where: λ = thermal conductivity
        α = thermal diffusivity
        c_p = specific heat
        d = density

d. Low-Cycle Fatigue Testing

Low-cycle fatigue testing was conducted in strain control, in argon, at 705°C (1300°F) at 0.75 to 3 percent total strain ranges, at strain rates of 0.0075 to 0.03/second, in continuous cycling, using a triangular waveform, with zero mean strain. Testing was conducted at P&W in a special environmentally controlled LCF rig.

The rig used is shown in Figure 21. The test mechanism consisted of a conventional hydraulic stroke apparatus connected through seals to the specimen grips inside a pressure vessel. Also inside the vessel were a removable fixed upper grip, a resistance furnace, clamp-on LVDT-type extensometers, and specimen thermocouples. The test apparatus was controlled by an MTS servohydraulic machine controller. The test cycle was generated by a sawtooth waveform generator. Throughout the test, tensile loads, compressive loads, and cyclic strains were plotted on a two-pen strip chart recorder. Periodically, cycling was slowed down and hysteresis loops (stress-strain) were plotted.

Several specimens were used for LCF testing. They are shown in Figure 22. The tests performed and specimens used are listed in Table 12. Testing procedure was as follows:

1. The specimen was installed in the grips and extensometer, the assembly was installed in the rig, covered with the furnace, and topped with the end plate to anchor the top grip. Thermocouple, LVDT, furnace, and water cooling leads were connected. The pressure vessel cover was attached.

2. The vessel was evacuated and refilled with argon three times, then filled to the specified pressure, which was maintained throughout the remainder of the test.

3. The furnace was turned on and allowed to stabilize at the specified temperature for 0.5 hour after everything reached 705°C (1300°F).

4. The control system was programmed. Testing began with slow 0.17 Hz cycling of the first 4 to 5 cycles until stresses had stabilized and smooth operation was confirmed. The strain rate was increased to the specified level and cycling continued. Periodically (20 to 100 cycles, depending on strain range), the cyclic frequency was slowed manually and hysteresis stress-strain loops were plotted.

5. When the logarithmic plot of cyclic load versus cycles deviated by 20 percent from linearity, cycling was terminated and the furnace turned off. When cool, the apparatus was disassembled and the specimen removed.

Evaluation of failed LCF specimens was by optical and scanning electron microscopy.

5. EVALUATION METHODS

a. Optical Microscopy

Bulk specimens for optical microscopy were sectioned and mounted in bakelite or epoxy. They were ground on silicon carbide paper (down to 600 grit), polished with 6- and 1-micron diamond, and final polished on a Syntron vibratory machine with a water — 0.05-micron alumina slurry for one half hour. Polished samples were etched with a fresh solution of 42 percent ammonium hydroxide/16 percent hydrogen peroxide (3 percent strength) — 42 percent water (all volume percent), then rinsed with water. Any smut that formed was gently wiped off the wet mount with a wet cotton ball. Samples were dried with compressed air.
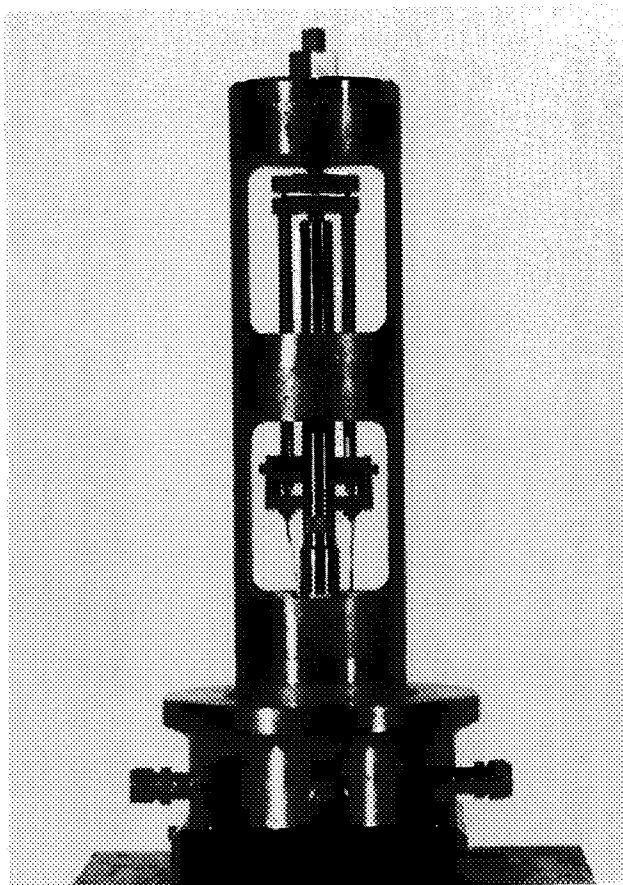
Test Vessel Open Showing
Extensometer System
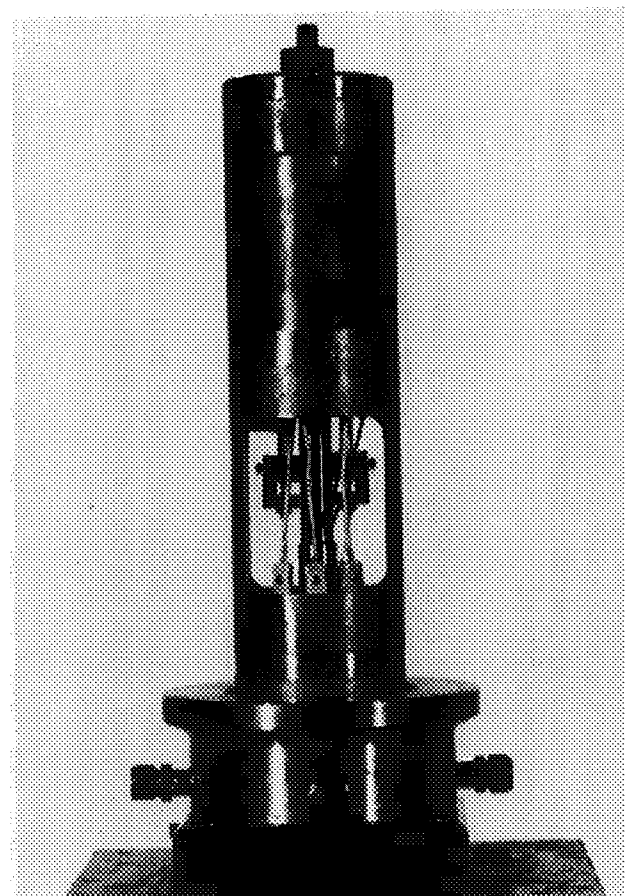
Test Vessel Open Showing
Furnace in Place

Figure 21. High-Pressure LCF Test Rig

Figure 22. Collared LCF Specimens (Dimensions in mm, Except Threads)

Powder specimens were mounted in epoxy. About 4 grams of the powder was poured into a 6-mm-(1/4-inch)-ID polyethylene test tube, followed by some mixed epoxy mounting compound. The powder and epoxy were mixed in the tube with a long thin stick. Then the test tube was centrifuged for 10 minutes and removed. After the epoxy had cured, the sample was tapped out of the mount. The clear top portion was cut off, and the powder sample was ground longitudinally through 600-grit SiC paper. The sample was then very carefully polished with 1-micron diamond paste and etched.

TABLE 12. — LOW-CYCLE FATIGUE TESTS PERFORMED

Alloy	Condition	Specimen	Strain Ranges 705°C (1300°F) Tests		
			3%	*1.5%*	*0.75%*
NASA-Z	As-received	17710-A	2	2	
993	CWCAR-1	16150		2	
993	CWCAR-2	17710-A	1	1	
995	AE	16150	2	1	1
995	AE	17710-A	1	1	
996	HWSA	17710-A	1	2	
1032	EC	17710-A	1	2	
1035	AE	17710-A	1	2	

Optical evaluation of hot-vacuum-compacted powder samples for contamination was conducted at 100× magnification on an etched surface. Rateable inclusions were defined as those exhibiting an area at 100× magnification equivalent to that of a 3-mm-(1/8-inch)-diameter circle. Metallic and non-metallic-appearing inclusions were counted separately and normalized to give the number of inclusions per square inch.

b. Scanning Electron Microscopy and Electron Microprobe

Scanning electron microscopy was conducted using ETEC Autoscan and Amray scanning electron microscopes (SEMs), and a JEOL 733 Superprobe microprobe. Specimen preparation was as above, except for test specimen fractures, which were examined as-is or with an ethanol ultrasonic cleaning. Both secondary electron and backscattered electron image modes were used. When needed, specimens were sputtered with gold (primarily powder specimens). Electron microprobe analyses were performed in a JEOL 733 Superprobe. Both wave-dispersive and energy-dispersive systems were used.

c. Transmission Electron Microscopy

Carbon extraction replicas were obtained from heavily etched samples prepared as described above. Acetone and acetyl cellulose replica tape were applied, allowed to dry, and then peeled off. The replica surface was coated with carbon, and then shadowed with chromium, in a Denton vacuum evaporator. The replica was trimmed and placed on a grid. The tape was dissolved in hot refluxed acetone and then the replica was dried.

Foil specimens were prepared from 0.5-mm-(0.020-inch)-thick slices cut with a low-speed diamond saw. The slices were ground to 0.15-mm-(0.006-inch)-thick on 600-grit silicon carbide SiC paper, then punched out into 3-mm disks. The disks were jet thinned in a South Bay Technology jet thinner using an electrolyte of 20 percent nitric acid in ethanol, at −15°C.

Consolidated MIT flake material (Appendix 2) was thinned for transmission electron microscopy (TEM) by ion milling jet-polished disks in a Gatan Dual-Beam Ion Mill. Two beams were used, at 20-degree incidence: each beam was set to yield a 6 kV gun voltage, a 0.6 mA current, and a 27-microamp specimen current. Vacuum was at 7×10^{-7} millitorr.

Replica and foil specimens were evaluated in a Philips EM 400 scanning transmission electron microscope (STEM).

d. Hardness Testing

Microhardness was determined using Zwick and Clark DMH2 testers with pyramidical indenters and using loads of 10 to 1000 g. Diamond pyramid hardness numbers resulted. Samples were mounted in epoxy.

Rockwell hardnesses were determined using a Wilson Rockwell Hardness Tester on the B and F scales. Most samples were mounted in epoxy. Rockwell hardnesses were converted to diamond pyramid hardnesses using the chart for copper alloys found in Reference 15.

e. X-Ray Diffraction Analyses

Lattice parameter and phase identification studies were performed on a Philips horizontal diffractometer with a curved graphite monochromator. Copper and cobalt x-ray tubes were used.

f. Chemical Analyses

Bulk chemical analyses were performed using electron microprobe techniques (above) and an inductively coupled plasma atomic emission spectrophotometer (ICP-AES). ICP-AES analyses were performed on NASA-Z, Amzirc, and Alloys 992 through 999, using milled chips for the first two and atomized powder for the rest. The alloys and appropriate standard elementals were dissolved in nitric acid (0.15 gram alloy in 20 ml concentrated acid, then diluted to 1000 ml). Silicon was dissolved by adding a bit of Hf. The solutions were analyzed in an ISA JY38 ICP-AES. Wavelengths used were as follows.

Elements	Wavelengths (nm)
Ag	328.088, 338.316
Zr	339.224, 343.850
Hf	264.146, 273.884
Si	251.626, 288.176
Al	394.436, 396.182

Oxygen analyses were performed on NASA-Z and Alloys 992 through 999, using a Leco TC36 Nitrogen-Oxygen Determinator with 0.5-gram samples.

A carbon analysis was performed on Alloy 999 using a Leco CS46 Carbon/Sulfur Determinator. Hydrogen analyses were performed on the MIT materials using a Leco RH1 Hydrogen Determinator.

Analyses of Alloy 992 and 993 powder water content were performed by measuring the weight loss of drying powder in a Dupont 951 Thermogravimetric Analyzer, under helium. Sample sizes of about 50 mg were heated to 550°C at 5°C/minute.

Oil analyses were performed on Alloys 992 through 999. A 50-gram powder sample was washed three times in 30 ml of freon for ester oils, or carbon tetrachloride for mineral oils. The solvent was then evaporated to 25 ml and analyzed in an infrared spectrometer at wavelengths of 3200 to 2800 cm^{-1} for ester oils and 1800 to 1650 cm^{-1} for mineral oils. The results were compared to those of standard solutions.

SECTION III
ALLOY SCREENING

The alloy screening study was undertaken to evaluate the potential of a large number of alloy systems. Alloys were chosen from several families of systems.

The first types were those that form elemental and copper-x precipitates from solution in copper, such as Cr, Cu_5Zr, Ag, Nb, and others having low solid solubility in copper. These alloys were formulated at concentrations that straddled the solid solubility limits of the constituents in copper. The dilute alloys were intended to be fully solutionable and used for age-hardening studies. The concentrated alloys were intended for studies of the effects of rapid solidification, in which case the excess insoluble constituents would form dispersions of primary precipitates that might be fine enough to contribute to strengthening and stabilization of the microstructure at elevated temperatures.

The second class of alloys were formulated to produce precipitates or dispersions of stable copper-free intermetallic compounds. Compounds were chosen that either had high melting points (and thus might be stable), or were cubic and had lattice parameters not very different from that of copper (and thus might resist coarsening at high temperatures). Alloys were formulated to produce about 2 volume percent of these compounds. The constituents were not necessarily of low solubility; it was believed that if stable enough in copper, the compounds might form rather than dissolve in copper.

The third type of alloys were formulated to produce dispersions of metal-borides upon solidification (the metal not being copper). High-melting-point borides were preferred. Generally, borides of metals having low solid solubilities in copper were preferred, so that any excess of boride former elements (due to boron losses) would precipitate rather than remain in solid solution and adversely affect conductivity. However, some high-solubility boride formers, such as titanium, were evaluated in the belief that if effective, ways could be found to adjust melting practices to compensate for boron losses and maintain high conductivity. Usually, alloys were formulated to produce about 2 volume percent of borides. Alloys were formulated with stoichiometric amounts of boron and the reactive metal, and sometimes also formulated with excess or insufficient boron to assess off-stoichiometric effects (which were found to be significant on earlier Fe-Al + TiB_2 alloy programs (16)). Alloys were evaluated in the conventionally cast + processed and the rapidly solidified + processed conditions.

Another class of alloys was formulated to produce dispersions or precipitates of copper-free silicides. Silicides have found use in other alloy systems as strengtheners and microstructural stabilizers. High-melting-point silicides composed of copper-soluble elements were chosen for these studies. Silicide concentrations were set at 2 volume percent.

All of the screening alloys were melted under argon in a water-cooled arc-melting device, using a tungsten electrode. Buttons were turned over and remelted at least once to promote homogeneity. Subsequent processing was tailored to allow evaluation of age-hardenability, recrystallization resistance, and adaptability to rapid solidification processing.

Rapidly solidified samples were prepared by passing an electron beam across button selections. This had been used successfully in the past to develop structures similar to rapid-solidification-rate (RSR) powder. It is superior to melt spinning because it produces a consolidated sample upon a substrate that can be worked conveniently, whereas ribbons must first be consolidated. This working step was considered important, since some rapidly solidified structures become thermally unstable if deformed. Since rapidly solidified copper alloys presumably would be hot-consolidated to make hardware, structural stability under some regimen of hot strain was important.

Not all of the screening alloys were electron-beam processed. Only those that were expected to form insoluble dispersions were considered for rapid solidification. Of those, some were not processed because conventional processing showed that the aging precipitates had little hardening effect: thus, primary precipitate dispersions would be no more beneficial.

Initial trials showed that rapidly solidified electron-beam passes in copper-zirconium alloys produced structures finer than those found in atomized copper-zirconium alloys produced prior to this program. This validation served as the basis for subsequent electron-beam processing of screening alloys.

Electron-beam-processed structures were much finer than as-cast structures (Figure 23). As a result, detection of recrystallization in electron-beam-processed zones was sometimes difficult. Recrystallization was not discussed in such cases in the following narrative.

1. FIRST-ITERATION SCREENING RESULTS

One major iteration of screening alloys (CB 1 - 37) was evaluated prior to the selection of compositions for the first atomization campaign. The alloy systems examined were based on the most promising systems described in the literature survey: copper-zirconium, copper-chromium, copper-silver, copper-hafnium, and copper-metal diboride.

a. Copper-Zirconium

The copper-zirconium system was chosen because it has served as the basis of zirconium copper (0.15 percent zirconium), one of the most softening-resistant commercial high-conductivity copper alloys available. In addition, the system served as a basis of sorts for NASA-Z and NARloy-Z™.

Three concentration levels of zirconium were studied: 0.2 percent, 0.4 percent, and 1.0 percent. None exhibited significant hardness or microstructural change when aged at 370 to 605°C (700 to 1200°F) or annealed at 650°C (1200°F) after solution treatment. This was expected. When processed by solution treatment + 40 percent cold rolling, subsequent aging at 370°C (700°F) and 480°C (900°F) produced insignificant changes in hardness or microstructure. However, aging at 650°C or annealing at 650°C after any aging cycle resulted in complete recrystallization and softening. In conventionally processed material, varying zirconium concentration only affected grain size, reducing grain size with increasing concentration.

Significant rapid solidification and concentration effects were observed in the supersaturated copper-zirconium alloys. As-solidified samples exhibited higher hardnesses than conventional cast and solutioned materials. In addition, annealed hardnesses were higher for the rapidly solidified + cold-worked conditions than for the cast + solutioned + cold-worked + aged conditions. Hardnesses were higher for the rapid-solidification-processed Cu-1.0%Zr alloy than for the Cu-0.4%Zr alloy.

The rapid-solidification-processed copper-zirconium materials exhibited finer microstructures than the conventionally processed materials (Figure 24); both as-solidified and after additional processing. Whereas conventionally processed supersaturated alloys exhibited primary precipitates of about 8 µm (80,000 Å), the rapidly solidified primary precipitates were on the order of 1,000 to 5,000 Å. Some primary precipitates or dispersions in cold-worked + annealed rapidly solidified copper-zirconium material are shown in Figure 25.
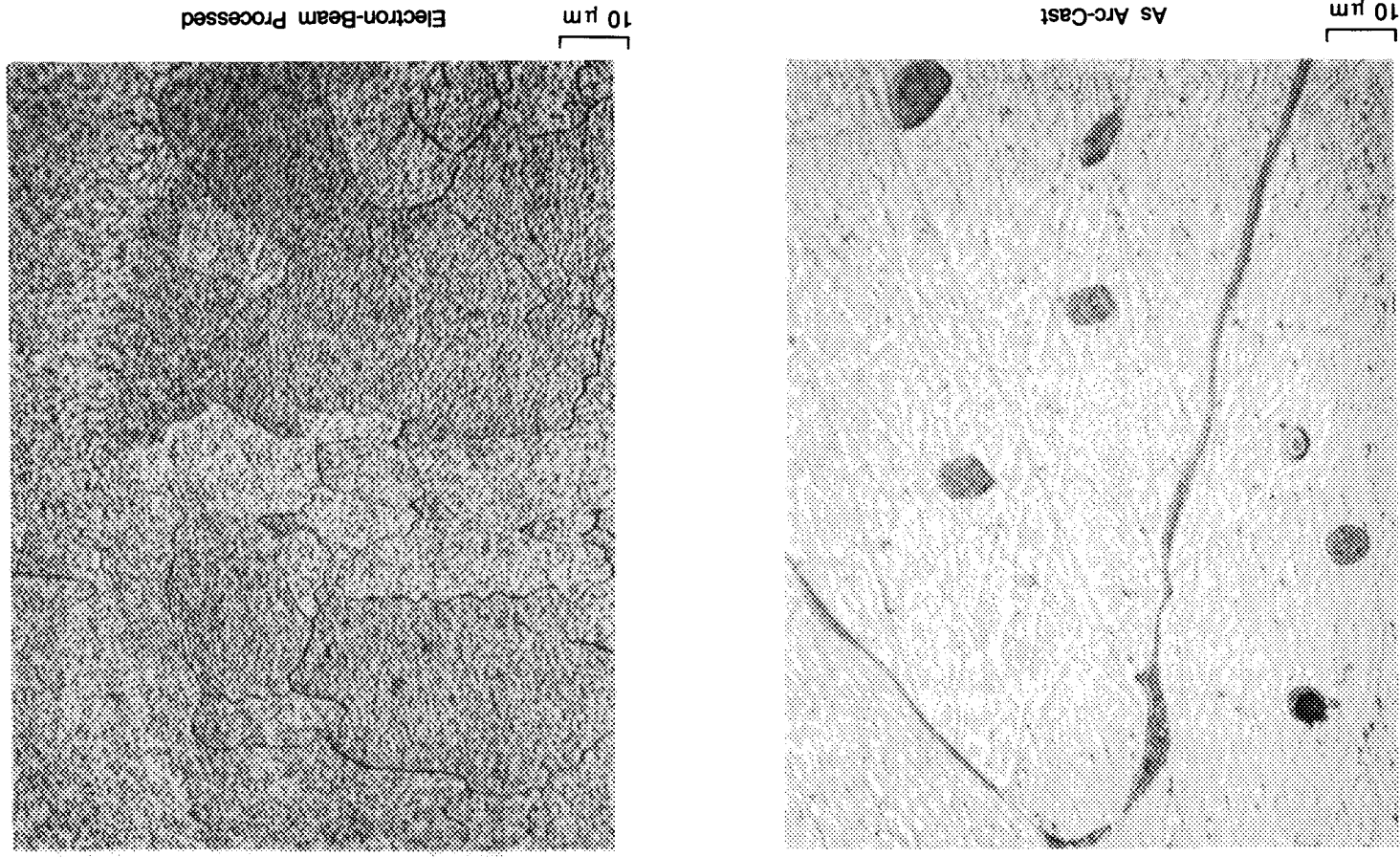
Figure 23. Microstructural Refinement Resulting From Electron-Beam Processing of Cu-1.3%Hf (CB-35): Optical

44
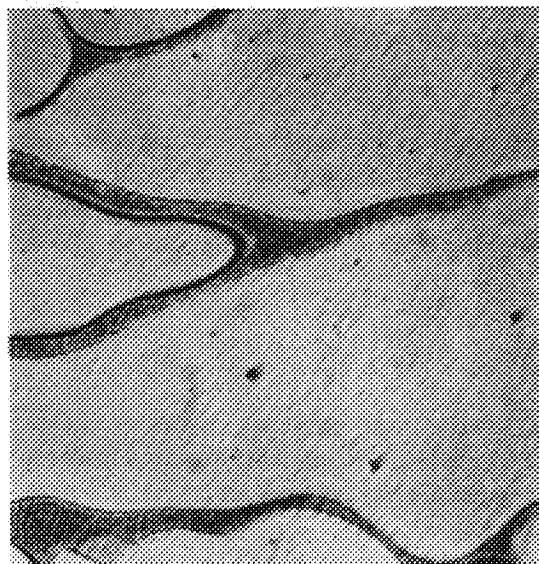
10 μm   Arc Cast
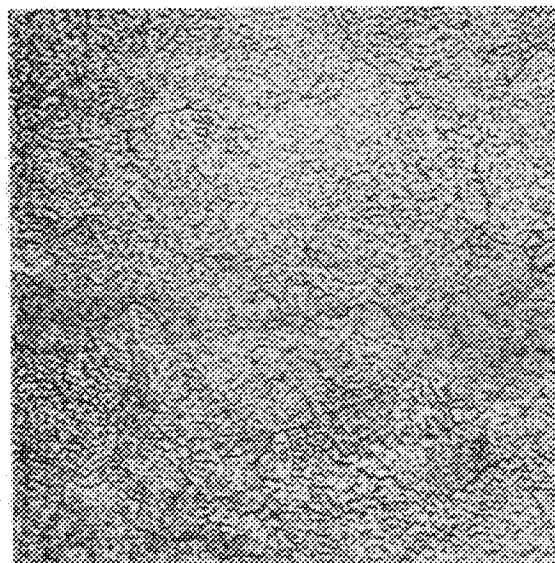
10 μm   Electron-Beam Pass

Figure 24. *Microstructural Refinement in CU-1%Zr (CB-7) by Electron-Beam Processing (Optical)*
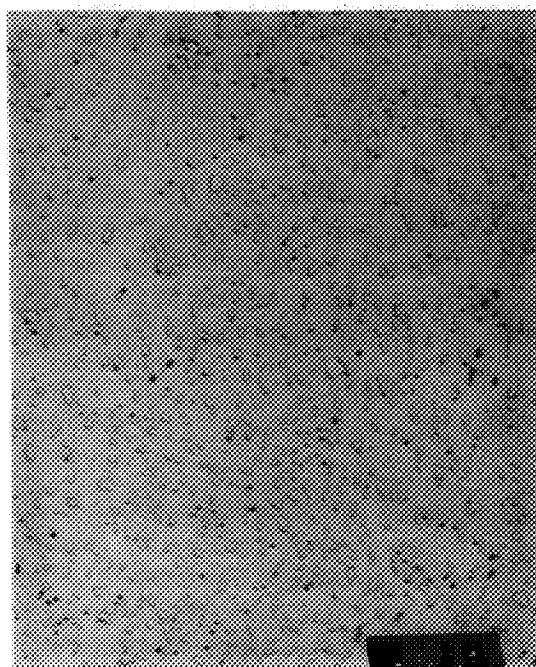
5μ
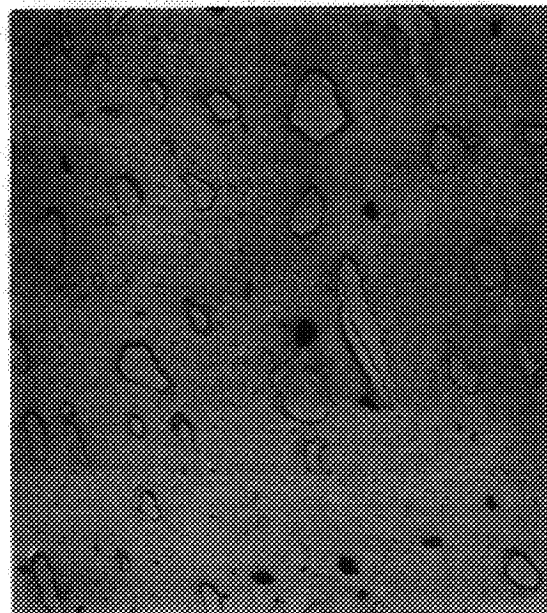
1μ

Figure 25. *Precipitates and Primary Dispersions in Electron-Beam-Processed + Cold-Worked + Overaged Cu-1.0%Zr (CB-7) Alloy (TEM Replica)*

45

X-ray diffraction studies supported the findings of Phillips (17) that the precipitate in this system was a face-centered cubic (FCC) Cu_5Zr compound. In the present study, a lattice parameter of 6.88 Å was measured for this compound.

Generally, studies demonstrated the ability of rapid solidification to disperse excess zirconium in copper-zirconium alloys, resulting in harder and somewhat more stable structures than those obtainable by conventional processing. However, Cu_5Zr dispersions in processed electron-beam welds were coarser than desired: 1,000 to 5,000 Å, versus the 200 to 500 Å generally accepted as necessary for strengthening.

b. Copper-Chromium

Several copper-chromium alloys were studied in the first screening iteration. Later, additional alloys (CB 43-45) were studied for confirmation because of possible elemental losses in the earlier alloys. The results of both sets of alloys generally agreed and are combined here.

Copper-chromium alloys were processed similarly to the copper-zirconium alloys. When solutioned, these alloys age-hardened significantly at 480°C (900°F). When solutioned + cold worked, subsequent aging at 480°C produced slight hardening, but aging or annealing at 650°C (1200°F) recrystallized the alloys. Only the 0.2 percent chromium alloy recrystallized (partially) at 480°C. Grain size was finest in the 1 percent alloy.

Unlike with the copper-zirconium alloys, electron-beam processing of copper-chromium alloys resulted in no hardness increase. But, the cold-worked electron-beam-processed material did not recrystallize when annealed at 650°C. The rapidly solidified (electron-beam-processed) structures were much finer than the conventional structures. However, the dispersions (chromium) in the rapidly solidified materials were coarser than desired: 1,000 to 5,000 Å (Figure 26).

Copper-chromium alloys were found to be highly age-hardenable in the solutioned condition, but only slightly age-hardenable after cold working. Rapid solidification processing greatly increased the recrystallization resistance, but not the hardness, of these alloys. As with the copper-zirconium system, rapid solidification dispersions were coarser than desired, indicating that chromium was not sufficiently stable for use as a high-temperature dispersion in copper.

c. Copper-Silver

The copper-silver system was evaluated because it served as the basis for NASA-Z and NARloy-Z™; large amounts of silver can be added to copper without significantly lowering conductivity; and silver should impart precipitation hardenability. One to 5 percent silver was added, the higher concentrations allowing precipitation reactions. The alloys were only processed conventionally, since excessively high concentrations were needed to reach supersaturation levels.

The alloys age-hardened only slightly. Annealing solutioned + age-hardened material did not appreciably change hardness or microstructure. When cold-worked, subsequent aging or annealing at 480°C (900°F) or above resulted in recrystallization and softening.

1 μm
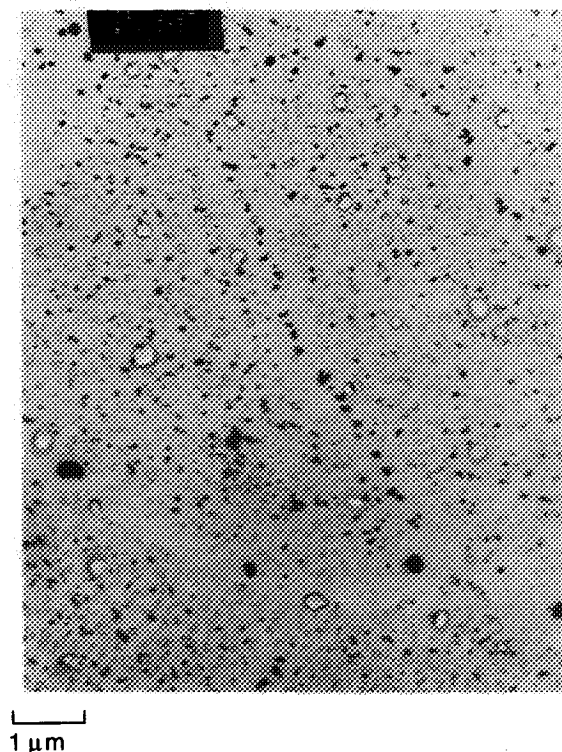
Figure 26. Dispersions or Precipitates in Electron-Beam + Cold-Worked + Annealed Cu-1.0%Cr (CB-23): TEM Replica

Precipitation in the 3 percent and 5 percent silver alloys was discontinuous, inward from the grain boundaries, as noted in the literature (18, 19, 20). This was most pronounced at higher aging temperatures, and is shown in Figure 27. Grain size decreased with increasing silver concentration up to 1 percent.

These results suggested that binary copper-silver alloys would not have promise because of their low age-hardenability and tendency toward discontinuous precipitation.

d. Copper-Hafnium

Several literature citations suggested that the copper-hafnium system could have promise as a base for a thrust chamber alloy (21). Thus, copper-hafnium compositions on both sides of the solubility limit were evaluated (CB 34, 35). The alloys were expected to form Cu_5Hf precipitates or dispersions.

Aging of these alloys produced slight hardening. When solutioned + cold-worked, these alloys recrystallized only when exposed to 650°C (1200°F) (where they fully softened).

47

L___J
1 μm

Figure 27. Discontinuous Precipitation in a Cu-5%Ag Alloy (CB-3, Solutioned + Aged): SEM

Electron-beam passes significantly refined the microstructures (Figure 23) and hardened the materials somewhat. The electron-beam-processed + cold-worked condition recrystallized at 650°C. Dispersions up to 4,000 Å in size were formed, after annealing.

The copper-hafnium alloys were not significantly harder or more stable than copper-zirconium alloys. They responded to rapid solidification, but recrystallization resistance was not improved. Age-hardening was not as great as expected.

e. Copper-Zirconium-Silver

Interest in this system was based on the accepted use of NARloy-Z™ and NASA-Z (Cu-3%Ag-0.5%Zr) and on the potential of combining the benefits of zirconium and silver additions. Two alloys, Cu-3%Ag-0.5%Zr and Cu-1.5%Ag-0.2%Zr, were made. The former was chosen because it is the same as NARloy-Z and NASA-Z; the high zirconium level should produce an insoluble dispersion upon rapid solidification; the silver might allow precipitation hardening. The latter composition was chosen because it seemed sensible to lower silver concentration to avoid any chance of discontinuous precipitation (seen in the binary copper-silver alloys), and to determine the need for the high zirconium level in the conventionally processed form of the alloy.

After solutioning, both alloys exhibited some age-hardenability, with the NASA-Z composition hardening more (Table 13). Only 650°C (1200°F) aging or annealing recrystallized (and softened) the solutioned + cold-worked (+ aged) alloys.

48

TABLE 13. — HARDNESSES OF SCREENING ALLOYS (DPH HARDNESS)

Alloy	Composition (wt.%)	As Solution	Sol. +Age (480°C)	Sol. + CW	Sol. + CW +Age	Sol. + CW + Age + Anneal	As EB	EB + CW	Electron Beam Passes EB + CW + Anneal EB Pass	Substrate*
CB-1	Cu-1.0Ag	50	46	117	63	50				
CB-2	Cu-3.0Ag	55	60	125	75	58				
CB-3	Cu-5.0Ag	70	69	140	75	72				
CB-4	Cu-0.5Zr-3.0Ag	62	80	138	138	75	93	169	84	
CB-5	Cu-0.2Zr	44	52	122	120	50				
CB-6	Cu-0.4Zr	45	50	100	95	57	78	148	71	
CB-7	Cu-1.0Zr	65	70	135	137	67	106	161	109	
CB-16	Cu-0.2Zr-1.5Ag	50	64	129	129	68				
CB-17	Cu-1.1Zr-0.3B	58	68	130	138	63	97	163	82	
CB-18	Cu-2.2Hf-0.3B	58	68	129	153	69	95	180	90	
CB-19	Cu-0.7Ti-0.3B	62	62	130	95	56	65	90	40	
CB-20	Cu-0.8MM-0.4B	52	52	133	54	51	86	139	88	
CB-21	Cu-0.4Cr	45	103	115	158	59	94	180	88	
CB-22	Cu-1.0Cr-0.8Zr	62	90	130	153	77	166	211	125	
CB-23	Cu-1.0Cr	52	98	117	127	65	58	115	90	
CB-24	Cu-0.2Zr-1.5Ag	–		–		68				
CB-25	Cu-0.4Cr-0.2Zr	50	80	120	142	68				
CB-26	Cu-0.6Zr-0.13B								76	48
CB-27	Cu-1.0Zr-0.13B								77	66
CB-28	Cu-0.6Zr-0.25B								71	50
CB-29	Cu-0.35Ti-0.16B								62	47
CB-30	Cu-0.50Ti-0.16B								59	46
CB-31	Cu-0.35Ti-0.30B								80	53
CB-32	Cu-0.4V-0.13B								59	50
CB-33	Cu-0.55Zr-0.16B-1.0Ag								77	57
CB-34	Cu-0.8Hf	53	60	130	145					
CB-35	Cu-1.3Hf	58	65	128	150	65			75	66
CB-36	Cu-0.2Zr-0.8Hf	52	58	153	138					
CB-37	Cu-0.8Zr-1.3Hf	68	68	140	153	86		174	110	85
CB-43	Cu-1.0Cr	53		135	153	66	67	117	117	

49

TABLE 13. — HARDNESSES OF SCREENING ALLOYS (DPH HARDNESS) (CONTINUED)

Alloy	Composition (wt.%)	As Solution	Sol. +Age (480°C)	Sol. + CW	Sol. + CW +Age	Sol. + CW + Age + Anneal	As EB	EB + CW	Electron Beam Passes EB + CW + Anneal EB Pass	Substrate*
CB-44	Cu-0.5Cr	46		120	156	77				
CB-45	Cu-0.2Cr	39		120	123	46				
CB-46	Cu-1.0Cr-0.8Zr	68		160	178	82	91	155	120	
CB-47	Cu-0.4Cr-0.8Zr	66		152			81	155	110	
CB-48	Cu-0.4Cr-0.2Zr	50		120	156	82	66	114	91	
CB-49	Cu-0.5V	70		128						
CB-50	Cu-0.2Zr-0.5Hf	50		142	143	61	85	124	107	
CB-51	Cu-0.6Zr-0.5Hf	60		143	148	64	85	128	102	
CB-52	Cu-0.6Zr-1.2Hf	64		148	168	68	85	128	102	
CB-53	Cu-0.7MM-0.3B									
CB-54	Cu-0.7MM-0.4B									
CB-56	Cu-0.4Y-0.3B	49		129	48	46	73	123	82	
CB-57	Cu-0.6V-0.2B						66			
CB-58	Cu-0.6Cr-0.2B						89	135	110	
CB-59	Cu-1.0Nb-0.2B						75	140	72	
CB-60	Cu-1.5Mo									
CB-61	Cu-1.5Mo-0.2B									
CB-62	Cu-0.1Al-0.3B						72	128		
CB-63	Cu-0.4Si-0.2B						72	143	62	
CB-64	Cu-0.2Cr-0.8Zr				156	82	91	150	114	
CB-65	Cu-2.0Cr-2.0Zr						184	241	177	
CB-66	Cu-0.2Y	47		115	48	47				
CB-67	Cu-0.4Y	46		113	53	50				
CB-68	Cu-1.0Y	60		138	63	60	100	158	74	
CB-69	Cu-0.4MM									
CB-70	Cu-1.0MM									
CB-71	Cu-0.8Zr-0.4Y	66		138	131	70				
CB-72	Cu-0.8Zr-1.0Y	73		148	125	73	113	158	136	
CB-73	Cu-0.8Zr-0.4MM									
CB-74	Cu-0.8Zr-1.0MM	56		127	127	63	94	159	85	
CB-75	Cu-0.4Cr-0.4Y	54		129	127	64				
CB-76	Cu-1.0Cr-1.0Y	60		135	123	68				
CB-77	Cu-0.4Cr-0.4MM									
CB-78	Cu-1.0Cr-1.0MM						88	160	78	
CB-79	Cu-0.4Mo									
CB-80	Cu-0.4Zr-0.4Mo									
CB-81	Cu-1.8Nb-0.3Si									
CB-82	Cu-1.2Cr-0.2Si	58		129	121	67	77	132	123	
CB-83	Cu-3.3Hf-0.4Si						160	160	114	
CB-84	Cu-1.0Ti-0.3Si	69		145	162	85	150	232	128	

TABLE 13. — HARDNESSES OF SCREENING ALLOYS (DPH HARDNESS) (CONTINUED)

Alloy	Composition (wt.%)	As Solution	Sol. +Age (480°C)	Sol. + CW	Sol. + CW +Age	Sol. + CW + Age + Anneal	As EB	EB + CW	Electron Beam Passes EB + CW + Anneal EB Pass	Substrate*
CB-85	Cu-1.7Zr-0.4Si						107	184	110	
CB-86	Cu-0.9Y-0.6Si						93	153	78	
CB-87	Cu-0.7Nb									
CB-88	Cu-1.3Nb						69			
CB-91	Cu-1.0Cr-1.0Nb	51		132	153	67	81	155	110	
CB-92	Cu-2.0Cr-2.0B				125	69	86	139	115	
CB-93	Cu-1.2V									
CB-94	Cu-0.2Zr-0.5V	56		123	127	70	70	136	99	
CB-95	Cu-0.8Zr-1.0V									
CB-96	Cu-0.4Cr-0.5V									
CB-97	Cu-1.0Cr-1.0V									
CB-98	Cu-0.4Cr-0.8Zr-1.0Ag						96	168	127	
CB-99	Cu-0.4Cr-1.0Ag	50		120	152	89	56	125		
CB-100	Cu-0.7Ti-0.3B-1.0Ag									
CB-101	Cu-0.8MM-0.4B-1.0Ag									
CB-102	Cu-1.0Cr-0.7Ti-0.3B	68		151	168	82	79	150	130	
CB-104	Cu-0.2Zr-0.7Nb									
CB-105	Cu-0.8Zr-1.3Nb	64		138	145	65	99	165	110	
CB-107	Cu-2.2Zr-0.2Al	83		159	154	84				
CB-108	Cu-1.1Ti-0.2Al	62	156	140	215	142				
CB-109	Cu-1.4Co-0.4V	64		110	102	106	64	97	79	
CB-110	Cu-1.4Ni-0.2Si	43		127	150	66				
CB-111	Cu-1.6Ag-1.4Y	59		133	68	71				
CB-112	Cu-1.0Cr-2.0Hf	59		153	199	119				
CB-113	Cu-1.1Fe-1.0Y	71		138	86	85				
CB-114	Cu-1.2Co-1.0Y	63		138	86	84				
CB-115	Cu-1.4Ni-0.2Al	39		110	48	45				
CB-116	Cu-0.6Cr-3.0Ag	56		140	174	95				
CB-117	Cu-0.8Hf-3.0Ag	57		162	166	75				
CB-118	Cu-0.6Cr-0.8Hf	57		145	170	80	76	119	102	
CB-119	Cu-0.6Cr-0.6Zr-3.0Ag	71		162	168	89				
CB-120	Cu-0.6Cr-0.8Hf-3.0Ag	69		162	179	84				
CB-121	Cu-0.6Cr-0.7Ti	62	150	148	181	84				
CB-122	Cu-0.6Zr-0.7Ti	69	145	153	181	86				
CB-123	Cu-0.8Hf-0.7Ti	63	166	153	174	104	83	136	82	

TABLE 13. — HARDNESSES OF SCREENING ALLOYS (DPH HARDNESS) (CONTINUED)

Alloy	Composition (wt.%)	As Solution	Sol. +Age (480°C)	Sol. + CW	Sol. + CW +Age	Sol. + CW + Age + Anneal	As EB	EB + CW	EB + CW + Anneal EB Pass	Substrate*
CB-124	Cu-1.0Ti-3.0Ag	64	150	156	186	144				
CB-125	Cu-0.6Cr-0.2Fe	55		123	162	83				
CB-126	Cu-0.6Cr-0.2Co	45		117	155	94	58	104	102	
CB-127	Cu-0.6Ni-0.2B	57	61	115	94	60	83	118	93	
CB-128	Cu-0.9Fe-0.2B	46	48	115	48	44	86	116	82	
CB-129	Cu-1.2Co-0.2B	60	55	115	49	46	86	130	93	
CB-130	Cu-1.9Hf-1.1Fe	74	74	140	100	60	94	120		
CB-131	Cu-1.9Hf-1.1Mn	63	76	145	162	76	98	144	93	
CB-132	Cu-1.9Hf-1.2Ni	70	78	136	120	74	92	159	112	
CB-133	Cu-1.9Hf-1.2Co	72	82	141	120	74	103	150	128	
CB-134	Cu-1.1Fe-0.5Ti	77	84	128	145	70	77	128	110	
CB-135	Cu-1.1Fe-1.0Nb	69	59	104	49	56	71	115		
CB-136	Cu-1.1Fe-1.0Zr	66	80	137	157	73	91	140	115	
CB-137	Cu-1.5Ni-0.6Zr	62	76	134	117	64	81	120	98	
CB-138	Cu-0.4Y-0.3B									
CB-139	Cu-1.0Nb-0.2B									
CB-140	Cu-0.6Al-0.3B									
CB-144	Cu-0.05Ti-0.01Hf-0.2Al									
Amzirc	Cu-0.15Zr	48	52	139	135	51				
NASA-Z	Cu-0.5Zr-3.0Ag	42	83	160	138	78	72	119	60	

Electron-beam passes on CB 4 (NASA-Z) refined and hardened the structure, compared to as-cast material (Figure 28). When cold-worked + annealed, the rapidly solidified material softened, but still exhibited finer microstructure and higher hardnesses than the cold-worked + annealed conventionally processed version. Dispersions in the rapidly solidified NASA-Z were similar in size to those seen in the rapidly solidified copper-zirconium alloys: 1,000 to 5,000 Å (Figure 29).

10 μm
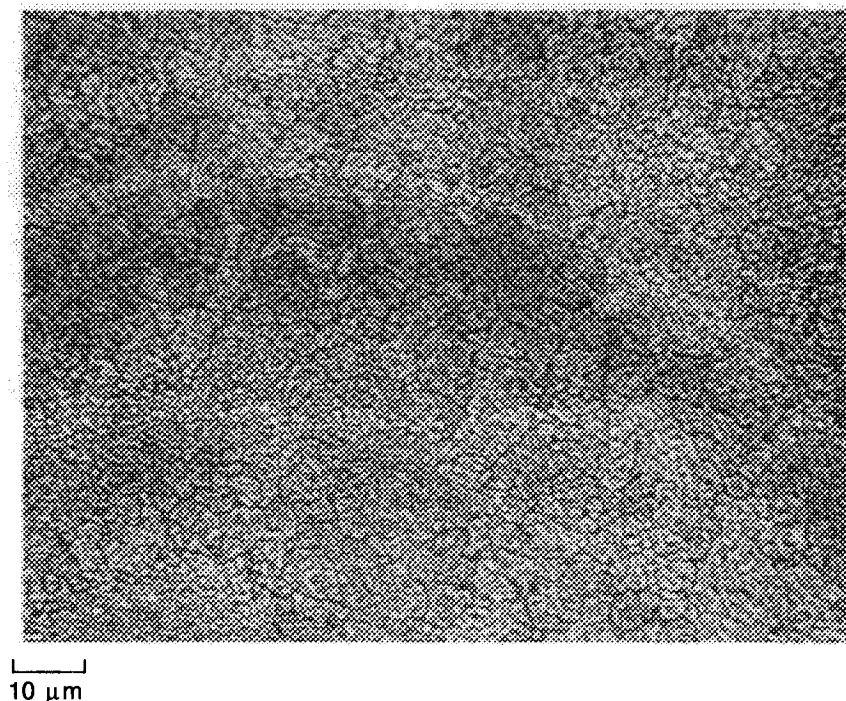
Figure 28. Microstructure of Electron-Beam Pass in Cu-3.0%Ag-0.5%Zr Alloy (CB-4): Optical

The precipitates or dispersions found in the NASA-Z composition were silver and $(Cu, Ag)_5Zr$. Scanning Transmission Electron Microscope (STEM) analyses reported compositions of Cu-16at.%Zr-7at.%Ag for the ternary compounds, similar to reported values (2,22). X-ray diffraction studies identified a silver phase and a phase almost identical in structure to Cu_5Zr (presumably the ternary Cu-Ag-Zr phase). This latter phase was almost face-centered cubic (FCC) (a=6.92Å), with double peaks near locations for some FCC Cu_5Zr peaks. This would suggest slight tetragonality for the ternary phase, agreeing somewhat with other investigations (22).

Notable in the high-concentration alloy (NASA-Z) was the absence of discontinuous silver precipitation, possibly an effect of the zirconium addition. However, slight precipitate-free zones were observed at grain boundaries after aging.

*Figure 29. Precipitates and Dispersions in Cu-3.0%Ag-0.5%Zr After Electron-Beam
Processing + Cold-Working + Annealing (CB-4): TEM Replica*

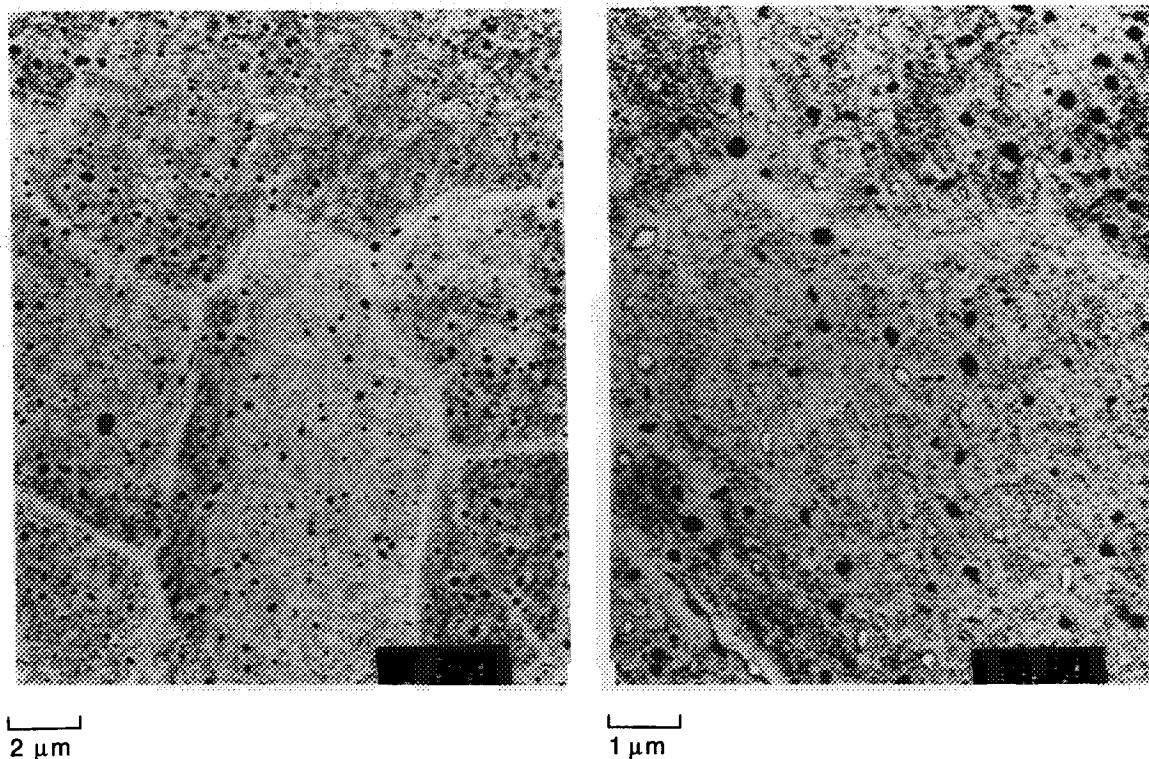Higher concentrations of zirconium and silver refined grain size in conventionally-processed forms. Some abnormal grain growth was observed in the dilute alloy; none was observed in the NASA-Z button.

Rapid-solidification processing was found to refine and harden copper-zirconium-silver alloys. The age hardenabilities of the alloys were not great, and they recrystallized easily at 650°C (1200°F). Therefore, their superiority to copper-zirconium alloys was not obvious.

f. Copper-Zirconium-Chromium

The copper-zirconium-chromium system has been noted in the literature as having superior temperature resistance and as being very age-hardenable (23, 24, 25). Several compositions were investigated: two in the first iteration (CB 22 and 25) and five in the second iteration (CB 46, 47, 48, 64, 65) for confirmation (chromium losses were suspected in the first lot; all are discussed here). The alloys were formulated to straddle the solubility limits of the copper-zirconium and copper-chromium binary systems (0.15 percent zirconium and 0.65 percent chromium (26, 27)), in various combinations.

Conventionally processed solutioned alloys were found to be age-hardenable, increasing on average from diamond pyramid hardness (DPH) 55 to DPH 85 (Table 13). The cold-worked forms age-hardened only slightly. More significant, however, was the tendency for these alloys to resist recrystallization at 650°C (1200°F) after solution + cold work + age. Only partial recrystallization and softening was observed, especially for the second-iteration lot of alloys. Stoichiometric effects (Zr:Cr ratio) were not significant.

54

Rapidly solidified copper-zirconium-chromium alloys also only partially softened when annealed at 650°C after cold work. However, this softening resistance was observed only with the second lot of alloys. Rapidly solidified forms were harder than comparable conventionally processed forms.

As with the other alloy systems, rapid solidification refined the structures of these alloys (Figure 30). Dispersions formed by rapid-solidification processing of copper-zirconium-chromium alloys were coarser than desired: 1000 to 5000 Å (Figure 31). Precipitates and dispersions formed in the alloys were identified as chromium and possibly the Cu_5Zr compound. No Cr_2Zr was found.

10 μm
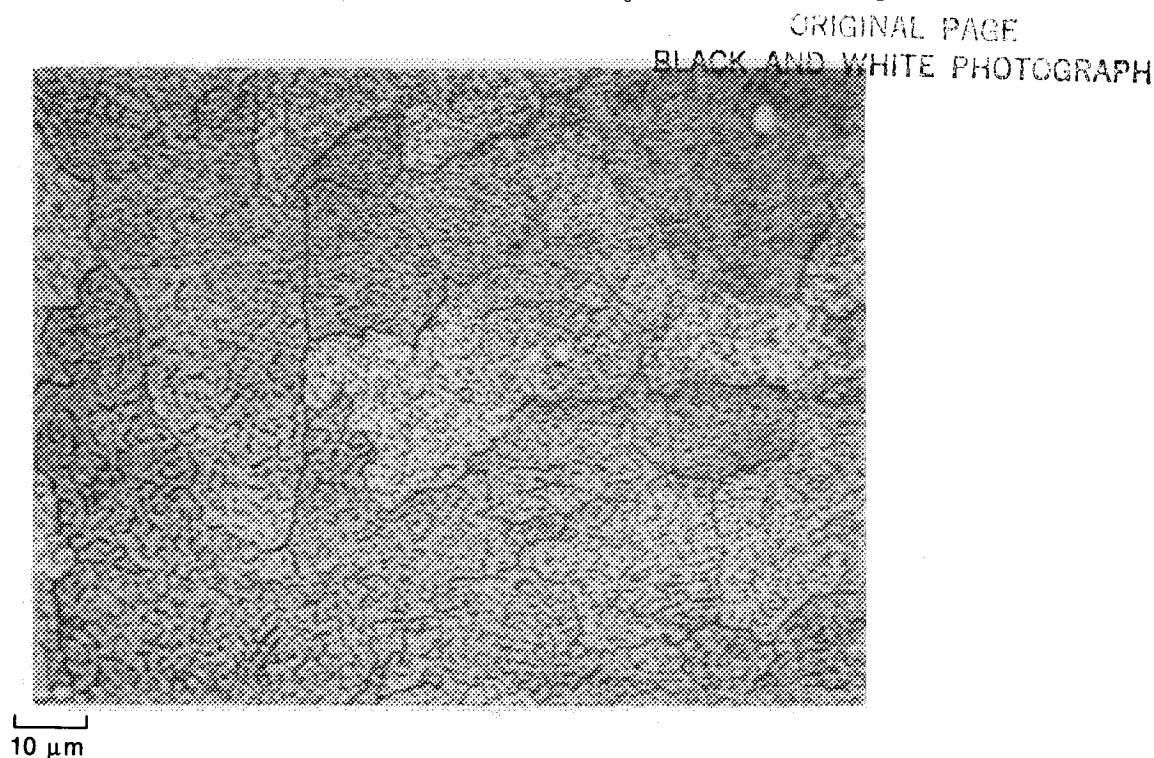
Figure 30. Microstructure of Electron-Beam Pass in Cu-0.8%Zr-1.0%Cr Alloy (CB-22): Optical

The copper-zirconium-chromium alloys were found to be very resistant to recrystallization and softening, but not as age-hardenable as expected. As with the copper-zirconium and copper-chromium systems, the dispersions were coarser than desired. The Cr_2Zr phase, which has a high melting point and might have been more stable than Cr or Cu_5Zr, did not form in these alloys. Nevertheless, these alloys did exhibit high hardness and recrystallization resistance, making the system a candidate for further study.

g. Copper-Zirconium-Hafnium

The literature review revealed that copper-zirconium-hafnium alloys showed a potential for a 38°C (100°F) increase in temperature capability over that of zirconium copper. Five copper-zirconium-hafnium compositions were made and studied (CB 36, 37, 50-52), two in the first iteration and three in the second iteration. Compositions straddled the solubility limits of both binary systems, 0.15% zirconium and 0.9% hafnium (21).

2 μm

Figure 31. Dispersions in Cu-1.0%Cr-0.5%Zr (CB-22) After Electron-Beam + Cold-Work + Anneal Processing: TEM Replica

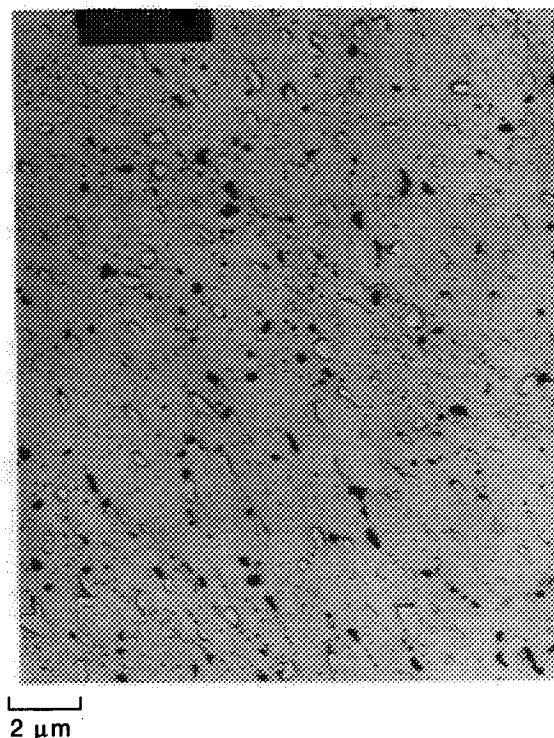The age hardenability expected from the literature review was not realized with these alloys. They were only slightly more age-hardenable than the copper-zirconium alloys, going from DPH 52 to DPH 58 (CB 36). Their resistance to recrystallization was about the same as that of copper-zirconium alloys. After solution + cold work, the alloys recrystallized only at 650°C (1200°F).

This system did respond well to rapid solidification. The rapidly solidified regions were much harder and finer in microstructure than the cast regions (Figure 32). Cold-worked electron-beam passes did not appear to recrystallize when annealed at 650°C, and softened only slightly, providing much better resistance than that of the copper-zirconium system. However, the dispersions were relatively coarse.

The precipitates and dispersions forming in these alloys were found to be about 13at.% Hf+Zr– 87at.% Cu: probably $Cu_5(Zr, Hf)$ (i.e., Cu_5Zr with hafnium substituting for some of the zirconium).

h. Copper + Borides

Pratt & Whitney has extensive experience in enhancing properties of iron-aluminides through the additions of TiB_2 dispersions by rapid solidification. Such dispersions have been about 200 to 1000 Å in size, depending on processing, and have been very effective in stabilizing microstructures at elevated temperatures. Application of this concept to copper alloys was undertaken through the study of TiB_2, HfB_2, ZrB_2, and mischmetal-B_6 (MMB_6) dispersions in

56

copper. The TiB_2 composition was a direct outgrowth of the iron-aluminide work. The HfB_2 and ZrB_2 compounds were used because of the low solubilities of hafnium and zirconium in copper, allowing retention of conductivity in the event of boron losses. The MMB_6 compound was used to evaluate another type of reactive metal boride.

Boride-containing buttons (CB 17 to 20) were melted from copper, boron, and stoichiometric amounts of the appropriate reactive elements. Resulting microstructures consisted of copper matrices containing randomly dispersed coarse 1 - 5 μm borides and, in all cases but $Cu-TiB_2$, a third phase comprised of the reactive metal and copper (Cu_5Zr, Cu_5Hf, Cu_6MM), Figure 33. (Evidently, some boron was lost through melting.) The presence of ZrB_2, TiB_2, HfB_2, MMB_6, and Cu_6MM was confirmed by x-ray diffraction.

Conventional processing of these alloys revealed low recrystallization resistance (except in alloys with an excess of hafnium or zirconium). However, the as-cast boride dispersions were too coarse to impart softening resistance. The coarse MMB_6 borides appeared very unstable.

Rapid-solidification (electron-beam) and subsequent processing of diboride-containing alloys resulted in dispersions such as those shown in Figure 34. The boride dispersions were trimodal: a fine 200 to 500 Å fraction, a 1000 to 3000 Å fraction, and a very coarse 1 μm fraction. The coarse dispersion was believed to be a result of incomplete boride dissolution during electron-beam processing (i.e. borides left over from buttons). The fine dispersion was believed to demonstrate the fundamental stabilities of the diborides. All diborides exhibited essentially the same stabilities.

Hardening and stabilizing effects of the dispersions were slight. The minimal effects were attributed to the nonideal dispersions.

Efforts were made to establish whether the coarse borides formed in the melt or upon solidification. These efforts involved the use of melt spinning to melt the alloys in a controlled fashion, and to rapidly solidify the alloys. Melt spinning allowed melt temperatures to be measured via an infrared thermometer, whereas the arc melting and electron-beam processes did not allow realistic melt temperature determination. Melt spinning was believed to give solidification rates as high as powder atomization or electron-beam processing. It was believed that the presence of very coarse borides in the ribbon would result from solubility problems rather than formation during solidification, and that variance of the melt temperature and dwell time (more easily controlled in this device) might yield clues to the elimination of this problem. Sections of CB 26 (Cu-0.6%Zr-0.13%B) were melted in the device and spun off a copper disk in the form of ribbon, using the parameters listed in the procedures section (Table 3).

Evaluation of the ribbons (Figure 35) showed the existence of coarse borides, with little dependence on varying melt temperatures from 1093°C to 1650°C (2000 to 3000°F). The borides appeared as coarse as those seen in the arc-melted buttons, and thus were believed to have nucleated in the melt. It appeared that melt temperatures nearer the melting points of the borides would be necessary for their solution in copper.

Electron-beam and melt-spinning trials indicated that slight amounts of MB2 borides could be dissolved in molten copper, be finely dispersed by rapid solidification, and resist coarsening at elevated temperatures. However, boride additions on the order of 2 volume percent would nucleate borides in the melt. The only methods that might avoid this problem were 1) high melt temperatures above 1650°C (3000°F), and 2) late additions of boron and/or the reactive metal immediately prior to rapid solidification.

58
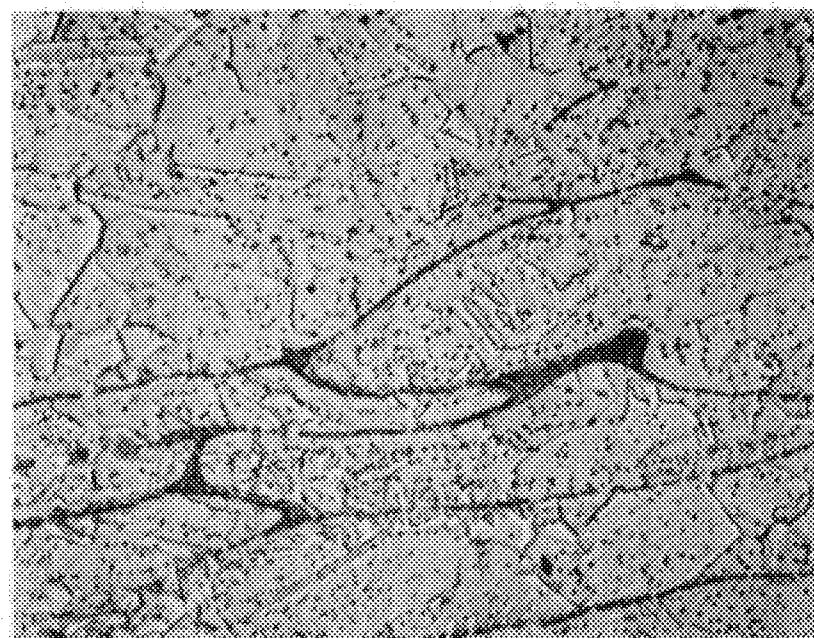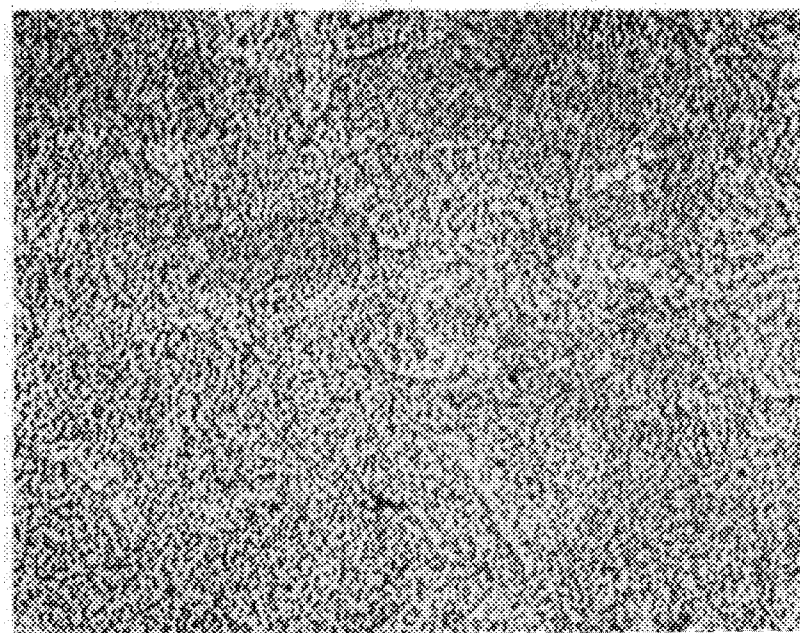
10 μm   Arc Cast

10 μm   Electron–Beam Processed

Figure 32. Effect of Electron-Beam Solidification on Microstructure of Cu-0.8%Zr-1.3%Hf
Alloy (CB-37): Optical

10 μm
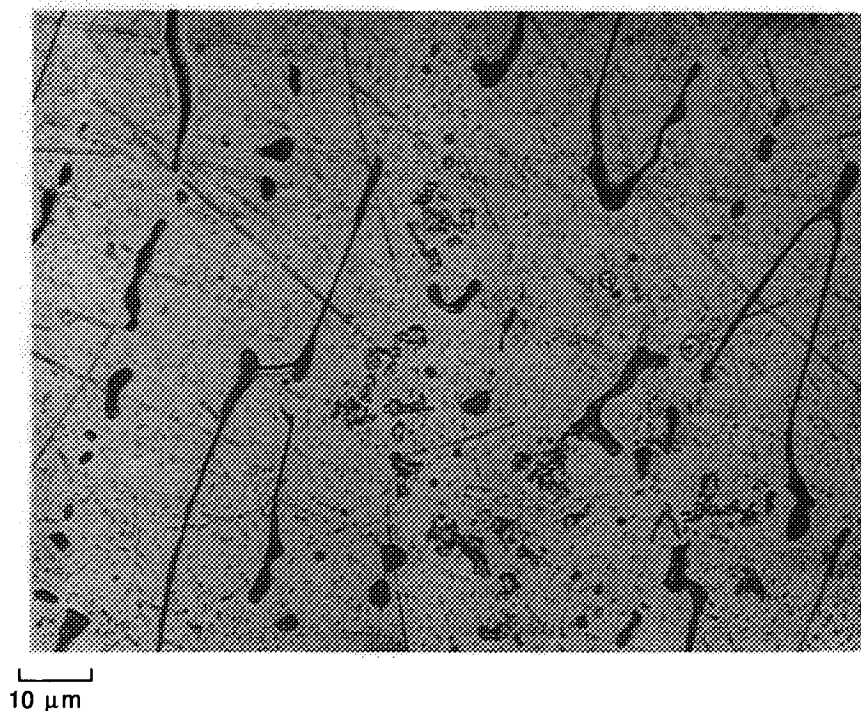
Figure 33. Borides (Center) and Cu-Zr Intermetallic Phase Formed in CB-17 Arc Casting (Optical)

2. SECOND-ITERATION SCREENING RESULTS

The second iteration of screening alloys had several goals: to produce more homogeneous chromium-containing alloys; to find dispersable intermetallic compounds that, through one mechanism or another, were stable and finely dispersed throughout processing and use; and to find borides that could be finely dispersed via the RSR process and remain finely dispersed through processing and use.

Improvement of chromium-containing button quality was attained with better process control in a new arc-melting device. Also, the use of carefully prepared copper-chromium master alloys (about 15 percent chromium) greatly minimized chromium segregation during arc melting. These techniques were used on the second-iteration chromium-containing alloys discussed in the last section.

59
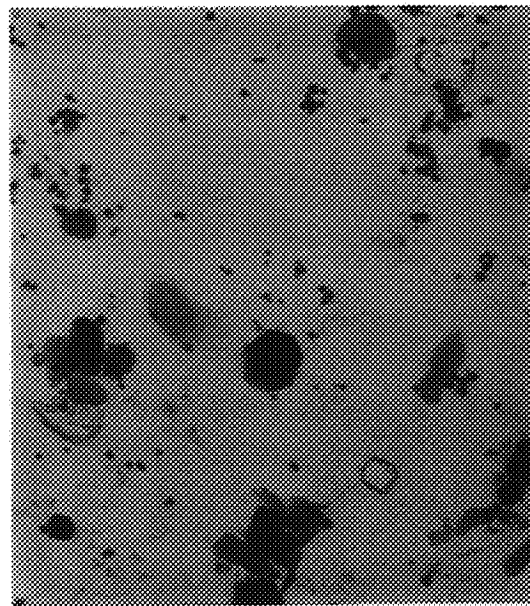
0.3 μm

5 μm

Fine
Cu + HfB₂
(TEM Replica)
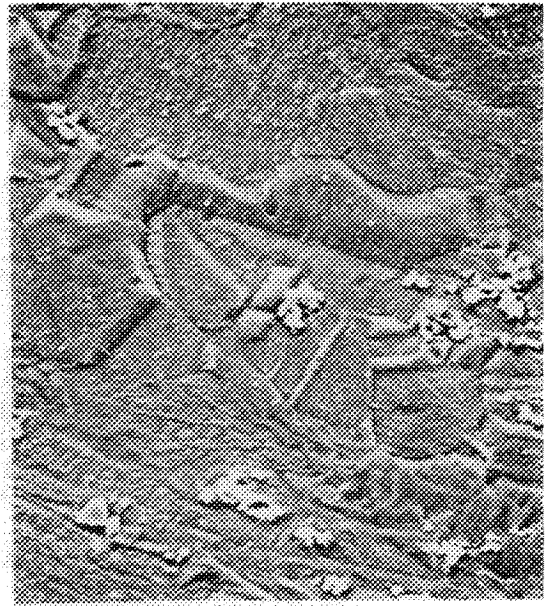
Very Coarse
Cu + TiB₂
(SEM)

Figure 34. Fine and Coarse Borides in Electron-Beam Passes

Two approaches were taken for the application of intermetallic phases as strengtheners in copper. One approach was the use of untried (or previously uncombined) elements or Cu-X compounds that precipitate from solid or solidifying copper, in manners similar to those of chromium and zirconium. New systems used additions of vanadium, mischmetal, yttrium, titanium, and niobium to either copper or first-iteration alloy systems. The approach involved additions to form copper-free intermetallics that would, by virtue of high melting points or low lattice mismatches with copper, be stable at elevated temperatures. The specific compounds are described later.

A number of alloys were formulated to produce metal borides of various stabilities (based on boride melting point) in an attempt to find borides that were dispersable by rapid solidification yet stable in copper at elevated temperatures.

Finally, some alloys were formulated to produce high-temperature silicides that might strengthen copper by remaining stable in copper at elevated temperatures.

10 μm
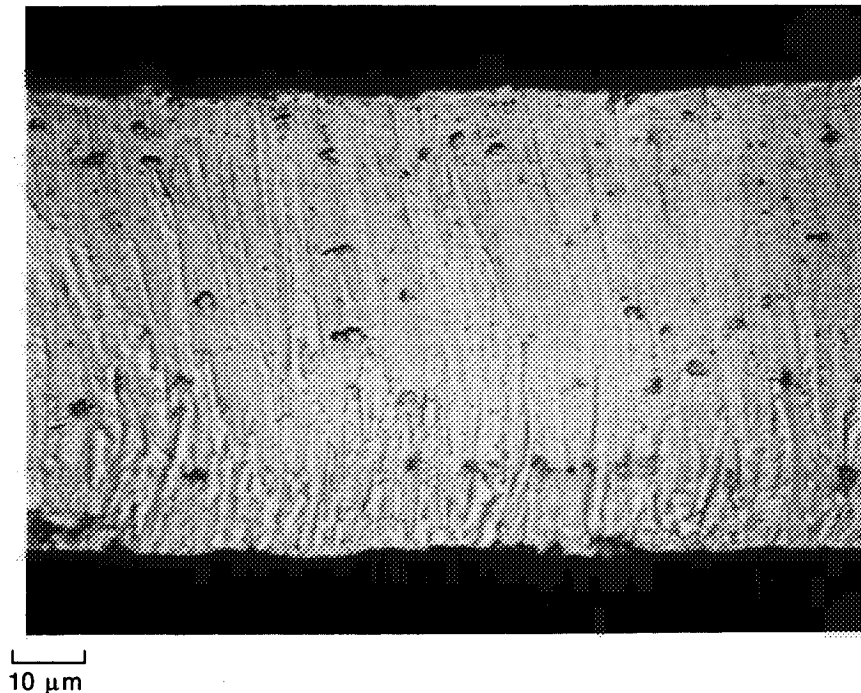
Figure 35. *Presence of Very Coarse Bordies in Representative Cu-Zr-B (CB-26) Melt-Spun Ribbon*

For the second iteration of screening alloys, processing was abbreviated by eliminating the solution + aged (and subsequent) conditions, so as to accommodate the large numbers of alloys being evaluated. Significant age-hardenability was discerned from the results of a post-cold-work 480°C (900°F) aging step. This was believed valid, insofar as those alloys that would be useful at 650°C (1200°F) or higher should be able to resist recrystallization during a 480°C age following cold work. Results of the second alloy screening iteration are described below.

a. Copper-Niobium

The copper-niobium phase diagram allows for solid-state precipitation reactions similar to those of copper-chromium. Based on this, copper-niobium alloys (CB 87 and 88) were formulated straddling the niobium solubility limit of 1 percent niobium (27).

When conventionally processed with cold work, the alloys recrystallized upon aging at 480°C (900°F). The recrystallization resistance was so low that hardnesses were not measured.

In the rapidly solidified + cold-worked conditions, the 1.3 percent niobium alloy recrystallized upon annealing to such an extent that the weld could no longer be found. The as-solidified hardness was low.

Niobium did not show potential as a hardener of copper, at least alone or at the concentrations investigated.

61

d. Copper-Niobium-Zirconium

Mandingo et al (28) found that niobium additions helped strengthen and stabilize zirconium copper. For the present program, copper-niobium-zirconium alloys (CB 104 and 105) were made straddling the binary solubility limits of 1 percent niobium and 0.15 percent zirconium.

When conventionally processed, the alloys were no more stable than zirconium copper. Both alloys recrystallized and softened when annealed at 650°C (1200°F) after solutioning + cold work + aging. Alloy CB 105 age-hardened very slightly at 480°C (900°F) after cold working.

Rapid solidification refined the structure, and hardened the material from DPH 65 to DPH 99. The electron-beam-processed material softened when annealed at 650°C after cold work. These alloys did not appear to offer advantages compared to copper-zirconium alloys.

c. Copper-Niobium-Chromium

Copper-niobium-chromium alloys were also made (CB 64 and 65), straddling the binary solubility limits of 1 percent niobium and 0.65 percent chromium.

When processed, performances were very similar to copper-niobium-zirconium alloys: recrystallization and softening occurred upon 650°C (1200°F) anneal (after solution + cold work + age). The cold-worked alloys age-hardened somewhat when annealed at 480°C (900°F).

When rapidly solidified, the alloys were finer and harder than comparable conventionally processed alloys. After cold working, the alloys softened when annealed at 650°C. The stabilities of these alloys were about the same as those of copper-zirconium alloys.

d. Copper-Vanadium

Other investigations indicated that copper-zirconium-vanadium alloys might provide an improvement over zirconium copper (29). The copper-vanadium phase diagram suggested precipitation hardenability similar to that of copper-chromium. Thus, copper-vanadium alloys were formulated, straddling the solid solubility limit (CB 49 and 93). When processed conventionally, with cold work, these alloys recrystallized at 650°C (1200°F) and sometimes at 480°C (900°F). The 1.2 percent vanadium alloy (CB 93) oxidized catastrophically during solution treatment (it appeared that interdendritic vanadium oxidized and liquified, promoting further oxidation). Therefore, this system was not investigated further.

e. Copper-Zirconium-Vanadium

The copper-zirconium-vanadium alloys did not exhibit the catastrophic oxidation observed during solution treatment of the copper-vanadium alloy. Two alloys were melted (CB 94 and 95), again straddling the binary solubility limits (0.15 percent zirconium and 0.7 percent vanadium (30)).

When processed conventionally, the alloys did not exhibit age hardenability in the solutioned + cold-worked condition, but did not soften during the 480°C (900°F) aging treatment. The alloys recrystallized completely upon subsequent annealing at 650°C (1200°F).

In the rapidly solidified conditions, Alloy CB 95 was harder than in comparable cast + wrought conditions. However, the cold-worked alloy softened and recrystallized at 650°C.

The copper-zirconium-vanadium alloys resisted softening and recrystallization as well as, but no better than, copper-zirconium alloys. No benefits could be attributed to the vanadium

additions. The catastrophic oxidation observed with the copper-vanadium alloys was not seen with the copper-zirconium-vanadium alloys. However, the possibility of oxidation reinforced the conclusion that vanadium additions to copper-zirconium alloys are not beneficial.

f. Copper-Chromium-Vanadium

Copper-chromium-vanadium alloys were formulated (CB 96 and 97), with concentrations straddling the binary solubility limits of 0.65 percent chromium and 0.7 percent vanadium.

In the cast + solutioned + cold-worked + aged conditions, the alloys recrystallized upon subsequent annealing at 650°C (1200°F) thereby exhibiting behavior equivalent to that of copper-chromium alloys.

As with the other alloy systems, electron-beam processing refined the alloy structures. The cold-worked electron-beam passes recrystallized after the 650°C anneal, which again was equivalent to copper-chromium alloys.

Overall, these ternary alloys exhibited softening and recrystallization resistance no better than that of copper-chromium alloys, so there were no obvious benefits derived from vanadium additions to the copper-chromium system.

g. Copper-Mischmetal

When added to copper, the rare earths form Cu_6X precipitates that might contribute to hardness or temperature resistance. CB 69 and 70 were mischmetal alloys (mischmetal is a mix of lanthanum, cerium, and other rare earths). These alloys were melted and processed to evaluate the effects of rare earth additions on copper.

The alloys were conventionally processed and found to recrystallize at 480°C (900°F) after cold working (hardness was not measured). When electron-beam processed, the alloys were refined, but they recrystallized during the 650°C (1200°F) test anneal.

The addition of misch metal did not appear to produce the softening resistance imparted by other additions such as zirconium, chromium, or hafnium. The Cu_6MM phase (whose presence was confirmed for the copper-mischmetal-boron alloy) appeared to be a weak hardener of copper alloys.

h. Copper-Mischmetal-Zirconium

Copper-mischmetal-zirconium alloys (CB 73 and 74) were formulated to straddle the binary solubility limit of 0.15 percent zirconium, at 0.4 percent and 1 percent mischmetal.

When processed conventionally, cold-worked material recrystallized and softened upon exposure to 650°C (1200°F). Cold-worked material did not age harden. Rapidly solidified samples exhibited finer and harder microstructures than conventionally processed conditions. Electron-beam-processed + cold-worked material fully recrystallized and softened when annealed at 650°C. These results were similar to those of copper-zirconium alloys, leading to the conclusion that the copper-zirconium system did not benefit from the addition of mischmetal.

i. Copper-Mischmetal-Chromium

This system was suggested by Nishiyama et al (31), who found that mischmetal additions improved the softening resistance of chromium-copper. Based on these results, two copper-misch-metal-chromium alloys (CB 77 and 78) were formulated, at high and low concentrations.

When processed conventionally with solution treatment and cold working, the alloys (CB 77 and 78) recrystallized during subsequent aging at 480°C (900°F), whereas the copper-chromium alloys recrystallized at 650°C (1200°F).

Electron-beam processing refined the structure substantially. However, the alloys also recrystallized and softened when annealed at 650°C after elecron-beam processing and cold work. The addition of mischmetal to the copper-chromium system did not appear to be beneficial.

j. Copper-Yttrium

Yttrium forms a Cu_6Y precipitate that might produce hardening in copper. Alloys containing 0.2 percent, 0.4 percent, and 1.0 percent yttrium (CB 66, 67, 68) were evaluated to determine the strengthening effects of this precipitate. Conventionally processed alloys were found to recrystallize and soften when aged at 480°C (900°F) after solution + cold work, however. The electron-beam processed alloys were harder, but fully softened and recrystallized when annealed at 650°C (1200°F) after cold work. In general, these alloys performed no better than copper-mischmetal alloys, and much worse than copper-zirconium and copper-chromium alloys.

k. Copper-Yttrium-Zirconium

Addition of zirconium to copper-yttrium alloys (CB 71 and 72, with compositions straddling the binary solubility limits) brought the properties up to the levels of copper-zirconium alloys. Cold-worked conventionally processed forms of the alloys neither age-hardened nor softened at 480°C (900°F). They recrystallized and softened only at 650°C (1200°F). Electron-beam processing hardened and refined the alloys. Annealing after rapid solidification + cold working recrystallized and partially softened Alloy CB 72. Hardness of the electron-beam-processed alloys were slightly higher than those of copper-zirconium alloys. However, benefits of yttrium additions to the copper-zirconium system were not significant.

l. Copper-Yttrium-Chromium

To complete the study of yttrium systems, chromium was added to copper-yttrium alloys, in amounts straddling the binary solubility limits (CB 75 and 76). These alloys did not exhibit age-hardening in the solutioned + cold-worked + aged condition. They recrystallized only at 650°C (1200°F). Electron beam processing refined the microstructures. However, subsequent cold working + annealing produced considerable dispersion coalescence (Figure 36). This phenomenon eliminated the alloy from further consideration.

m. Copper-Molybdenum, Copper-Molybdenum-Zirconium, Copper-Molybdenum-Boron

Work at MIT on dispersion of molybdenum in copper (32) prompted in-house trials. Available phase diagrams suggested that small amounts of molybdenum could be dissolved in molten copper and dispersed upon solidification. These trails were not successful. Apparently, temperatures sufficient to dissolve molybdenum in copper could not be attained during arc melting. The resultant buttons were not evaluated.

n. Copper-Chromium-Hafnium

Both the copper-chromium and copper-hafnium systems were evaluated earlier. Their combination was evaluated with alloy CB 118, formulated with chromium and hafnium levels slightly above their binary solubility limits.
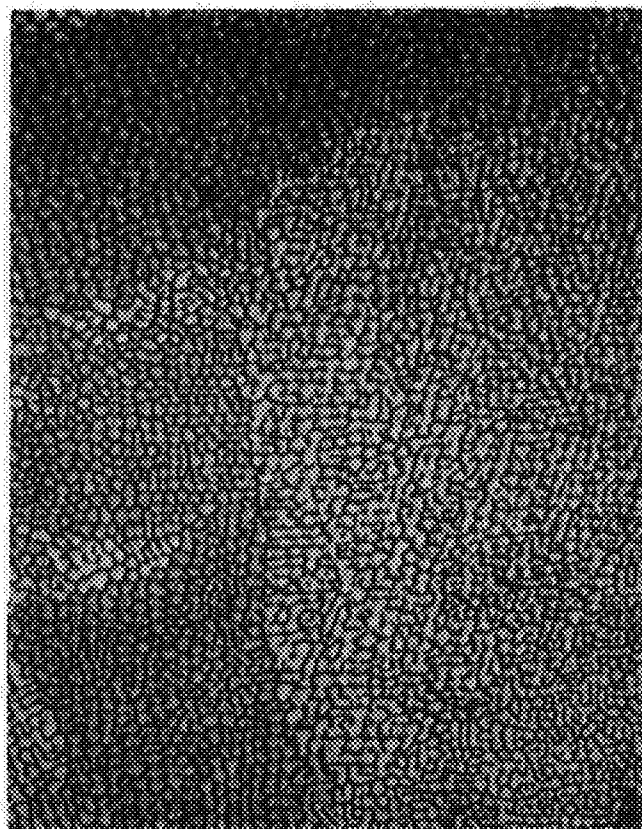
10 μm   Electron-Beam Pass Only

10 μm   EB Pass + Cold Worked + Annealed

Figure 36.   *Precipitate Coalescence in Cu-Y-Cr Alloy (CB-76) Electron-Beam Pass After Cold Working + Annealing (Optical)*

When conventionally processed, the alloy hardened significantly when aged after cold work. The cold-worked + aged alloy softened and recrystallized upon annealing at 650°C (1200°F).

Rapid solidification hardened the alloy and refined its structure. Cold working further hardened the alloy and subsequent annealing at 650°C only slightly softened the alloy.

Microprobe analysis revealed a precipitate composed of about 89at.%Cu-1at.%Cr-10at.%Hf. The structure of the precipitate was not determined.

These results were at least as good as those for copper-chromium alloys, and better than those for copper-zirconium and copper-hafnium alloys. It was not clear whether the effects of combining chromium and hafnium were additive or synergistic.

o. Copper-Chromium-Silver

The copper-chromium-silver system also was a combination of systems that showed promise as binaries. Alloys (CB 99 and 116) were formulated at high and low chromium and silver concentrations.

When processed conventionally, both responded in similar manners. Both hardened upon cold working, further hardened upon subsequent aging at 480°C (900°F), and partially recrystallized upon a further anneal at 650°C (1200°F). The more-concentrated alloy (CB 116: high silver) was slightly harder in all conditions.

Only Alloy CB 99 was electron-beam processed (116 was used to examine age-hardening by silver). As solidified, electron-beam-processed CB 99 was quite soft. Cold working hardened the weld, but subsequent annealing recrystallized and softened the weld. This may be attributable to the moderate chromium content.

The copper-chromium-silver alloys exhibited much higher hardness and better recrystallization resistance than the copper-silver alloys. The discontinuous precipitation seen with the binary copper-silver alloys was not observed with these ternary alloys. Compared to the copper-chromium alloys, these ternary alloys exhibited equivalent hardnesses but possibly lower recrystallization resistance, especially in the rapidly solidified condition.

p. Copper-Chromium-Zirconium-Silver

To address the effects of combining the three baseline systems, two alloys (CB 98 and 119) were formulated from the copper-chromium-zirconium-silver system. The most significant difference between the two alloys was the silver concentration and resultant ability to precipitate silver (the alloys contained 1 percent and 3 percent silver, respectively).

Both alloys responded similarly to conventional processing, recrystallizing only at 650°C (1200°F). Aged hardness of the alloy containing 3 percent silver was almost identical to that of an equivalent silver-free alloy (CB 46). Apparently, the silver had little effect.

Only one alloy was electron-beam processed: CB 98 (lower silver was not expected to benefit from rapid solidification). This alloy hardened as a result of rapid solidification, further hardened upon cold working, and was only slightly softened by a subsequent 650°C anneal. Its hardnesses were very similar to those of a similar silver-free alloy (CB 46).

In general, these quaternary alloys were very similar to their silver-free counterparts.

q. Copper-Hafnium-Silver

Another ternary combination of promising binaries was copper-hafnium-silver. One alloy, CB 117, was formulated from this system to investigate precipitation hardening when hafnium and silver were combined.

When processed conventionally, the alloy did not harden or soften when aged after cold work. It softened upon subsequent annealing at 650°C (1200°F). Because the silver addition was not expected to enhance the response of the hafnium addition to rapid solidification, the alloy was not electron-beam processed. In general, this alloy exhibited properties equivalent to those of the copper-hafnium alloys.

r. Copper-Chromium-Hafnium-Silver

Another combination alloy system was copper-chromium-hafnium-silver. One alloy, CB 120, was studied. It responded to processing similarly to the silver-free variant (CB 118), age-hardened at 480°C (900°F) and recrystallizing and softening when annealed at 650°C (1200°F). There were little hardness differences between the ternary alloy and the silver-free binary alloy.

Since silver was not expected to respond much to rapid solidification, this alloy was not electron-beam processed.

s. Copper-Titanium-X

Titanium is a potent age hardener of copper. However, due to its high solubility, it lowers conductivity to unacceptably low levels. Nevertheless, it was deemed worthwhile to investigate additions of titanium with other elements (zirconium, hafnium, chromium, silver — CB 121 - 124) to increase hardness while determining if the secondary additions would lower titanium solubility.

The first system, copper-titanium-chromium (CB 121), exhibited high age-hardenability, even after cold work (Table 13). When solutioned and cold worked, it recrystallized only at 650°C (1200°F). The copper-titanium-zirconium alloy (CB 122) responded in an identical manner.

The copper-titanium-hafnium and copper-titanium-silver alloys (CB 123 and 124) responded to conventional processing in the same way as the latter two alloys. However, their annealed, recrystallized hardnesses were much higher. Suspecting that part of this hardness was due to spinodal titanium aging during the vacuum furnace cool, the two alloys were reannealed at 650°C and water quenched. This lowered the copper-titanium-silver hardness considerably, but lowered the copper-titanium-hafnium alloy hardness only slightly.

Electron-beam processing of the copper-titanium-hafnium alloy increased its hardness. Cold working further hardened the electron-beam zone, but subsequent annealing recrystallized the zone and softened it to the as-solidified hardness.

Microprobe analyses indicated that the coarser precipitates in the CB 123 alloy were 78.5at.%Cu-1.5at.%Ti-18at.%Hf (probably a Cu_5Hf structure).

Of these titanium-containing alloys, only the copper-titanium-hafnium alloy exhibited superior hardness after annealing. However, it still recrystallized after a 650°C (1200°F) anneal. Also, sufficient titanium may have remained in solution in the alloy to decrease its thermal conductivity to unacceptably low levels.

t. High-Melting-Point Intermetallic Phases

A survey of high-temperature intermetallics (by melting point) revealed nine compounds not investigated that might be useful for strengthening copper. These were: $HfFe_2$, $HfMn_2$, $HfNi_2$, $HfCo_2$, Fe_2Ti, Fe_2Nb, Fe_2Zr, Ni_4Zr, and Ti_3Al. Since some of the constituents had high solubilities in copper, it was hoped that the high stabilities of these phases might limit their solution in copper. Alloys formulated to contain 2 atomic percent of these compounds were melted and evaluated (CB 108, 130 to 137).

When solutioned and cold worked, only the copper-iron-niobium alloy recrystallized upon heating at 480°C (900°F). The alloys that age-hardened at 480°C did so only slightly (Table 13). The others all recrystallized and softened when annealed at 650°C (1200°F). In some cases, ternary rather than binary precipitates were found (by microprobe, atomic percent): Cu-33Ni-23Hf, Cu-33Co-24Hf, and Cu-20Zr-1.5Fe. Also, Cu-19at.%Ti formed instead of Ti_3Al in the copper-titanium-aluminum alloy (CB 108).

Rapidly solidified versions of the alloys were harder than comparable conventionally processed conditions. All rapidly solidified alloys softened when annealed at 650°C after cold work. Hardnesses were similar to those of copper-zirconium alloys.

u. Intermetallic Low-Mismatch Phases

Bearing in mind that coherent low-lattice-mismatch precipitates and dispersions tend to exhibit greater dimensional stability at elevated temperatures, a survey of cubic compounds compatible with copper and having lattice parameters between 3.506 Å and 3.723 Å (± 3 percent that of copper) and between 7.01 Å and 7.45 Å (± 3 percent that of a doubled copper lattice) was conducted. The resulting compounds are listed in Table 14. Other compounds were rejected for having low melting points. To these was added Zr_3Al (21 percent mismatch, but the melting point and zirconium made it look attractive.)

TABLE 14. — LOW-MISMATCH PHASES ADDED TO COPPER ALLOYS (33)

Compound	Lattice Parameter	Mismatch with Copper
Ni_3Al	3.567 Å	1.3%
Co_3V	3.567 Å	1.5%
Ni_5Si	3.510 Å	3.0%
AgY	3.619 Å	0.1%
Cr_2Hf	7.05 Å	2.5% (2 Cu lattices)
Fe_2Y	7.35 Å	1.7% (2 Cu lattices)
Co_2Y	7.22 Å	0.1% (2 Cu lattices)

Two additional systems chosen were copper-chromium-cobalt and copper-chromium-iron. The goal was to alloy the chromium precipitates with cobalt and iron, thereby decreasing the precipitate lattice parameter and consequently the mismatch (which is normally 2.2 percent along the copper <110> and chromium <111> mating direction).

Alloys were melted to contain about 2 volume percent of the phases, assuming complete precipitation (CB 107, 109-115, 125, and 126).

When processed conventionally, with a cold-work step, most of these alloys recrystallized at 480°C or 650°C (900°F or 1200°F). The copper-nickel-aluminum, copper-cobalt-yttrium, copper-iron-yttrium, and copper-silver-yttrium alloys recrystalized and softened during 480°C aging trail. However, the copper-chromium-hafnium, copper-nickel-silicon, copper-chromium-iron, and copper-chromium-cobalt alloys hardened when aged at 480°C. The copper-zirconium-

aluminum alloy recrystallized at 650°C. The copper-nickel-silicon, copper-cobalt-vanadium, copper-chromium-hafnium, copper-chromium-iron, and copper-chromium-cobalt alloys partially recrystallized at 650°C.

Precipitates that formed in these alloys were identified in several cases (by electron microprobe), in Table 15.

TABLE 15. — PRECIPITATES IN SOME SCREENING ALLOYS

Alloy	Alloy System	Planned Precipitate	Actual Precipitates
CB 107	Cu-Zr-Al	Zr_3Al	Cu- 10at.%Zr
CB 109	Cu-Co-V	Co_3V	Co_xV
CB 111	Cu-Ag-Y	AgY	Cu-1at.%Y-18at.%Ag
CB 112	Cu-Cr-Hf	Cr_2Hf	Cr, Cu_xHf
CB 113	Cu-Fe-Y	Fe_2Y	Cu-1at.%Fe-12at.%Y
CB 126	Cu-Cr-Co	Cr(w/Co)	Cr

Consequently, only in the copper-chromium-cobalt and copper-cobalt-vanadium alloys were anything near the desired precipitates observed. The copper-cobalt-vanadium alloy generated a cobalt-vanadium precipitate where Co_3V was desired. The copper-chromium-cobalt alloy generated a chromium precipitate (no cobalt was detected) where a chromium precipitate containing a small amount of cobalt was desired (cobalt may exist in the precipitate, at undetectable levels).

The copper-chromium-cobalt and copper-cobalt-vanadium alloys appeared most promising and were subjected to electron-beam processing. Neither alloy was hardened by rapid solidification. Upon subsequent cold work + anneal at 650°C (1200°F), the rapidly solidified copper-cobalt-vanadium alloy recrystallized and softened. The copper-chromium-cobalt alloy did not recrystallize nor soften.

v. Borides

Both the first-iteration screening and first-iteration powder metallurgy efforts demonstrated that HfB_2, ZrB_2, TiB_2, and MMB_6 borides were insoluble in molten copper at practical temperatures and therefore unprocessable to dispersions by rapid solidification processes available at P&W. Ultimately, ten more boride systems (CB 53 to 63, CB 127 to 129, and CB 138 to 140) were evaluated, looking for one that was soluble in the copper melt, yet insoluble and stable in solid copper to act as an effective dispersion. These systems were expected to form MMB_6, YB_6, VB_2, CrB_2, NbB_2, AlB_{12}, SiB, $(Cr,Ti)B_2$, NiB_2, FeB, and CoB_2.

Of the systems investigated, MM-B (retried), V-B, and Cr-B appeared to precipitate borides in the melt during arc melting. When subjected to electron-beam passes, these borides did not appear to dissolve.

The other systems, Al-B, Nb-B, Y-B, Si-B, Ni-B, Co-B, and Fe-B, appeared to precipitate borides (unidentified) only upon solidification of the arc melts. Moreover, they appeared to redissolve and reprecipitate upon electron-beam processing. However, the effectiveness of the resulting dispersions was no greater than that of zirconium additions. Softening and recrystallization resistance of the rapidly solidified sections of these alloys was no greater than that of copper-zirconium electron-beam passes. In addition, the dispersions in the copper-yttrium-boron, copper-niobium-boron, copper-aluminum-boron, and copper-silicon-boron alloys underwent considerable coalescence when annealed at 650°C (1200°F) after cold work.

69

Other boride-forming alloys containing third additions (Zr-B-Ag, Ti-B-Ag, MM-B-Ag, Cr-Ti-B) were melted (CB 33, 100, 101, 102, respectively), to determine if the third elements increased boride solubilities in the liquid alloy. Boride precipitation still occurred in the liquid.

This completed the investigations of borides in screening alloys. Of the 14 borides investigated, none were found that were both dispersable by rapid solidification and stable at elevated temperatures in copper.

w. Silicides

Silicides are another class of high-temperature phases often employed as strengtheners in alloys. A review of phase diagrams of silicon and copper-compatible elements revealed the possible applicability of Nb-Si, Cr-Si, Hf-Si, Ti-Si, Zr-Si, and Y-Si additions. Alloys were formulated to produce the following stoichiometries and phases: Nb_5Si_3, Cr_5Si, Hf_3Si_2, Ti_5Si_3, Zr_3Si_2, and YSi_2, all at 2at.% concentrations (CB 81 to 86).

In most cases, the alloys produced ternary Cu-Si-X silicides: $Cu_4Si_4Nb_5$ (by microprobe), $Cu_4Hf_3Si_2$ (x-ray diffraction), Cu_2Ti_2Si (microprobe), $Cu_4Zr_3Si_2$ (x-ray), and Cu_5YSi_2 (microprobe). Only the copper-chromium-silicon alloy (CB 82) produced a binary silicide: the expected Cr_3Si (microprobe).

In the conventionally processed conditions, all of the alloys recrystalized and softened at 650°C (1200°F), and the yttrium and niobium-containing alloys recrystallized at 480°C (900°F); results no better than those of copper-zirconium alloys.

In the electron-beam processed, rapidly solidified conditions, the alloys were harder than their conventionally processed conditions. However, they all underwent softening and recrystallization during the post-cold-work 650°C anneal. The Cu-Cr_3Si alloy softened the least. The rapidly solidified copper-hafnium-silicon and copper-titanium-silicon alloys softened considerably, but since they started out very hard, they still exhibited high hardnesses. The high initial hardness of the rapidly solidified hafnium-containing alloy may have resulted from the high 3.3 percent hafnium concentration. The high initial and cold-worked hardnesses of the titanium-containing alloy may have resulted from spinodal hardening by the titanium. The softening resistances of all but the rapidly solidified copper-chromium-silicon alloys were no better than that of copper-zirconium alloys.

3. SUMMARY OF SCREENING RESULTS

For the most part, those alloy systems that contained zirconium, chromium, and hafnium exhibited the best resistance to recrystallization and softening. Generally, alloys containing chromium exhibited the highest age-hardenability. Zirconium additions imparted good recrystallization resistance, but little age-hardening. Hafnium additions also imparted good recrystallization resistance, but, contrary to what was expected from the literature, age-hardening response was slight.

The effects of silver additions were not significant. Age-hardening was expected, but little was found. Ternary additions to copper-silver suppressed the discontinuous precipitation observed in the binary alloys. Silver additions did not appear to increase the recrystallization resistance of other copper-x alloy systems.

The other alloying additions expected to precipitate elementally or as copper-based compounds had little beneficial effects. Mischmetal and yttrium additions were inferior to zirconium, chromium, and hafnium additions. The ternary alloys containing mischmetal and yttrium were found to be no better than copper-zirconium. Molybdenum was, within the

processing limits used, insoluble in copper. Vanadium additions did not improve the alloys either, and appeared to promote catastrophic oxidation in some alloys. Niobium did not appear to be any more effective as a hardener than chromium.

Of the titanium alloys that exhibited high hardnesses, only one was found in which the hardness was not spinodally produced by slow cooling, and which might be considered stable in a rocket engine environment. This was the copper-titanium-hafnium alloy, which produced a complex ternary precipitate.

The alloys formulated to produce high-temperature intermetallic phases tended instead to form ternary compounds containing copper. Their properties were not promising.

The addition of low-mismatch compounds generally did not improve softening or recrystallization resistance (compared to copper-zirconium alloys). In many cases, the expected compounds did not even form; ternary compounds containing copper formed instead. Two exceptions were copper-cobalt-vanadium and copper-chromium-cobalt, which exhibited good softening and recrystallization resistance. The former appeared to form cobalt-vanadium precipitates. In the latter alloy, cobalt was not detected in the chromium precipitates. However, cobalt levels were low and possibly hard to detect.

The inability to find a useable boride for dispersion strengthening was a major disappointment. Some diborides were very stable at elevated temperatures, but they were not effectively dispersed by the processes employed. Other borides were processable to fine dispersions, but were not stable.

Only one of the silicon-containing alloys looked promising: copper-silicon-chromium. This alloy formed a binary chromium-silicide believed to be Cr_3Si. This alloy was slightly more resistant to recrystallization and softening than copper-chromium alloys. The remaining silicon-containing alloys produced ternary copper-containing silicides and were not promising.

Based on hardness, age-hardenability, softening resistance, and recrystallization resistance, the following alloy systems exhibited the best potential for further study:

Copper-Chromium
Copper-Hafnium
Copper-Zirconium
Copper-Silver-Chromium
Copper-Silver-Chromium-Zirconium
Copper-Silver-Hafnium
Copper-Silver-Zirconium
Copper-Chromium-Cobalt
Copper-Chromium-Hafnium
Copper-Chromium-Zirconium
Copper-Cobalt-Vanadium
Copper-Hafnium-Titanium
Copper-Hafnium-Zirconium

SECTION IV
POWER METALLURGY ALLOYS AND NASA-Z

1. ALLOY SELECTION

Based on the alloy screening results, compositions were selected for atomization. Alloys were atomized in two lots: the first lot after the first screening iteration, and the second lot after the second screening iteration.

At the end of the first screening iteration, the copper-hafnium, copper-zirconium, copper-zirconium-silver, and copper-zirconium-boron systems were selected for atomization. Copper-zirconium and copper-hafnium had exhibited good recrystallization and softening resistance. The powder metallurgy copper-zirconium-silver alloy would allow comparison with conventionally processed NASA-Z. And finally, even though problems were expected with boride dispersion, the stabilities of borides were so great that their use had to be investigated.

Other first-iteration screening systems were not atomized. The copper-hafnium-zirconium system did not appear appreciably better than either binary system. Only two copper-zirconium-chromium alloys had been studied, and they appeared no better than copper-zirconium (later ones performed better). Also, the literature had suggested that alloys containing chromium were less ductile than copper-zirconum alloys (14).

Powder alloys had to be prioritized because when the atomizer is converted to a different system, such as from nickel to copper, the first few runs are expected to contain contamination from the prior alloy system. Such runs are said to wash the atomizer (via dilution) of contaminants. Usually, three such wash runs are needed to flush out the system. Depending on the expected use of the powder, wash run powders may be discarded or used for experiments. For this program, wash runs were used to make compositions of secondary interest or higher risk, with the expectation that, even contaminated, the powders would yield valuable information.

The systems chosen from the first screening iteration were prioritized, and composition levels were chosen. The alloys of primary interest were:

Cu-0.6%Zr
Cu-0.55%Zr-0.17%B
Cu-0.5%Zr-3.0%Ag

The zirconium level in the copper-zirconium alloy was set moderately above the solubility limit, to produce a dispersion of primary Cu_5Zr precipitates. The copper-zirconium-boron alloy was formulated to produce 1 volume percent borides, with a little extra boron for melting losses. The third alloy was formulated to the NASA-Z composition.

Wash heat alloys were:

Cu-1.1%Zr-0.34%B
Cu-1.1%Hf
Cu-0.8%Zr

The first alloy was formulated to produce 2 volume percent borides, with a little extra boron, and to assess the processability of zirconium diborides. The second alloy, copper-hafnium, was run as a wash heat because it was riskier than copper-zirconium. Its composition was set above the solid solubility limit to produce a dispersion of primary Cu_5Hf precipitates. The last alloy was chosen to assess zirconium concentration effects.

As atomization progressed, alloy formulations were changed somewhat to those in Table 16. The differences from those proposed were a change in boron level for the primary copper-zirconium-boron alloy (997), and the repetition of two primary alloys at Cu-0.65%Zr (998) and Cu-0.5%Zr-3.0%Ag (999). The boron level for Alloy 997 was dropped because numerous very coarse borides were observed in the boron-containing wash alloy, indicating a very low solubility of ZrB_2 in molten copper. The two duplicate runs were part of an effort to reduce the incidence of very fine oxides in the powder. These two runs employed reducing conditions in the atomization device to inhibit oxidation of the zirconium in the melt. In addition, Run 998 employed a small zirconium increase to compensate for zirconium losses observed with Runs 994 and 995.

TABLE 16. — ATOMIZATION RESULTS

Run	Alloy Composition (wt.%)	Charge Weight (kg)	Poured Weight (kg)	-80 Mesh Collected (kg)	Main Collector (kg)	Lower Chamber (kg)	Wall & Ceiling Depoist (kg)	Comments
992	Cu-1.1Zr-0.34B	70	45	NA	5	23	9	Late abort – skulls.
993	Cu-1.1Hf	69	64	29	35	11	8	
994	Cu-0.8Zr	110	65	12	14	27	16	Late abort – skulls.
995	Cu-0.6Zr	68	64	23	24	2	24	
996	Cu-0.5Zr-3.0Ag	68	64	23	43	9	8	
997	Cu-0.55Zr-0.05B	69	65	34	37	14	11	
998	Cu-0.65Zr	69	36	NA	6*	5	23	Late abort – skulls.
999	Cu-0.5Zr-3.0Ag	70	68	48	49	8	2	
1032	Cu-0.8Hf-0.7Ti	74	63	23	24	4	27	
1033	Cu-0.6Cr-0.2Co	76	71	31	34	7	22	
1034	Cu-1.4Co-0.4V	72	66	2	2	31	26	Collector clogged.
1035	Cu-1.0Cr-0.6Zr	73	65	39	41	2	16	
1036	Cu-0.6Zr-1.1Hf	75	69	10	11	1	53	
1037	Cu-1.0Cr-0.6Zr-3.0Ag	76	6	0	0	0	0	Abort – nozzle clog.
1038	Cu-1.0Cr-0.6Zr-3.0Ag	70	65	19	20	2	37	
1039	Cu-1.0Cr-3.0Ag	73	67	0	0	NA	0	Oil leak – powder ruined.
1040	Cu-0.6Zr-1.1Hf	74	10	0	0	0	0	Abort – nozzle clog.
1041	Cu-0.6Zr-1.1Hf	80	75	13	14	4	50	
1042	Cu-1.4Co-0.4V	71	66	21	22	5	29	
1043	Cu-1.0Cr-3.0Ag	72	68	NA	30	0	29	

* Air Exposed

After the remainder of the screening effort was finished, additional alloy systems were identified for possible atomization. They were:

Copper-silver-chromium
Copper-silver-chromium-zirconium
Copper-silver-hafnium
Copper-cobalt-chromium
Copper-cobalt-vanadium
Copper-chromium
Copper-chromium-hafnium
Copper-chromium-silicon
Copper-chromium-zirconium
Copper-hafnium-titanium
Copper-hafnium-zirconium

From these, three high-risk systems were chosen for atomization as wash heats and formulated as:

Cu-1.4%Co-0.4%V
Cu-0.6%Cr-0.2%Co
Cu-0.8%Hf-0.7%Ti

Another four systems were chosen for primary runs and formulated as:

Cu-0.6%Zr-1.0%Cr
Cu-0.6%Zr-1.0%Cr-3.0%Ag
Cu-0.6%Zr-1.1%Hf
Cu-1.0%Cr-3.0%Ag

Notably absent were copper-chromium-hafnium, which was believed to be too similar to copper-chromium-zirconium to merit a trial at that time; copper-silver-hafnium, which was very similar to copper-silver-zirconium; copper-chromium, which was the least promising of the series; and copper-chromium-silicon, which was considered to be a high-risk alloy and reserved for some future (unrealized) wash run.

These alloys were atomized as formulated above. Some were repeated to compensate for bad runs.

2. ATOMIZATION RESULTS

High-conductivity copper alloys atomized easily in the Pratt & Whitney (P&W) rapid-solidification-rate (RSR) atomization device, forming spherical powder quite similar to that of other alloy systems. Some unique problems were encountered, but none were unsurmountable.

One such problem was that the copper powder, being soft, bonded weakly to the atomizer wall upon impact. For some atomization runs, substantial portions of the powder were deposited on the wall of the device, significantly reducing the yields of collected powder. Process and equipment constraints were such that the most expedient remedy was to melt large heats (150 pounds) to ensure that collected powder yields were adequate for use.

Other problems involved introduction of alloying additions without loss or reaction in the melt. For zirconium, late additions, crucible charging, and copper-zirconium master alloy charges were tried. Late additions were found to work best, minimizing slag formation and zirconium losses. Late additions were also used for hafnium and, later, silver additions. Attempts were made to minimize oxidation in the melt and subsequent formation of fine oxides in the powder (Figure 37) by bubbling hydrogen through the melt (Runs 998 and 999) and using a graphite tundish (999). These methods did not produce noticeable improvements and were discontinued.

Production of boride-containing powder was complicated by reaction and formation of borides in the melt. Attempts to resolve this by increasing melt temperature were hindered by power limitations and the tendency for the melt to splash at high power levels. The highest melt temperature attained, 1500°C (2730°F), was not adequate to prevent boride formation.

10 μm

Figure 37. Backscatter Electron Image (SEM) Showing Possible Fine Oxides in Cu-Zr (Alloy 995) Powder

Since chromium was somewhat difficult to melt in copper (due to a miscibility gap), all alloys containing chromium were pre-melted as master alloys in a separate VIM furnace that was capable of higher temperatures than the atomizer furnace.

Additional difficulties encountered in atomization were generic in nature and consisted of turbine (disk drive) oil seal leaks, plugging of the atomizer nozzle, and unstable atomization at the rim of the disk (requiring atomizer shut-down or causing large splats that reduced powder yield or clogged the atomizer outlet).

When the wall deposition phenomenon was ignored, yields were acceptable. Yields of collected -80 mesh powder and areas of loss are listed in Table 16. Wall deposition was the most consistent source of losses. This phenomenon was not found to depend upon any controllable process parameters. Another significant source of loss was the infrequent tendency for the fine powder to sit in the bottom head of the device rather than flow into the collector can. At least once, this was aggrivated by wall deposits falling off and clogging the atomizer outlet. Powder flow can be assured by using blowdown nozzles to flush out the lower head.

The powders produced for this program were finer than those typically produced by the RSR process. Size fraction analyses are shown in Figures 38 and 39. The fineness of these powders were attributed to the high atomizer speeds used. Fine powder was intentionally produced, as it was expected to solidify more rapidly. The large, very coarse fractions exhibited by Runs 994, 996, and 998 resulted from unstable atomization and splashing off the disk. Even those runs exhibited a larger-than-normal fine fraction, however.
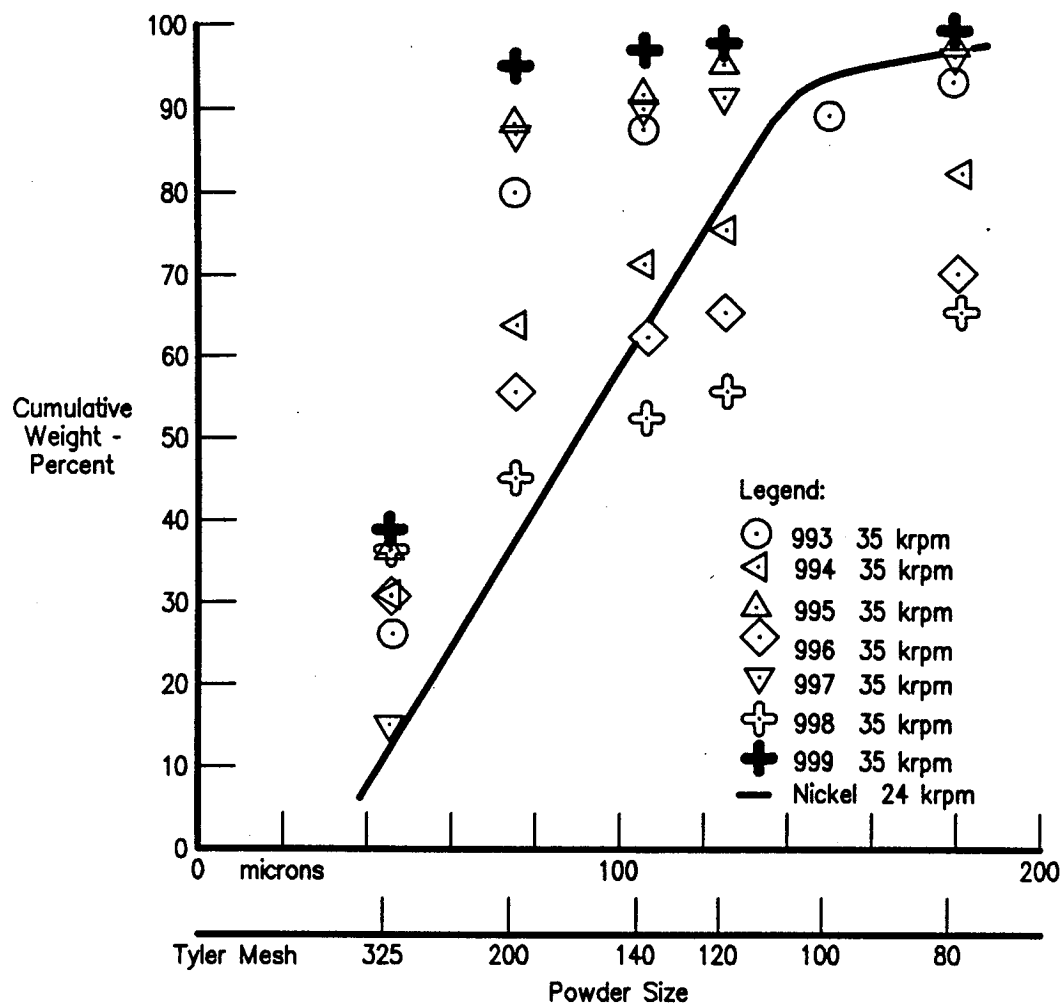
75

Figure 38. Size Analysis of Collected Powder (Runs 993 Through 999)

a. Chemical and Contamination Analysis of Powders

Chemical analyses were performed on a number of the alloys. The results are listed in Table 17. Analyses were made by inductively coupled plasma-atomic emmision spectroscopy (ICP-AES) and by electron microprobe (wavelength-and energy-dispersive). The ICP-AES method was considered reliable. ICP-AES was not used with the second powder alloy series due to budgetary constraints. Some of the microprobe results were unreliable. Overall, powder alloy compositions were close to aim compositions. Some zirconium losses were observed when it was added to the charge instead of as a late addition. Boron losses always occurred.
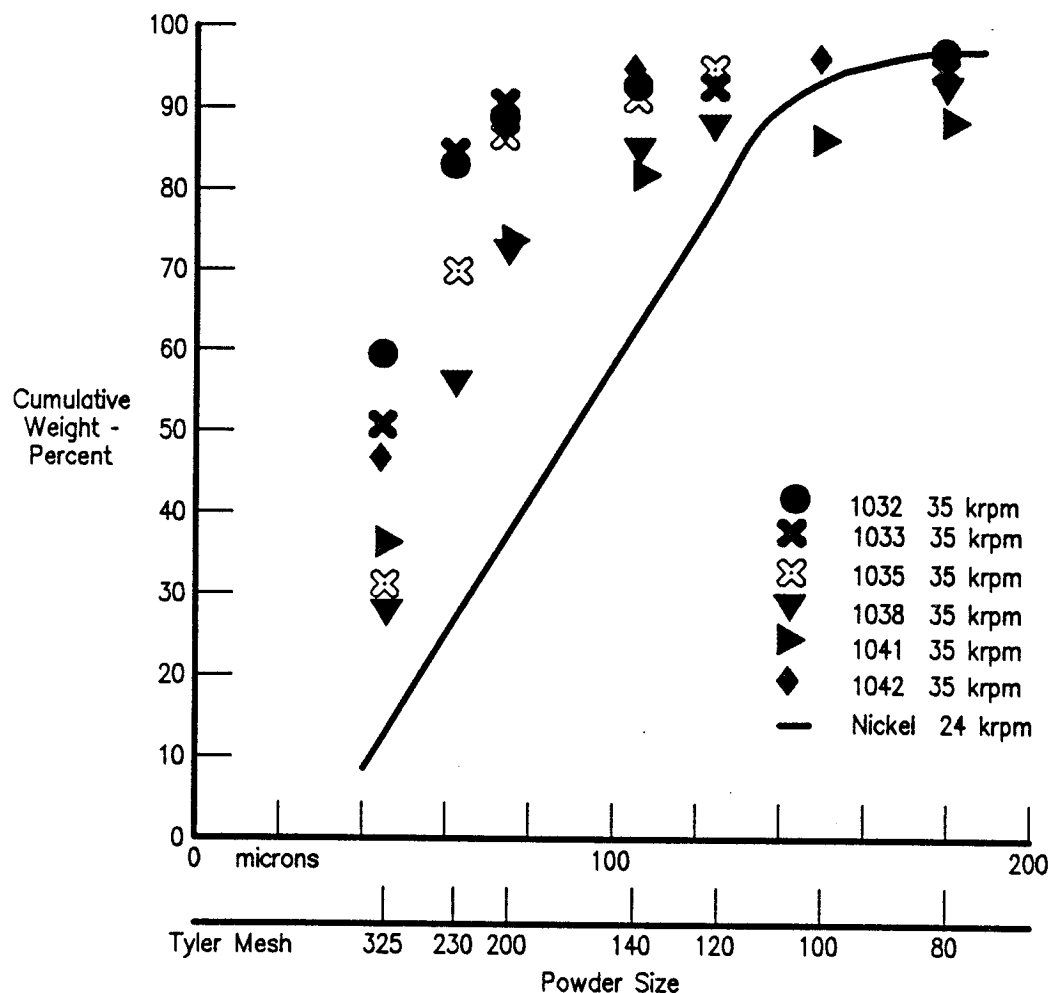
Figure 39. Size Analyses of Collected Powder (Runs 1032 Through 1042)

Additionally, trace element analyses of oxygen, carbon, and silicon levels were performed on some of the first-series alloys. The results are listed in Table 17. After the first run, oxygen levels stabilized at less than 40 ppm (by weight). For comparison, NASA-Z had 10 ppm oxygen. Hydrogen bubbling of the melt did not significantly affect oxygen levels in the alloys (Alloys 998 and 999). Alloy 999, made using a graphite tundish, picked up 30 ppm of carbon. Silicon pickup from the crucible was less than 0.3 percent (the same as NASA-Z), while aluminum contamination was not detected.

Contaminants were documented for the first series of alloys (Table 18). Since oil contamination was observed in Run 992, oil analyses were performed on the first lot of powders to document improvement. Oil contamination was essentially zero for 993 and later runs.

77

TABLE 17. — CHEMICAL ANALYSES OF ALLOYS

Alloy/Run	Aim Composition (wt.%)	Actual Composition, ICP-AES (wt.%)	Actual Composition, Electron Microprobe (wt.%)	Oxygen (ppm /wt)	Others**
992	Cu-1.1Zr-0.34B	Cu-1.1Zr-0.24B		90	
993	Cu-1.1Hf	Cu-1.1Hf	Cu-1.5Hf	30	
994	Cu-0.8Zr	Cu-0.66Zr	Cu-0.6Zr	20	
995	Cu-0.6Zr	Cu-0.48Zr	Cu-0.45Zr	30	0.3Si
996	Cu-0.5Zr-3.0Ag	Cu-0.50Zr-2.8Ag	Cu-0.51Zr-3.1Ag	20	
997	Cu-0.55Zr-0.05B	Cu-0.51Zr-0.03B		20	
998	Cu-0.65Zr			30	
999	Cu-0.5Zr-3.0Ag	Cu-0.48Zr-2.91Ag		40	0.3Si, 30 ppm C
1032	Cu-0.8Hf-0.7Ti		Cu-0.8Hf-0.9Ti		
1033	Cu-0.6Cr-0.2Co		Cu-0.6Cr-0.2Co		
1034	Cu-1.4Co-0.4V		Cu-1.4Co-0.2V		
1035	Cu-0.6Zr-1.0Cr		Cu-0.52Zr-1.0Cr		
1036	Cu-0.6Zr-1.1Hf		Cu-0.5Zr-1.2Hf		
1038	Cu-1.0Cr-0.6Zr-3.0Ag		Cu-0.7Cr-0.7Zr-3.0Ag		
1042	Cu-1.4Co-0.4V		Cu-1.4Co-0.2V		
1043	Cu-1.0Cr-3.0Ag		Cu-0.9Cr-2.8Ag		
NASA-Z1*	Cu-3.0Ag-0.5Zr	Cu-0.44Zr-3.0Ag	Cu-3.1Ag-0.5Zr	10	
Amzirc*	Cu-0.15Zr	Cu-0.15Zr	Cu-0.15Zr		

* Commercially supplied
**Si by ICP-AES

TABLE 18. — POWDER CONTAMINATION

	Rateable inclusions/in^2 (100x)		
Run/Alloy	Other Powder	Ceramics	Oil
992	69	42	160 ppm
993	3	3	0.7 ppm
994	33	5	4.6 ppm
995	19	6	1.0 ppm
996	12	5	0.2 ppm
997	5	3	<0.1 ppm
999	8	4	<0.1 ppm

Inclusions counted in a compaction.
Oil determined with loose powder.

Contaminant inclusions were counted in Alloys 992-999. After filters were installed in the helium recirculation system, contamination by ceramics and prior metal powders was generally reduced to acceptable levels.

Contamination analyses were not performed on the second series of alloys. The first series of atomization runs showed that high oil levels in powder led to clumping of the powder. Thus, later powder runs that did not clump (all of 1032 — 1043, except 1039) were judged acceptable. Since the installation of filters in the helium recirculation system had reduced contamination to acceptably low levels, and since mechanical tests had shown no relationship between inclusions and failure for Alloys 993 through 999, Alloys 1032 through 1043 were not systematically screened for inclusions. Any severe contamination would be obvious upon examination of the extrusions.

b. Powder Microstructures

Microstructures of RSR-atomized high-conductivity copper alloys resembled those of many other RSR systems studied earlier. Powders were fine spherical particulates, exhibiting secondary dendrite arm spacings of 1-5 μm. Figures 40-44 illustrate the microstructures of several of the alloys (those not shown had microstructures similar to that of Alloy 995). All exhibited fine dispersion of the alloying elements, with the exception of Alloys 992 and 997, which also exhibited coarse 1-10 μm ZrB_2 particles (Figure 40). These were believed to have formed in the melt.

With few exceptions, the RSR process was well-suited to the atomization of fine, spherical, rapidly solidified, high-conductivity copper alloy powders. While some difficulties were encountered in powder making, all could be resolved if production quantities were needed.
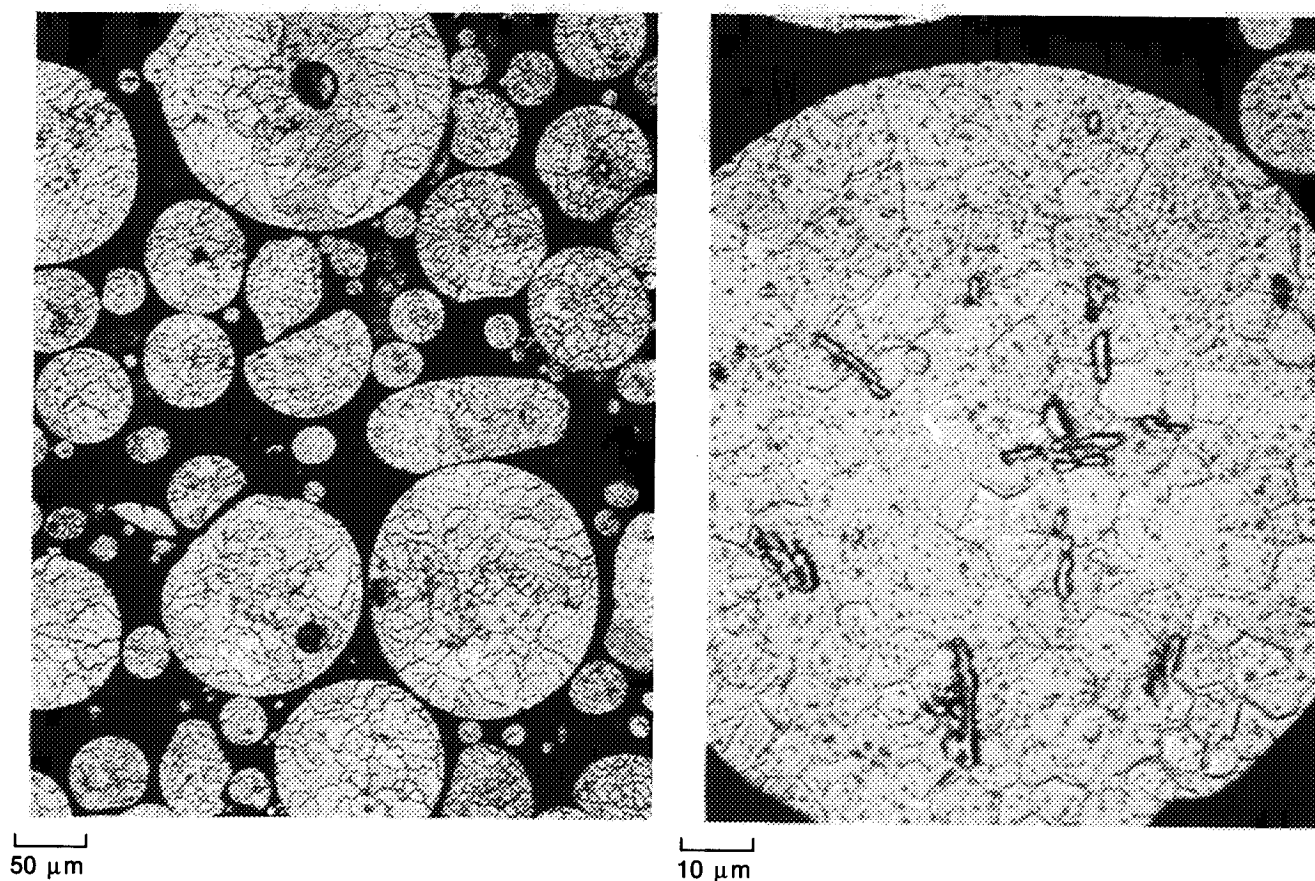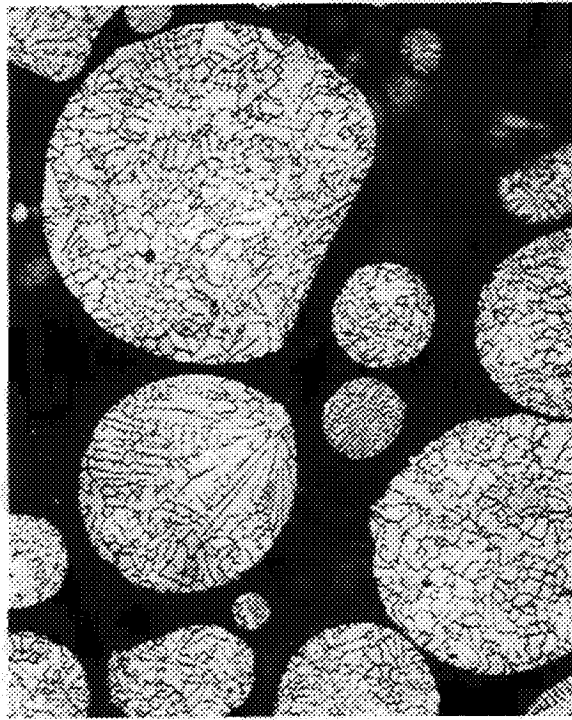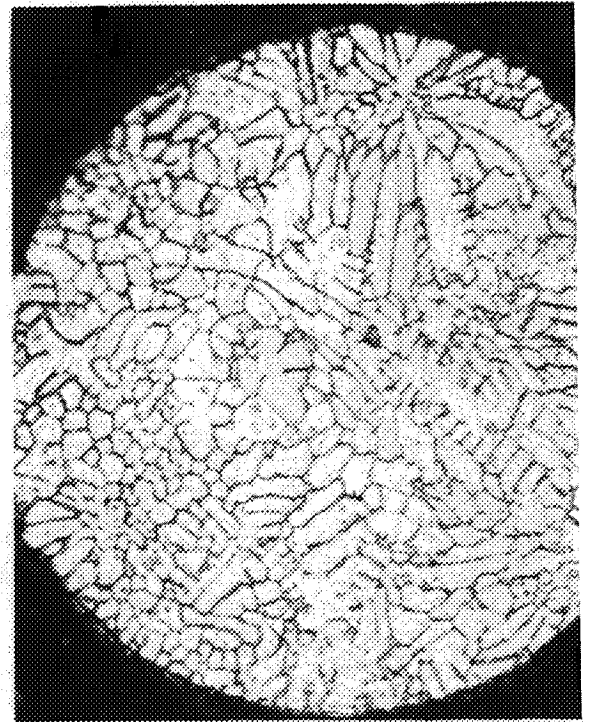

50 μm   10 μm

Figure 40. Structure of -80 Mesh Alloy 992 Powder (Cu-1.1%Zr-0.3%B) Showing Borides at 1000X (Right)

20 μm

10 μm

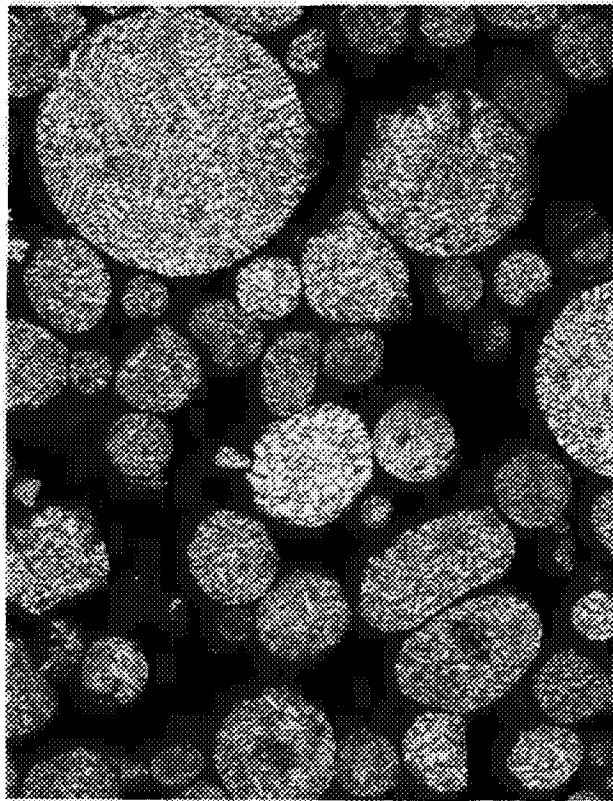*Figure 41.   Structure of -80 Mesh Alloy 993 Powder (Cu-1.1%HF)*
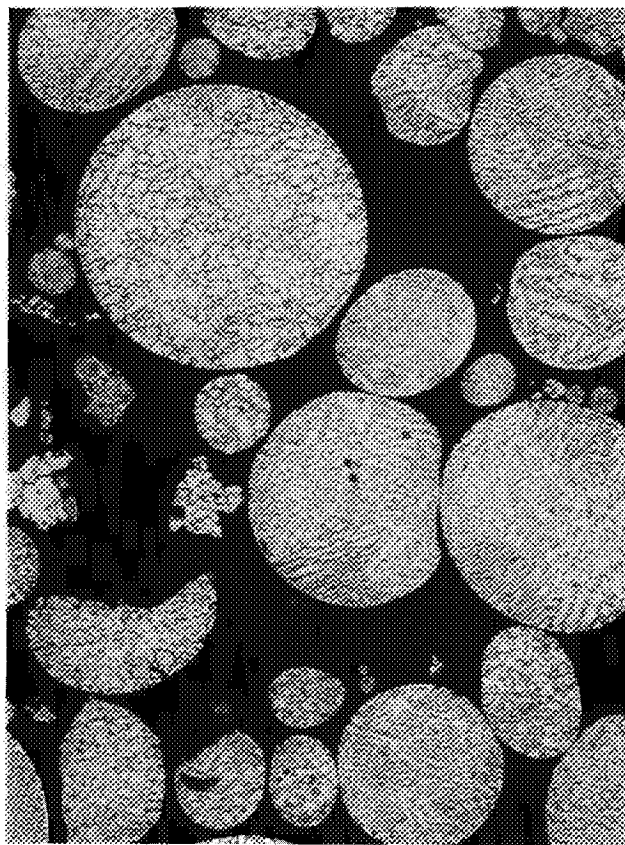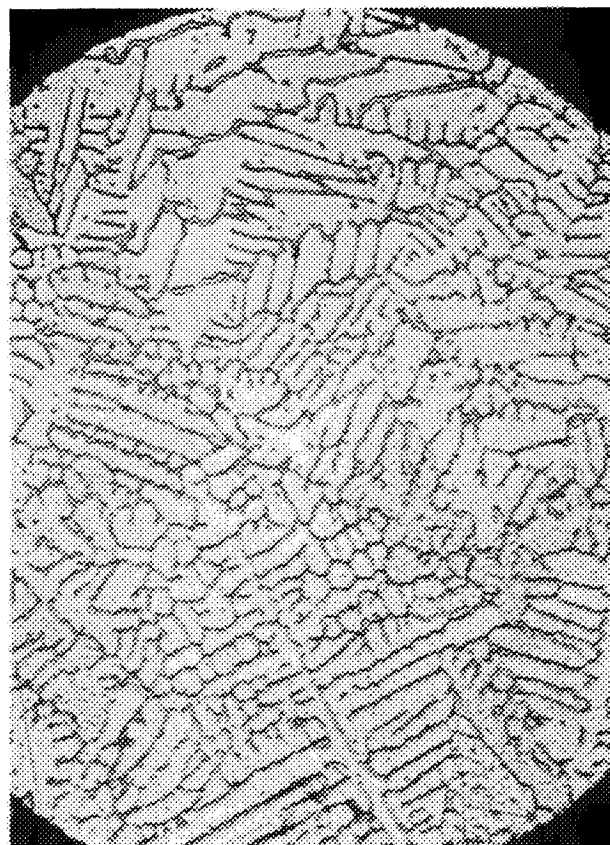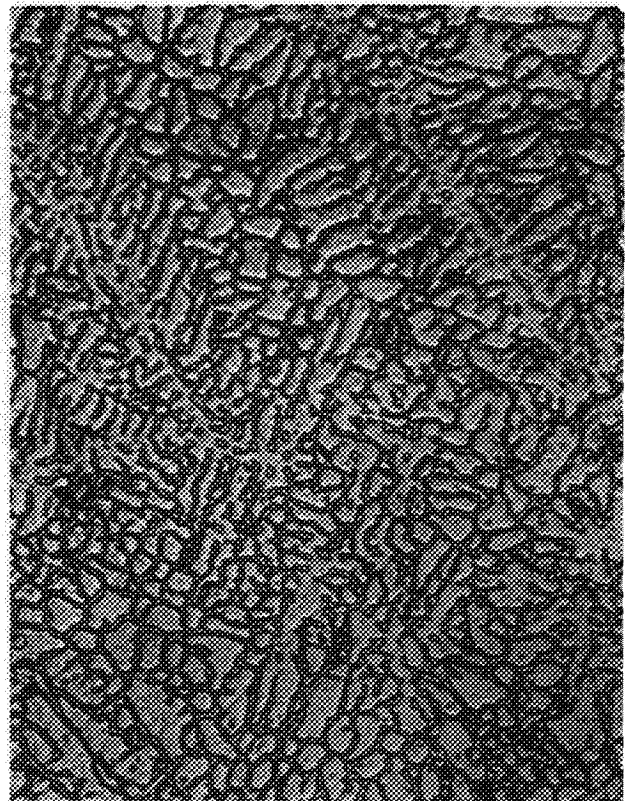
50 µm

10 µm

Figure 42.   Structure of -80 Mesh Alloy 995 Powder (Cu-0.6%Zr)
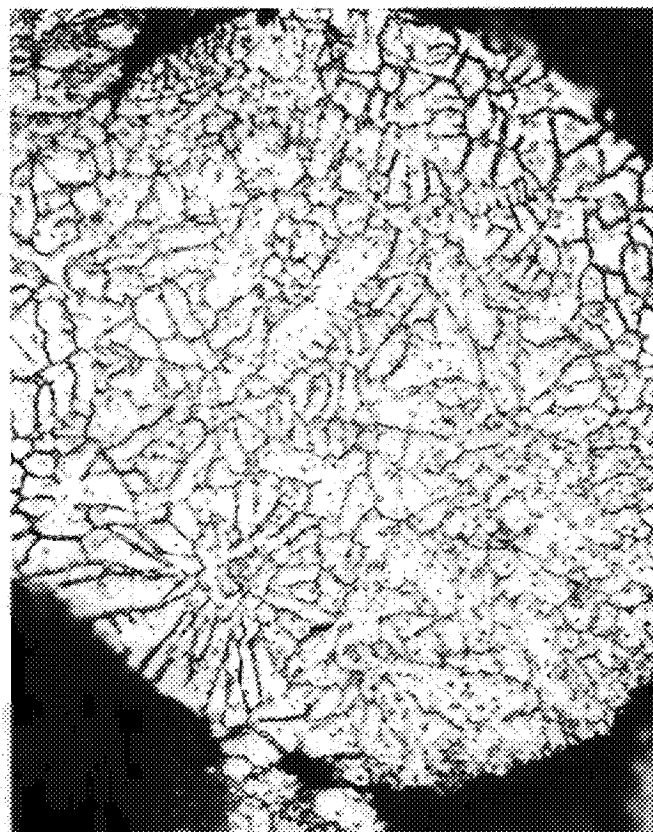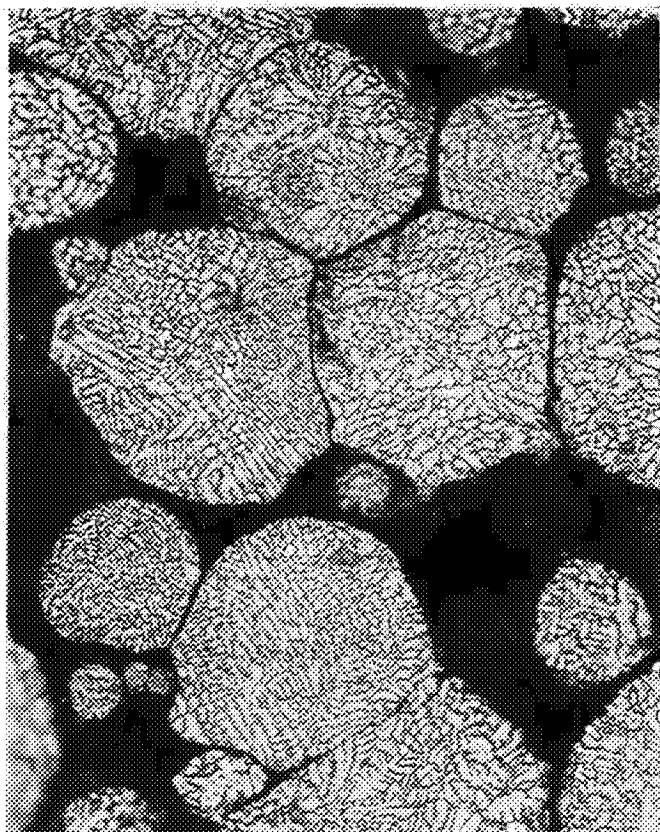
81

50 μm   10 μm

Figure 43. Structure of -80 Mesh Alloy 996 Powder (Cu-0.5%Zr-3.0%Ag)

82

20 μm   10 μm

Figure 44.   Structure of -80 Mesh Alloy 1035 Powder (Cu-1.0%Cr-0.6%Zr)

3. PROCESS AND EVALUATION OF POWDER METALLURGY (PM) COPPER ALLOYS

Rapidly solidified, high-conductivity copper powder alloys were consolidated and subjected to a variety of processing sequences to allow assessment of processing effects on strength, hardness, microstructure, and stability at elevated temperatures, as well as to produce bulk materials for mechanical testing. Processing conditions were tailored to allow evaluation in a number of conditions including as-extruded, solution-treated, aged, cold-worked, and combinations of these; both as-processed and as-annealed (650°C/12 hour) after processing. The processing matrix was less extensive for the 1000 series of alloys (Figures 18 and 19) than for the 900 series (Figures 16 and 17) due to experience gained from evaluation of the first set of alloys.

Preliminary evaluation of processed PM alloys was by metallography and room-temperature hardness. Of interest metallographically were ease of recrystallization, grain growth, and dispersion/precipitate morphologies. Hardness testing looked for age-hardening capability and softening resistance upon anneals. Hardness results are listed in Table 19.

83

TABLE 19. — DIAMOND PYRAMID HARDNESSES OF PROCESSED PM ALLOYS

Alloy	AE	E+N	E+CW	E+CW+A	E+CW+(A)+N	E+S	E+S+A	E+S+A+N	E+S+CW	E+S+CW+A	E+S+CW+A+N
993	94	82	138	114	66	60	63	59	118	108	86
995	92	80	118	96	68	55	53	52	106	106	51
996	106	76	146	96	84	70	80	62	126	134	72
997	92	74	126	102	72	54	56	56	106	106	60
999	96	88	126	122	74	61	64	63	118	134	74
1032	106	100	156	–	86	78	146	76	146	168	122
1033	88	74	114	–	60	50	61	54	106	112	56
1035	122	106	142	–	108	70	98	66	126	146	72
1036	102	98	132	–	96	73	82	72	130	130	73
1038	130	98	158	–	91	80	160	78	154	160	86
1042	94	98	118	–	98	61	66	69	102	69	66
1043	138	88	154	–	88	76	106	76	142	142	76

AE, E = Extruded
N   = 650°C (1200°F)/12 hr annealed
S   = Solutioned
A   = Aged, 480°C (900°F)/2 hr
CW   = Cold worked

Results of these studies were used to select alloys and material conditions for preliminary tensile testing. Tensile testing was performed at 705°C (1300°F) (the projected maximum wall temperature) at strain rates approaching 0.1/second (projected chamber strain rate). Tensile results were evaluated to rank alloys for characterization.

a. Consolidation

Powder metallurgy copper alloys were consolidated by hot extrusion at 650°C (1200°F) in evacuated copper cans. Extrusion conditions and results were summarized in Table 9.

Whenever sufficient powder existed, the -230 mesh powder fraction was canned for extrusion consolidation. Coarse powder fractions were not studied because: 1) Little coarse powder was produced, 2) the types of dispersions produced in these alloys were not expected to be sensitive to subtle solidification rate differences, especially after consolidation; and 3) because fine powder was so easily produced, the ability to use coarser powder could be addressed later, if needed, when alloys were chosen for hardware fabrication.

Extrusion of P&W powder alloys was done exclusively at 650°C (1200°F). The intention was to minimize temperature while accomplishing full consolidation. The works of Grant, et al (34, 35) suggested 650°C. Initial trials with Alloy 993 indicated that this temperature was satisfactory, so it was used for the remainder of the program. The Massachusetts Institute of Technology (MIT) specified the temperatures used for their extrusions.

Extrusion ratios were chosen to produce bar stock of sizes suitable, after additional processing, for test specimens. Generally, two ratios were used per alloy. Early extrusions were made at 8:1 and 12:1 ratios. The 8:1 extrusion billets were hot-compacted prior to extrusion to ensure complete consolidation during extrusion. The larger (8:1) extrusions were to be subjected to additional working, whereas the smaller (12:1) extrusions were intended only for heat treatment. As experience showed that smaller extrusions could be used for these purposes, later extrusions were made at 10:1 and 20:1 extrusion ratios.

C-2

All extrusions were fully consolidated. No problems were encountered with the extrusion efforts. Resulting microstructures are addressed in the next section.

b. Alloy Processing and Behavior

Powder metallurgy copper alloys were processed by various combinations of extrusion, hot work, cold work, solution treatment, and aging to assess the effects of these processes on microstructure, hardness, and tensile properties. Processed conditions were subjected to anneal cycles at 650°C (1200°F) for 12 hours to assess their stability at elevated temperatures. Results are discussed below for each alloy.

(1) Alloy 992: Cu-1.1%Zr-0.34%B (aim)

Alloy 992 powder was not consolidated. It was oily, due to an atomizer oil seal failure, and exhibited massive borides fromed by reaction in the melt. Alloy 997, which contained less boron and exhibited fewer massive borides, was consolidated and evaluated instead.

(2) Alloy 993: Cu-1.1%Hf

Powder metallurgy Cu-1.1%Hf exhibited good recrystallization and softening resistance in a variety of conditions. Its responses to processing are detailed below:

(a) **As-Extruded Conditions** — As extruded, Alloy 993 exhibited a warm-worked fibrous structure with an extremely fine grain size (1 μm) and a diamond pyramid hardness (DPH) of about 95 (Figure 45). Transmission electron microscopy (TEM) showed precipitates to be about 1000-5000 Å. Aging at 480°C (900°F) or annealing at 650°C (1200°F) produced no observable changes in the fibrous microstructure, but the latter softened the material slightly, to about DPH 85.

(b) **Extruded and Cold-Worked Conditions** — Cold working of the extruded structure resulted in a similar, though harder (DPH 138), fibrous structure. An aging temperature anneal did not recrystallize the cold-worked material, but did soften it slightly (to DPH 114). Anneals at 650°C recrystallized these materials almost completely, to grain sizes of 5-10 μm and hardnesses of about DPH 70 (Figure 45).

(c) **Extruded + Solutioned (+Aged) Conditions** — Solution treatment at 925°C (1700°F) completely recrystallized the extrusions to grain sizes of 5-10 μm and a hardness of DPH 60 (Figure 46)). Aging at 480°C (900°F) only slightly hardened the material, to DPH 63, with no apparent change in microstructure. Annealing as-solutioned or aged forms at 650°F (1200°F) produced no apparent microstructural or hardness change (about DPH 55 to 60).

(d) **Extruded + Solutioned + Cold-Worked Conditions** — Cold working solutioned material produced an elongated grain structure and increased hardness significantly (to DPH 118). Subsequent aging at 480°C did not change the microstructure and only slightly softened the material (DPH 108). Annealing cold-worked or cold-worked + aged materials further softened the material (DPH 86) but did not appear to cause recrystallization.
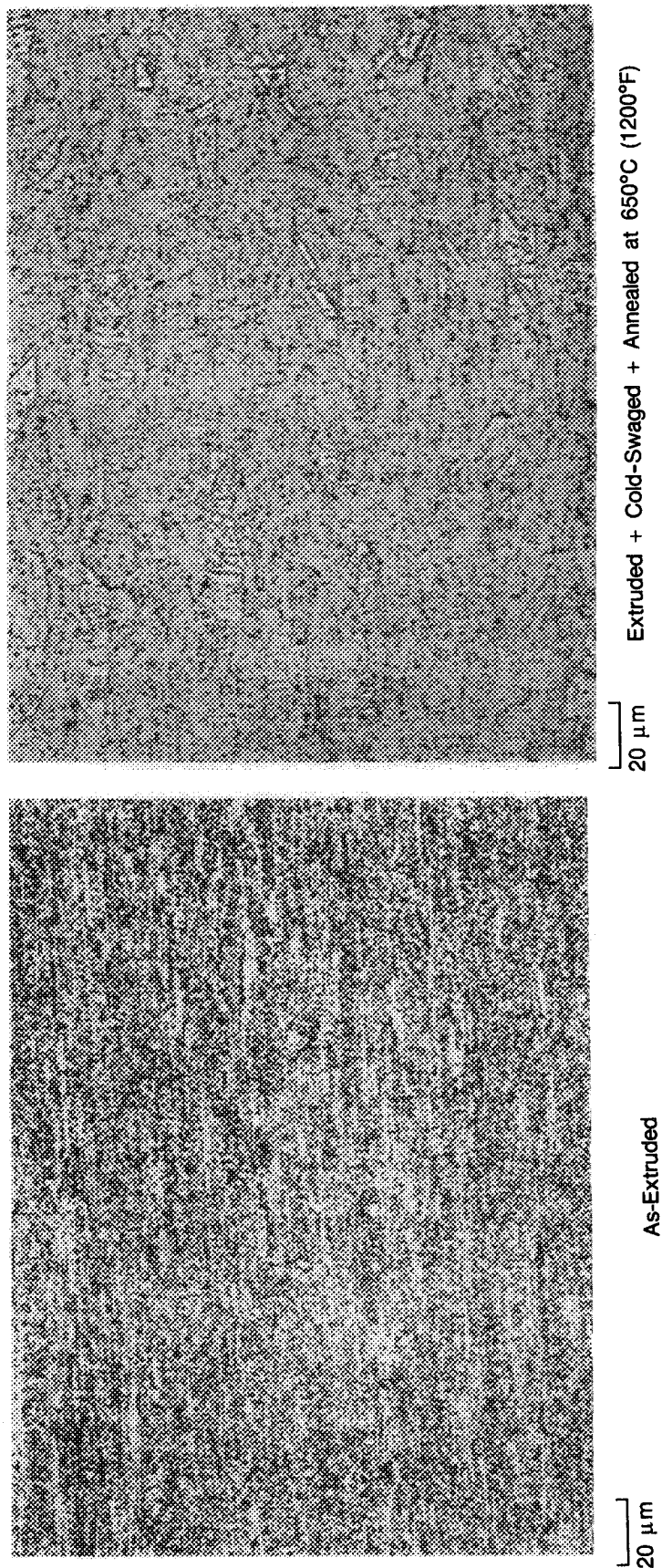
Extruded + Cold-Swaged + Annealed at 650°C (1200°F)

As-Extruded

Figure 45. *Microstructures of Extruded and Cold-Swaged + Annealed Alloy 993*
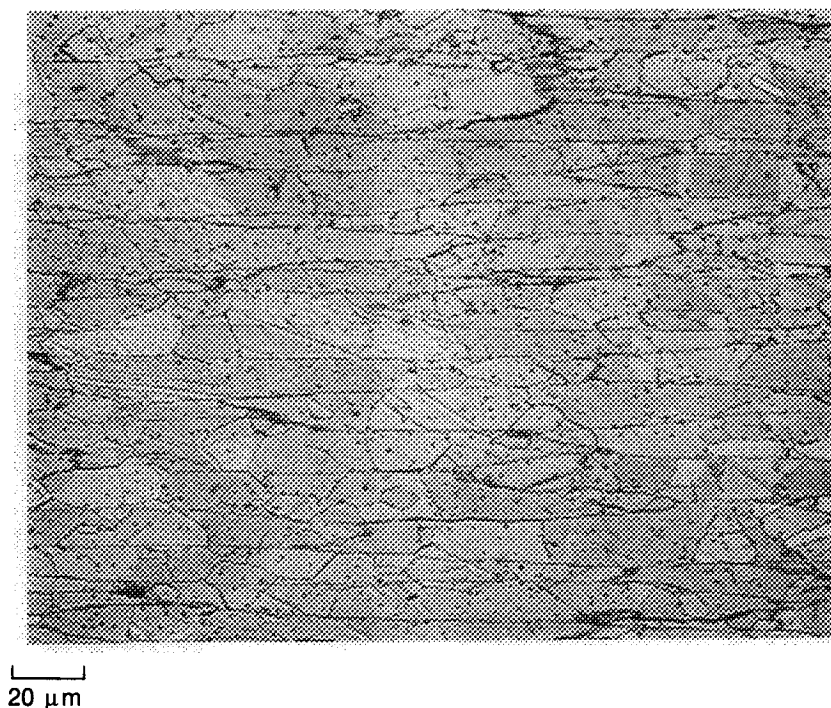
86

L____J
20 μm

Figure 46.   Solution-Treated Alloy 993

Dispersions in PM Cu-1.1%Hf were coarser than desired: 1000 to 3000 Å (Figure 47). The TEM microstructure of as-extruded bar was essentially strain-free (Figure 47), with grain/subgrain sizes of about 0.5 to 2 μm. Dispersion composition determined by scanning transmission election microscopy (STEM) was $Cu_{4.4}Hf$, reasonably close to Cu_5Hf, cited in the literature (35).

Of the conditions seen, the as-extruded and the solutioned + cold-worked + aged were hardest and most resistant to recrystallization at 650°C (1200°F). They also represented two significantly different material conditions: as-extruded being ultra-fine-grained, fibrous, over-aged and warm-worked; solutioned + cold-worked + aged being fine-grained, equiaxed, aged, and cold-worked. For these reasons, both conditions were chosen for preliminary tensile testing.

Results of tensile testing are shown in Table 20. The solutioned + cold worked + aged material exhibited higher strengths and lower elongations than the as-extruded material. Both failed by localized ductile necking (to 96 percent reduction in area). No internal voids were found in the failure region.

Microstructures of failed tensile specimens indicated at least partial recrystallization in the gage section (Figure 48). Nickel alloy powder inclusions were surrounded by smooth cavitation, unassociated with the failures. Failures were essentially crack-free. Shear zones were evident.
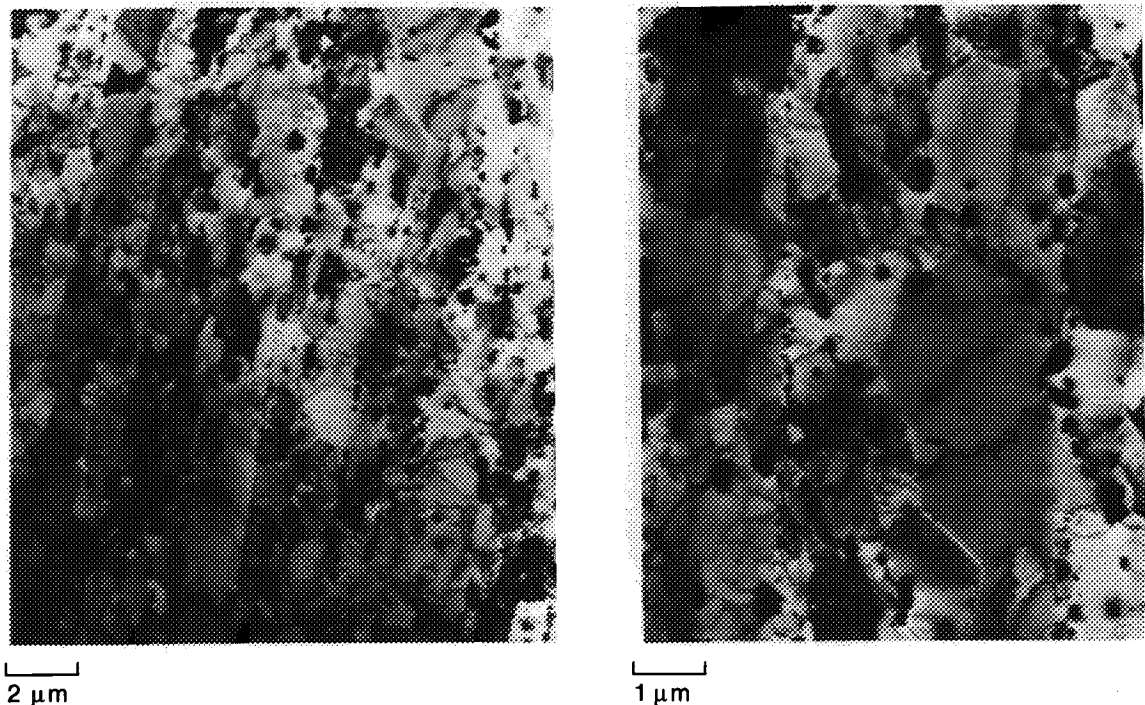
Figure 47. Electron Micrographs (TEM-Foil) Showing Dispersions in Alloy 993

Dispersions coarsened during tensile testing at 705°C (1300°F) to about 2000-8000Å, (Figure 49). Finer, often rodlike copper-hafnium precipitates were also observed. Energy-dispersive spectra of the latter, determined using STEM, yielded a composition of $Cu_{6.6}Hf$ — reasonably close to Cu_5Hf, considering the presence of background matrix copper. Grain/subgrain sizes were about 1-2 μm.

In an effort to increase the elevated temperature strength of Alloy 993, process studies were undertaken, with a goal of increasing grain size. Generally, grain growth upon solution treatment had been observed to be limited by prior particle boundaries. A way had to be found to force grain boundaries past these prior particle boundaries. It was found that 870°C (1600°F)/50 percent hot-working + solution-treatment at 940°C (1725°F) coarsened grain size to about 80 μm (Figure 50).

Additional Alloy 993 was processed for tensile testing: hot-worked + solutioned + aged (HWSA), and hot-worked + solutioned + cold-worked + aged (HWSCWA). They were tensile tested at 705°C (1300°F). Results are listed in Table 18. The cold-worked condition exhibited high strengths, but low elongation. The solutioned + aged condition was weaker than any other Alloy 993 condition tested.

TABLE 20. — AVERAGED TENSILE PROPERTIES AT 705°C (1300°F)**

Alloy	Serial No. (Condition)	Strain Rate (s⁻¹)	Yield Strength*		Tensile Strength		Elongation in 4d (%)	Reduction in Area (%)	Number of Tests
			MPa	ksi	MPa	ksi			
993	AE	0.06	49.5	9.9	62.5	12.5	50	96	2
993	SCWA-211	0.06	60.5	12.1	73.0	14.6	34	96	2
993	SCWA-3	0.10	139.9	20.3	139.9	20.3	8	92	1
993	HWSA	0.10	62.7	9.1	74.4	10.8	32	91	1
995	AE-2	0.06	77.2	11.2	97.8	14.2	41	98	2
995	SCWA-211	0.06	43.4	6.3	74.4	10.8	62	98	2
995	AE-3	0.10	76.5	11.1	90.3	13.1	46	98	2
996	AE	0.06	62.0	9.0	92.3	13.4	104	90	2
999	SA	0.06	62.0	9.0	96.5	14.0	98	85	3
999	SCWA-211	0.06	65.5	9.5	100.6	14.6	77	80	3
999	HW	0.10	112.3	16.3	128.2	18.6	42	85	1
999	HWSA	0.10	73.0	10.6	114.4	16.6	49	67	1
997	AE	0.06	73.0	10.6	91.6	13.3	46	97	2
997	SCWA-111	0.06	48.2	7.0	73.7	10.7	76	97	2
NASA-Z	1	0.06	73.0	10.6	107.5	15.6	90	79	2
NASA-Z	1	0.10	84.0	12.2	80.5	16.1	66	65	2
1032	AE	0.10	88.2	12.8	115.8	16.8	31	94	3
1032	SCWA-1	0.10	99.2	14.4	149.5	21.7	35	93	3
1035	AE	0.10	91.6	13.3	166.0	24.1	26	89	3
1035	EC	0.10	96.5	14.0	184.0	26.7	14	89	3
1036	AE	0.10	88.2	12.8	125.4	18.2	28	94	2
1038	AE	0.10	92.3	13.4	134.4	19.5	30	88	3
1038	SA	0.10	86.1	12.5	116.4	16.9	38	83	3
1042	AE	0.10	92.3	13.4	114.4	16.6	45	88	2
1043	AE	0.10	72.3	10.5	110.2	16.0	76	50	2
1043	SCWA	0.10	72.3	10.5	107.4	15.6	63	49	2

* 0.6 s⁻¹ strain rate tests employed crosshead deflectometer for strain data collection.

** See Appendix A for individual test results.

Microstructures of coarse-grained Alloy 993 tensile specimens exhibited little recrystallization, except for a slight amount in the immediate area of the fracture (Figure 50). Necking was localized, with cup/cone type fractures.

(3) Alloy 994: Cu-0.8%Zr

This alloy was not processed to bar stock, since it was somewhat contaminated by nickel (Table 16), and was not significantly different from Alloy 995.

└────┘
100 μm   Grip Region   └────┘
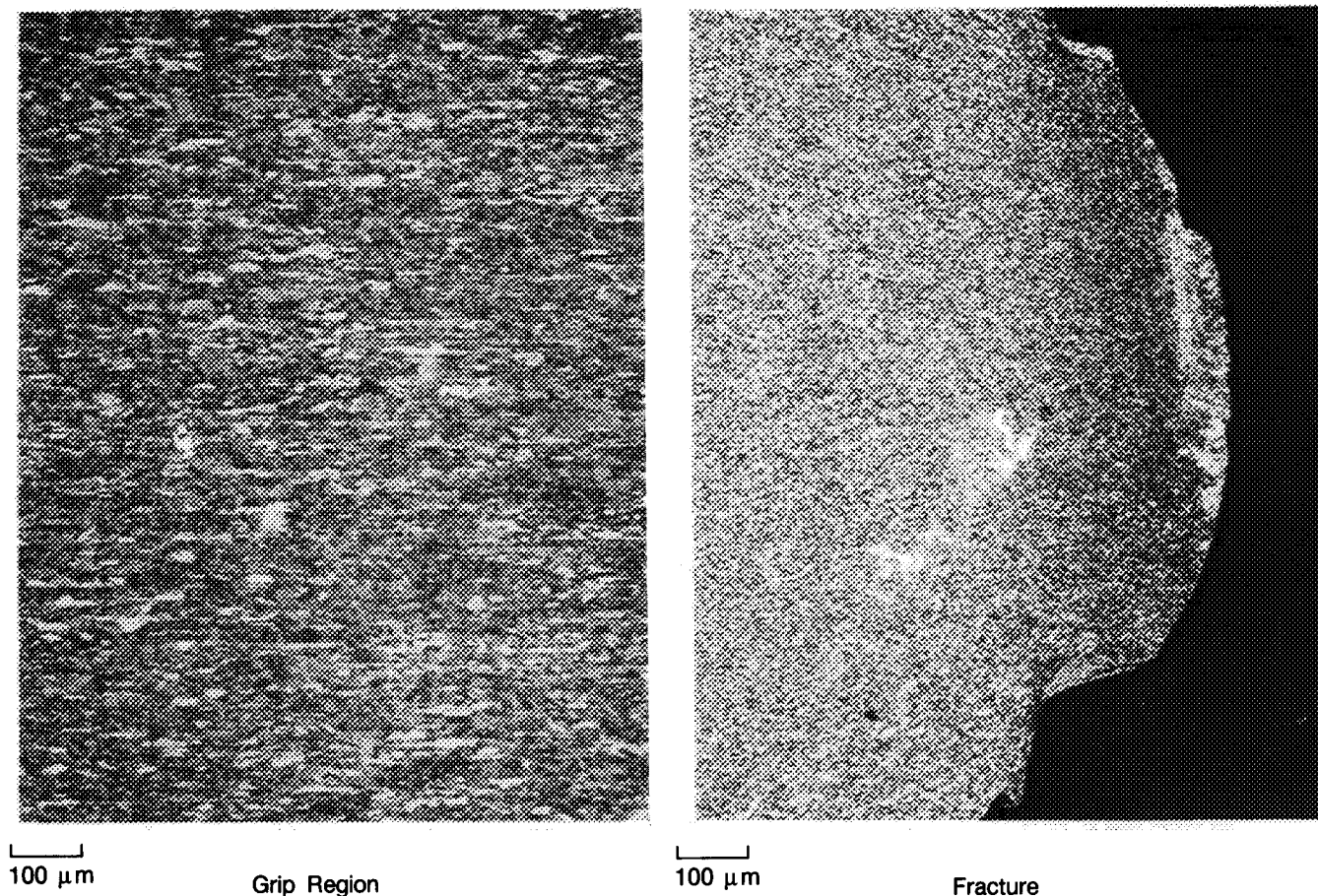   100 μm   Fracture

*Figure 48. Microstructures in Solutioned + Cold-Worked + Aged Alloy 993 (SCWA-211)
Tensile Tested at 705°C (1300°F)*

(4) Alloys 995 and 998: Cu-0.6%Zr and Cu-0.65%Cr

Powder metallurgy Cu-Zr alloys also exhibited fairly good recrystallization and softening
resistance, although not quite as good as that of Cu-Hf alloys. The responses of Alloys 995 and
998 to processing were idential, and thus are discussed as one alloy: 995.

(a) **As-Extruded Form** — Extruded Alloy 995 exhibited a warm-worked fibrous
structure with an extremely fine grain size (1 μm) (Figure 51) and a
hardness of DPH 92. Exposure to an aging temperature of 480°C (900°F)
produced neither microstructure nor hardness (DPH 94-96) changes.
However, exposure to stability testing at 650°C (1200°F) slightly softened
the materials to about DPH 85 and recrystallized about 25 percent of the
microstructure (Figure 51).

(b) **Extruded + Cold-Worked Conditions** — Cold-working of the extruded
microstructure resulted in a similar fibrous structure (optional), but did
increase hardness significantly, to DPH 118. Annealing at the 480°C
temperature did not change the optical microstructure, but did soften the

90

material significantly, to DPH 96. Further annealing at 650°C recrystallized the alloy (Figure 51), and softened it to DPH 68.

(c) **Solutioned + Aged Conditions** — Solution treatment at 925°C (1700°F) recrystallized the extrusion (Figure 52) resulting in grain sizes of 5-10 μm and hardnesses of DPH 55-60. Aging at 480°C (and/or annealing at 650°C) neither hardened the alloy nor changed its microstructure.

(d) **Solutioned + Cold-Worked Conditions** — Cold-working of solutioned Alloy 995 hardened it to DPH 106 and produced a cold-worked microstructure (Figure 52). Annealing at 650°C recrystallized (Figure 52) and softened (DPH 51) the alloy.

As-extruded samples of Alloy 995 were evaluated using TEM. Dispersions were somewhat coarse (about 1000-3000Å) (Figure 53). Grains/subgrains were about 0.5 μm to 1 μm in size, and exhibited little strain.
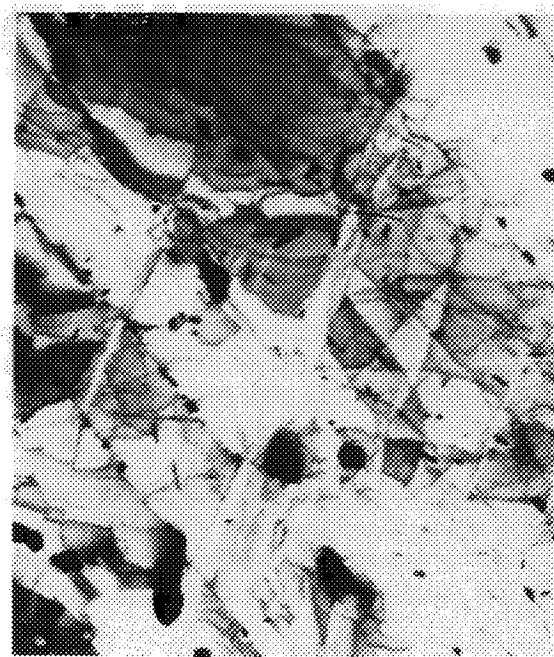

2 μm

Figure 49. Electron Micrograph of Alloy 993 (SCWA-211) Tensile Tested at 705°C (1300°F). Note Rod-Like Precipitates

The only worked form of Alloy 995 that exhibited any stability at 650°C (1200°F) was the as-extruded condition. Likewise, it was the only form of the alloy that remained hard after 650°C exposure. For these reasons, the as-extruded condition was chosen for preliminary tensile testing. A solutioned + cold-worked + aged condition was also chosen for testing because that was the condition of Amzirc (commercial Cu-0.15%Zr) that has shown highest elevated-temperature strength.

L_____J
100 μm
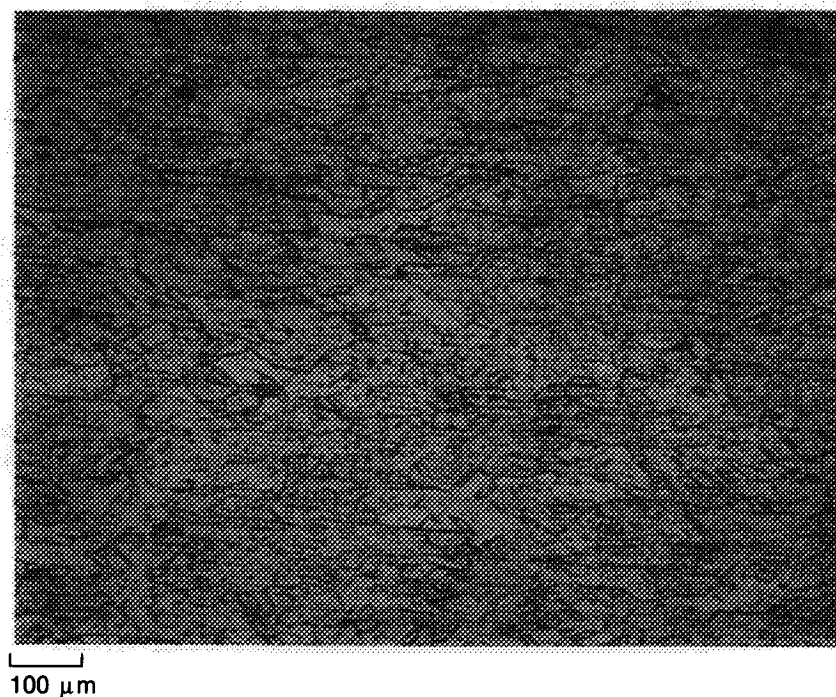
Figure 50. Microstructure of Alloy 993 Processed to Increase Grain Size (HW + S)

The tensile tests (Table 18) revealed that the as-extruded condition was stronger and less ductile than the solutioned + cold-worked + annealed condition. This correlated with the better softening resistance of the former condition. As with Alloy 993, failure was by localized smooth necking. Little void formation or cracking was observed.

Microscopy of failed Alloy 995 tensile specimens (Figure 54) revealed little recrystallization (at least little change from the input microstructure). Cavitation was observed around nickel particles, but was ductile and uninvolved with failure. Transmission electron microscopy did not reveal significant changes in the microstructure of as-extruded material after testing.

(5)   Alloys 996 and 999: Cu-05%Zr-3%Ag

Alloys 996 and 999 are powder versions of the NASA-Z (and NARloy-Z™) composition, and were made to assess the effects of rapid solidificazation and powder metallurgy on NASA-Z. NASA-Z and NARloy-Z™ are used in the solutioned + aged condition. However, the powder versions were subjected to the same processing matrix as the other alloys to allow study of processing effects.

(a)   As-Extruded Conditions — As-extruded microstructures were at least 50 percent recrystalized, with grain sizes of 2-5 μm (Figure 55). Hardnesses ranged from DPH 94 to 106. Annealing at 480°C (900°F) produced no changes in microstructure or hardness. Annealing at 650°C (1200°F) produced fully recrystallized microstructures (Figure 55) with grain sizes of 1-6 μm and hardnesses of DPH 70 to 88.

(b) **Extruded + Cold-Worked Conditions** — Cold-working resulted in a structure similar to that of the extrusion, but at a greater level of hardness (DPH 126-146). Annealing at 480°C produced some softening (DPH 96-122) and probably some recrystallization. Annealing at 650°C recrystallized (Figure 55) and softened (DPH 74-84) the alloy.

(c) **Solutioned + Aged Conditions** — Solution treatment of Alloy 996 completely recrystallized the microstructure to 5-10 μm grain sizes, resulted in some abnormal grain growth (Figure 56), and softened the material to DPH 61-70. Subsequent aging at 480°C increased hardness slightly, to DPH 64-80, without changing the optical microstructure. Annealing solutioned or aged material resulted in hardnesses of DPH 62-64, with no change in optical microstructure.

(d) **Solutioned + Cold-Worked Conditions** — Cold-working solutioned material hardened it significantly (DPH 118-126) and produced a cold-worked microstructure. Subsdequent aging at 480°C did not change microstructure or hardness. Further annealing at 650°C softened (DPH 72-74) and recrystallized the material to about 10 μm grain size (Figure 56).

TEM evaluation of 996/999 as-extruded samples showed that dispersion sizes were similar to earlier alloys: 2000-4000Å, (Figure 57). Dispersion compositions were about 76at.%Cu-14at.%Zr-10at.%Ag (68wt.%Cu-18wt.%Zr-14wt.%Ag) — similar to values found in other investigations (2,22). Fine silver precipitates were also seen. Grains or subgrains were about 2 μm in size and relatively strain-free.

Some conditions (primarily as-extruded) of Alloys 996/999 produced abnormal grain growth upon solution treatment. Grains were as large as 2 mm. Usually, abnormal grains were confined to the periphery of the bar, indicating a strain or heat-up rate effect. Subsequent cold work + annealing recrystallized the abnormal grains to a fine-grained condition.

All of the strained forms of Alloys 996/999 softened and recrystallized at 650°C (1200°F). Only the strain-free form, solutioned + aged, exhibited much stability at 650°C; it probably overaged. As no forms were outstanding, two extremes in microstructure were chosen for preliminary tensile tests: finer-grained fibrous as-extruded, and coarse-grained, cold-worked solutioned + cold-worked + aged. In addition, solutioned + aged material was tested for comparison to NASA-Z, which is solutioned + aged.

The tensile test results (Table 20) revealed little effect of processing on tensile properties at 705°C (1300°F). It is believed this was due to 1) solutioning of Ag precipitates at the test temperatures; 2) the extensive recrystallization that took place in all three conditions during tensile deformation. Both would tend to equalize the materials.

Failure of tensile specimens was characterized by long continuous necking (indicative of work hardening) and somewhat brittle fracture involving grain boundary cracking (Figure 58). Numerous grain boundary cracks were observed in the region surrounding the fracture. Recrystallization was quite evident in the gage section, increasing in severity with proximity to the fracture.
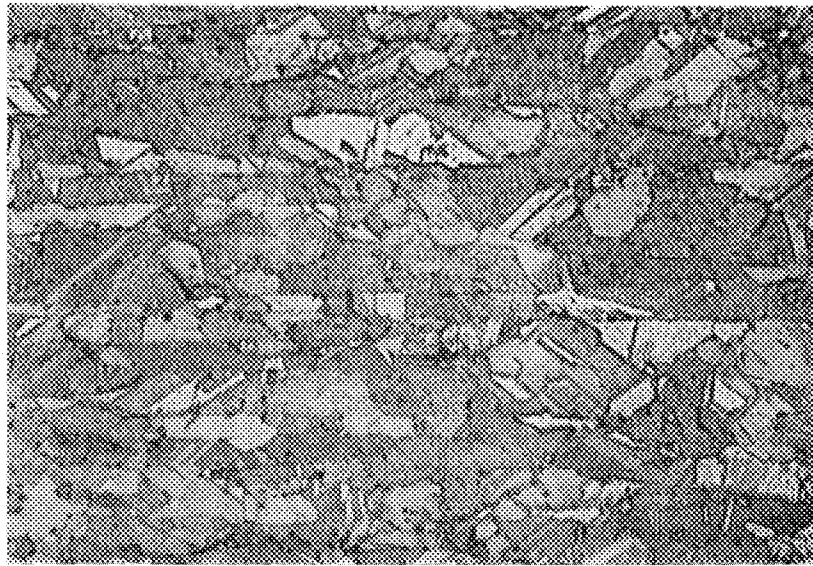
93

20 μm   As-Extruded

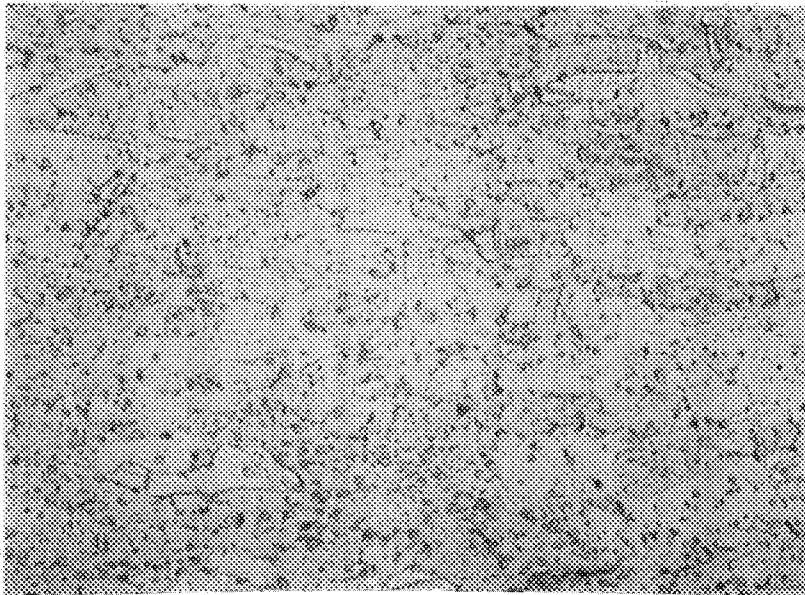

20 μm   Extruded + Annealed at 650°C (1200°F)

20 μm   Extruded + Cold-Swaged + Annealed at 650°C (1200°F)

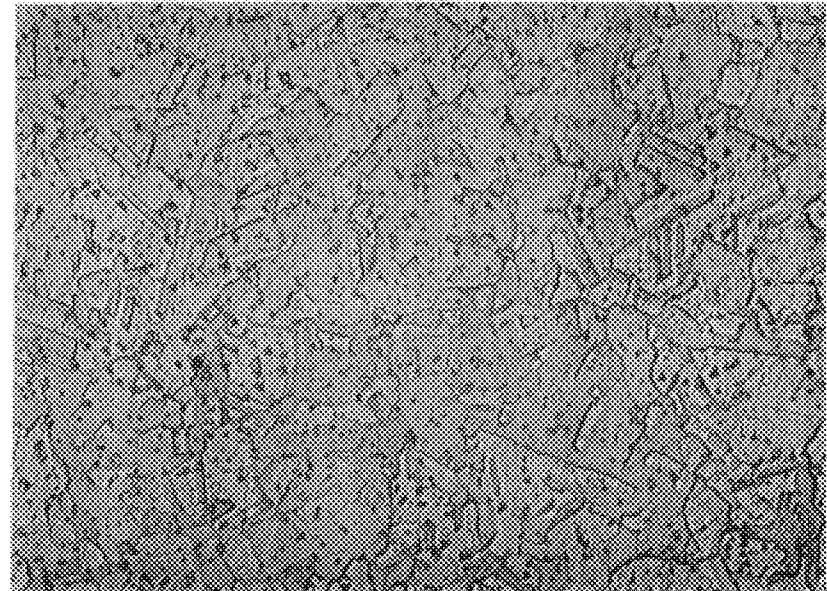*Figure 51. Microstructures of Processed Alloy 995*

20 µm   As-Solutioned

20 µm   Solutioned + Cold-Swaged

20 µm   Solutioned + Cold-Swaged + Aged + Annealed

Figure 52. Microstructures of Solution-Treated and Processed Alloy 995
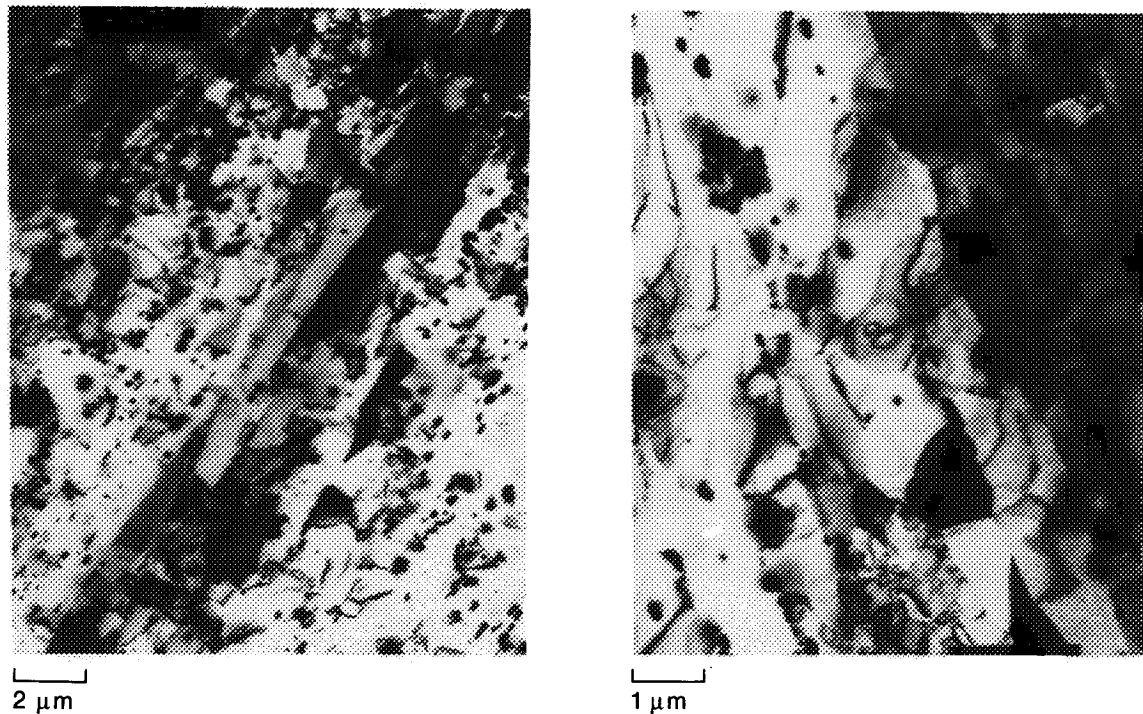
2 μm   1 μm

*Figure 53.   Electron Microstructures of Alloy 995 (Cu-0.6Zr), as Extruded (TEM-Foil)*

Later in the program, additional processing work was done with Alloys 996/999 to produce coarser-grained material for testing. The intention was to increase elevated-temperature tensile strengths to those of NASA-Z, and to duplicate the NASA-Z microstructure for LCF testing to establish whether powder metallurgy NASZ-Z could be used instead of cast + wrought NASA-Z. Bars of Alloy 999 were hot-worked 50 percent at 870°C (1600°F), producing the worked microstructure in Figure 59. Solution treatments produced recrystallization and grain growth to 40-80 μm grain sizes (NASA-Z is 60-100 μm) (Figure 59). Tensile specimens were prepared by hot-working and hot-work + solution + age. Tensile properties of each are listed in Table 20. The hot-worked + solutioned + aged properties were roughly equivalent to those of NASA-Z. The hot-worked verision was significantly stronger than NASA-Z, evidently because of strain hardening.

Both conditions experienced considerable recrystallization and grain refinement during the 705°C (1300°F) tensile tests (Figure 60). Failure was like that of the other Alloy 996/999 specimens: grain boundary cracking, with uniform necking and elongation.

(6)   Alloy 997: Cu-0.55%Zr-0.05%B

Alloy 997 was formulated to contain about 0.35 volume percent ZrB_2, as well as 0.2 percent excess zirconium, which would form Cu_5Zr primary and aging precipitates. As noted earlier, the powder exhibited a few coarse diborides. Any fine borides were expected to act as a dispersion strengthener, stabilizing the microstructure and retaining cold work at elevated temperatures.

96

L____J   L____J
100 μm   Grip Region   100 μm   Fracture
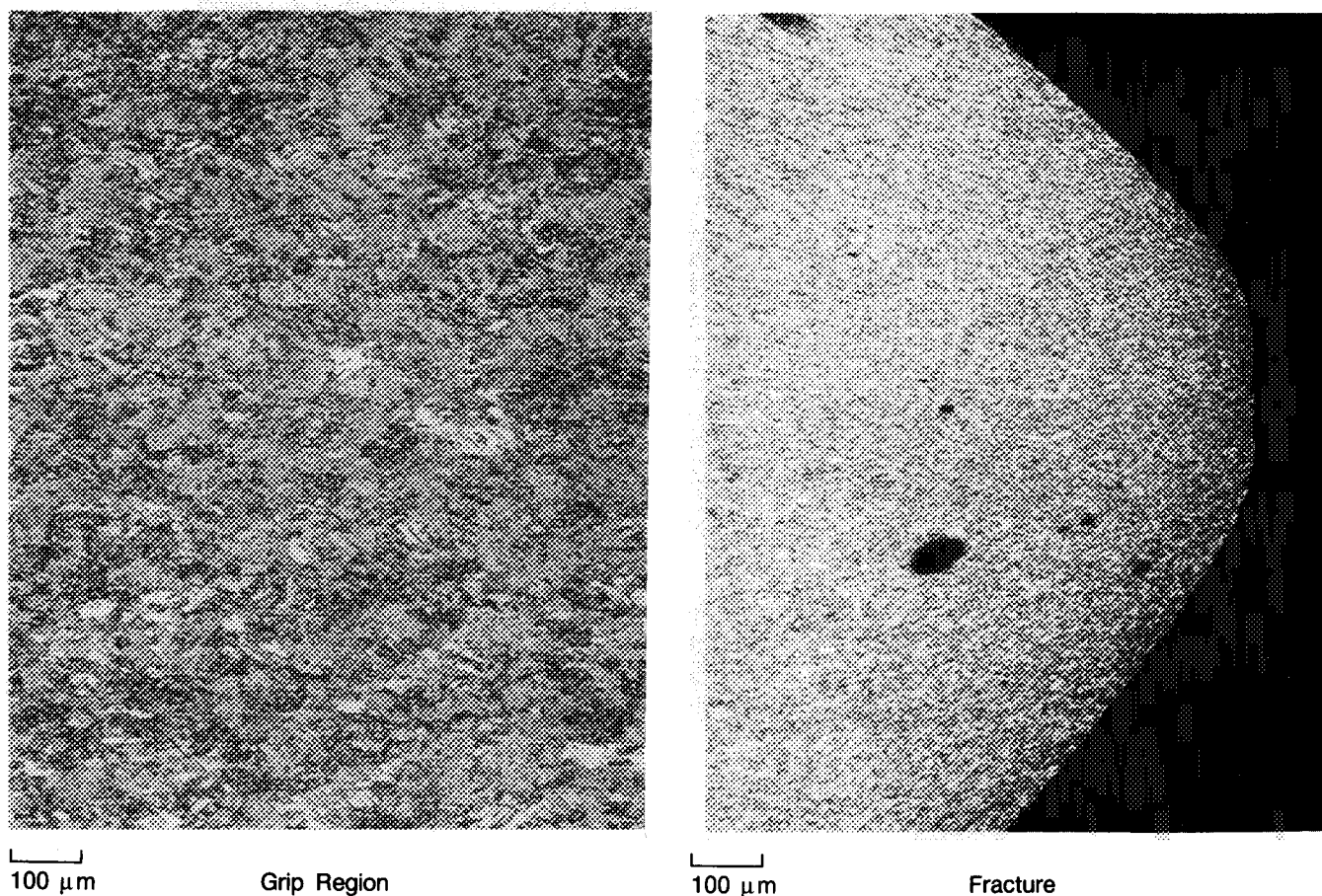
*Figure 54.   Microstructures in Solutioned + Cold-Worked + Aged Alloy 995 (SCWA-211)
Tensile Tested at 705°C (1300°F)*

Effects of processing on the alloy were nearly identical to those observed for Alloys 995/998
(Cu-Zr). See the Alloys 995/998 narrative for a description, and consult Table 19 for the exact
hardnesses observed.

Electron microscopy of extruded Alloy 997 did not reveal any fine borides, just a Cu-Zr
dispersion similar to that in Alloy 995.

To evaluate the effect of the small boron addition to Alloy 997, the conditions of Alloy 997
chosen for preliminary tensile testing (as-extruded and solutioned + cold worked + aged) were
the same as those used for testing of Alloy 995 (copper-zirconium).

Tensile test results were almost identical to those of Alloy 995 (Table 20), also supporting
the absence of a fine boride dispersion. Fracture modes were similar to those of Alloy 995: the
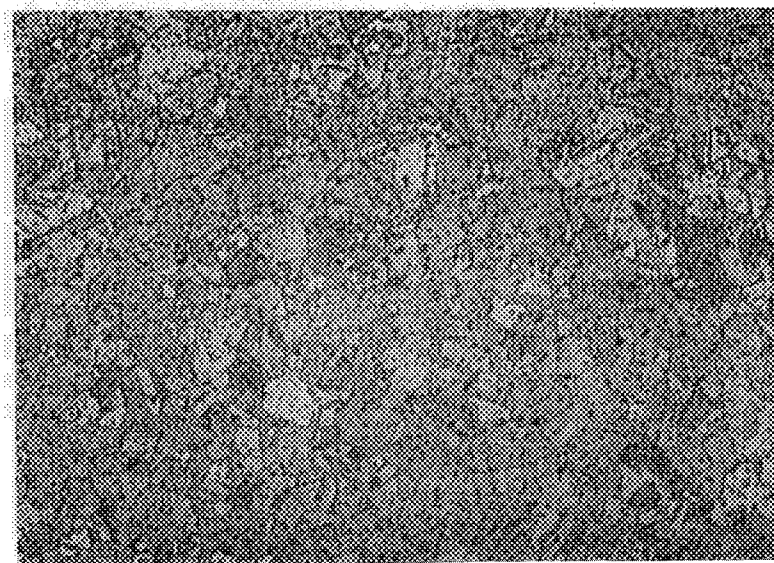coarse borides did not embrittle the alloy.

97
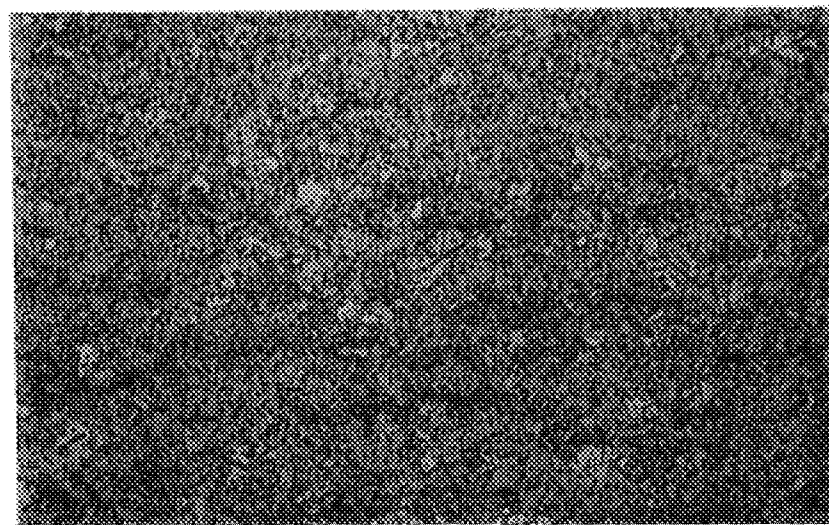
20 μm   As-Extruded

20 μm   Extruded + Annealed
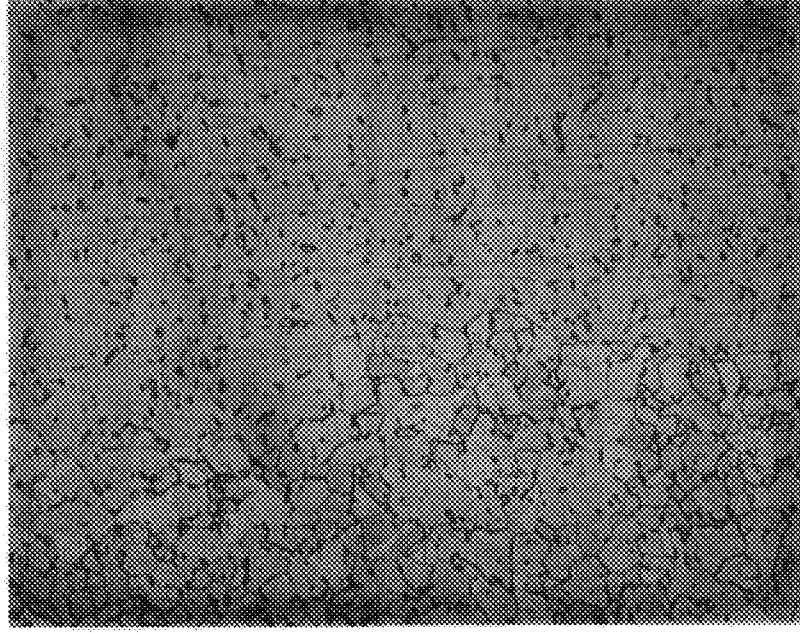
20 μm ·   Extruded + Cold-Swaged + Annealed

Figure 55.   Microstructures of Processed Alloy 996

Solutioned

20 μm

Solutioned + Cold-Worked +
Aged + Annealed at 650°C (1200°F)

20 μm

Figure 56. Microstructure of Processed Alloy 996, Showing Abnormal Grain Growth Upon Solution Treatment
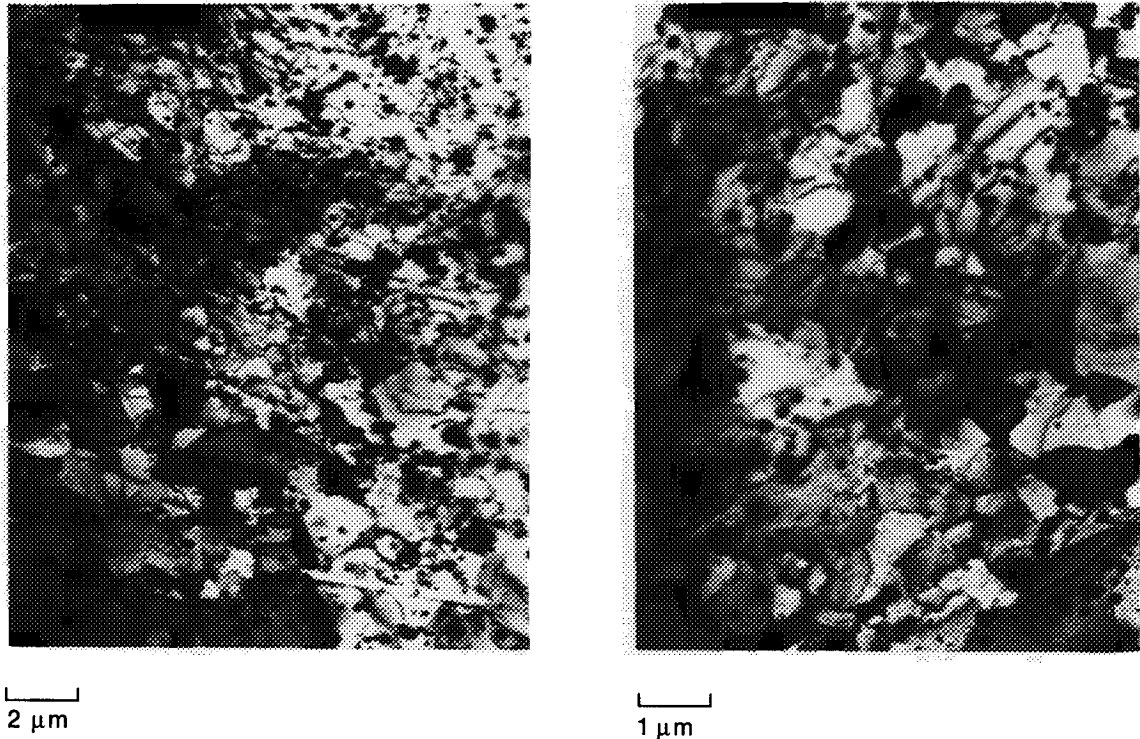
2 μm   1 μm

Figure 57. Electron Micrographs (TEM-Foil) of As-Extruded Alloy 996

(7) Alloy 1032: Cu-0.7%Tl-1.1%Hf

Alloy 1032 exhibited significant age hardenability, and good microstructural stability at 650°C (1200°F) after certain processing sequences. Specific results of processing are detailed below.

(a) As-Extruded Conditions — The as-extruded microstructure was partially recrystallized, fibrous, with grain sizes of less than 5 μm (Figure 61). Annealing at 650°C (1200°F) changed neither hardness (DPH 100) nor microstructure.

(b) As-Extruded + Cold-Worked Conditions — Cold working increased hardness to DPH 155, and subsequent annealing at 650°C recrystallized (Figure 61) and softened (DPH 85) the alloy.

(c) Solutioned + Aged Conditions — Solution treatment at 925°C (1700°F) completely recrystallized (Figure 61) and softened (DPH 80) the alloy. Grain size was 5-10 μm. Aging at 480°C (900°F) hardened the alloy to DPH 146, but subsequent annealing at 650°C overaged and softened the alloy to DPA 76.

(d) Solutioned + Cold-Worked Conditions — Cold working of solutioned Alloy 1032 hardened it to DPH 132 and produced a cold-worked microstructure. Subsequent aging at 480°C further hardened the alloy to DPH 168. Further annealing at 650°C overaged the material, reducing the hardness to DPH 122, but did not produce recrystallization (Figure 61).

100

L___J		L___J	
100 μm	Grip Region	100 μm	Fracture
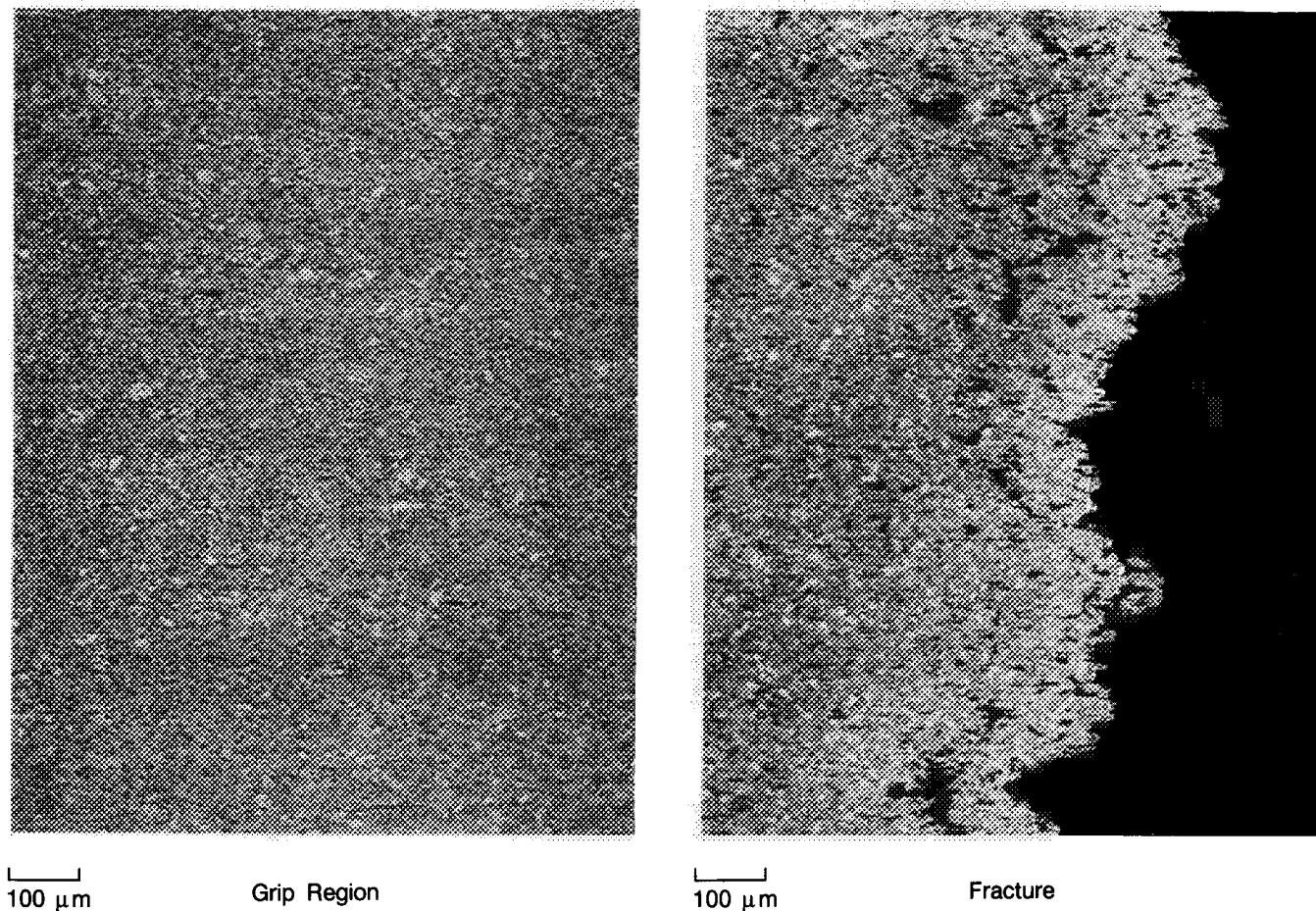
*Figure 58.   Microstructures of Solutioned + Aged Alloy 999 (SA) Tensile Tested at 750°C
(1300°F)*

The second-phase forming in this alloy could not be identified by X-ray diffraction. It was probably the Cu_5Hf type proposed for the copper-titanium-hafnium screening alloy.

Highest as-annealed 650°C hardness resulted from as-extruded and solutioned + cold worked + aged (S + CW + A) materials, so both were chosen for preliminary tensile tests. These alloy forms also appeared to be among the most thermally stable for this alloy.

Results (Table 18) paralleled the above observations. The S + CW + A condition was much stronger than the as-extruded conditions, with attendant elongation losses. Failure was by localized ductile necking. Little cracking was observed. Neither condition recrystallized upon testing.

├─────┤
100 μm   Hot-Worked

├─────┤
100 μm   Hot-Worked + Solutioned

Figure 59. Microstructures of Alloy 999 Processed to Increase Grain Size
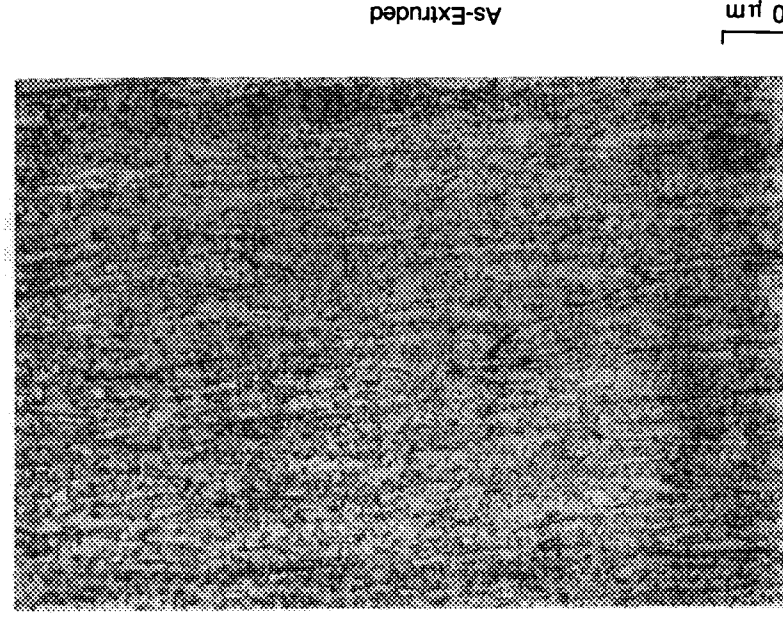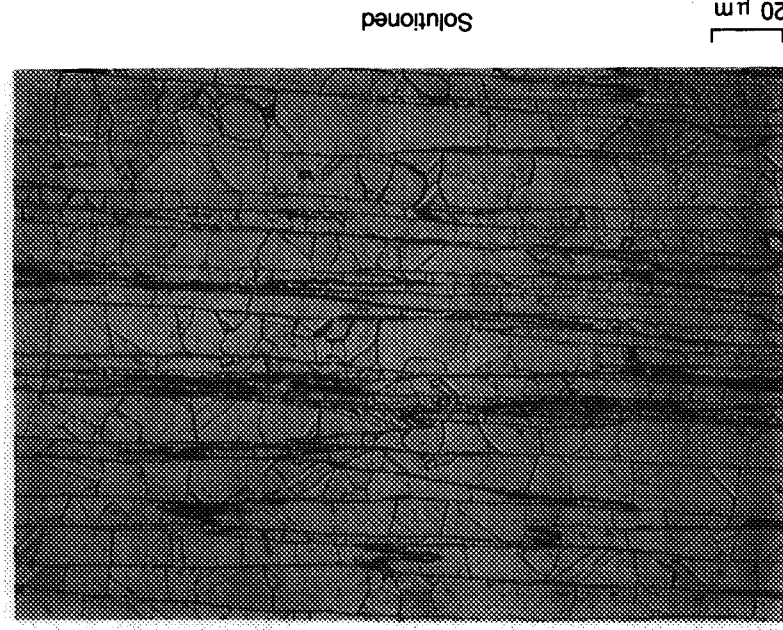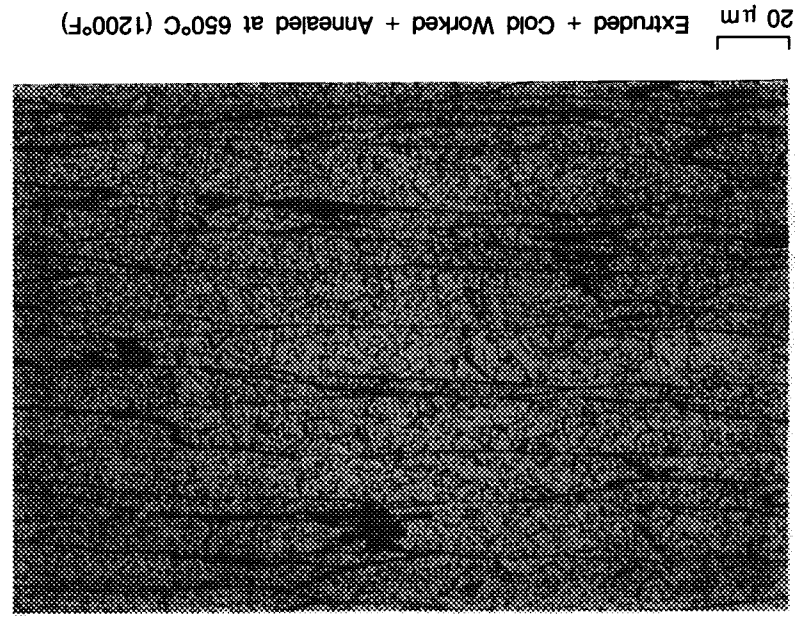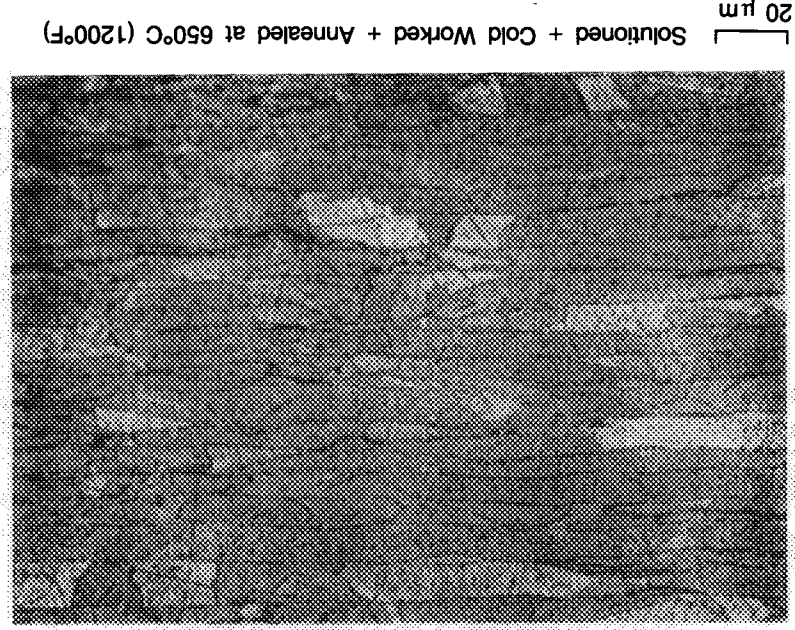
Grip Region

100 μm

Gage/Fracture

100 μm
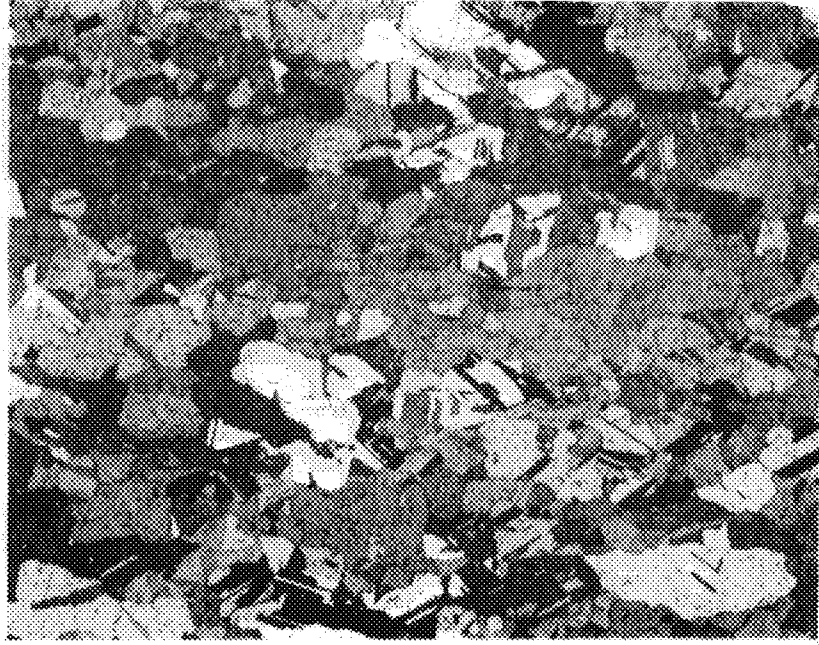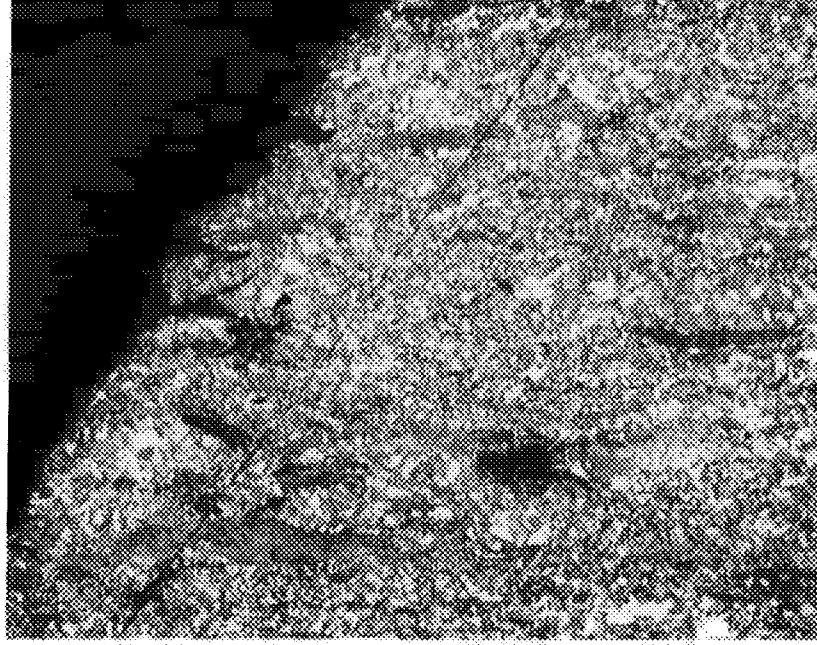
Figure 60. Microstructures in Coarsened, Solutioned + Aged Alloy 999 (HWSA) Tensile Tested at 705°C (1300°F). Note the Recrystallization in the Gage Region

103

(8) Alloy 1033: Cu-1.0%Cr-0.2%Co

Alloy 1033 was expected to form chromium-based precipitates that were more stable than those found in conventional copper-chromium alloys. Partial substitution of cobalt for chromium in the precipitates was expected to decrease lattice-to-precipitate mismatch and increase the stability of the precipitates at elevated temperatures. As it turned out, however, this alloy did not exhibit very good high-temperature stability.

(a) **As-Extruded Conditions** — This alloy exhibited a coarser as-extruded microstructure than seen for most other alloys (Figure 62). Grains were elongated, recrystallized, and about 3-4 μm in size. Hardness was DPH 80. Annealing at 650°C (1200°F) softened the alloy slightly (DPH 74), and appeared to produce large, overaged precipitates (Figure 62).

(b) **Extruded + Cold-Worked Conditions** — Cold working hardened the extrusion to DPH 114. Subsequent annealing at 650°C (1200°F) recrystallized (Figure 62) and softened the alloy (DPH 60).

(c) **Solutioned + Aged Conditions** — Solution treatment softened (DPH 50) and recrystallized (grain size 5-10 μm) the alloy (Figure 63). Subsequent aging only slightly hardened the alloy, to DPH 61. Further annealing at 650°C softened the alloy to DPH 55.

(d) **Solutioned + Cold-Worked Conditions** — Cold working the solutioned alloy increased the hardness to DPH 96. Subsequent aging slightly hardened the alloy to DPH 110. However, the alloy recrystallized (Figure 63) and softened (DPH 56) upon annealing at 650°C.

Analysis confirmed the presence of cobalt and chromium in the alloy. However, cobalt could not be found in the large chromium precipitates (microprobe). Because of the low chromium concentration, chromium X-ray diffraction peaks could not be detected to determine whether the cobalt was alloying in the chromium phase and changing its lattice parameter.

This alloy did not exhibit much stability or hardness retention at elevated temperatures, so it was not selected for preliminary tensile tests.

(9) Alloy 1035: Cu-1.0%Cr-0.6%Zr

Alloy 1035 exhibited age hardenability and, in some cases, very good softening resistance at 650°C (1200°F). It benefitted from precipitates of Cr and Cu_5Zr. Responses to processing are described below:

(a) **As-Extruded Conditions** — As-extruded Alloy 1035 exhibited a warm-worked ultra-fine-grained (1 μm) fibrous microstructure (Figure 64). Hardness was DPH 115. Annealing at 650°C (1200°F) had essentially no effect.

(b) **Extruded + Cold-Worked Conditions** — Cold working hardened the extrusion to DPH 142, with little optically discernable microstructural change. Subsequent annealing at 650°C softened the alloy back to DPH 110, with no observable recrystallization.

(c) **Solutioned + Aged Conditions** — Solution treatment recrystallized the alloy to 5-10 μm grain sizes (Figure 64). Hardness dropped to DPH 70.

Aging at 480°C (900°F) increased hardness substantially, to DPH 100. However, additional annealing at 650°C overaged the alloy, softening it to DPH 65.

(d) Solutioned + Cold-Worked Conditions — Cold working solutioned material increased hardness to DPH 120. Subsequent aging at 480°C increased hardness to DPH 144, with no change in microstructure. Additional annealing at 650°C (1200°F) recrystallized (Figure 64) and softened (DPH 72) the alloy.

The alloy conditions exhibiting highest softening resistance at 650°C were the as-extruded and extruded + cold-worked conditions. Both were chosen for preliminary tensile testing.

Results (Table 19) showed that both alloys exhibited roughly equivalent strengths at 705°C (1300°F). However, the cold-worked condition exhibited lower elongations than the as-extruded (warm-worked) condition.

Tensile failures were by localized ductile necking; little cracking was observed. The as-extruded condition did not recrystallize upon testing. The extruded + cold-worked condition coarsened slightly upon testing.

(10) Alloy 1036: Cu-0.6%Zr-1.1%Hf

Alloy 1036 represented a combination of the Cu-Zr and Cu-Hf systems — both of which gave promising results earlier in the program as Alloys 993 and 995. The ternary alloy exhibited slightly more resistance to softening at 650°C (1200°F) and generally higher post-anneal (650°C) hardnesses than either of the binary alloys. Processing effects are described below.

(a) As-Extruded Conditions — Like the binaries, Alloy 1036 extruded to a warm-worked, fibrous, ultra-fine-grained microstructure (Figure 65). Hardness was DPH 110. Annealing at 650°C produced little change (hardness was DPH 100).

(b) Extruded + Cold-Worked Conditions — Cold working the as-extruded microstructure hardened it to DPH 130. The microstructure did not change observably. Subsequent annealing softened the alloy to DPH 100, but did not recrystallize it.

(c) Solutioned + Aged Conditions — Solution treatment resulted in softening (DPH 75) and recrystallization to a fine-grained (5-10 μm) equiaxed microstructure (Figure 65). This form of the alloy did not age-harden at 480°C (900°F), or soften further upon annealing at 650°C.

(d) Solutioned + Cold-Worked Conditions — Cold working hardened the solutioned alloy to DPH 130. Subsequent aging at 480°C had no effect. However, the alloy recrystallized (Figure 65) and softened to DPH 70 upon annealing at 650°C.

This alloy did not age-harden, which was not surprising, since Alloys 993 and 995 did not age harden either. Since the as-extruded and extruded + cold-worked conditions equally showed the most promise for high-temperature use, the as-extruded condition was chosen for preliminary tensile tests.

The tensile strengths obtained (Table 20) were not particularly high. Failure was by localized ductile necking; no cracking was observed. The fine fibrous microstructure was not changed by testing.

106

(11) Alloy 1038: Cu-06%Zr-3.0%Ag-1.0%Cr

Alloy 1038 served as a chromium-containing extension of the copper-zirconium-silver (NASA-Z) system. It exhibited the high age-hardenability found in many other chromium-containing alloys, as well as the predisposition toward recrystallization found in high-silver alloys such as NASA-Z. More-detailed processing effects are described below.

(a) **As-Extruded Conditions** — Alloy 1035 extruded to a warm-worked, fibrous, ultra-fine structure (Figure 66) (DPH 130). Annealing at 650°C (1200°F) softened (DPH 98) and recrystallized the alloy (grain size 2-8 μm).

(b) **Extruded + Cold-Worked Conditions** — Cold working increased the hardness of the extrusion to DPH 160. Subsequent annealing at 650°C recrystallized, (Figure 66) and softened (DPH 90) the alloy.

(c) **Solutioned + Aged Conditions** — Solution treatment of the extrusion at 925°C (1700°F) recrystallized the microstructure to equiaxed 5-10 μm grains (Figure 66) and softened the alloy to DPH 80. Aging at 480°C (900°F) hardened the alloy to DPH 160, but subsequent annealing at 650°C (1200°F) overaged and softened the alloy to DPH 78.

(d) **Solutioned + Cold-Worked Conditions** — Cold working the solutioned alloy hardened it to DPH 154. Subsequent aging at 480°C did not impart significant additional hardening (DPH 160). Annealing (after age) at 650°C softened (DPH 90) and recrystallized the alloy (Figure 66).

The forms chosen for preliminary tensile testing were as-extruded, and solutioned + aged. All of the post-anneal alloy forms had exhibited recrystallized microstructures and most exhibited hardnesses in the DPH 90 range. As there was minimal difference in post-anneal hardnesses, variety in microstructure and imput hardness became the criteria, so the fine-grained as-extruded and coarser hardened + solutioned + aged forms became candidates for testing.

Strengths of the two conditions (Table 20) were essentially equivalent: the as-extruded material was slightly stronger and more ductile. With the addition of silver, failure mode resembled those of copper-zirconium-silver alloy: diffuse necking and cracking at the failure. The alloy also recrystallized in the neck region (Figure 67).

20 µm

As-Extruded

20 µm
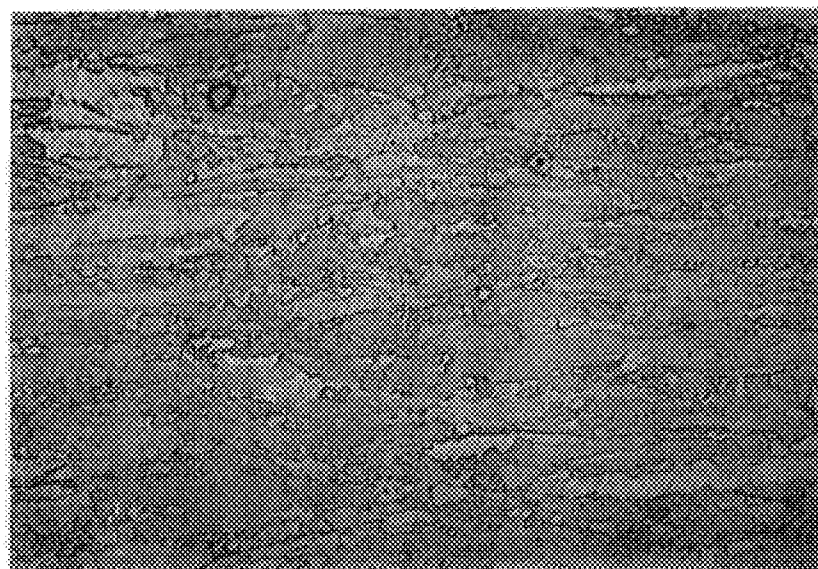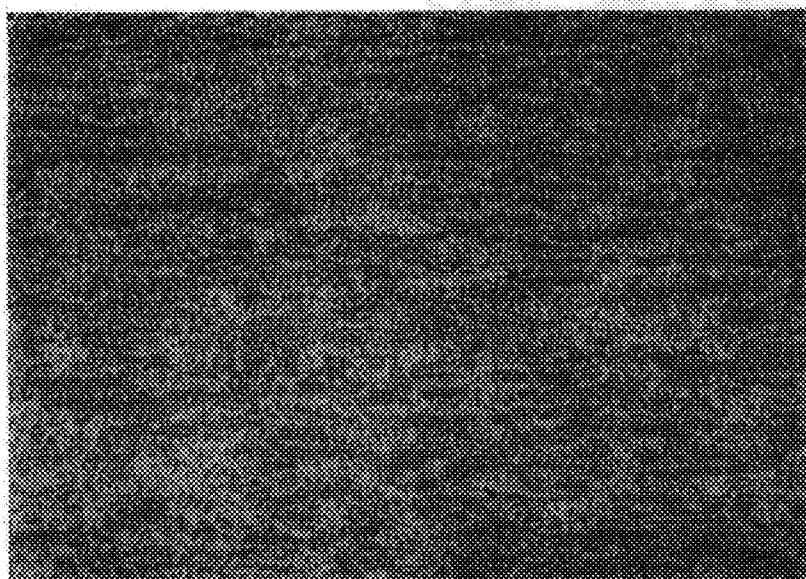
Extruded + Annealed at 650°C (1200°F)
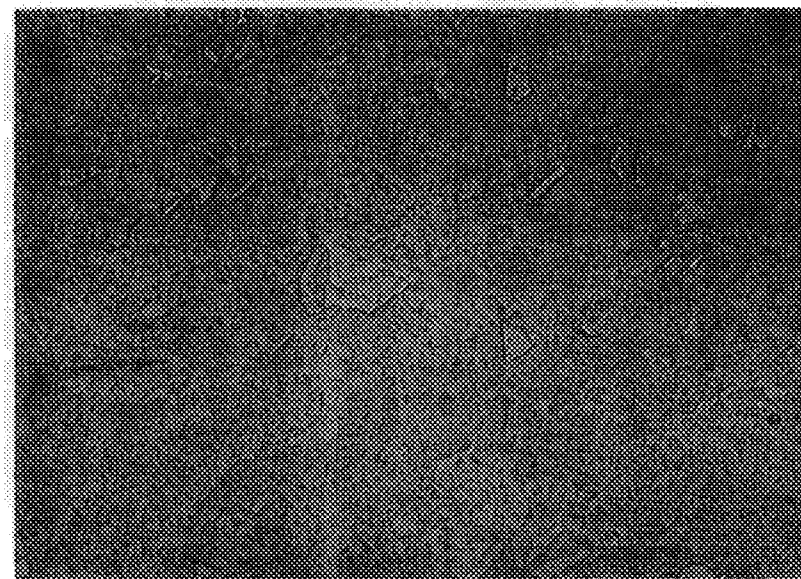
20 µm

Extruded + Cold-Worked +
Annealed at 650°C (1200°F)

Figure 62. Microstructures of Processed Alloy 1033

Solutioned + Cold-Swaged + Aged +
Annealed at 650°C (1200°F)

20 μm

Solutioned

20 μm

Figure 63. Microstructures of Processed Alloy 1033, After Solution Treatment
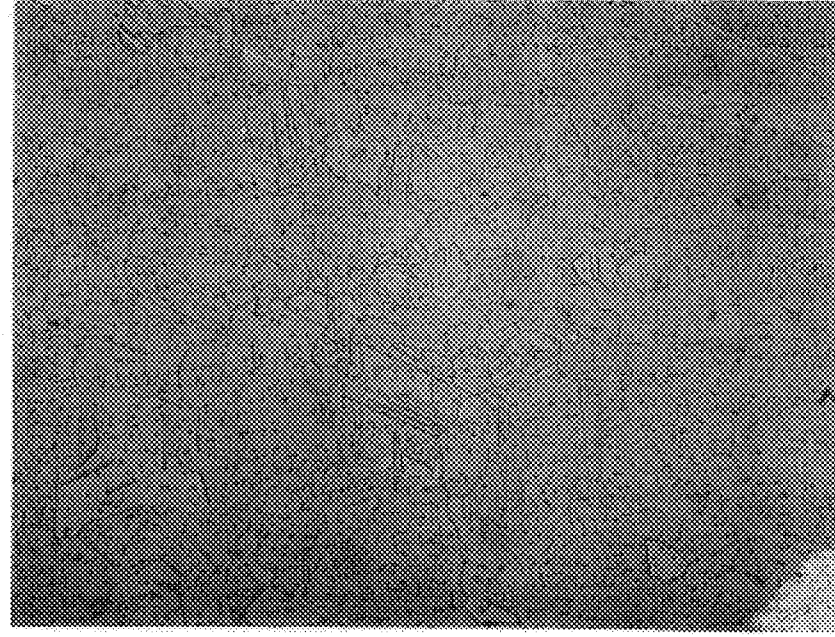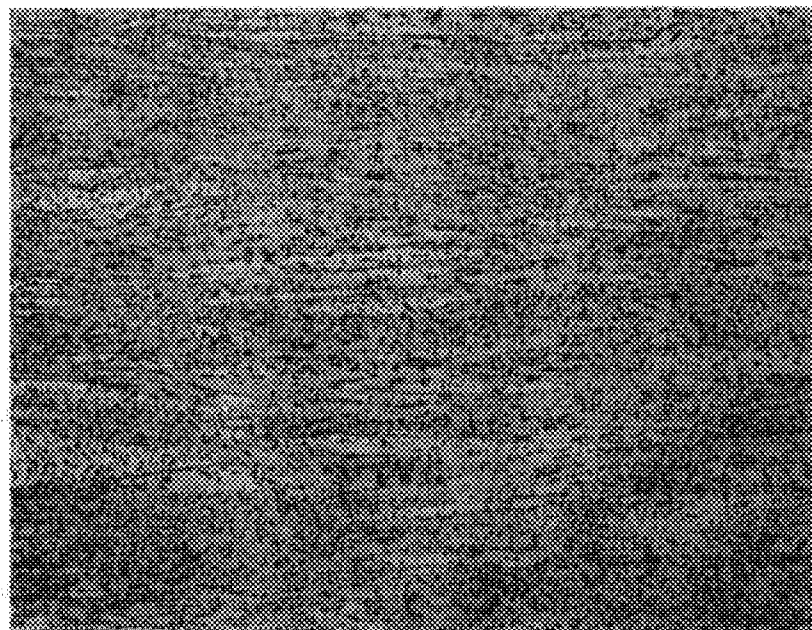
20 μm   As-Extruded
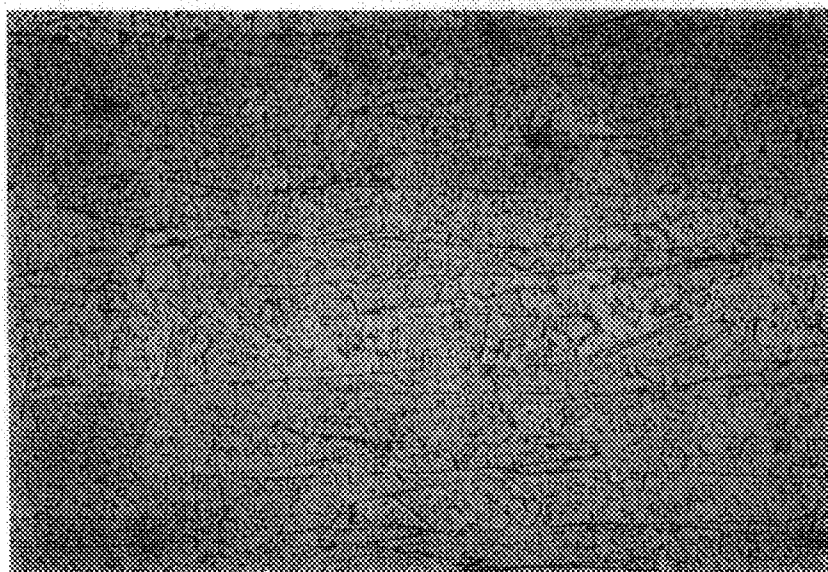
20 μm   Solutioned

20 μm   Solutioned + Cold-Worked + Aged +
Annealed at 650°C (1200°F)

Figure 64. Microstructures of Processed Alloy 1035

Solutioned

20 μm

Solutioned + Cold-Swaged + Aged + Annealed

20 μm

As-Extruded

20 μm
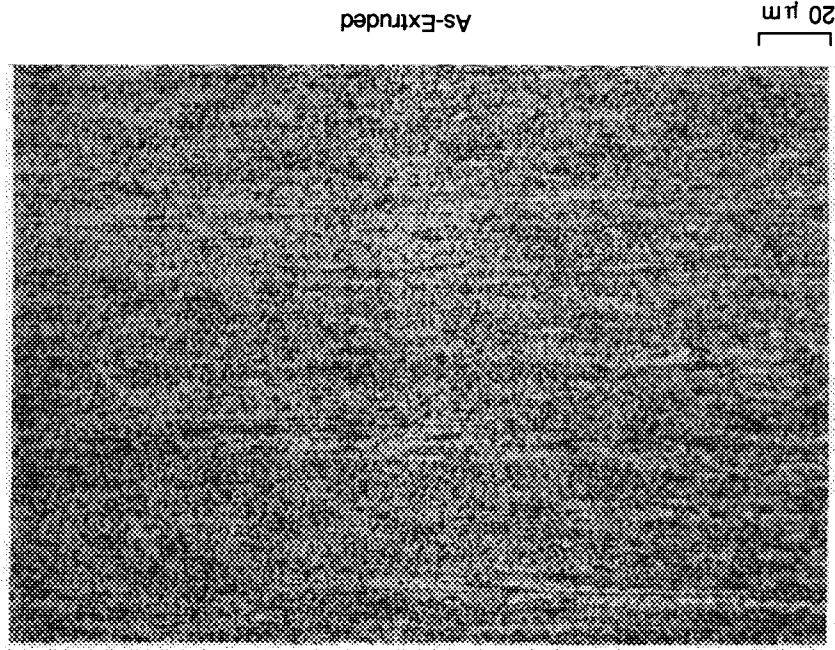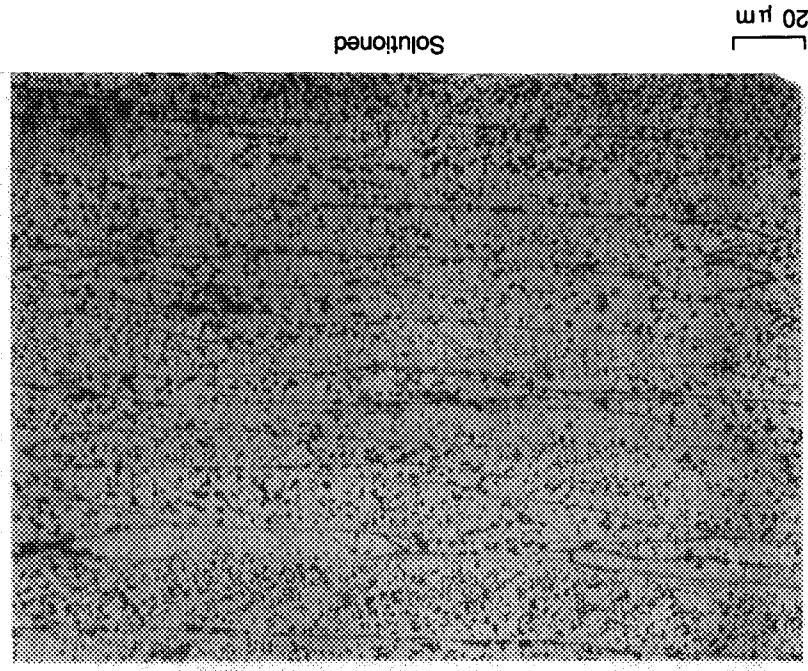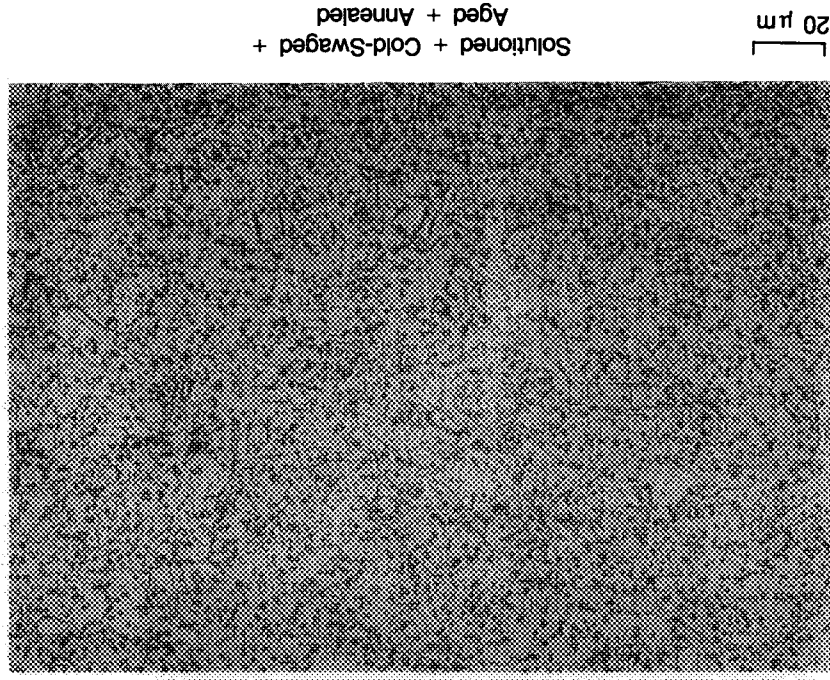
Figure 65. Microstructures of Processed Alloy 1036
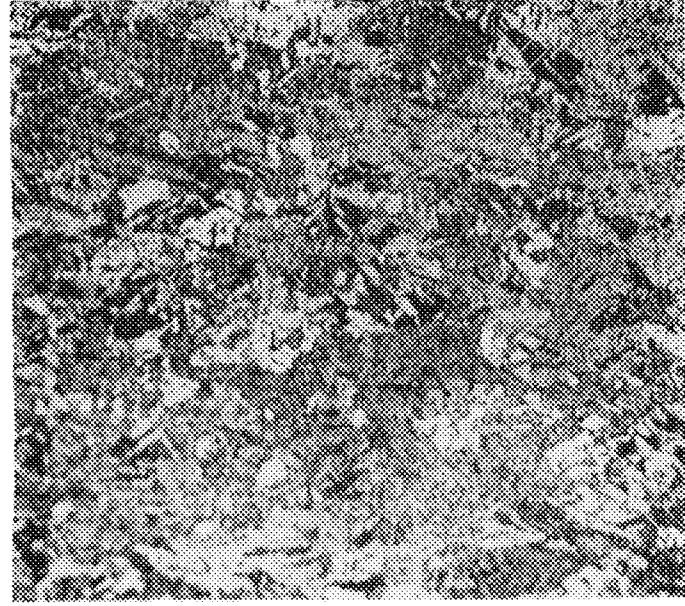
111

112

20 μm

Solutioned

20 μm

Solutioned + Cold-Worked + Aged + Annealed at 650°C (1200°F)

20 μm

As-Extruded

20 μm

Extruded + Cold-Swaged + Annealed at 650°C (1200°F)

113
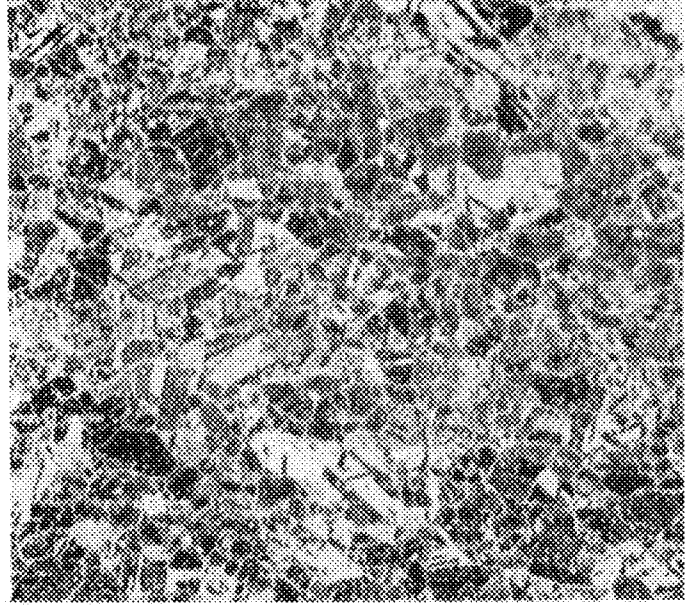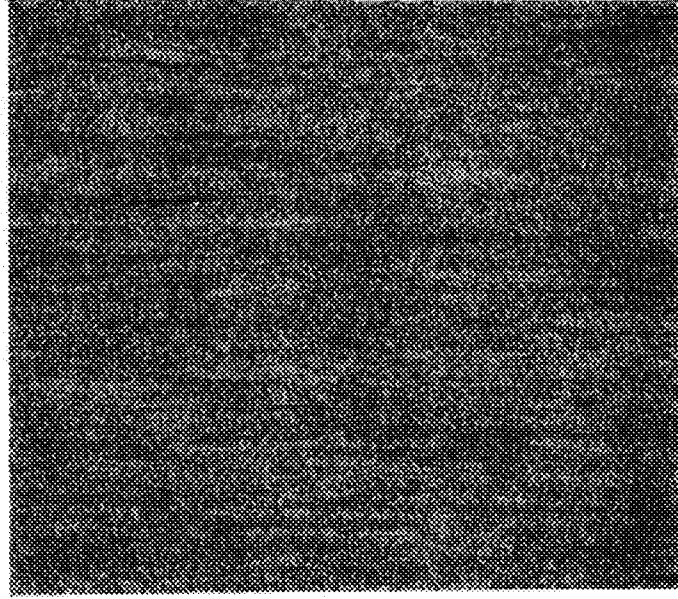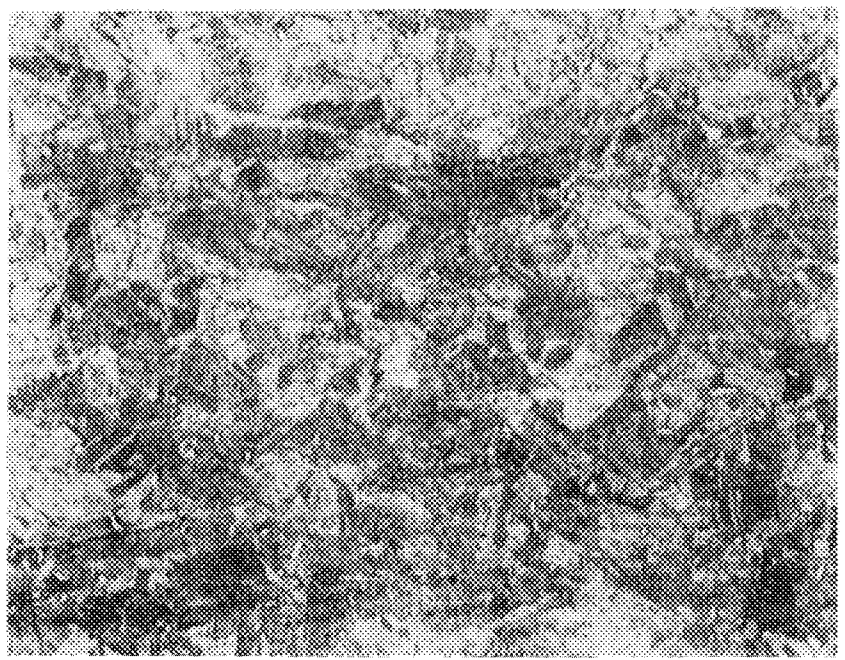
20 µm   Grip   20 µm   Near Fracture

Figure 67. Microstructures of Tensile-Tested Alloy 1038

(12) Alloy 1042: Cu-1.4%Co-0.4%V

Alloy 1042 was originally a wash-heat composition. Since the wash heat (No. 1034) did not produce sufficient powder for use, another run was made (No. 1042). This alloy exhibited no age-hardenability and good properties only in conditions having fibrous (as-extruded type) microstructures.

(a) **As-Extruded Conditions** — The alloy produced an ultra-fine-grained, fibrous, warm-worked microstructure upon extrusion (Figure 68). Annealing at 650°C (1200°F) did not change microstructure or hardness (DPH 100).

(b) **Extruded + Cold-Worked Conditions** — Cold working of the extrusion increased hardness somewhat (DPH 120). Annealing at 650°C (1200°F) softened the cold-worked alloy slightly (DPH 100), but recrystallization was not apparent.

(c) **Solutioned + Aged Conditions** — Solution treatment resulted in a soft (DPH 60) fine-grained (5 μm) recrystallized material (Figure 68). No changes were produced by subsequent aging or anneals.

(d) **Solutioned + Cold-Worked Conditions** — Cold working of solutioned material produced hardening (DPH 100). Subsequent aging at 480°C (900°F) softened (DPH 70) and recrystallized the alloy (Figure 68). Further annealing at 650°C (1200°F) produced no further changes.

Because of the low alloy concentrations used, phases could not be detected or studied by cursory X-ray diffraction.

The Alloy 1042 exhibited highest resistance to softening and was hardest in the as-extruded and extruded + cold-worked conditions. Since both conditions were very similar, the as-extruded form was chosen for preliminary tensile tests. This alloy condition exhibited average strengths at this temperature, (Table 20). Failure was by localized ductile necking. Little microstructural change was observed upon testing.

(13) Alloy 1043: Cu-1.0%Cr-3.0%Ag

Alloy 1043 was formulated to combine the age hardening capabilities of chromium and silver additions. The alloy was found to be quite susceptible to recrystallization, which was not surprising, since NASA-Z, which also contains 3 percent silver, is susceptible to recrystallization. Specific responses to processing are described below.

(a) **As-Extruded Conditions** — Alloy 1043 extruded to a fine, fibrous, warm-worked structure (Figure 69) with a hardness of DPH 130. Annealing at 650°C (1200°F) softened (DPH 90) and recrystallized the material.

(b) **Extruded + Cold-Worked Conditions** — Cold working the extrusion hardened it slightly (DPH 150). Subsequent annealing at 650°C recrystallized and softened the material to DPH 90 (Figure 69).

(c) **Solutioned + Aged Conditions** — Solution treatment recrystallized (Figure 69) and softened (DPH 75) the extrusion. Subsequent aging hardened the alloy to DPH 110, but further annealing softened it back to DPH 75.

114

(d) Solutioned + Cold-Worked Conditions — Cold working increased the hardness of solutioned material to DPH 140. Subsequent aging at 480°C (900°F) produced no increase in hardness. Further annealing at 650°C recrystallized the material and softened it to DPH 75 (Figure 69).

Alloy 1043 was found to age harden in a manner similar to other Cu-Cr-X alloys. It also was found to be most stable in the as-extruded condition. Therefore, preliminary tensile test material conditions were chosen with these histories: as-extruded, and solutioned + cold-worked + aged.

The results (Table 20) did not show much difference in properties between the two conditions. As with the other two silver-containing alloys (NASA-Z/996/999 and 1038), this alloy failed by diffuse necking and cracking. Voids and cracks (at grain boundaries) were observed around the failure. Recrystallization was evident in the neck region, as with other silver-containing alloys.

4. EVALUATION OF NASA-Z

NASA-Z is NASA-LeRC's version of NARloy-Z™. The primary differences between the two alloys are melting source (AMAX for NASA-Z), melting conditions (NASA-Z under argon, NARloy-Z™ in vaccum), and processing (NASA-LeRC oversees processing [forging + heat treat] of NASA-Z).

Five pieces of NASA-Z were supplied for this program. Two were hollow cylindrical forgings, named NASA-Z1 and NASA-Z2. The other three were apparently either pancake sections or billet slice sections, named NASA-Z3, 4, and 5. NASA-Z1 and 2 were originally believed to be equivalent. However, test specimen blanks revealed the presence of very large (> 2mm) grains in NASA-Z2, Figure 70). These were absent from NASA-Z1 (Figure 70). Additional material was requested and supplied as NASA-Z3, 4, and 5. Microstructures of these forgings were similar to NASA-Z1.

The microstructure of NASA-Z typically exhibited 50-100 μm equiaxed grains. The grain boundaries, and to some extent interiors, exhibited coarse primary Cu-Zr-Ag precipitates (Figure 70). Also evident were annealing twins, and intragranular etch attack suggestive of fine precipitates from the aging treatment.

Preliminary tensile tests were done on NASA-Z with the first iteration of powder alloys, at a strain rate of 6 percent per second. The results (Table 20) exhibited very high elongations and relatively low reductions of area. Failure was by grain boundary cracking (Figure 71) explaining the low reductions of area. Extensive grain deformation and recrystallization were observed in the test specimens — indicative of a high level of work hardening. This behavior was observed only in NASA-Z and other silver-containing alloys, and was believed to result from silver solid solution or precipitate hardening (although precipitate hardening was never found to be more than slight).

Also evident in NASA-Z tensile specimens was surface roughening, believed to result from its larger grain size. Fine-grained PM alloys (even Cu-3%Ag-0.5%Zr) did not exhibit such roughening.

115

Figure 68 Microstructures of Processed Alloy 1049
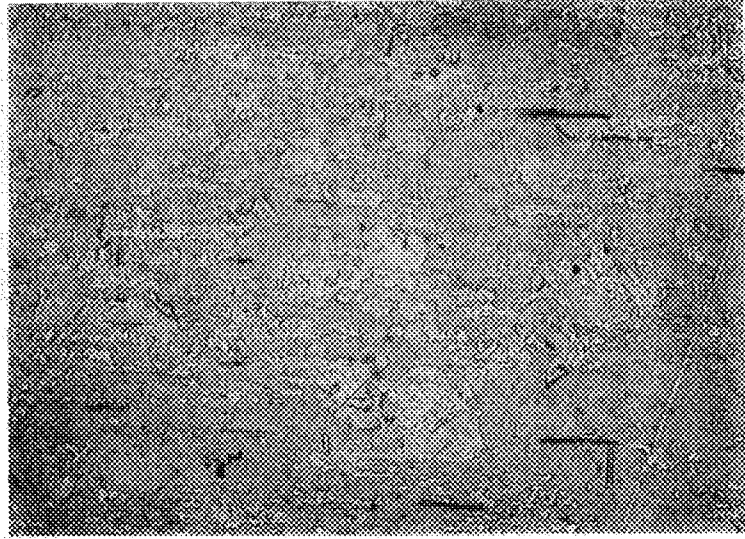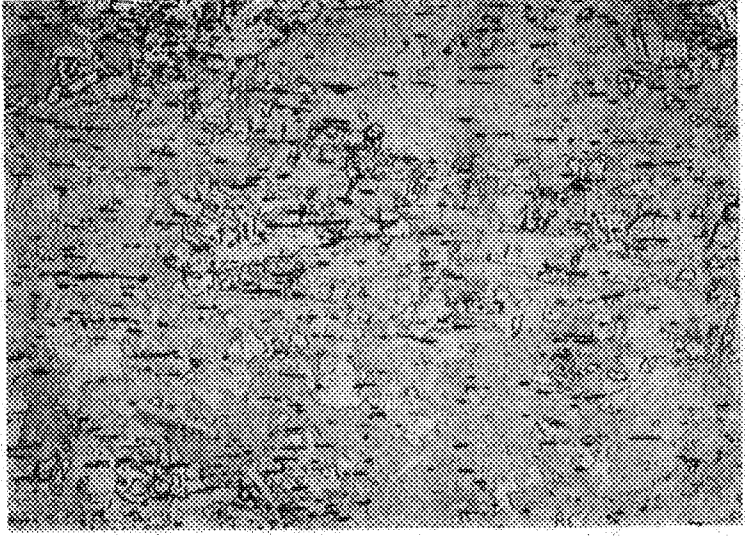
Solutioned + Cold-Worked + Aged
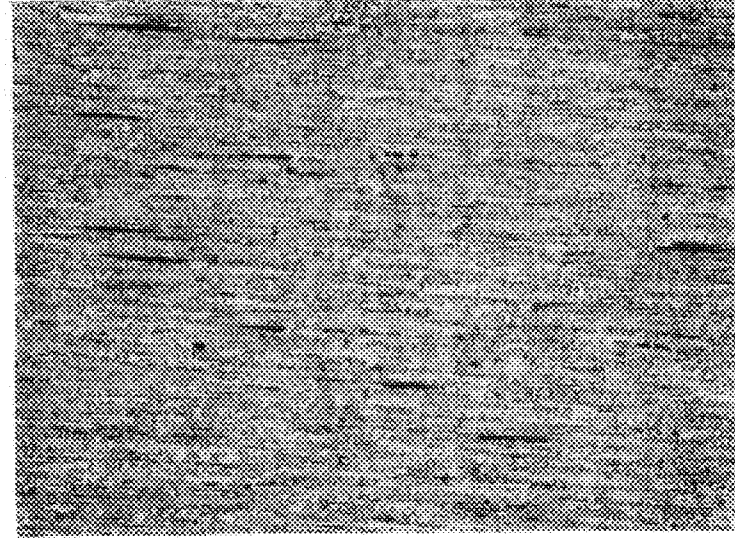
50 μm

Solutioned + Cold-Worked

50 μm
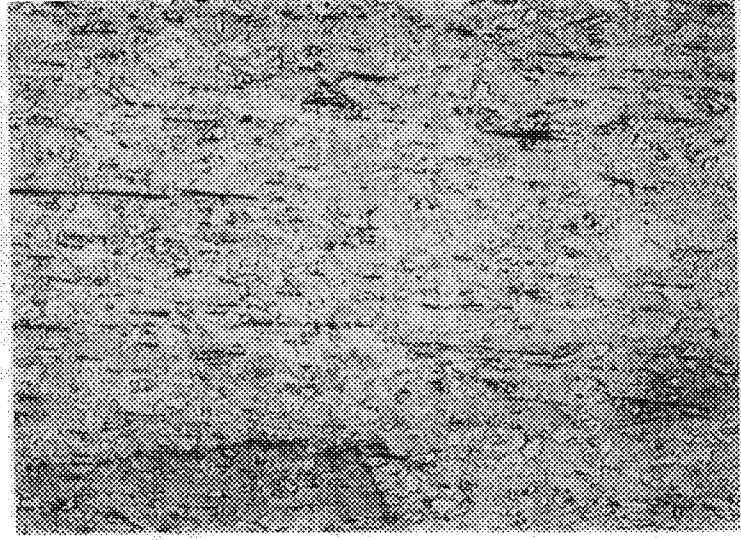
Solutioned

50 μm

As-Extruded

50 μm
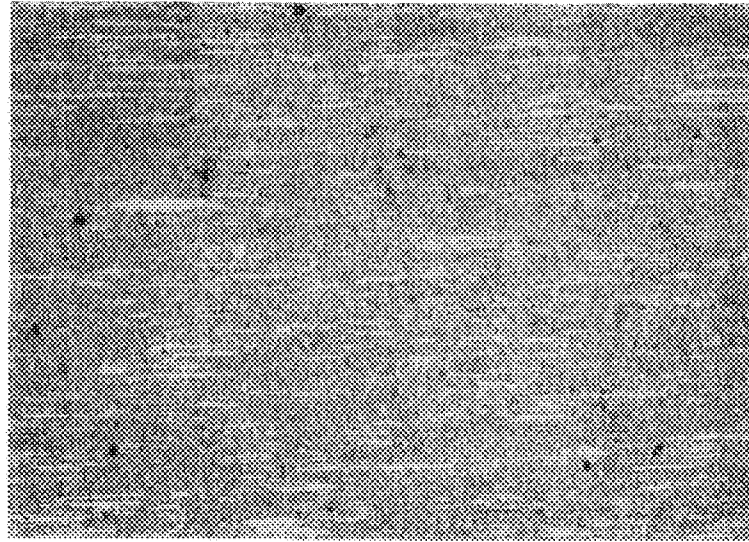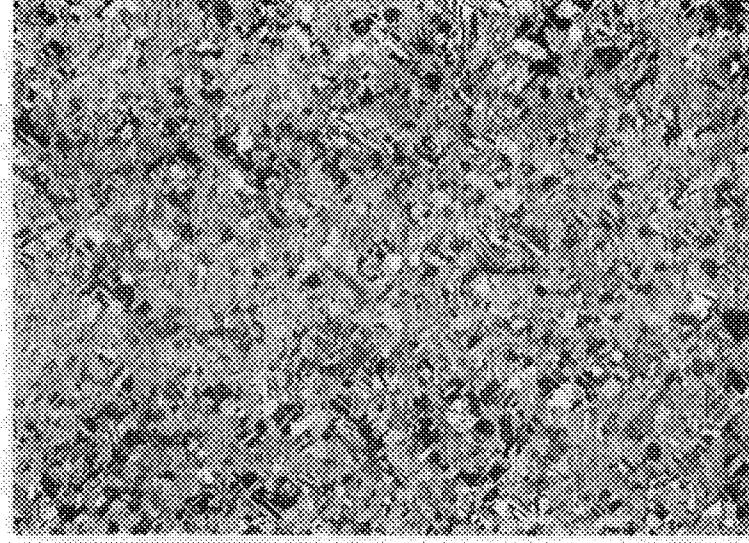
Figure 69. Microstructures of Processed Alloy 1043

117
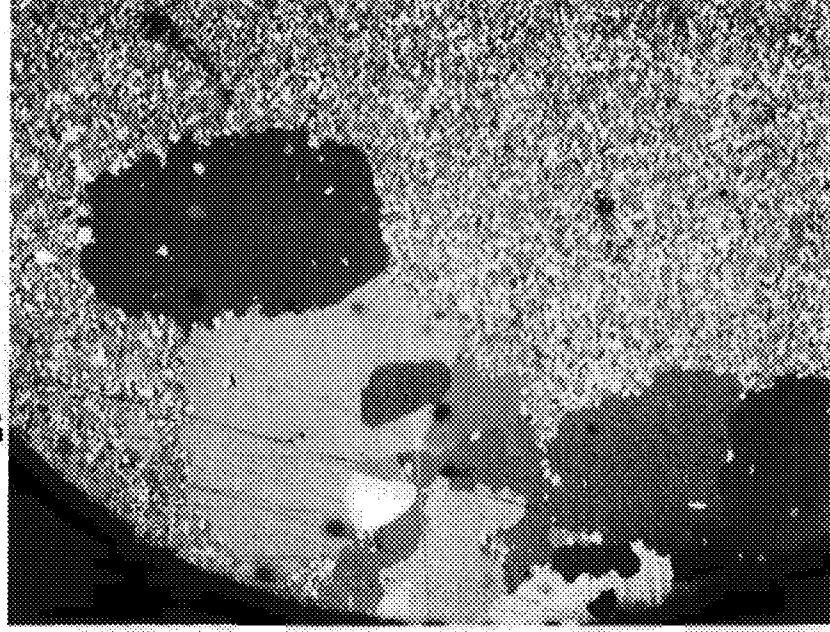
NASA - Z - 2
Abnormal Grains

1 mm
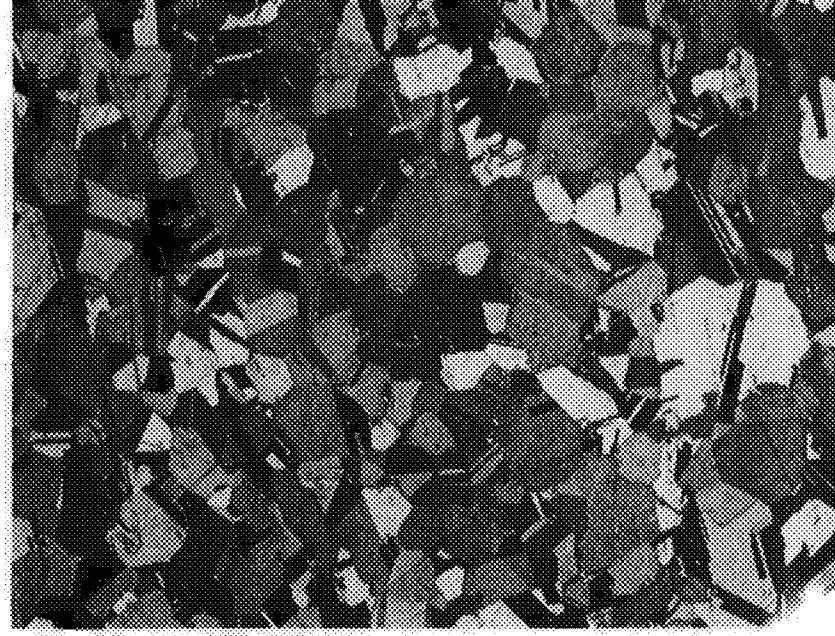
NASA - Z - 1

100 µm

Figure 70. Microstructures of NASA-Z

At Fracture

100 μm
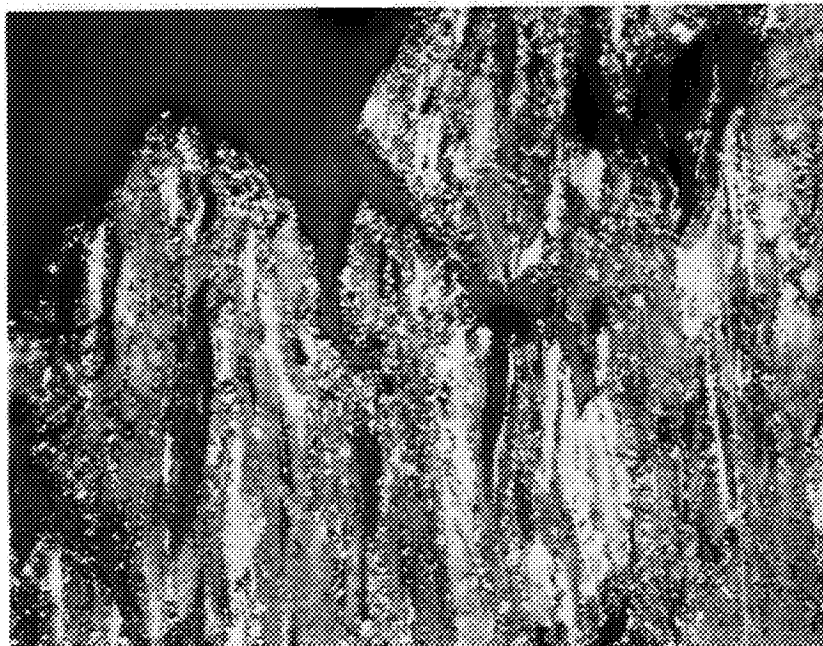
Grip Region

100 μm

Figure 71. Microstructures in NASA-Z Tensile Specimen Tested at 705°C (1300°F)

Tensile tests at 10 percent per second strain rate (for characterization) yielded somewhat different properties (Table 20) but similar structural phenomena. The significantly lower elongation may have resulted from a localized furnace gradient found later.

5. DISCUSSION

Overall, the second-iteration alloys were stronger than the first-iteration alloys. Strengths were also dependent on processing, as evidenced by the twofold increase observed with Alloy 993 when processed differently.

The strongest alloys at 705°C (1300°F) were

993	Cu-1.1%Hf
1032	Cu-0.7%Ti-0.8%Hf
1035	Cu-0.6%Zr-1.0%Cr

Moderately strong alloys were

996/999	Cu-0.5%Zr-3.0%Ag
1036	Cu-0.6%Zr-0.7%Hf
1038	Cu-0.6%Zr-1.0%Cr-3.0%Ag
1042	Cu-1.4%Co-0.4%V
1043	Cu-1.0%Cr-3.0%Ag

Weakest were

995	Cu-0.6%Zr
997	Cr-0.55Zr-0.05%B

Those alloys based on chromium, hafnium, zirconium, and silver additions performed best. Therefore, novel superior systems were not found. The novel systems, such as copper-cobalt-vanadium, borides, and copper-cobalt-chromiun, were inferior to more conventional systems. One system, $Cu + ZrB_2$, was completely unsuccessful.

NASA-Z exhibited properties near the midpoint of the PM alloy property range. The most significant difference between it and the PM alloys was its large grain size. This appeared to promote the surface roughening observed on tested NASA-Z tensile specimens and absent on other alloy specimens.

Processing was instrumental in demonstrating equivalence between conventional NASA-Z and powder metallurgy NASA-Z (Alloys 996/999). Early tests of powder metallurgy NASA-Z showed it to be weaker, but more ductile, than conventional NASA-Z. Additional processing work resulted in materials (999 HW and 999 HWSA) with strengths roughly equivalent to or higher than those of conventional NASA-Z.

Microstructures of the alloys were all fairly similar. Those that did not contain Ag extruded to warm-worked structures and had a greater tendency to stay that way. Addition of silver tended to increase susceptibility to recrystalllization during extrusion, sometimes during processing, and during testing, possibly by increasing the strain hardening coefficient.

Those alloys not containing silver failed by smooth localized necking (to nothing). Silver-containing alloys failed by diffuse necking and grain boundary cracking. The diffuse necking implied a greater degree of strain-hardening during testing, while the grain boundary cracking

indicated a grain boundary weakness that may have been related to precipitate-free zones (seen in NASA-Z) or dynamic recrystallization at grain boundaries (seen in NASA-Z tensile tests).

The dispersions formed in the powder metallurgy alloys were not as fine as were desired for effective strengthening. About an order of magnitude too coarse, they resulted from the instabilities of the compounds used. However, attempts (during screening) to find more stable dispersions were unsuccessful. By the start of the second powder iteration, extremely fine dispersions were no longer expected from the available systems. However, benefits from the reduced segregation produced by rapid solidification were still expected. Such benefits would be most evident in fatigue testing (covered in a later section) and in hardware manufacture.

SECTION V
ALLOY CHARACTERIZATION

After evaluation, several alloys were selected for characterization, along with NASA-Z. Characterization consisted of thermal conductivity testing, tensile testing, creep testing, and low-cycle fatigue (LCF) testing at up to 705°C (1300°F) which was the maximum anticipated Orbital Transfer Vehicle (OTV) chamber temperature.

These properties were identified by preliminary design studies as having the greatest effect on thrust chamber performance and life. Thermal conductivity testing was tailored to produce thermal conductivities over the entire range of room temperature to 705°C. Tensile testing was performed at 540°C (1000°F) and 705°C at a high strain rate to simulate the loading experienced in thrust chamber use. Creep testing was conducted at 705°C at the alloy yield stress to produce post-yield creep rates to predict thrust chamber hold behavior. Low-cycle fatigue testing was performed at 705°C under strain control with a simple, fully reserved no-hold cycle (a more-sophisticated test was not defined). LCF strain rates were high to simulate thrust chamber conditions. LCF strain ranges ran from 0.75 percent to 3 percent. All tests were conducted in a vacuum or in argon to prevent oxidation.

Four developmental alloys were chosen for characterization, along with NASA-Z. These were Alloys 993, 995, 1032, and 1035. Alloys 993, 1032, and 1035 were chosen for their high strengths. Alloy 995 was chosen because of its similarity to Amzirc, which has demonstrated better LCF performance than NASA-Z. As characterization progressed, Alloy 1032 was found to have very low thermal conductivities and was dropped from the characterization effort. Alloy 996, processed to a grain size equivalent to that of NASA-Z, was LCF tested to determine whether it could be processed to yield properties equivalent to its conventionally-processed counterpart, NASA-Z (this would allow the fabrication of chambers from powder metallurgy NASA-Z).

The alloys were characterized in the following conditions:

993 Cu-1.1%Hf	Hot-worked + solutioned + cold-worked (30%) + aged
995 Cu-0.6%Zr	As-extruded
996 Cu-0.5%Zr-3%Ag	Hot-worked + solutioned + aged
1032 Cu-0.7%Ti-1.1%Hf	Solutioned + cold-worked + aged
1035 Cu-0.6%Zr-1.0%Cr	As-extruded
NASA-Z	As-supplied by NASA LeRC

Conditions were chosen based on preliminary tensile tests (last section). Alloy 993 was processed to the type of condition shown to produce highest strengths, but cold-worked less to increase ductility somewhat. Alloy 995 was tested as-extruded, because that was found earlier to be its strongest condition. Alloy 996 was hot-worked + solutioned + aged to produce a condition that was microstructurally similar to NASA-Z. Alloy 1032 was solutioned + cold-worked + aged because that condition exhibited significantly higher tensile strengths and elongations than the as-extruded condition. Alloy 1035 was tested as-extruded, because this condition exhibited significantly higher ductilities than the slightly stronger extruded + cold-worked condition.

1. RESULTS OF CHARACTERIZATION TESTING

a. Thermal Conductivity

Thermal conductivity was measured from room temperature to 705°C (1300°F) by thermal diffusivity measurements at the Purdue Thermophysical Properties Laboratories. The diffusivity

method was selected because it allowed the use of a relatively small specimen. Purdue was selected because of its experience in measuring both specific heat and thermal diffusivity, which are required to calculate thermal conductivity.

Prior to testing, all specimens were annealed (before machining) at 705°C (1300°F) for one hour followed by air cooling. This was done to simulate prior exposure to the 705°C use temperature.

The results for Alloy 993, 995, 1032, 1035, and NASA-Z are shown in Figure 72 (numerical results are tabulated in Appendix A). The results are computed from Purdue diffusivity and specific heat data, and Pratt & Whitney (P&W) density measurements (995 and NASA-Z density measurements were temperature-corrected using data from (37)).

Thermal conductivity results for Alloys 995 and NASA-Z were in reasonable agreement with those of NARloy-Z™ and Amzirc obtained from the literature. Alloy 995 had the highest conductivities, while Alloy 993 had conductivities about 5 percent lower than those of NASA-Z. Alloy 1035 was essentially equivalent to NASA-Z. However, Alloy 1032, containing titanium, exhibited such low conductivities that it was dropped from the characterization effort.

b. Tensile Results

The selected alloys were tensile tested at 540°C (1000°F) and 705°C (1300°F) in argon, using a strain rate of 10 percent per second to approximate thrust chamber conditions. Tensile strength, 0.2 percent yield strength, elongation, and reduction in area were reported.

Alloys 993, 995, 1035, and NASA-Z were tested. Complete results are tabulated in Table 20. At 705°C, Alloy 1035 exhibited the highest strengths. Far lower in strength were NASA-Z and Alloy 993, then Alloy 995. NASA-Z exhibited the highest elongation but lowest reduction in area. At 540°C, Alloy 993 was strongest, closely followed by Alloy 1035, and then NASA-Z and Alloy 995. The powder alloys again exhibited significantly higher reductions in areas than NASA-Z. Strength variations were observed with Alloy 993 at 540°C and attributed to grain size variations, finer being stronger. Temperature gradients later found in the retort may have affected strengths and elongations somewhat, but should have done so consistently.

Additional tensile tests were performed on Alloys 995 and NASA-Z at low strain rates to produce proportional limits for use in specifying creep tests. The results (Table 21) showed that these materials were very strain-rate-sensitive at 705°C. Tensile strengths dropped by up to 37 percent with the decrease in strain rate.

c. Creep Test Results

Creep rates were measured at 705°C (1300°F), at the proportional limits of the alloys. This was intended to measure creep rates at the yield points, so as to determine creep resistance in the hold portion of the chamber cycle. Tensile tests were carried out at a stain rate of 0.0005 per second to determine the proportional limits, and creep tests were conducted at the respective proportional limit stresses at 705°C. Creep test loads were applied at a strain rate of 0.1 per second.

123
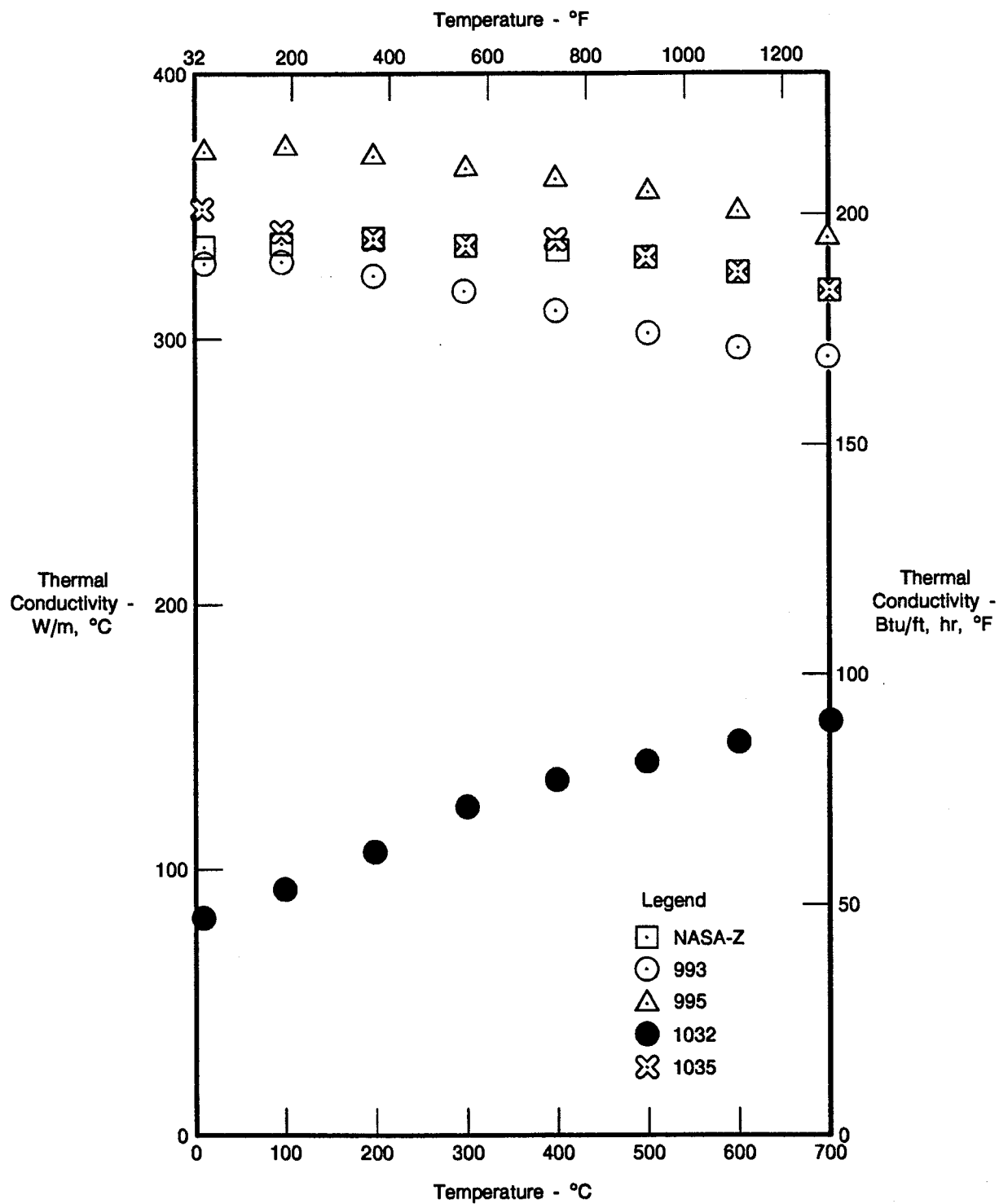
Figure 72.   *Thermal Conductivities of Copper Alloys Annealed at 705°C (1300°F) for 1 Hour Prior to Test*

TABLE 21. — ALLOY CHARACTERIZATION TENSILE PROPERTIES (AVERAGED)

Alloy – Condition	Yield Strength MPa	Yield Strength ksi	Tensile Strength MPa	Tensile Strength ksi	Elongation in 4D (%)	Reduction in Area (%)	Number of Tests
705°C (1300°F) – 0.1/sec							
NASA-Z1	84	12.2	111	16.1	71	66	3
993 – CWCAR	87	12.6	98	14.2	21	96	2
995 – AE	77	11.2	90	13.1	46	98	2
1035 – AE	92	13.3	166	24.1	26	89	3
540°C (1000°F) – 0.1/sec							
NASA-Z1	125	18.1	186	27.0	37	62	3
993 – CWCAR	188	27.3	228	33.1	20	87	5
995 – AE	121	17.6	157	22.8	38	98	2
1035 – AE	171	24.8	219	31.8	28	88	2
705°C (1300°F) – 0.0005/sec							
NASA-Z1	65	9.4	70	10.2	21	63	1
995 – AE	60	8.7	65	9.4	23	95	1

The results are shown in Figure 73. Even though tested at a lower stress, Alloy 995 exhibited higher creep rates and shorter lives than NASA-Z. There was a significant amount of scatter in the results, probably resulting from the difficulties encountered in loading the sample at such high strain rates and stopping quickly at the test stress.
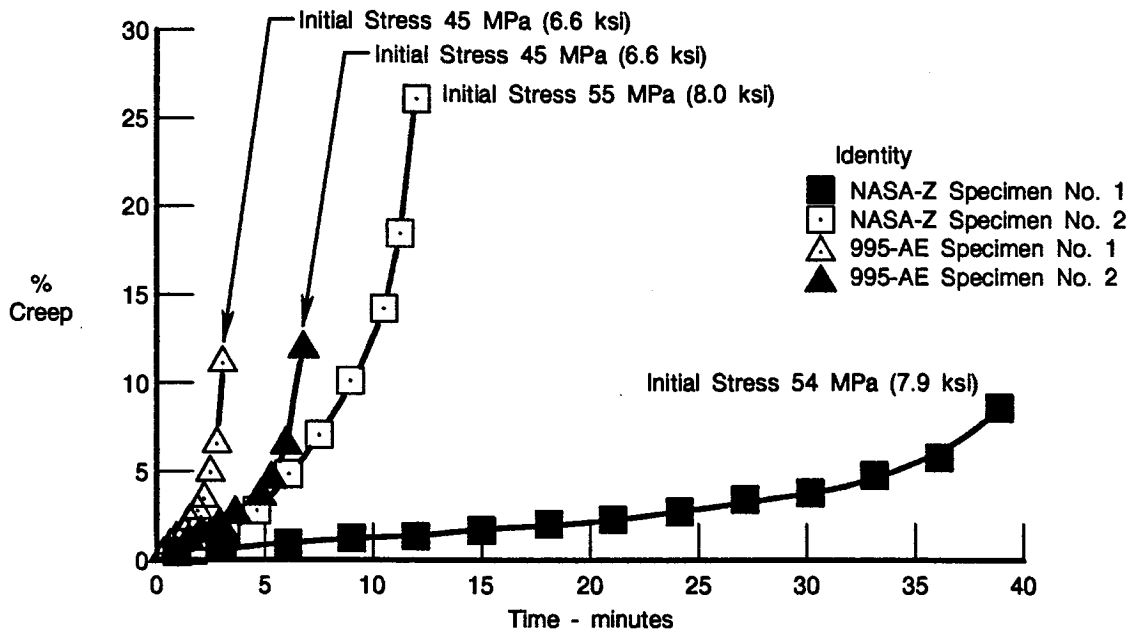
Figure 73. High-Stress Creep Results at 705°C (1300°F) for NASA-Z and Alloy 995 (Loaded at ε = 0.1/Second)

Additional creep testing was not performed. Design studies concluded that creep rate had only a slight effect on cyclic strain range. In light of this conclusion and the difficulty of performing these tests, they were discontinued.

d. Low-Cycle Fatigue Testing

Low-cycle fatigue testing of Alloys 993, 995, 1035, and NASA-Z was conducted as part of the characterization effort. Alloy 996 was also tested to allow comparison of its properties with those of its counterpart, NASA-Z. Alloy 1032 was tested as well, as part of the specimen configuration trials.

Low-cycle fatigue testing was performed at 705°C (1300°F) under strain control in a 210 kPa (30-psig) inert argon atmosphere. Tests were preformed using fully reversed cycles (no holds) at a frequency of 0.5 Hz.

Because copper alloys had not been LCF tested previously at P&W, some development work was necessary before valid tests could be performed. This work included test machine selection and modification, specimen design and revision, and trial testing.

The LCF tests were performed in a P&W high-pressure hydrogen LCF machine because this device allowed testing of a high-conductivity material under strain control in a controlled atmosphere. This was the most appropriate test rig available at P&W. As trial testing progressed, modifications to the linear variable displacement transformer (LVDT) extensometer were needed, adding cooling to alleviate the overheating experienced in early testing (attributed to the use of a low-pressure argon atmosphere instead of high-pressure hydrogen).

Specimen configurations had to be established and modified also, to accommodate the high plastic strains encountered in this testing effort. Initially, the specimen was configured as shown in Figure 22. The cylinderical gage section allowed simple calculation of strain, while the collars allowed the solid attachment of the extensometry needed for the high strain ranges and strain rates planned for this testing effort. As trials progressed, a new specimen evolved (Figure 22) with smaller-diameter collars to avoid collar deformation, a shorter gage length to minimize buckling, and a slightly increased shoulder diameter to avoid failure outside the collar.

Strain rates of 0.1/second were initially planned. However, testing was actually conducted at strain rates produced by a cyclic frequency of 0.5 Hz: 0.0075 to 0.03/second (depending upon strain range), as this was the fastest the LCF rig could be run in a precisely controlled manner.

Trial tests established a failure criterion somewhat more sophisticated than complete fracture. Since the specimen could not be observed, fracture could not be seen when it occurred. Specimens removed from initial trials were destroyed because testing had continued for several additional cycles after fracture. In addition, the extensometry could not accommodate the collisions of the post-fracture specimen halves. It had been observed during testing that the cyclic stress range dropped due to softening at a rate that was linear when plotted logarithmically. As failure began, the stress dropped at an increasing, nonlinear rate. Concurrently, cusping appeared on the stress-strain hysteresis loops, at stress ranges generally corresponding to 20 percent deviations from the linear relationship. Since cusping generally indicates the presence of cracking in the specimen, failure (N_f) was defined as the point at which at 20 percent deviation from the linear (log) cyclic stress-versus-cycles relationship occurred. All values of N_f were calculated in this manner. Cycling of the specimens was terminated after N_f was reached and before complete fracture occurred, avoiding damage to the specimens and the extensometry.

Results of the LCF testing are listed in Table 22 and plotted as strain range versus life in Figure 74. Alloy 993 exhibited the longest life, followed by Alloy 995. NASA-Z exhibited significantly shorter LCF life, about 25 percent of Alloy 993 at 3 percent strain range. Alloy 996 fatigue life was close to that of NASA-Z. Alloy 1035 exhibited the shortest fatigue life. Presentation of the data as plastic strain range versus life, Figure 75, looked essentially the same as total strain range versus life.

TABLE 22. — COPPER STRAIN CONTROL TEST RESULTS

Material	Specimen Number	Strain Range (%)	Initial Stress Range MPa	Initial Stress Range ksi	Nf/2 Stress Range MPa	Nf/2 Stress Range ksi	Cycles to Failure	Specimen Configuration
993	1	1.5	145	21	83	12	988	16150
993	2	1.5	131	19	83	12	1100	16150
995	3B	3.0	138	20	103	15	260	16150
995	3C	3.0	145	21	96	14	369	16150
995	3D	0.75	145	21	83	12	4200	16150
995	3E	1.5	145	21	90	13	800	16150
1032	32A	1.5	220	32	138	20	920	17710-A
1032	32B	1.5	234	34	138	20	760	17710-A
1032	32C	3.0	241	35	158	23	350	17710-A
995	3J	1.5	158	23	96	14	1705	17710-A
995	3K	3.0	138	20	103	15	475	17710-A
993	93A	1.5	186	27	96	14	1420	17710-A
993	93B	3.0	152	22	103	15	615	17710-A
NASA-Z4	Z4A	1.5	165	24	158	23	485	17710-A
NASA-Z4	Z4B	3.0	186	27	179	26	142	17710-A
NASA-Z5	Z5A	1.5	172	25	172	25	250	17710-A
NASA-Z5	Z5B	3.0	207	30	213	31	198	17710-A
1035	35A	1.5	317	46	262	38	210	17710-A
1035	35B	1.5	310	45	255	37	200	17710-A
1035	35C	3.0	296	43	255	37	102	17710-A
996	96A	1.5	186	27	193	28	245	17710-A
996	96B	1.5	179	26	152	22	410	17710-A
996	96C	3.0	200	29	214	31	112	17710-A

(All tests 705°C (1300°F) $\bar{e}_m$ = 0, cyclic freq. = 0.5 Hz, 210 kPa (30 psi) Argon environment)
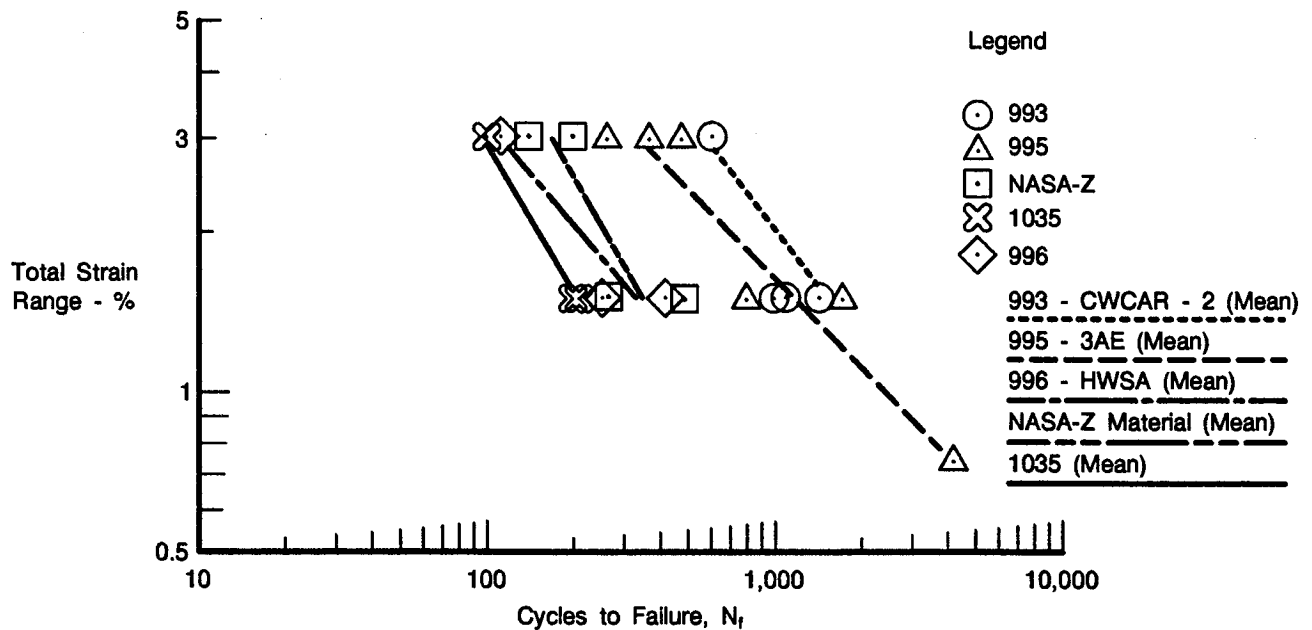
Figure 74. Strain Control Fatigue Testing of RSR Copper in Argon, Using Collared Strain Control Specimen, 210 kPa Argon Environment at 705°C (1300°F); Mean Strain = 0, Cyclic Frequency = 0.5 Hz

127

Examination of the LCF specimens (shown in Figure 76) revealed that Alloys 993 and 995 failed by formation of gross shear bands and yield instabilities along those shear zones. On the other hand, NASA-Z failed by formation of numerous cracks. These failures resembled those of the tensile tests, where the 993, 995, and other silver-free alloys failed by localized, very ductile necking, whereas the NASA-Z and other silver-containing alloys failed by uniform necking and cracking (usually along grain boundaries).
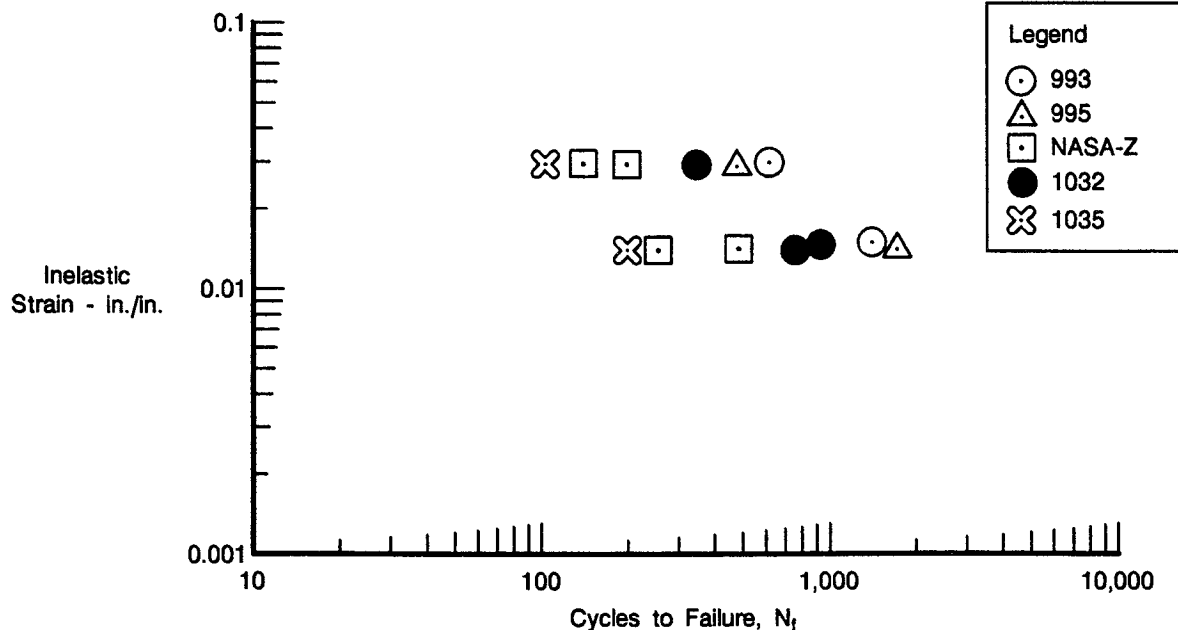
Figure 75. Inelastic Strain at NF/2 Versus Cycles to Failure for Copper Alloys (Various Cycles; True Inelastic Strain)

Cyclic stress ranges are plotted in Figures 77a and 77b, and show that NASA-Z was cyclically stable while Alloys 993, 995, and 1035 all softened somewhat. Evident from this data was the tendency for the alloys that exhibited lower cyclic stress ranges to exhibit longer lives. Alloy 1035, which was strongest in tensile testing and exhibited the highest cyclic stress ranges, exhibited the shortest cyclic life. Alloy 993 softened during testing to reach one of the lowest cyclic stress ranges and exhibited the longest life.

This phenomenon was evaluated through the analyses of hysteretic damage. When the tensile hysteretic energy at $N_f/2$ (area in the tensile portion of the cyclic stress-strain hysteresis loop) was plotted versus specimen life (Figure 78) the trend for life to increase with decreasing hysteretic energy was very obvious. This seemed to suggest that life would increase even further with softer materials. However, that was not the case in earlier tests at Mar-Test, where oxygen-free, high-conductivity (OFHC) copper exhibited significantly lower lives than NARloy-Z™ and Amzirc (3, 4, 6).

128
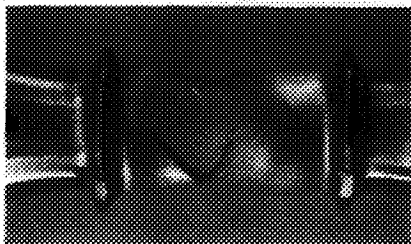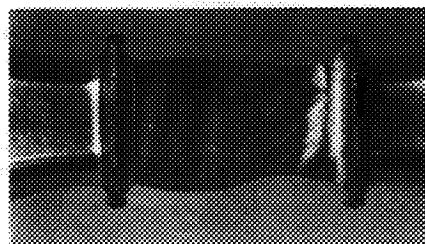
RSR 993, 1.5% $\Delta\varepsilon$, N_f = 1420

RSR 995, 1.5% $\Delta\varepsilon$, N_f = 1705
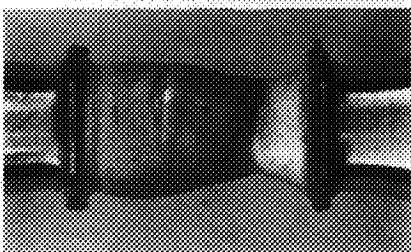
RSR 993, 3.0% $\Delta\varepsilon$, N_f = 616
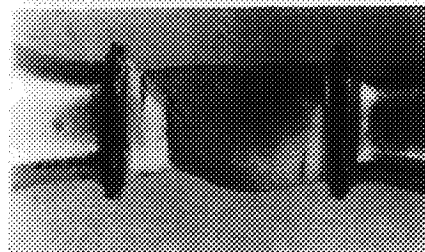
RSR 995, 3.0% $\Delta\varepsilon$, N_f = 475
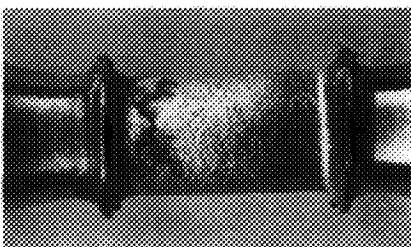
NASA-Z4, 1.5% $\Delta\varepsilon$, N_f = 485

NASA-Z5, 1.5% $\Delta\varepsilon$, N_f = 250
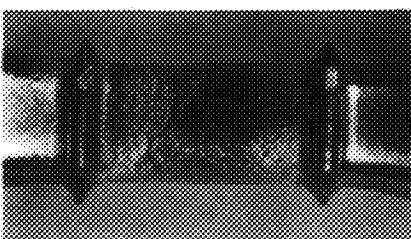
NASA-Z4, 3.0% $\Delta\varepsilon$, N_f = 142
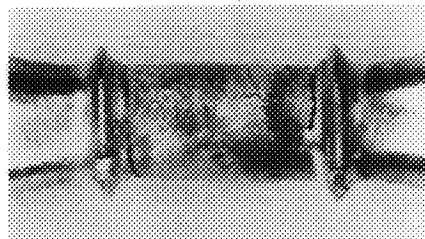
NASA-Z5, 3.0% $\Delta\varepsilon$, N_f = 198

Figure 76. Deformation Characteristics of RSR 993, RSR 995, and NASA-Z

129
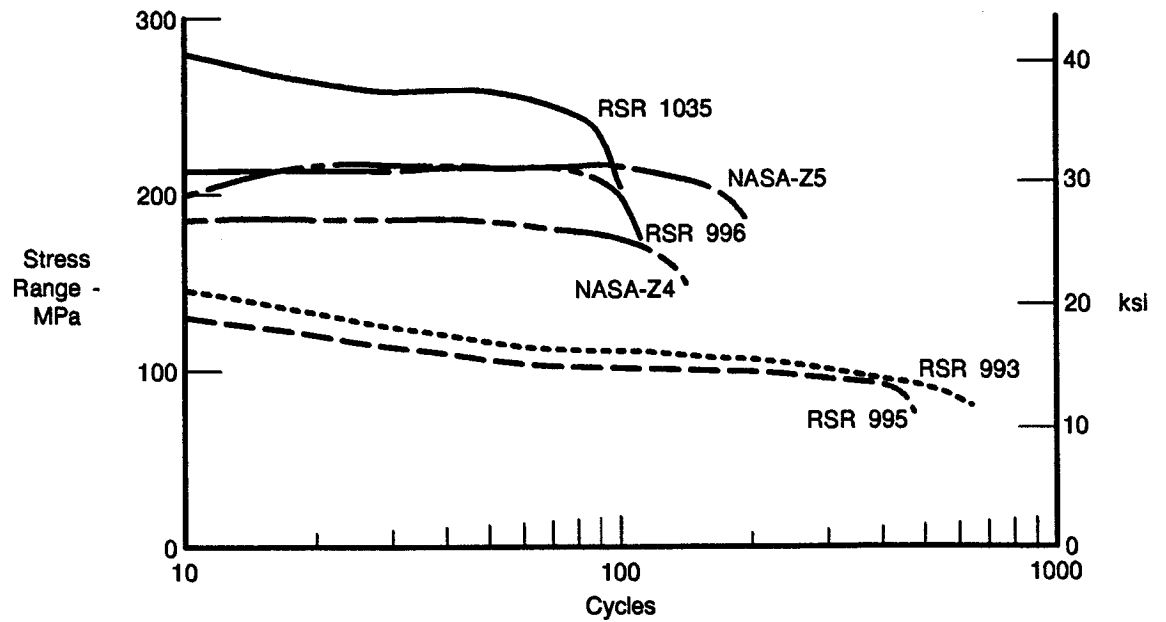
Figure 77a. Cyclic Stress Range Effects on LCF Life (Cyclic Stress Ranges for LCF Test at $\triangle \varepsilon_t = 3.0\%$)
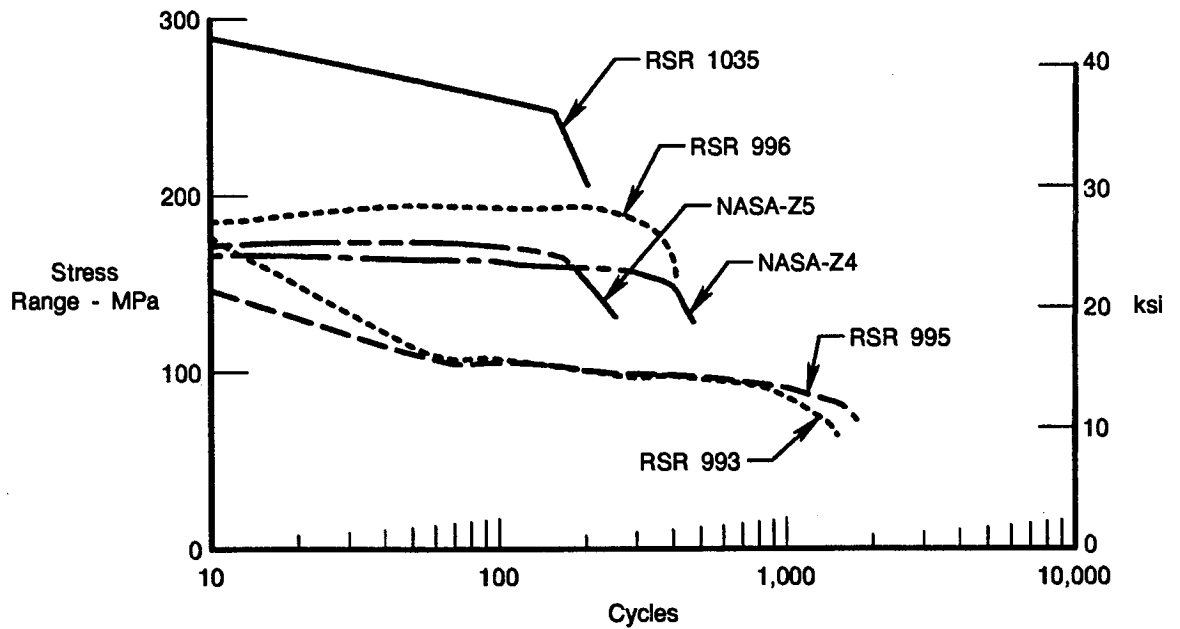
Figure 77b. Cyclic Stress Range Effects on LCF Life (Cyclic Stress Ranges for LCF Testing at $\triangle \varepsilon_t = 1.5\%$)

130
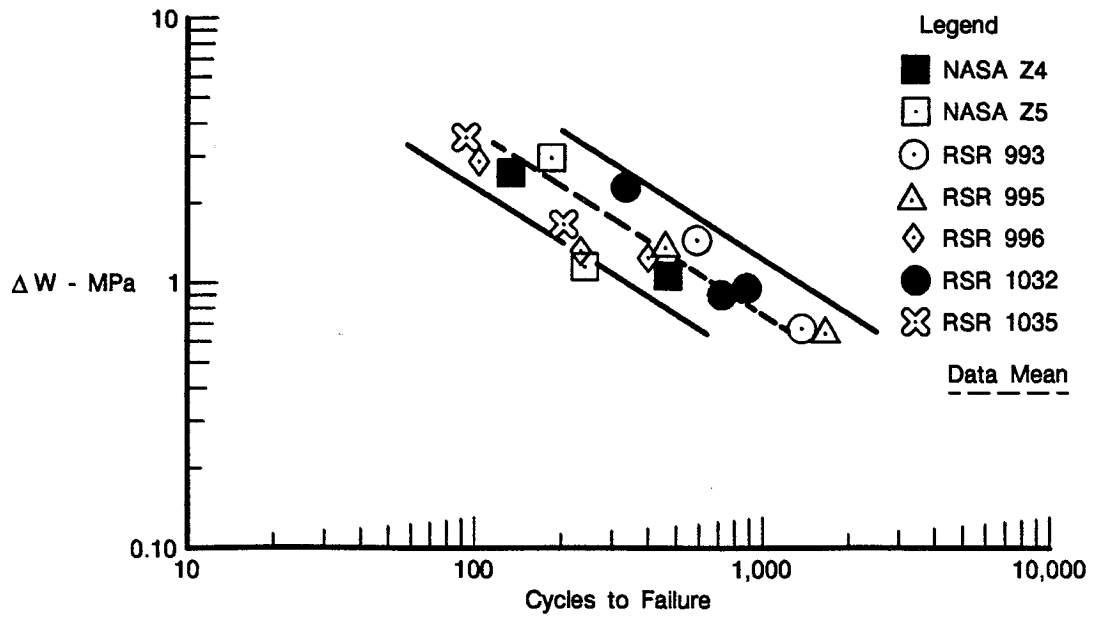
Figure 78. *Hysteretic Energy Damage Function Versus Cycles to Failure for Copper Alloys (Various Cycles; True Inelastic Strain)*

Based on LCF testing, Alloy 993 exhibited the greatest potential for use in a long-life reuseable thrust chamber. Alloy 995 was almost as good. Alloy 996, which was a powder metallurgy version of NASA-Z, had LCF life about as good as that of NASA-Z, demonstrating that NASA-Z composition thrust chambers could be made via powder metallurgy with no life debit.

131

SECTION VI
CONCLUSIONS

The goal of this program was to develop rapidly solidified powder metallurgy (PM) high-conductivity copper alloys that would last longer than NASA-Z in thrust chamber applications. The intention was to use rapid solidification to introduce highly stable dispersions to strengthen and stabilize copper at temperatures up to 705°C (1300°F). Highly stable phases such as borides, silicides, and high-temperature intermetallics were studied, as well as more conventional, less stable copper-based and elemental dispersoids. The high-stability phases were found to be either unprocessable in copper or of no more benefit than zirconium additions. The more conventional phases based on zirconium, chromium, hafnium, and silver additions were the most beneficial.

Based on the best available test, low-cycle fatigue (LCF) Alloy 993 (Cu-1.1%Hf) exhibited the best potential as an improvement over NASA-Z, with 705°C LCF lives four times those of NASA-Z at a 3 percent strain range. Alloy 993 also exhibited higher strengths than NASA-Z, with thermal conductivities only slightly less than those of NASA-Z.

Alloy 995 (Cu-0.6%Zr) also exhibited LCF lives greater than those of NASZ-Z, along with better thermal conductivities, but with slight strength debits.

Alloy 1035 (Cu-0.6%Zr-1.0% Cr), which exhibited very high strengths, exhibited low LCF lives at 705°C (slightly lower than NASA-Z). Thermal conductivities were equivalent to those of NASA-Z.

Finally, LCF tests showed that powder metallurgy NASA-Z (Alloy 996) could be equivalent to cast + wrought NASA-Z, so with some development work, NASA-Z chambers could be made via powder with no life debits.

Thus, the result of this program was, among other things, the identification of rapidly solidified Cu-1.1%Hf as an alloy showing great potential for use in reuseable, long-life thrust chambers. To bring this alloy into use, concentration effects need to be determined, processing work needs to be done to better control microstructure, some LCF testing should be done on other processed conditions, and more sophisticated cyclic tests should be developed and performed.

Other tasks suggested by this program are:

- Development of more-valid cyclic tests.

- More cyclic testing of other conditions of Alloy 995 to see if its life can be improved, as well as testing of Amzirc for comparison.

- More work with the copper-zirconium-chromium and copper-chromium-based systems to find a way to exploit the strength levels obtainable with chromium while improving LCF resistance.

- More study to develop a better understanding of silver effects, so as to support further alloy development and to support present and future use of NASA-Z.

- More work aimed at introduction of stable dispersoids into copper, either through rapid solidification, internal oxidation, coreduction, or mechanical alloying.

132

APPENDIX A
THERMAL CONDUCTIVITY
AND
TENSILE TEST RESULTS

TABLE 23. — THERMAL CONDUCTIVITY RESULTS

Alloy	Units**	22°C (73°F)	100°C (212°F)	200°C (392°F)	300°C (572°F)	400°C (752°F)	500°C (932°F)	600°C (1112°F)	700°C (1292°F)
NASA-Z	Watts	334.8	335.3	336.1	333.5	332.8	328.7	324.2	317.6
	BTU	193.5	193.8	194.3	192.8	192.4	190.0	187.4	183.6
993	Watts	327.8	327.5	322.6	316.6	309.7	302.1	296.5	293.4
	BTU	189.5	189.3	186.5	183.0	179.0	174.6	171.4	169.6
995	Watts	370.0	370.9	368.7	363.1	359.5	354.8	346.9	337.7
	BTU	213.9	214.4	213.1	209.9	207.8	205.1	200.5	195.2
1032	Watts	81.0	93.2	107.4	122.7	133.0	140.3	147.9	156.6
	BTU	46.8	53.9	62.1	70.9	76.9	81.1	85.5	90.5
1035	Watts	349.1	340.6	337.3	334.6	335.8	329.4	322.8	317.3
	BTU	201.8	196.9	195.0	193.4	194.1	190.4	186.6	183.4

** Units: watts/m, °C and BTU/ft, hr, °F.
   Specimens annealed 704°C (1300°F)/1 hr/AC prior to test.
   NASA-Z and 995 results corrected for thermal expansion.

TABLE 24. — TENSILE TEST RESULTS

Alloy	Serial No./Condition	Test Temperature	Strain Rate (s-1)	Yield Strength* MPa	Yield Strength* ksi	Tensile Strength MPa	Tensile Strength ksi	Elongation in 4d (%)	Reduction in Area (%)	Suspected Gradient**
NASA-Z	1	705°C	0.1	—	—	118	17.2	80	67	X
				87	12.6	110	15.9	71	63	X
				82	11.9	105	15.2	61	68	X
		705°C	0.06	72	10.5	108	15.6	92	78	
				74	10.8	108	15.6	88	79	
		705°C	0.0005	65	9.4	70	10.2	21	63	X
		540°C	0.1	119	17.3	187	27.2	39	66	X
				130	18.9	185	26.9	35	58	X
993	AE	705°C	0.06	73	10.6	92	13.4	50	96	
				63	9.2	80	11.6	58	98	
	SCWA-211	705°C	0.06	80	11.6	98	14.3	34	96	
				87	12.6	103	14.9	38	98	
	HWSCWA	705°C	0.1	140	20.3	140	20.3	8	92	X
	HWSA	705°C	0.1	63	9.1	74	10.8	32	91	X
	CWCAR-1	705°C	0.1	95	13.8	96	14.0	23	95	X
				80	11.6	100	14.5	20	96	X
		540°C	0.1	229	33.3	236	34.2	15	89	X
				174	25.3	177	25.7	13	89	X
	CWCAR-3	540°C	0.1	207	30.1	247	35.9	25	87	
				168	24.4	242	35.2	23	84	
				161	23.4	238	34.6	23	86	
995	AE-2	705°C	0.06	76	11.1	101	14.6	34	97	
				78	11.3	94	13.7	48	98	
	AE-3, AE-4	705°C	0.1	79	11.5	92	13.4	44	97	X
				74	10.8	88	12.8	47	98	X
		705°C	0.0005	60	8.7	65	9.4	23	95	X
		540°C	0.1	120	17.4	147	21.3	40	98	X
				123	17.9	167	24.2	36	97	X
	SCWA-211	705°C	0.06	43	6.2	72	10.4	51	97	
				44	6.4	78	11.3	73	99	
996	AE	705°C	0.06	68	9.8	94	13.7	84	90	
				61	8.9	91	13.2	123	91	
997	AE	705°C	0.06	71	10.3	91	13.2	47	96	
				75	10.9	92	13.4	44	98	
	SCWA-111	705°C	0.06	48	7.0	73	10.6	76	97	
				48	6.9	74	10.8	65	98	
999	SA	705°C	0.06	63	9.1	101	14.7	77	82	
				61	8.9	91	13.2	120	89	
				—	—	96	14.0	97	86	
	SCWA-211	705°C	0.06	—	—	105	15.2	76	80	
				73	10.6	101	14.6	83	79	
				58	8.4	99	14.4	72	81	
	HW	705°C	0.1	112	16.3	128	18.6	42	85	
	HWSA	705°C	0.1	73	10.6	114	16.6	49	67	

TABLE 24. — TENSILE TEST RESULTS (CONTINUED)

Alloy	Serial No./Condition	Test Temperature	Strain Rate (s-1)	Yield Strength*		Tensile Strength		Elongation in 4d (%)	Reduction in Area (%)	Suspected Gradient**
				MPa	ksi	MPa	ksi			
1032	AE	705°C	0.1	83	12.0	114	16.5	32	94	X
				94	13.7	118	17.2	35	94	X
				—	—	116	16.8	27	94	X
	SCWA-1	705°C	0.1	94	13.7	152	22.0	18	92	X
				100	14.5	149	21.6	45	94	X
				103	14.9	147	21.4	43	92	X
1035	AE	705°C	0.1	97	14.1	166	24.1	31	90	X
				83	12.0	165	23.9	24	88	X
				96	13.9	168	24.4	23	89	X
		540°C	0.1	158	23.0	218	31.7	28	87	
				184	26.7	220	31.9	28	88	
	EC	705°C	0.1	103	14.9	183	26.6	11	88	X
				91	13.2	180	26.1	9	81	X
				—	—	190	27.5	22	90	X
1036	AE	705°C	0.1	86	12.5	128	18.6	28	94	X
				91	13.2	123	17.8	28	94	X
1038	AE	705°C	0.1	92	13.3	136	19.7	33	88	X
				93	13.5	136	19.7	32	88	X
				92	13.4	132	19.1	24	88	X
	SA	705°C	0.1	86	12.5	116	16.9	48	83	X
				85	12.4	120	17.4	34	81	X
				86	12.5	114	16.5	33	84	X
1042	AE	705°C	0.1	96	13.9	112	16.3	45	88	
				88	12.8	117	17.0	45	88	
1043	AE	705°C	0.1	68	9.9	110	15.9	85	59	
				76	11.1	110	16.0	67	41	
	SCWA	705°C	0.1	76	11.0	111	16.1	58	46	
				69	10.0	103	15.0	68	52	

* 0.6 s^{-1} strain rate tests employed crosshead deflectometer for strain data collection.
** Some tests were conducted before a thermal gradient was found in the furnace.

I. FORGING TRIAL OF POWDER METALLURGY ALLOY

Development of a powder-metallurgy copper thrust chamber requires that the powder-metallurgy alloys be processable into forms from which chambers can be made. A small study was undertaken to determine whether hot-compacted rapid solidification rate (RSR) copper powder could be hot-forged and then cold-worked without workability problems. The powder was hot-compacted because that process resembled hot isostatic pressing (HIP), which would be most appropriate for consolidation of large thrust chamber preforms. Forging was performed because HIP or hot compaction would not be expected to work the microstructure sufficiently prior to use. Cold working was evaluated because some chambers are cold-spun to shape. Alloy 997 (-80 mesh) was used because it was available.

The powder was hot-compacted as described in the earlier Procedure section. A 2.5 cm-diameter by 4.5 cm-long cylinder was machined and then forged isothermally (the only method available at Pratt & Whitney) at 760°C (1400°F), using a strain rate of 0.1/minute, to a total upset of 85 percent (6 mm thick). The resulting pancake is shown in Figure 79. No cracking occurred.

The pancake was then cold cross rolled 60 percent (2.5 cm thick). Again, no problems or cracking occurred (Figure 79). The resulting microstructure (Figure 80), was very fine grained: less than 10 μm grain size.

This study demonstrated the feasibility and ease of processing powder, via HIP consolidation, into useable thrust chamber performs.

## II. PRODUCTION OF NASA-Z MATERIALS AT PRATT & WHITNEY (P&W)

Initial supplies of NASA-Z provided by NASA Lewis Research Center (LeRC) were limited. When it became evident that testing needs exceeded these supplies, an effort was made to produce conventional NASA-Z at P&W (This was called PWNASZ to differentiate it from LeRC material).

The alloy (Cu-0.5%Zr-3.0%Ag) was a vacuum-induction melted (VIM No. 1866 — see the earlier Procedure section for specifics) and cast into two cylindrical ingots (10 cm diameter by 22 cm). The pipe was cut off the ingots, which were then machined into right cylinders for hot working.

One cylinder, PWNASZ-1 (85 mm diameter by 110 mm long) was pancake forged to 17 mm thick in an isothermal forging press at 845°C (1550°F) and a strain rate of 0.1/minute. The resulting pancake, shown in Figure 81, was free of cracks and looked very good.

The other cylinder, PWNASZ-2 (74 mm diameter by 125 mm), was hot-extruded at 845°C (1550°F) and 22:1 extrusion ratio into a 16 mm-diameter bar (see the Procedures section for other data). It also worked well without cracking, but the extrusion was not very straight.

Upon completion of hot-working, additional NASA-Z was supplied by NASA LeRC, so the PWNASZ was not processed further.
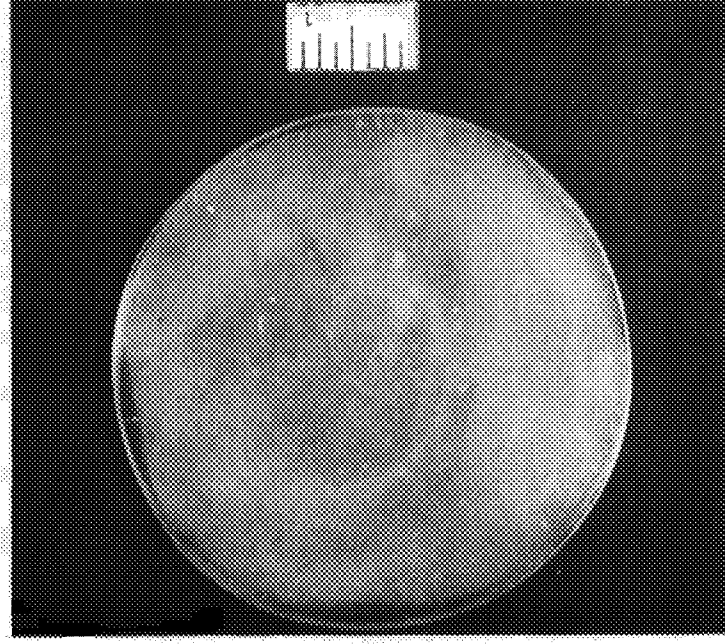
Hot-Forged + Cold-Rolled
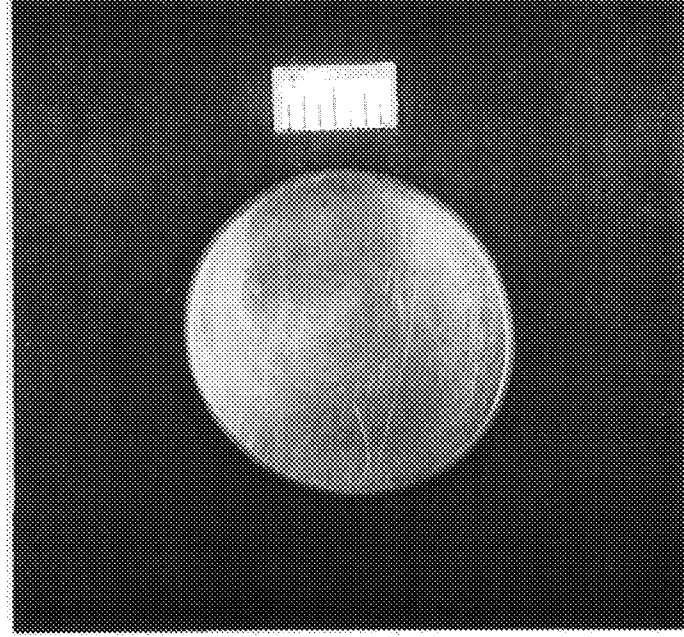
Hot-Forged

Figure 79. Forged Pancake and Rolled Sheet Made From Hot-Compacted Alloy 997 Powder
(Scale is 1 Inch)

139

20 μm

Figure 80. Microstructure of Alloy 997 After Hot Compacting + Hot-Forging + Cold-Rolling
+ Annealing at 650°C (1200°F)

Figure 81. NASA-Z Composition Pancake Cast + Hot-Forged at P&W (Scale is in Inches)

III. MIT MATERIALS

Two of the alloys produced by the Massachusetts Institute of Technology (MIT) were consolidated at P&W. The alloys were canned and consolidated by hot extrusion. Two extrusion cans were filled with the following alloys:
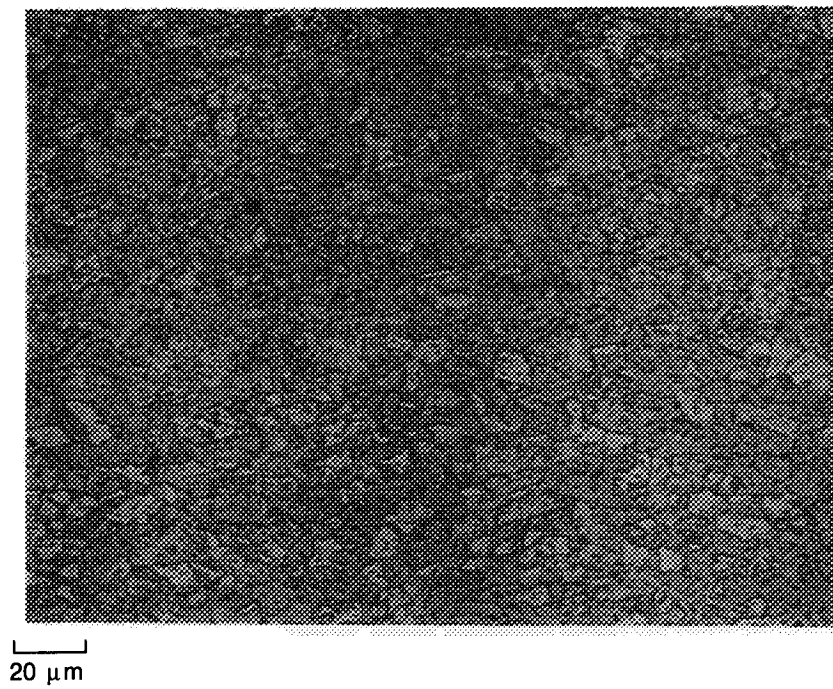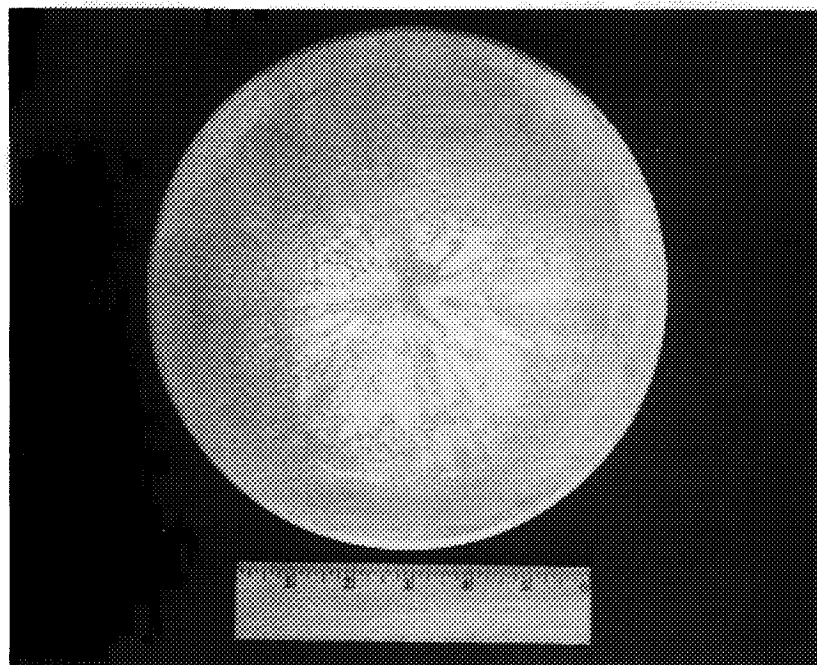
MIT-4: -75+45-micron-diameter Cu-1.1%Hf powder. Powder made at P&W (run 993), screened at MIT to size fraction, hydrogen-reduced at MIT.

MIT-5: Attrited Cu-Hf-O flakes. Powder made at P&W (993 — Cu-1.1%Hf). MIT screened 75-micron size fraction, attrited powder 12-30 hours in Szegvari attritor in ethanol to produce flakes and oxidize hafnium to hafnia, dry-ball milled under argon for 30 hours (to spheroidize), reduced in hydrogen.

The extrusion cans were filled using the following hot pumpdown technique:

1. The extrusion can was filled with the particulate in the drybox, capped, transferred to the outgasser, uncapped, and quickly attached.

2. The system and filled can were pumped out for 2 hours cold. System vacuum levels were about 5×10^{-5} microns. Meanwhile, a thermocouple was affixed to the can, the can was wound with nichrome heater tape, and the assembly was wrapped with insualtion.

3. After the 2-hour cold pumpdown, the heater was turned on, with an upper limit of 450°C (840°F). Pumping continued through heating. The following steady-state can outer diameter temperatures were reached after about 3 hours:

   MIT-4: 415°C (789°F)

   MIT-5: 450°C (840°F)

4. Hot pumping continued, while maintaining a system vacuum of about 5×10^{-10} microns. When a total pumping time of 24 hours had been reached, filler tube was crimped, and the heater was turned off. The filler tube weld seal was made after the can had cooled.

Both alloys were extruded at 700°C (1290°F), with an extrusion ratio of 20:1 (other specifics of the extrusion process can be found in the Procedure section).

The first alloy, MIT-4, extruded to a microstructure typical of Alloy 993 (Cu-1.1%Hf).

The second alloy, MIT-5, was a copper-hafnium alloy that had been attrited in ethanol to promote oxidation of some of the hafnium to produce a fine dispersion of hafnia. The resulting flakes had been dry-ball milled to agglomerate them so they would pack better in an extrusion can. The particulates supplied by MIT are shown in Figure 82. They exhibited a layered structure presumed to result from the flakes, and holes.

141

Figure 82. Structure of Cu-HF-HFO$_2$ Flake Alloy Supplied by MIT

500 µm

100 µm

142
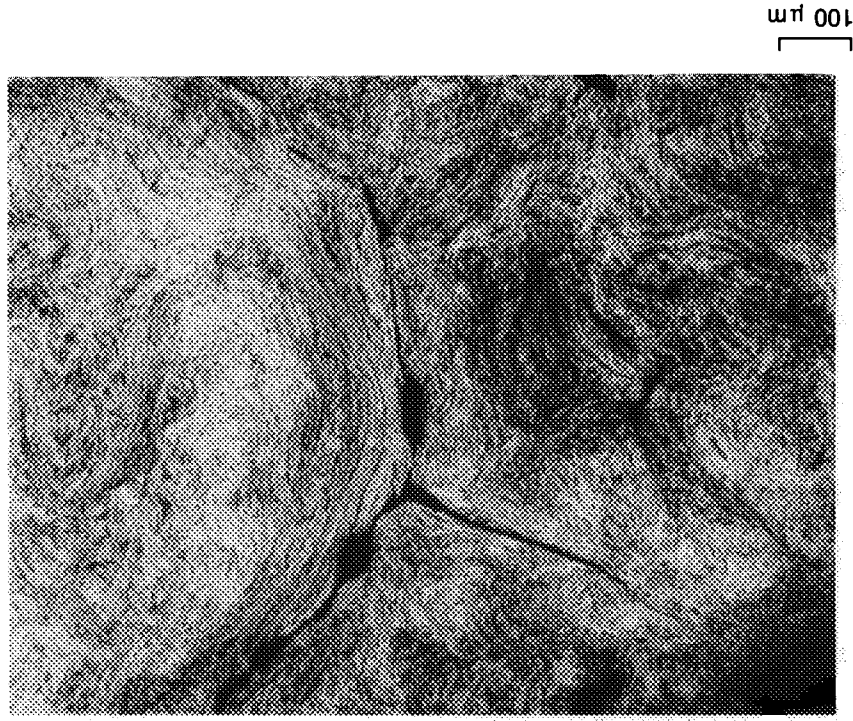
Extrusion of the flake alloy resulted in the structure shown in Figure 83. Voids and elongated structures (believed to have been prior particulates) were evident. The voids were believed to have resulted from incomplete consolidation (due to the holes in the particulates and due to the poor packing efficiency of the coarse particulates) or entrapped gasses. Hot swaging 50 percent at 760°C (1400°F) closed many of the voids (Figure 83).

However, annealing at 870°C (1600°F) appeared to reopen some of the voids, indicating possible entrapped gases. Hydrogen analyses revealed a hydrogen concentration of 20 ppm (wt). This was much greater than the solubility limit given by Elliot (27), so hydrogen entrapment may have caused the voids.

The MIT-5 flake alloy bar was hot-swaged 50 percent at 760°C (1400°F) and subjected to 705°C (1300°F) compression tests. Compression testing was used because it might be less sensitive than tensile testing to the void defects.

Compression test specimens were 6 mm-diameter by 19 mm-long right cylinders. Tests were conducted on an MTS servohydraulic programmable tensile tester, equipped with special extensometer-capable compression test grips. The specimen and linear variable displacement trransformer (LVDT)-type extensometers were attached to the grips, and thermocouples were attached to the specimen. The assembly was heated in a clamshell furnace, heating the specimen to 705°C (1300°F). The specimen was held 30 minutes at temperature and then compressed at a strain rate of 0.001/second. Force and strain data were collected on an X-Y plotter. Yield strength (0.2 percent) was reported. Four tests were performed.

Results of the compression tests are shown in Table 25, along with the slow-strain-rate yield strengths found earlier for NASA-Z and Alloy 995. The yield strengths for the flake alloy were much lower. A tested specimen is shown in Figure 84. All of the compression specimens exhibited bending of the prior particles and decohesion between the particles. Recrystallization was not evident.

A fine dispersion was seen in the flake alloy by transmission electron microscopy (TEM), Figure 85. It could not be conclusively identified, although electron diffraction patterns somewhat resembled those of hafnia.

This was a cursory evaluation of the MIT materials, since full evaluation of these materials was part of the MIT effort.

+ Annealed

100 μm
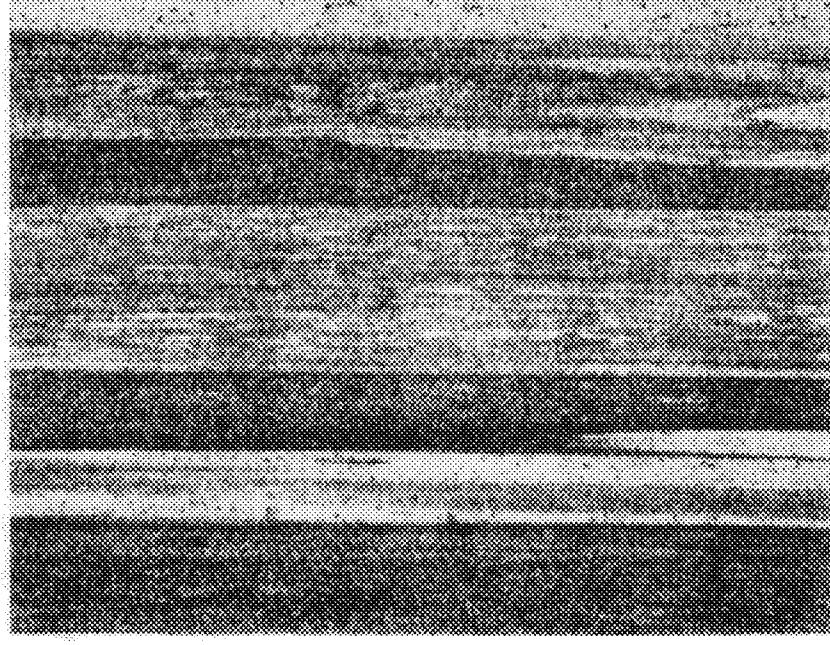
Extruded + Hot-Swaged

100 μm

As-Extruded

100 μm

144
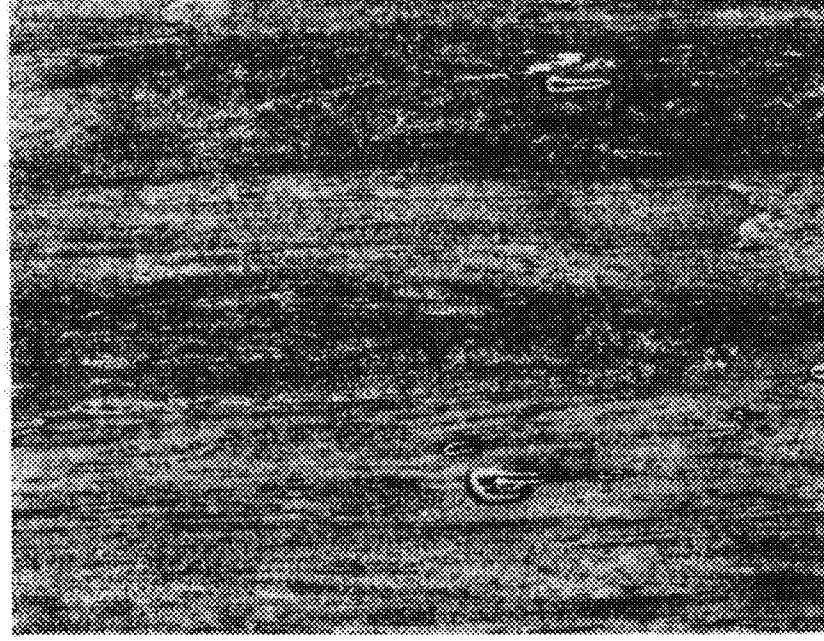
TABLE 25. — YIELD STRENGTHS OF MIT-5, NASA-Z, AND ALLOY 995 AT
705°C (1300°F)

Alloy	Condition	Yield Strength (0.2%)		No. of Tests	Test Type
		MPa	ksi		
MIT-5	Hot Swage	19	2.7	4	Compression
995	As-extruded	60	8.7	1	Tensile
NASA-Z	As-supplied	65	9.4	1	Tensile

Strain rate = 0.0005/second tensile, 0.001/second compressive.
Tensile test in argon; compression in air.
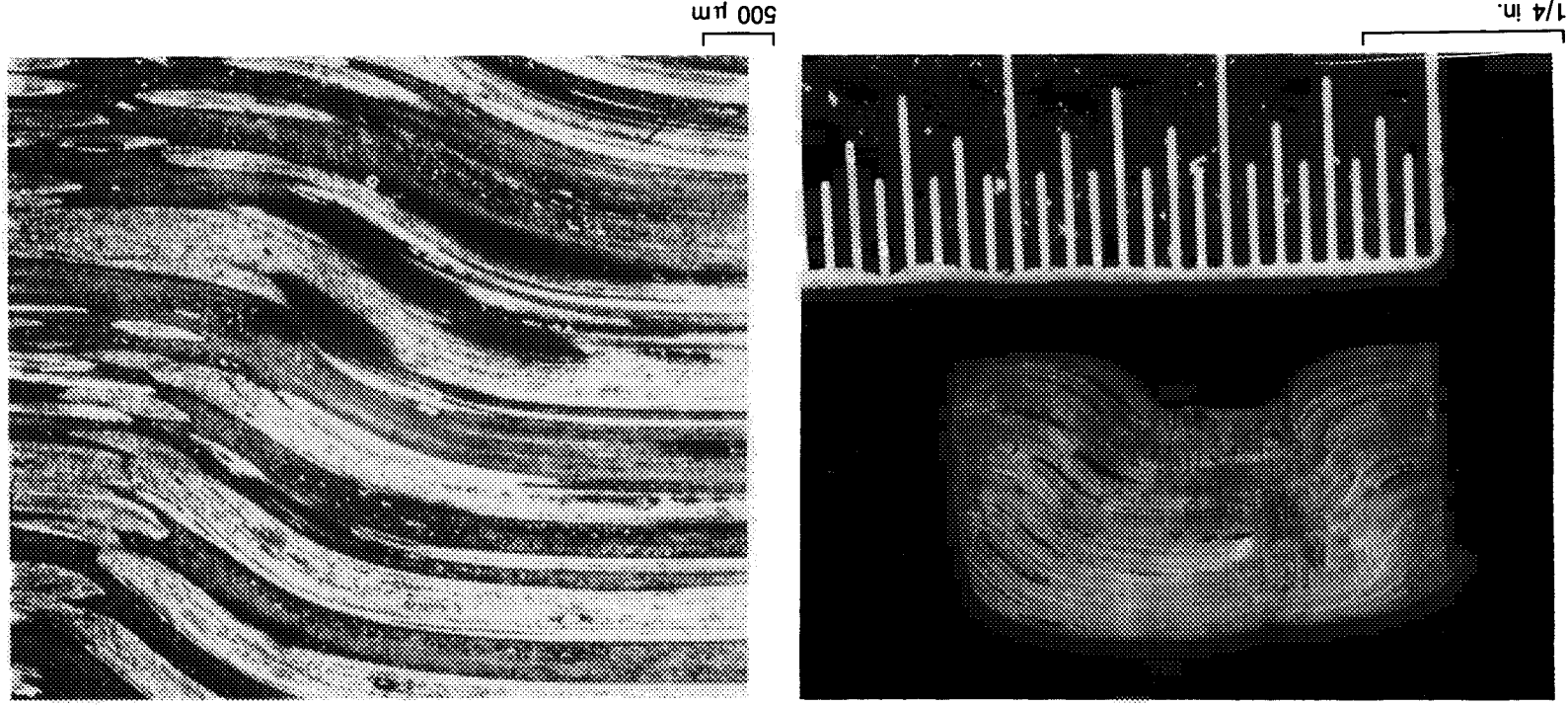
Figure 84.   MIT Cu-Hf-HfO₂ Flake Alloy 705°C (1300°F) Compression Test Specimen

146

1 μm

1 μm

Figure 85.   Electron Micrographs of Extruded + Hot-Swaged MIT Cu-Hf-HfO₂ Flake Alloy
(TEM-Foil)

147

APPENDIX C
NARLOY-Z™ BASELINE
MATERIAL PROPERTY
VARIATION STUDY

FOREWORD

This document presents an assessment of the impact of variations in candidate material properties in a thrust chamber liner for use in an advanced Orbital Transfer Vehicle (OTV) rocket engine. The work was conducted by Pratt & Whitney/Government Products Division (P&W/GPD) of the United Technologies Corporation (UTC) for the National Aeronautics and Space Administration — Lewis Research Center (NASA-LeRC) under Contract NAS3-23858-C.1 with Mr. J. M. Kazaroff as Task Order Manager.

Mr. J. R. Brown was the Program Manager for this effort, and Messrs. M. E. Combs, J. S. McPherson, and J. H. Moore were the principal investigators. Mr. M. E. Combs was the author of this report.

SECTION C.1
INTRODUCTION

The design and development of a durable, reusable rocket propulsion system for an Orbit Transfer Vehicle (OTV), as currently planned by NASA, requires the identification and development of a suitable material for use in the rocket engine combustion chamber liner. Such a material must be able to withstand prolonged engine operation at high temperatures and high pressures, as well as the cyclic effects of multiple starts and multiple thrust levels.

Current OTV rocket engine design concepts are based on those developed under the Advanced Expander Cycle Engine Point Design (Contract NAS8-33567). The most promising materials to date for the OTV application include copper alloys such as copper-zirconium, copper-silver, or a copper-silver-zirconium system similar to NARloy-Z, a proprietary alloy developed by Rocketdyne (Ref. 37). The thermal conductivity of copper allows sufficient heat transfer to cool the chamber for increased life while heating the fuel for improved engine efficiency.

NARloy-Z has demonstrated longer chamber life capability than other copper base alloys, but its high-temperature LCF properties fall short of those desired by Pratt and Whitney for the OTV application. Test chamber results indicate that most cracks initiate from inclusions in the material (Ref. 37). The current program (under Contract NAS3-23858) has as its goal the development of a rapidly solidified alloy that satisfies the OTV thrust chamber material property requirements. It is believed that rapid solidification and selective alloying will reduce or eliminate undesirable inclusions and will produce fine, stable dispersions for LCF property enhancement.

The purpose of the study presented in this report is to determine the impact of variations of mechanical material properties on thrust chamber strain range, using NARloy-Z as a material baseline. Some tradeoffs in material properties may be necessary in order to achieve the required properties for the OTV thrust chamber application. Since strain range is directly related to LCF life, the impact on strain range is an indication of the impact on life. However, the chemistry changes that may be required to achieve the desired properties may affect the LCF capability. While strain range can be predicted, the LCF capability of an alloy cannot be predicted. The LCF capability of candidate materials will be evaluated by thermal-mechanical specimen tests.

150

The effect of the variations in material properties on strain range was analytically determined with a computer model of the thrust chamber wall. The analysis used a MARC three-dimensional (3-D) finite element model of the area of the thrust chamber where strains were predicted to be maximum. Temperatures and pressures were incremented through transient conditions simulating start-up to maximum thrust to shutdown. The analysis began with a baseline model using NARloy-Z properties for the coolant tube passage and an electroformed nickel close-out. Subsequent analyses varied the material properties of the coolant passage, one property change at a time, to determine the effects of individual property changes on strain range.

C.2.A Marc Analysis

Thrust chamber strains and maximum strain locations were determined using a three-dimensional (3-D) elastic-plastic MARC analysis. MARC is a general purpose finite element analysis program whose capabilities include non-linear analysis (i.e., plasticity, creep, large-displacement), as well as heat transfer, buckling, etc. The model consisted of 20-node isoparametric brick elements with 27 internal integration points (MARC element 21, Figure 86). The analysis was stepped through a series of temperature and pressure increments, simulating the transient conditions of a mission cycle from start-up to maximum thrust to shutdown. The solution of each increment became part of the cumulative history of the mission cycle before the next increment was applied, as required for elastic-plastic analysis. Stress-strain behavior was approximated using a piecewise linear (tangent stiffness) approach. An initial elastic solution was scaled to the yield point where the elastic-plastic solution began. In general, load increments above the yield point were kept at 10 percent or less of the load at the yield point to prevent drift from the yield locus.
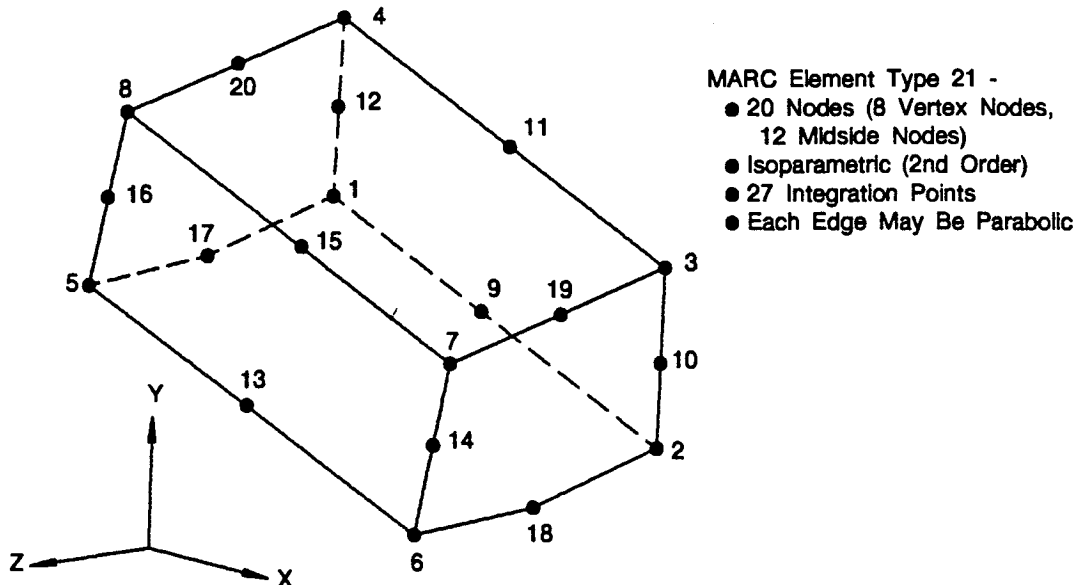

Figure 86. MARC 20-Node Isoparametric Brick Element

Experience has shown that a 3-D model is required with this type of configuration and loading to accurately predict strains (Ref. 38). An original consideration was to do the baseline material study with a 3-D analysis and the comparitive studies of varying material properties with a simpler two-dimensional (2-D) model at the maximum strain location, based on the results of the 3-D analysis (Ref. 39). However, the timely availability of a lower-cost computer job priority classification at Pratt and Whitney allowed an 85 percent reduction in computer costs for certain large-volume, overnight computer jobs. Consequently, it was decided to use the 3-D analysis in the comparitive material studies as well as in the baseline study for additional accuracy at reduced cost. It will be shown that the 3-D analysis predicted axial shifts in maximum strain locations that would not have been predicted with a simpler 2-D model. The shifts were due to internal load re-distributions for some of the material property variations.

C.2.B Configuration

Current OTV rocket engine design concepts are based on those developed under the Advanced Expander Cycle Engine Point Design (Contract NAS8-33567). The thrust chamber liner in this configuration has axial coolant passages with longitudinal ripples formed over each passage (Figure 87). The ripples have been shown analytically to reduce strains in the chamber wall (Ref. 40). The liner is composed of a candidate copper alloy (the material under study), and an electroformed nickel closeout.
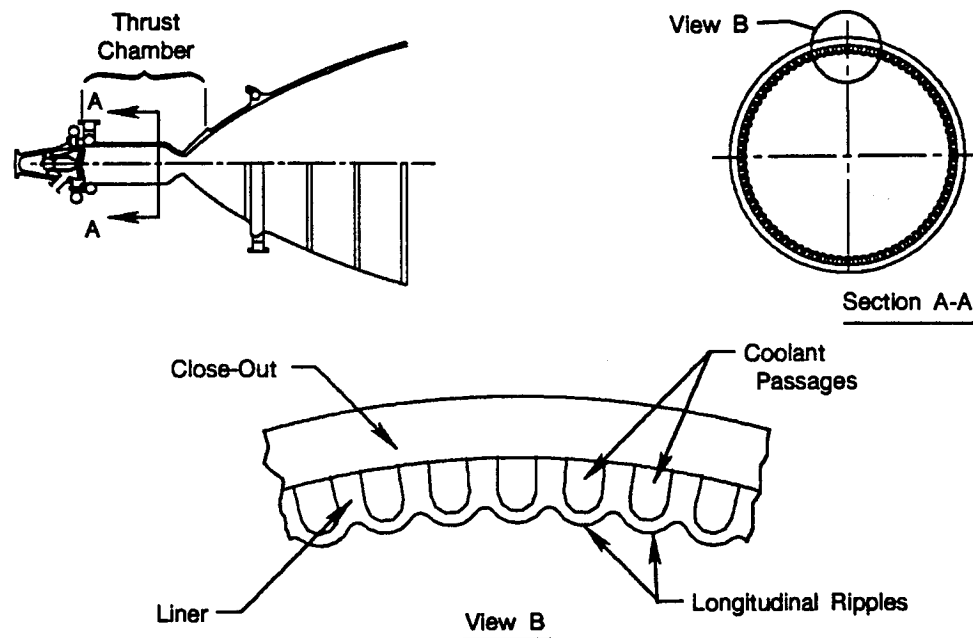
Figure 87. Combustion Chamber Configuration With Longitudinal Ripples Over Coolant Passages

The MARC model was constructed to include the highest strain location predicted by thick-wall cylinder equations. The highest strain location occurred near the peak temperature location on the inner wall of the chamber, approximately one inch upstream of the nozzle throat plane (Figure 88a). The MARC model consisted of a length of the chamber wall from the nozzle throat plane to a point two inches upstream, allowing about one inch length fore and aft of the predicted highest strain location. The half-width of a single coolant passage was modeled between radial symmetry planes, one plane passing through the centerline of the passage and the other plane

passing through the centerpoint between passages (Figure 88b). The size of the elements was varied so that areas of high temperature/high strain gradients consisted of more elements (a finer mesh), and areas of nearly-constant temperature consisted of fewer elements (Figure 89), saving computer time and cost without loss of accuracy. Each side was constrained to move parallel to the radial symmetry plane defining it (Figure 90).

C.2.C Material Properties

The thrust chamber liner consisted of a machined copper alloy coolant passage (the candidate material under study) and an electroformed nickel closeout. NARloy-Z (Cu-3%Ag-0.5%Zr) was chosen as the basis for the material properties of the copper alloy in this study since it has demonstrated longer chamber life capability than other copper alloys tested to date (Ref. 37). NARloy-Z is a proprietary alloy developed by Rocketdyne. The properties for NARloy-Z were obtained from industry literature on copper base alloys (Refs. 37, 41, and 42). The properties for the electroformed nickel close-out were obtained from industry data used in the design study described in Ref. 40.

A baseline analysis was first done using NARloy-Z properties for the candidate material. Subsequent analyses varied the candidate material properties from the baseline, one property change at a time, to determine the effect of each property change on strain range. The amounts of the changes were based on a study of the variability of material properties in current copper base alloys. Based on the literature survey, the material properties of copper alloys can vary from those of NARloy-Z by the amounts shown in Table 26, as follows.

2.0 in.

Highest Strain Occurs Near Area of
Highest Metal Temperature
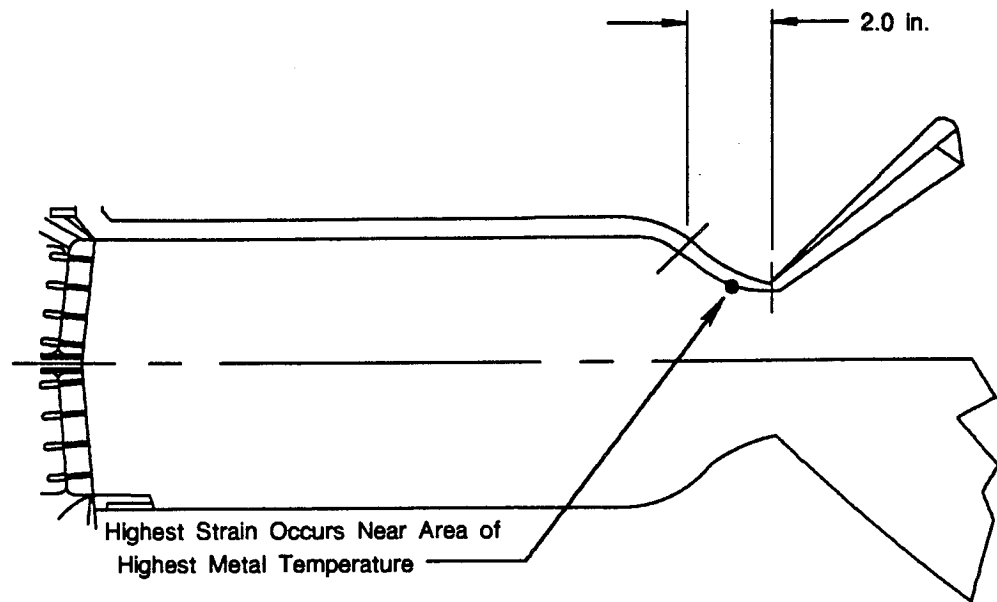
a. Length of Model Includes Predicted Area
of Highest Metal Temperature

Electroformed
Nickel Close-Out

2.25 deg

Radial Symmetry Planes

Copper Alloy Liner
(Candidate Material)
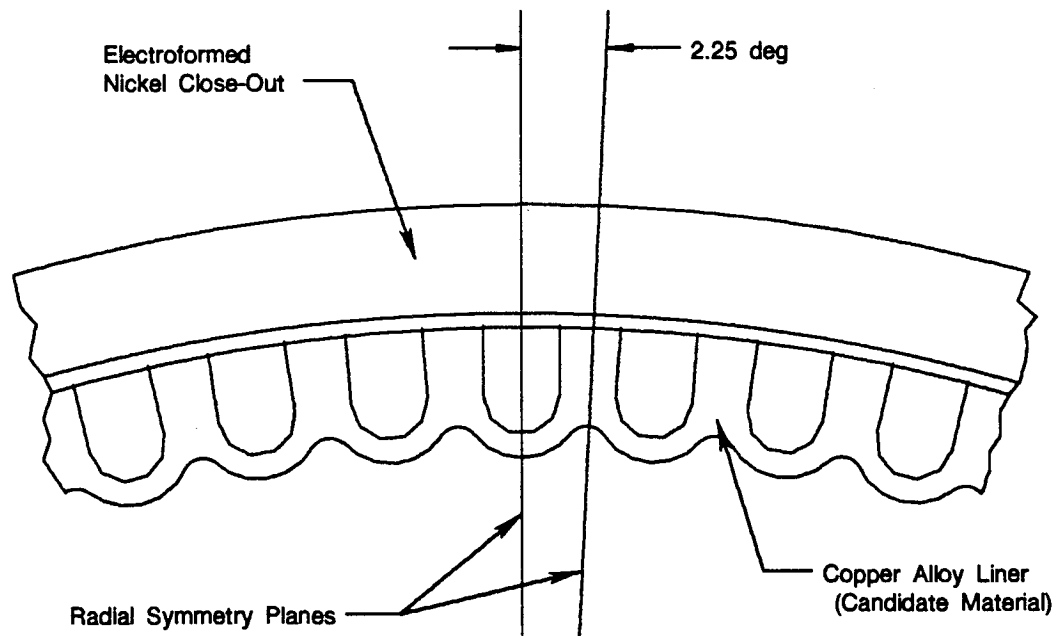
b. Half-Width of Coolant Passage Modeled
Between Radial Symmetry Planes

Figure 88. Section of Thrust Chamber for MARC Model

154

Section A-A.

Detail View of
Typical Cross-Section

Model Composed of
Three-Dimensional (3-D)
Brick Elements
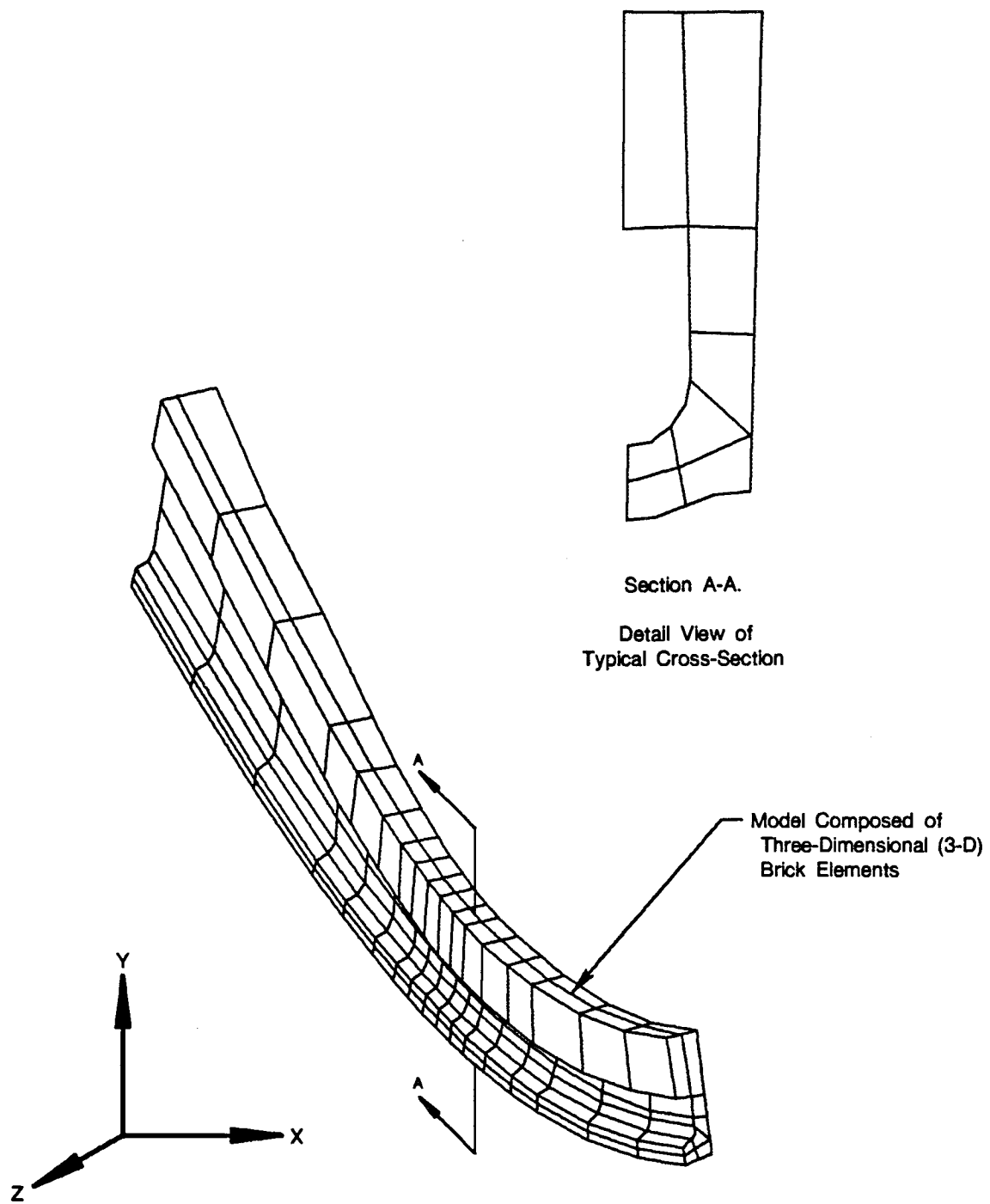
Figure 89. MARC Model
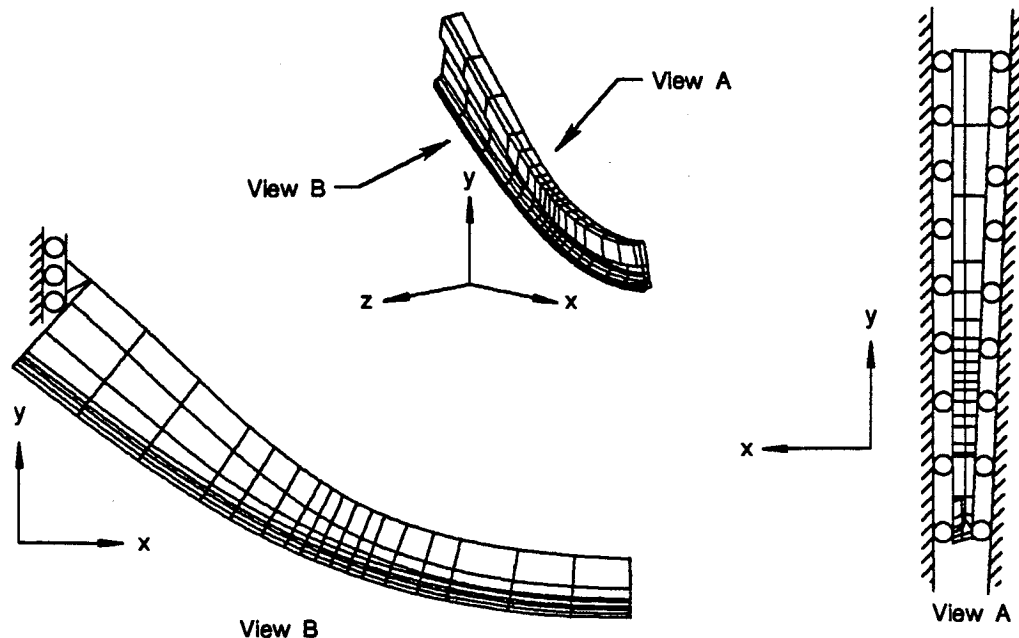
Figure 90. MARC Model Boundary Constraints

Table 26. Material Property Variations of Copper Base Alloys

Material Property	Variation Relative to NARloy-Z		
Young's Modulus (E)	−20%	to	+35%
Coef. of Thermal Expansion (α)	−8%	to	+8%
Yield Stress (σ_y)	−55%	to	+165%
Coef. of Thermal Conductivity (k)	−15%	to	+10%
Creep Strain Rate ($\dot{\varepsilon}_c$)	0.2×	to	5.0×

Using the values in Table 26 as guidelines, a MARC analysis was performed for each of the material property changes listed below to determine the isolated effect of each change on thrust chamber strain range. The analyses of the following property changes did not include creep effects:

- Baseline (NARloy-Z), with no creep
- +35% E
- −20% E
- +10% α
- −10% α
- +50% σ_y
- −50% σ_y
- +10% k
- −15% k

The remaining MARC runs included creep, assuming ten minutes hold time at full throttle, to determine the effects of changes in creep strain rate, as follows:

- Baseline (NARloy-Z), with creep
- 5.0× $\dot{\varepsilon}_c$
- 0.2× $\dot{\varepsilon}_c$

The baseline run and all varying material property runs involved only one cycle to obtain the relative effects of property changes on total strain range in the chamber wall. Actual

materials may tend to harden or soften with time; however, the strain range is not expected to be significantly different from that predicted in the MARC analyses. The mean strain may vary, but since the determination of LCF life is more dependent on strain range than on mean strain, it is felt that the analysis of one cycle was sufficient for the purpose of comparison without loss of accuracy.

Creep is a complicated phenomenon that is very dependent on time-related properties. Hardening and softening characteristics that affect creep ratcheting after several cycles can only be determined by specimen tests of candidate materials. Thermal-mechanical tests with creep-dwell should also be done to evaluate the effect on LCF capability.

The effect of the cyclic strain rate is another parameter that can only be evaluated by testing. The LCF specimen tests will address this parameter; however, the high cyclic strain rate expected in an actual rocket thrust chamber during real mission usage may not be achieved in specimen tests due to laboratory equipment limitations.

C.2.D   Mission Cycle

The model was subjected to a loading cycle simulating the conditions of an OTV mission from start-up to maximum thrust to shutdown. Figure 91 illustrates the nature of the cycle by the thermal response of the peak temperature location in the chamber wall vs time. The initial cooldown phase of the cycle occurred as fuel flowed through the coolant passages prior to ignition. The cooldown was assumed to lower the temperature of the thrust chamber from 70°F to a uniform −100°F. The acceleration, set to begin at time 0, brought the engine to full throttle in 1.022 seconds. The engine was held at full throttle until the thermals approached steady state, at 7.987 seconds into the cycle.
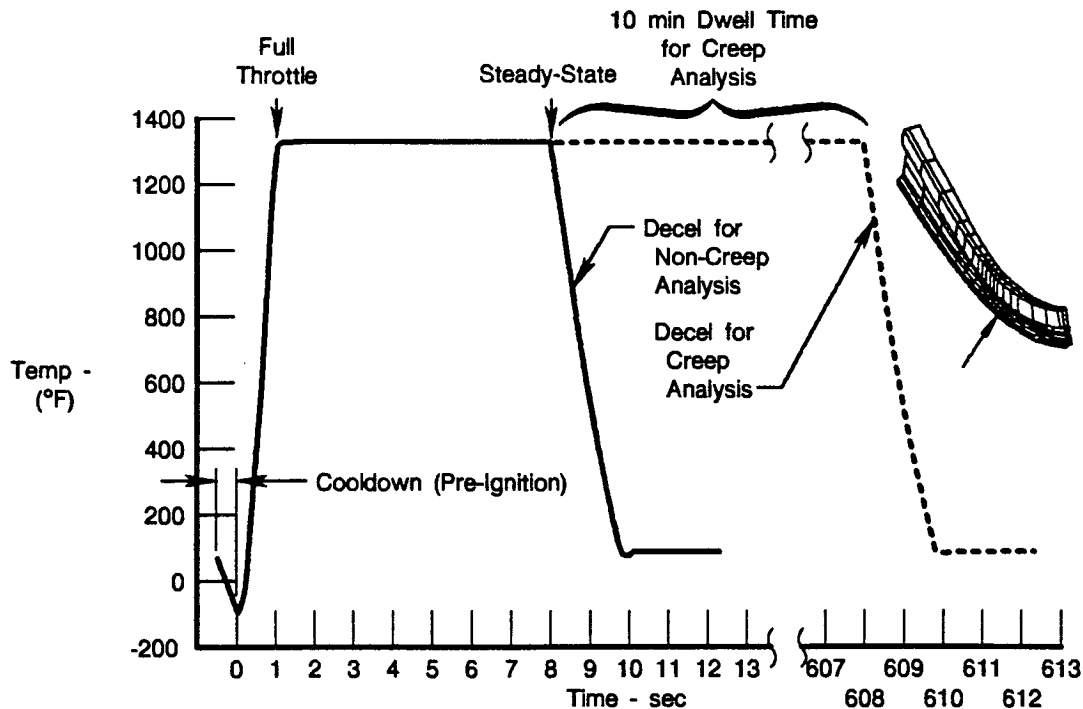

Figure 91.   Thermal Response of Hot Spot vs Time

At the steady-state point (7.987 seconds), two courses were taken in the remainder of the analysis. For all material property studies except creep strain rate, the engine was immediately decelerated to shutdown. The deceleration required 1.912 seconds to shutdown (9.899 seconds into the cycle), and an additional 2.411 seconds following the shutdown for thermals to approach steady state. For the creep strain rate study, the engine was held at full throttle for an additional 10 minutes after the steady-state point to exercise the creep option in the MARC analysis. The engine was then decelerated following the 10-minute hold in the same manner as described above.

To simulate the transient conditions of the mission cycle, the analysis was stepped through a series of temperature and pressure load increments, corresponding to specific timepoints throughout the mission. Individual temperatures were calculated and assigned directly to each integration point for each element of the MARC model. These temperature values were generated for each increment through the mission by means of in-house heat transfer decks. The same temperature values were used for all material variation studies except that of thermal conductivity, for which separate heat transfer analyses were required for new temperature values.

The fuel pressure inside the coolant passage was assumed to increase linearly with time during the first 1.022 seconds of the acceleration, from 0 psi to 3900 psi. The combustion pressure in the thrust chamber (outside the coolant passage) was assumed to respond similarly, from 0 psi to 1550 psi. Both pressures remained constant during full-throttle, and decreased linearly with time to 0 psi at deceleration. Figure 92 shows the response of the pressure loads with time.
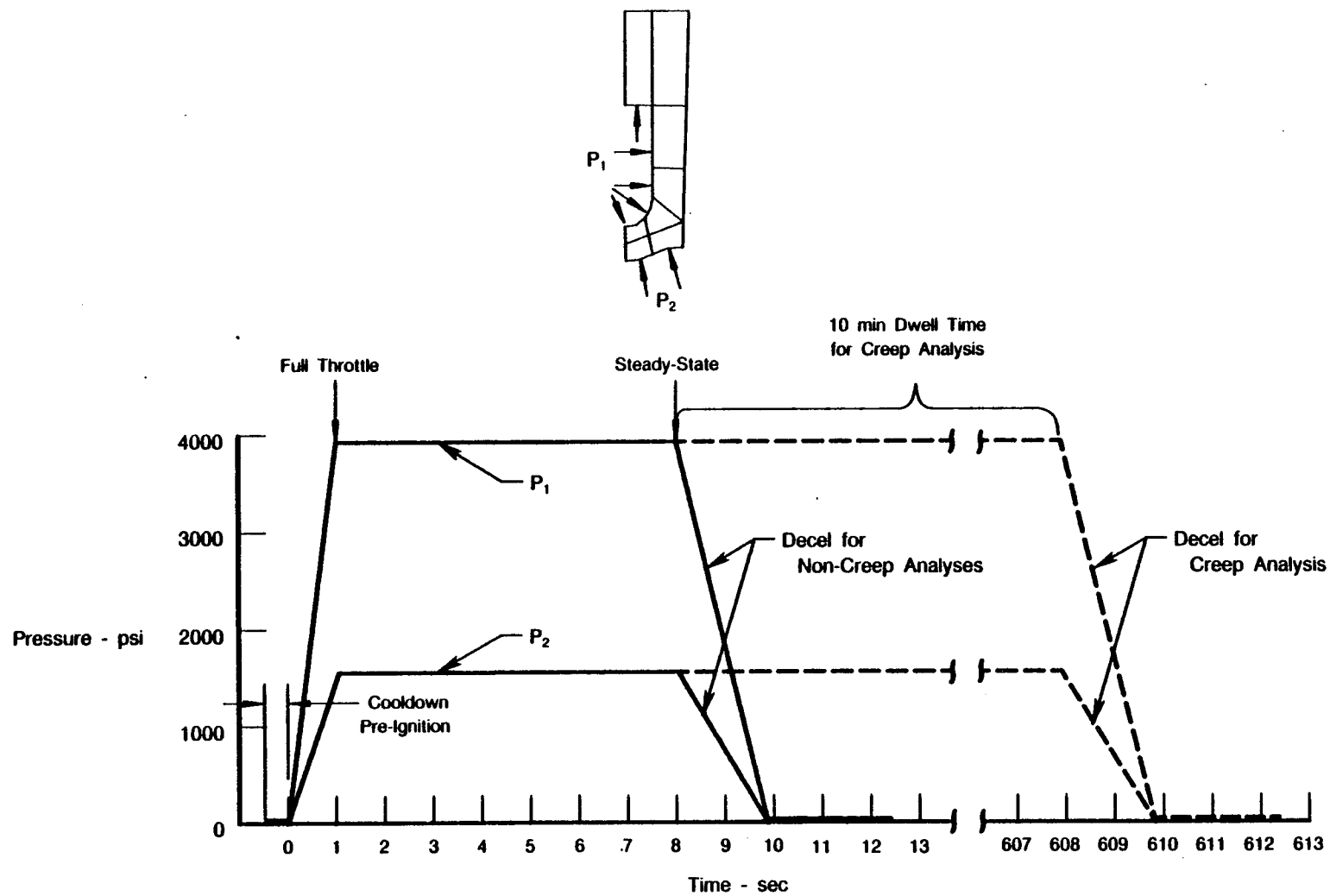
Figure 92. *Pressure Loads vs Time*

159

Output from the MARC analysis included stresses, strains, deflections, and temperatures. MARC provided output data for every integration point of every element in the model, and for each increment throughout the mission. The voluminous output from each MARC run was stored on magnetic tape for interactive graphics post-processing. Plots of stresses, strains, and temperatures via MARC post-processing utilities were used to determine the critical values and locations in the model, and to observe their behavior as a function of time.

The output parameter of prime consideration was the effective, or Von Mises, strain. The effective strain is used in structural analysis to evaluate the elastic-plastic and creep behavior of materials. The effective strain is a measure of the effect of multi-axial strains in terms of a single, equivalent uniaxial tensile strain, based on the distortion energy theory. The effective strain was calculated within MARC using Equation (1), as follows:

$$(1) \quad \varepsilon_{eff} = 2/3 \, (\varepsilon_x^{\;2} + \varepsilon_y^{\;2} + \varepsilon_z^{\;2} + 1/2 \, (\varepsilon_{xy}^{\;2} + \varepsilon_{yz}^{\;2} + \varepsilon_{xz}^{2} \,))$$

where ε_x, ε_y, and ε_z are component strains in the X, Y, and Z directions,

and ε_{xy}, ε_{yz}, and ε_{xz} are shear strains in the XY, YZ, and XZ planes.

The results of the material property study are given in Table 27, which summarizes the effect of the individual property changes on the maximum effective strain and strain range. The material property with the greatest effect on strain was the coefficient of thermal expansion (α). Details of the baseline analysis and the individual property changes are presented in the paragraphs following Table 27.

Table 27. *Summary of Effective Strains and Strain Ranges for Variations in Material Properties*

Material Property	Max. Eff. Strain	Change Relative To Baseline (%)	Max. Eff. Strain Range	Change Relative To Baseline (%)
Baseline (NARloy-Z)	0.03588	—	0.03962	—
+35% E	0.03624	+1.0	0.04029	+1.7
−20% E	0.03551	−1.0	0.03883	−2.0
+10% α	0.04009	+11.7	0.04454	+12.4
−10% α	0.03164	−11.8	0.03493	−11.8
+50% σ_y	0.03579	−0.3	0.03965	+0.1
−50% σ_y	0.03837	+6.9	0.04148	+4.7
+10% k	0.03453	−3.8	0.03847	−2.9
−15% k	0.03819	+6.4	0.04154	+4.8
Baseline w/creep	0.03610	+0.6	0.03993	+0.8
5.0× $\dot{\varepsilon}_c$	0.03615	+0.8	0.04003	+1.0
0.2× $\dot{\varepsilon}_c$	0.03604	+0.4	0.03983	+0.5

C.3.A Baseline Properties

The first results studied were for the NARloy-Z baseline material properties. Figure 93 shows the locations of peak values of strain and temperature. The peak temperature occured on the combustion side of the liner at approximately 0.89 inch upstream from the nozzle throat plane, and the maximum effective strain range occured on the coolant side of the liner at approximately 1.48 inches upstream from the nozzle throat plane.

Figure 94 shows the distribution of metal temperatures at full throttle through the cross-section at the highest temperature location. The metal temperature ranged from approximately 400°F in the nickel closeout to over 1300°F in the copper liner. The temperatures shown in Figure 94 are based on nodal values extrapolated from the integration point values by the MARC post-processor. The temperatures actually used for analysis comparisons were those assigned directly to the element integration points, as given in the MARC output data.

Stresses and strains were caused mainly by the large thermal gradients in the chamber wall (Figure 94). In addition, the coefficient of thermal expansion for the copper liner was significantly higher than that for the nickel close-out. Consequently, the hotter copper liner had a tendency to expand radially outward, but was restrained by the cooler nickel close-out. The radial restraint resulted in a high compressive hoop load in the liner (Figure 96), which was the major LCF driver in the thrust chamber cycle.

Figures 95 through 98 are history plots of metal temperatures, stresses, and strains for critical locations. The time scales are expressed in increments, which correspond to the temperature and pressure load increments discussed in Section C.2.D. Each increment represents a specific time point in the mission cycle. Table 28 lists the increment numbers and their corresponding mission time points for the baseline analysis.

The effective strain range was calculated from the cyclic maximum and minimum values of effective strain. Since the effective strain is always a non-negative value (Equation 1), the parameters used to calculate the effective strain were examined to determine if the actual strains were tensile or compressive. In Figure 98, the effective strain initially peaked at increment 3. In Figure 97, the hoop component of strain was positive (tensile) at increment 3. At increment 24, the effective strain (Figure 98) peaked again, but the hoop strain (Figure 97) was negative (compressive). The other components of strain exhibited similar sign reversals at peak values of effective strain (Figure 97). Based on the behavior of the component strains, the resultant value of the effective strain range was the sum of the values of effective strain at increments 3 and 24 (Figure 98), not the zero-to-peak value of increment 24 (the highest peak).

The maximum strain range location occurred inside the coolant passage in the radius of the domed wall (Figure 93). Both the radial and the hoop strains were large in this location, as seen in Figure 97. The radial strain was the result of the compressive hoop load forcing the dome to bulge outward (i.e., toward the chamber centerline). Figure 99 shows the deflected shape of a cross-section of the model at full throttle for the maximum strain location. The magnitude of the deflections are exaggerated for clarity.

Maximum Effective
Strain = 0.03588

Maximum Temperature = 1332 °F

Maximum Effective
Strain Range = 0.03962
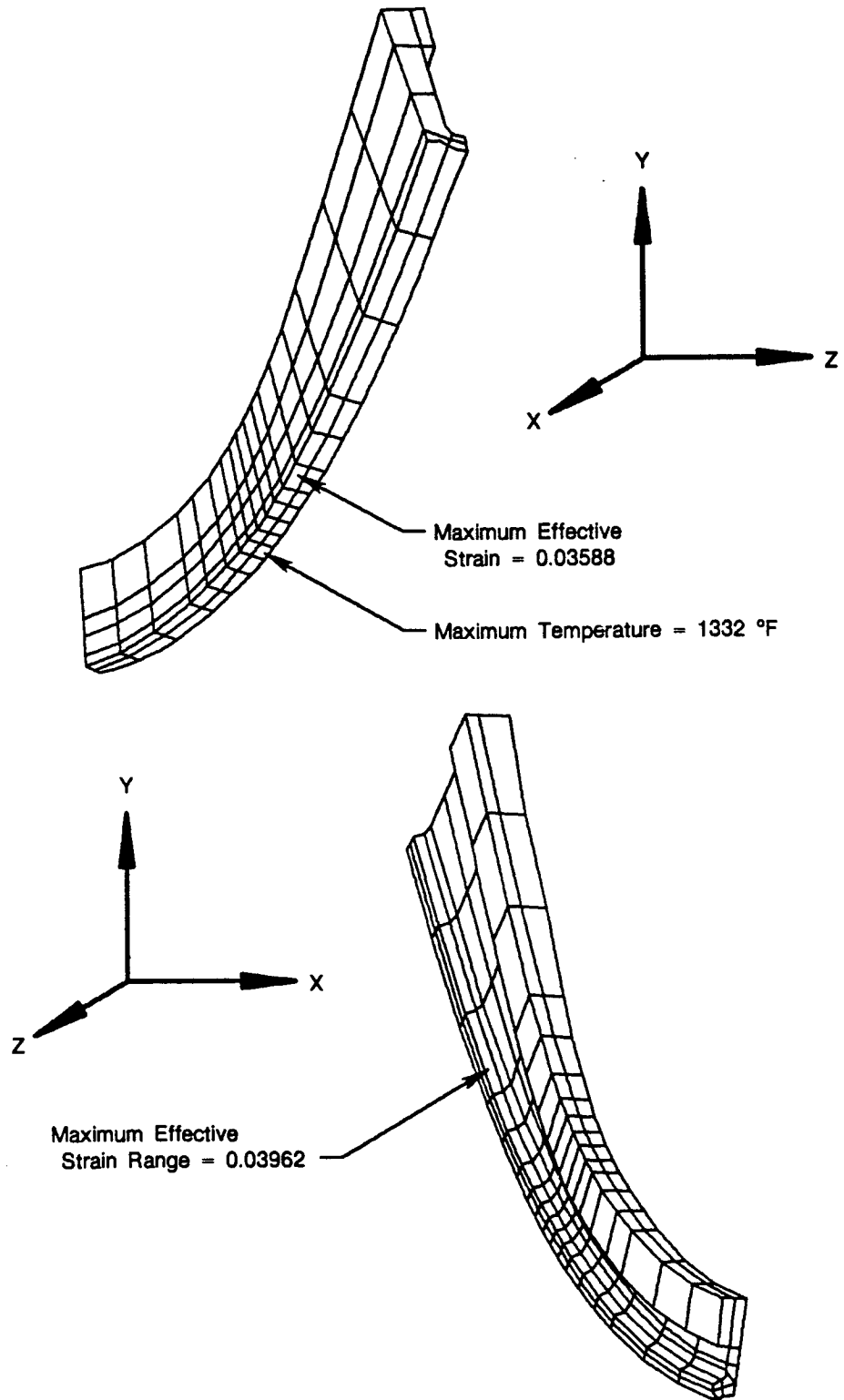
Figure 93.   Baseline Analysis: Peak Values and Locations

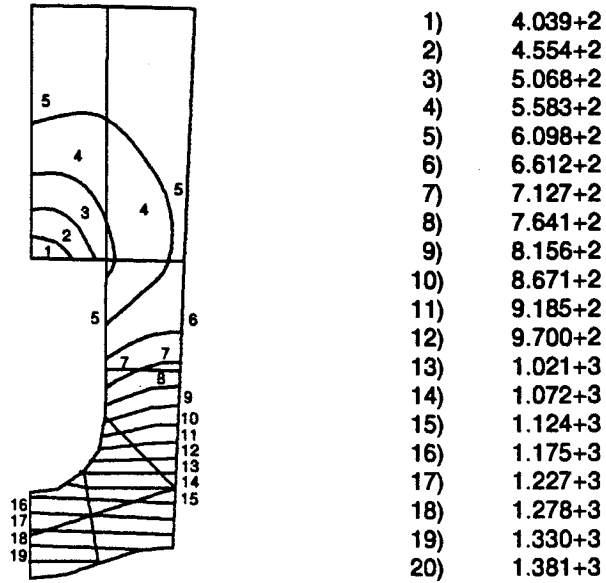|	
1)	4.039+2
2)	4.554+2
3)	5.068+2
4)	5.583+2
5)	6.098+2
6)	6.612+2
7)	7.127+2
8)	7.641+2
9)	8.156+2
10)	8.671+2
11)	9.185+2
12)	9.700+2
13)	1.021+3
14)	1.072+3
15)	1.124+3
16)	1.175+3
17)	1.227+3
18)	1.278+3
19)	1.330+3
20)	1.381+3

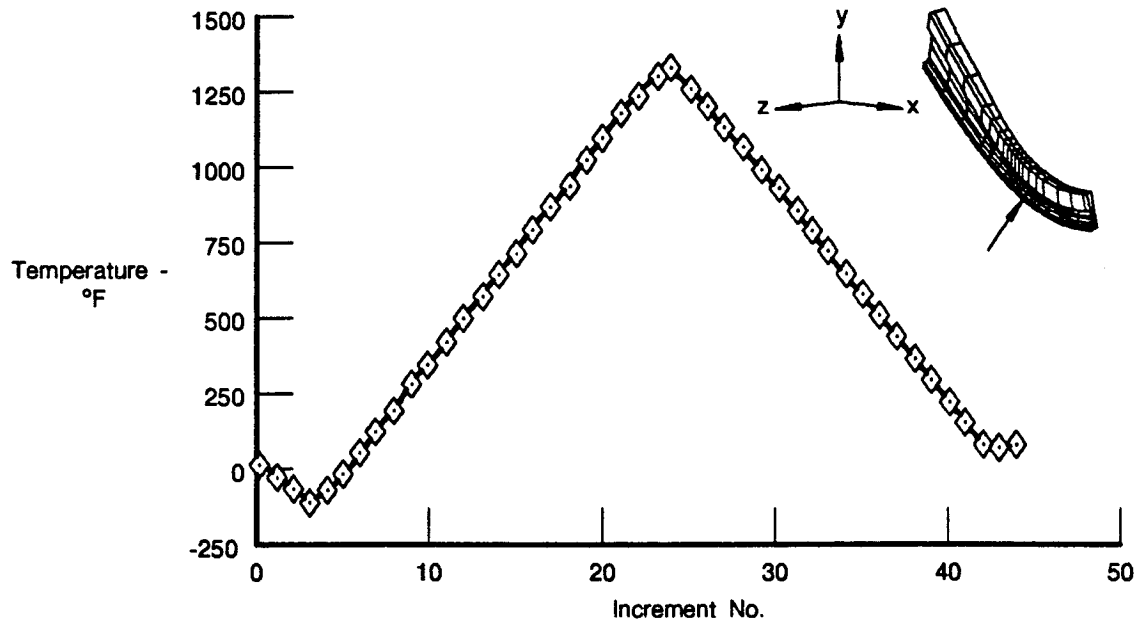*Figure 94. Baseline Analysis: Temperature Contour Plot*

Figure 95. Baseline Analysis: Maximum Temperature vs Increment Number
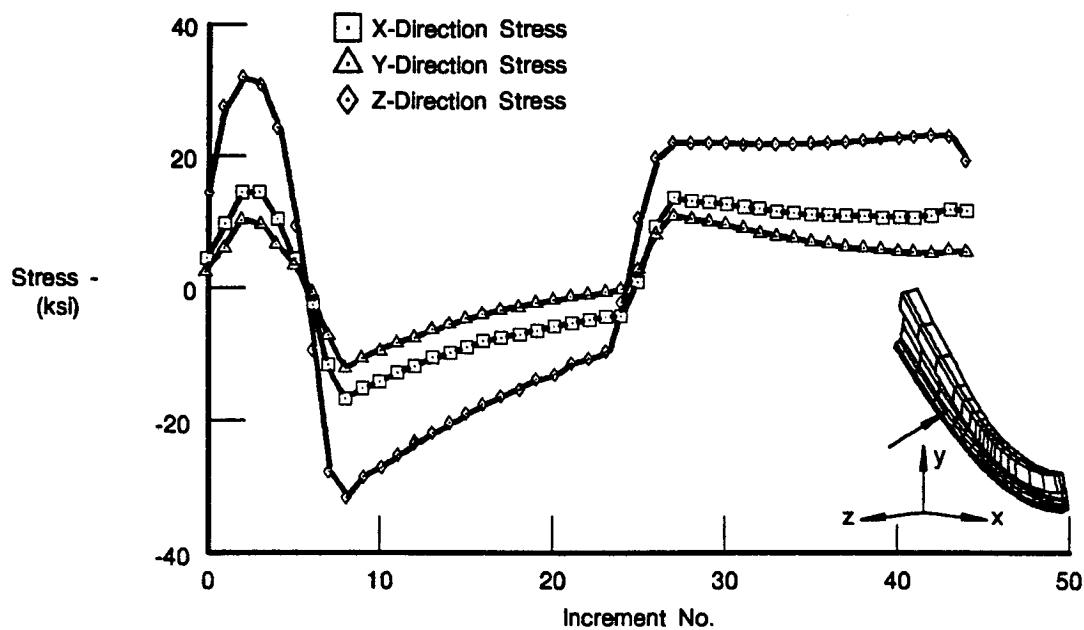
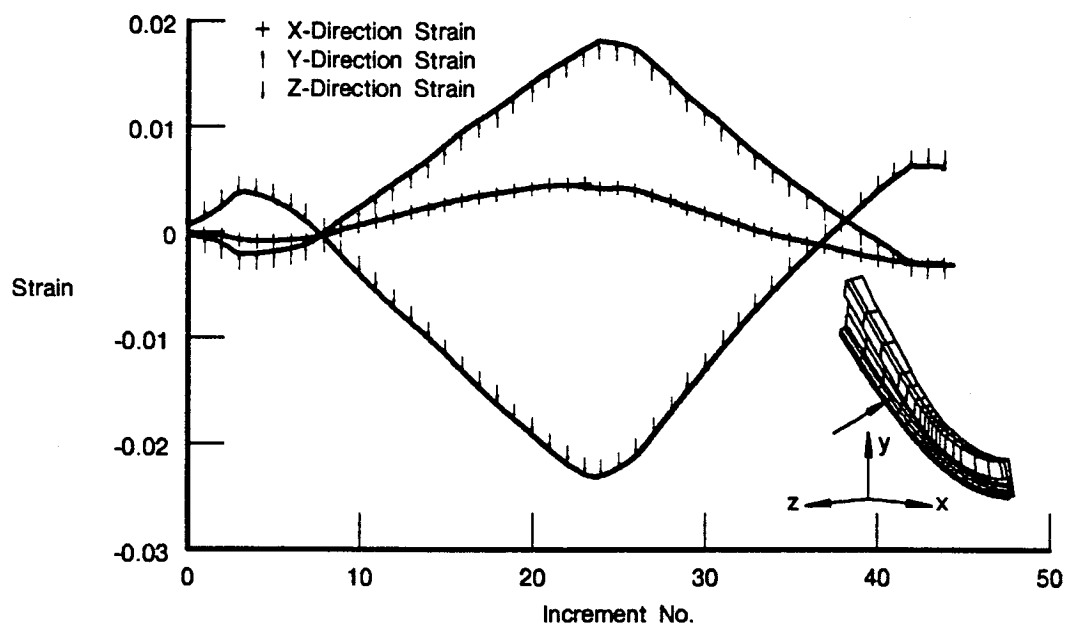*Figure 96.* *Baseline Analysis: Component Stresses vs Increment Number*

Figure 97. *Baseline Analysis: Maximum Component Strains vs Increment Number*
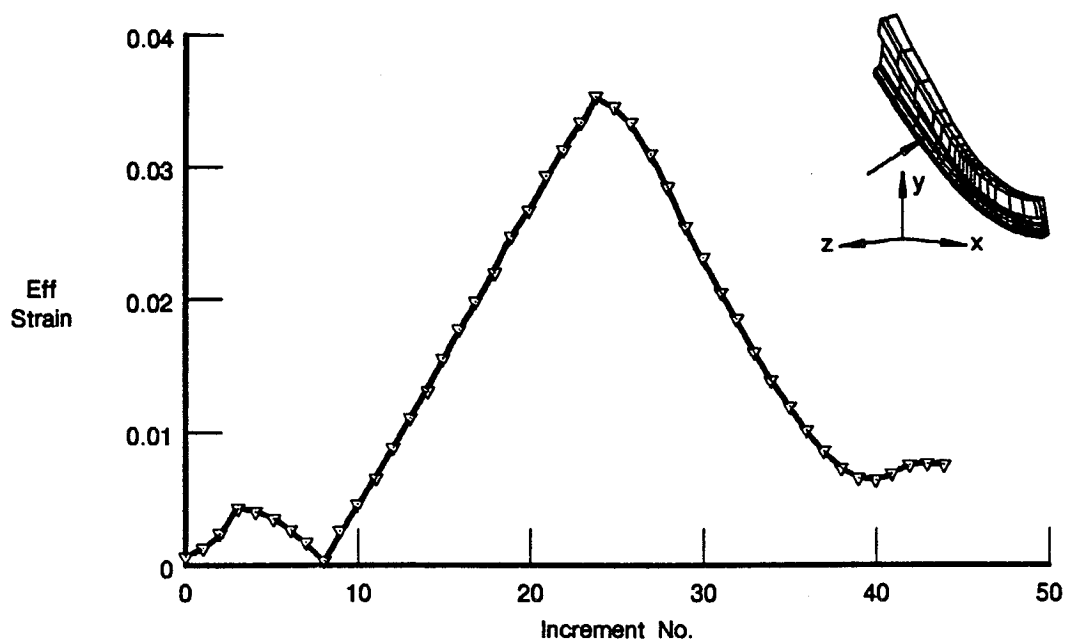
Figure 98. Baseline Analysis: Maximum Effective Strain vs Increment Number

Table 28. *MARC Increment No. vs Mission Time for the Baseline Analysis*

MARC Incr No.	Time (sec)	Comments	MARC Incr No.	Time (sec)	Comments
Initial	—	Pre-Ignition	22	0.9757	
State		Cooldown	23	1.0220	Full Throttle
0	—		24	7.9870	Steady-State
1	—				(Start Decel)
2	—		25	8.0870	
3	0.0000	Start Accel	26	8.1520	
4	0.1201		27	8.2440	
5	0.1996		28	8.3110	
6	0.2605		29	8.4050	
7	0.3203		30	8.4750	
8	0.3695		31	8.5740	
9	0.4186		32	8.6470	
10	0.4632		33	8.7500	
11	0.5092		34	8.8460	
12	0.5543		35	8.9340	
13	0.5978		36	9.0380	
14	0.6392		37	9.1330	
15	0.6869		38	9.2470	
16	0.7293		39	9.3530	
17	0.7697		40	9.4840	
18	0.8074		41	9.6110	
19	0.8597		42	9.7890	
20	0.8941		43	9.8990	End Decel
21	0.9425		44	12.3100	

---- Original Shape
———— Deflected Shape

Figure 99.   Baseline Analysis: Deflected Shape Plot

C.3.B   Young's Modulus

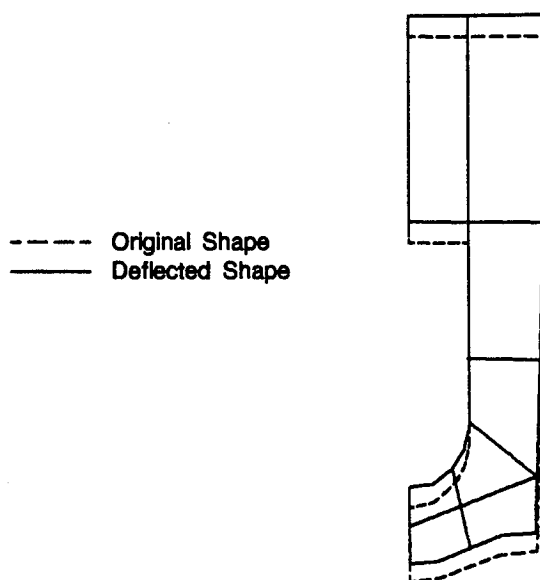Variations in Young's Modulus had only a nominal effect on strain range as compared to other property changes (Table 27). The effect of Young's Modulus was determined by increasing its value 35 percent and decreasing its value 20 percent from the baseline. The changes in Young's Modulus were made independently; the other properties were left unchanged. Figure 100 is a plot of the values of maximum effective strain and strain range as a function of Young's Modulus. The location of the maximum effective strain remained the same through the range of values for Young's Modulus, but the location of the maximum effective strain range shifted slightly upstream when Young's Modulus was decreased 20 percent.

C.3.C   Coefficient of Thermal Expansion

Among the material properties studied, the coefficient of thermal expansion (α) had the greatest influence on thrust chamber strain range. The effect of changes in α was determined by increasing and decreasing its value 10 percent from the baseline. The changes were made independently, with the other properties left unchanged.

Figure 101 is a plot of the values of maximum effective strain and strain range as a function of α. The correlation was essentially linear, with small changes in α producing significant changes in strain. This indicated the strong influence of thermal effects on thrust chamber strains. As the α of the copper liner was decreased, the tendency of the copper to expand decreased proportionately, reducing the thermal fight in the chamber wall. This in turn reduced the compressive hoop loads. Similarly, when α was increased, the compressive hoop loads increased.
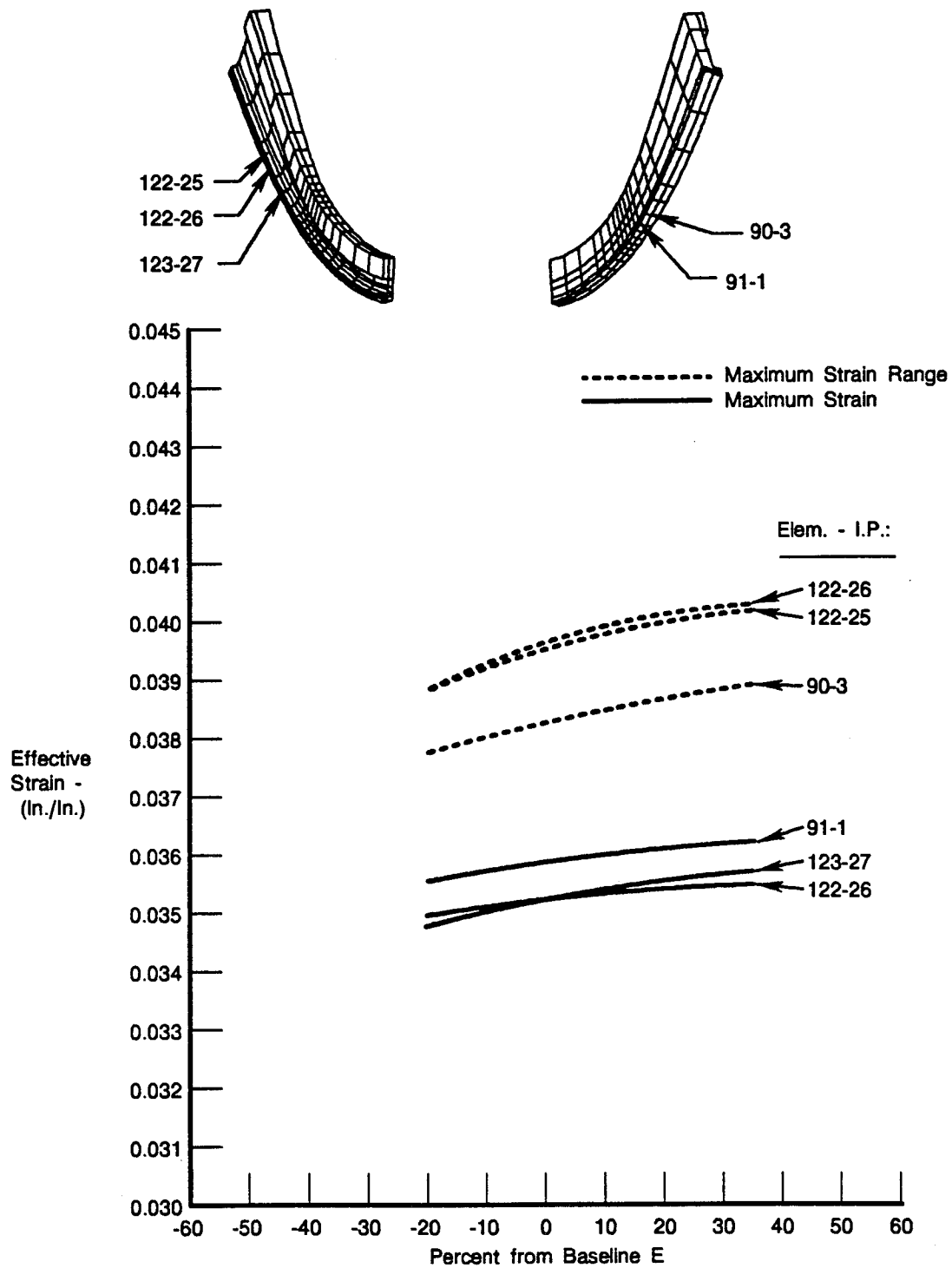
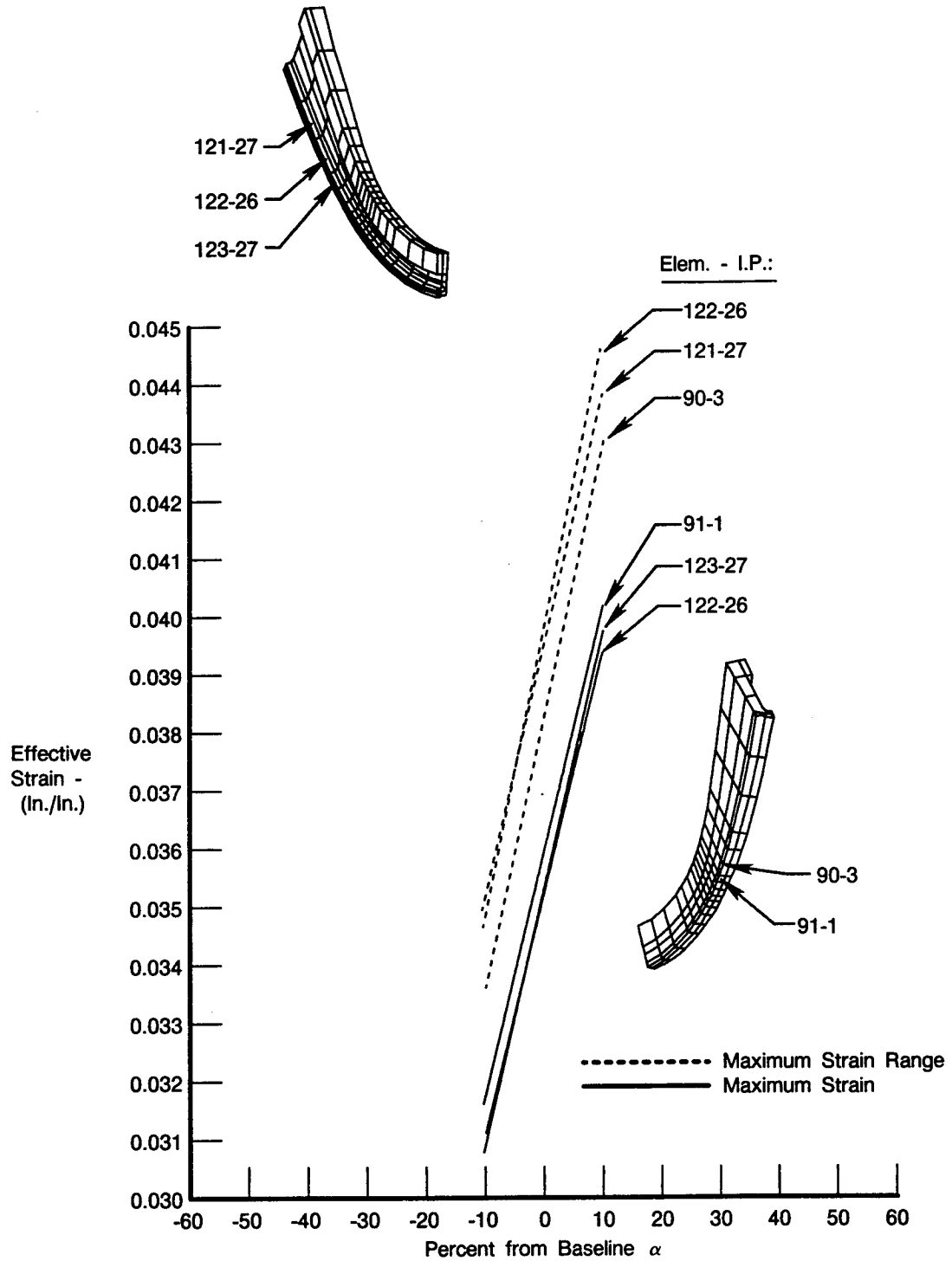166

Figure 100. Effective Strain vs Young's Modulus (E)

167

Figure 101. Effective Strain vs Coefficient of Thermal Expansion (α)

The location of the maximum effective strain remained the same in the model through the range of values for α, but the location of the maximum effective strain range shifted upstream when α was decreased 10 percent.

168

C.3.D Yield Stress

Variations in yield stress had a moderate effect on strain range, compared to other property changes (Table 27). The effect of yield stress was determined by increasing and decreasing its value 50 percent from the baseline. The changes were made independently, with the other properties left unchanged.

Figures 102 and 103 are plots of the maximum effective strain and strain range as a function of yield stress. The strain on the inside surface decreased as the yield stress of the material was decreased from the baseline (Figure 102). However, the strain on the outside surface increased as the yield stress was decreased (Figure 103), and the outside surface became the maximum strain location of the model at the lower value of yield stress. The maximum strain on the outside surface occurred in the fluted radius between the longitudinal ripples (Figure 104). For the baseline properties, the stresses on the outside surface were near the yield point. When the yield stress was decreased 50 percent, the outside surface material yielded under the hoop load, allowing higher compressive strain values and relieving the compressive strain on the inside surface.

As the yield stress was increased 50 percent from the baseline, the material on the outside surface behaved elastically, resulting in higher stiffness and lower compressive strain values (Figure 103). Consequently, more compressive hoop load was forced into the inside surface material, producing slightly higher strain values. But again, the higher yield stress resulted in higher stiffness and the compressive strain values on the inside surface did not increase significantly over those of the baseline properties (Figure 102). Load redistributions within the model may be observed as maximum strain locations shifted axially from one point to another as the yield stress was varied (Figures 102 and 103).

The plot in Figure 105 is a condensation of Figures 102 and 103, showing only the maximum values of strain from both the inside and outside surfaces of the model through the range of yield stress values.

C.3.E Thermal Conductivity

Variations in thermal conductivity had a substantial effect on strain range. However, with only a small range of thermal conductivity values considered, the overall impact was only moderate compared to other property changes (Table 27). The effect of thermal conductivity was determined by increasing its value 10 percent and decreasing its value 15 percent from the baseline. The changes were made independently, with the other properties left unchanged.

Changes in thermal conductivity were simulated by reassigning new temperature values to the MARC model. The new temperature values were calculated with in-house heat transfer decks (Section C.2.D) using the adjusted values of thermal conductivity in the heat transfer analyses.

Figure 106 is a plot of the maximum effective strain and strain range as a function of thermal conductivity. The effect of a lower thermal conductivity was slower heat transfer and a higher temperature on the outside surface of the copper liner. The higher temperature increased the tendency of the copper liner to expand, increasing the compressive hoop strains in the liner. Conversely, the effect of a higher thermal conductivity was a lower temperature and lower compressive hoop strains in the liner.
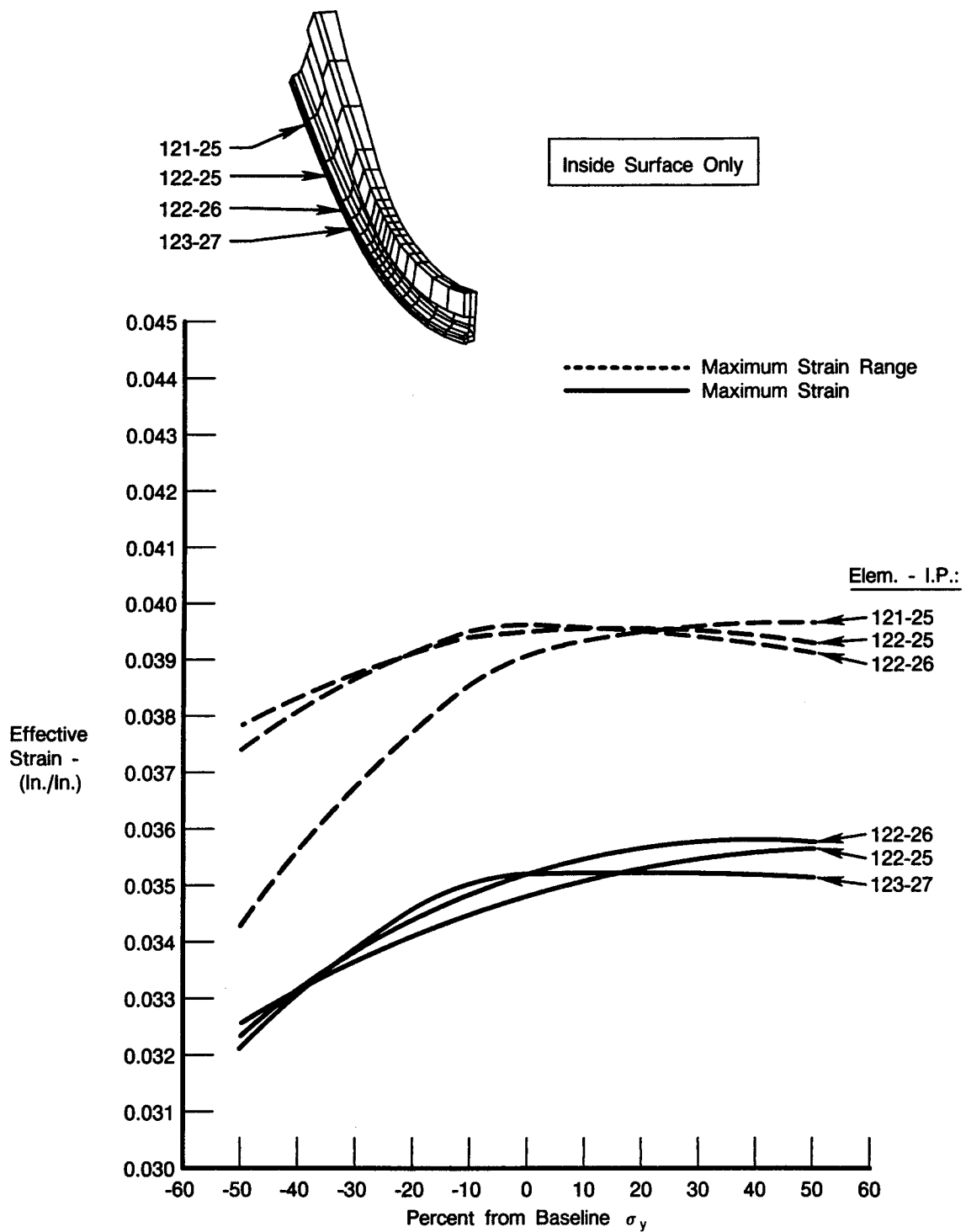
169

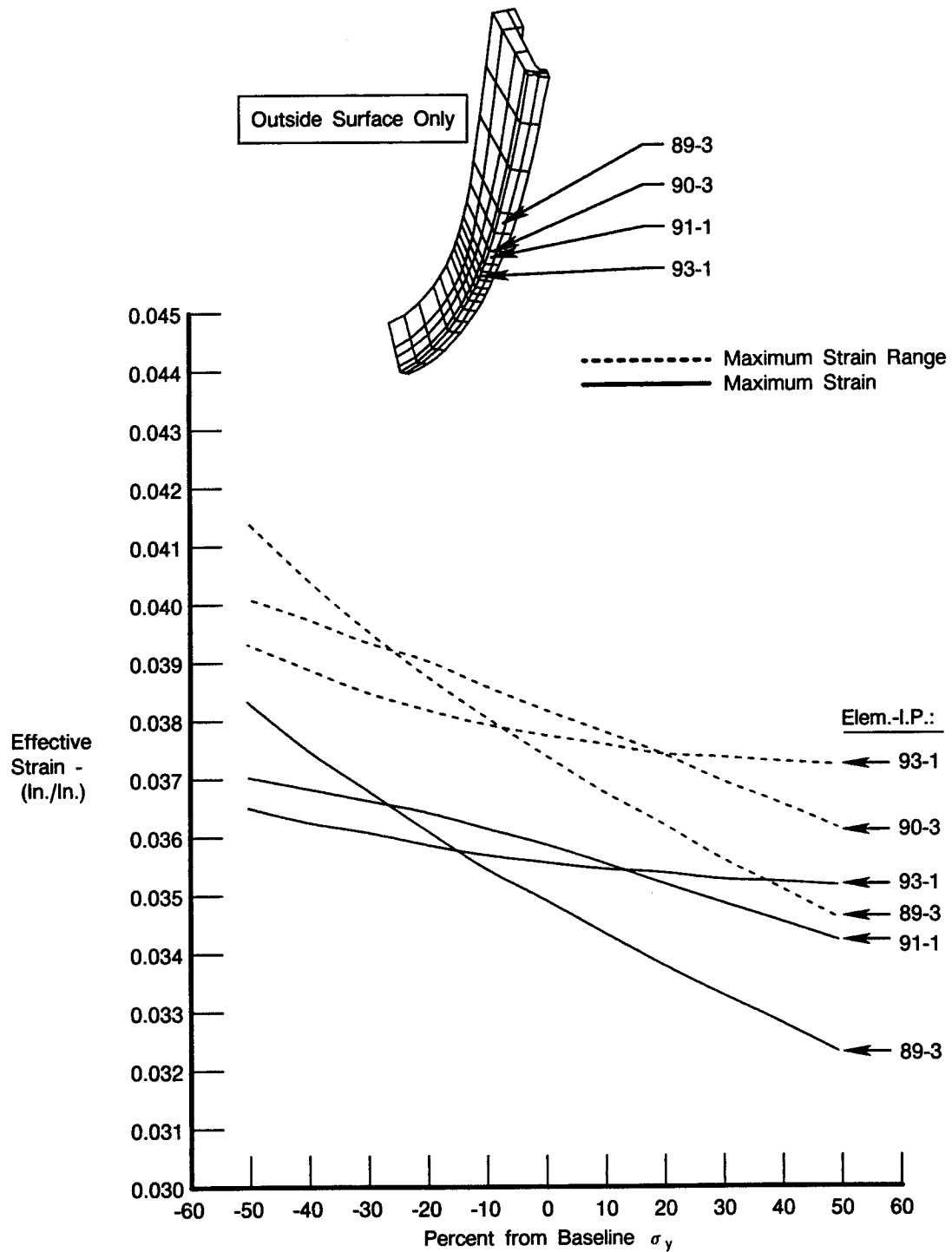*Figure 102. Effective Strain vs Yield Stress (σ_y), Inside Surface Only*

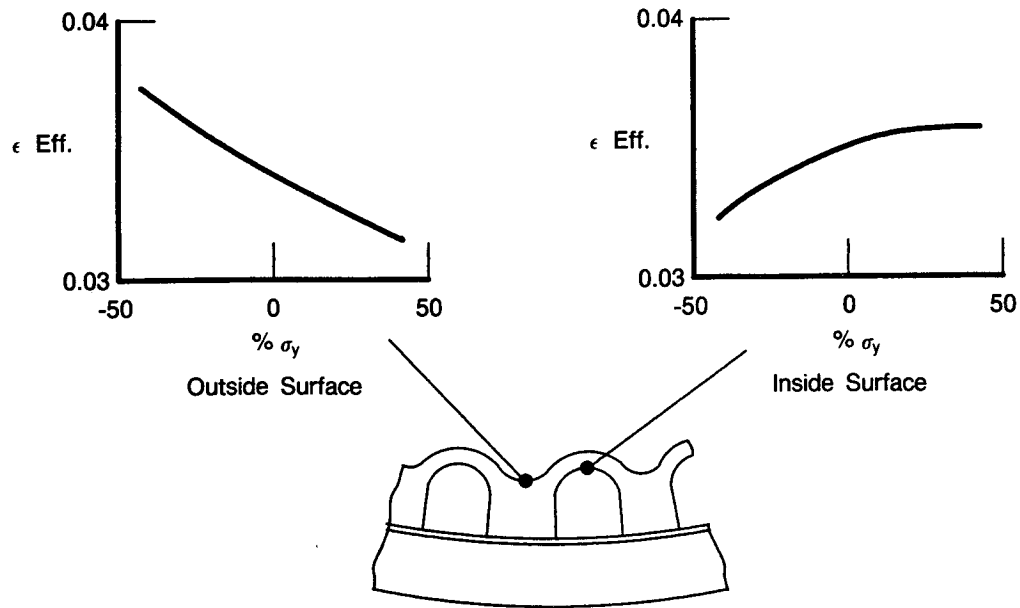*Figure 103.* *Effective Strain vs Yield Stress (σ$_y$), Outside Surface Only*

Figure 104. Effective Strain vs Yield Stress (σ_y), Locations of Maximum Strain

C.3.F Creep Strain

Variations in creep strain rate had only a very slight effect on strain range. The effects of creep were determined by exercising the creep option in MARC, with a ten-minute hold at full-throttle steady-state conditions. A creep analysis was first done for the baseline material, assuming NARloy-Z creep characteristics. Additional analyses were done for changes in the creep rate, assuming rates which were both one-fifth and five times that of the baseline material. Figure 107 is a plot of the maximum effective strain and strain range as a function of the creep strain rate.

C.3.F.1 Baseline Creep Strain vs Baseline Without Creep

The creep analysis indicated that creep strain had an insignificant impact on the overall effective strain, at least under the conditions assumed for this study. Ten minutes of creep resulted in only a 0.8 percent increase in the effective strain range (Table 27). The creep strain was expected to be larger than it was, considering the high metal temperatures on the surface of the copper liner. Creep usually becomes more significant with higher temperatures. However, in the case of the copper liner, the higher temperatures also resulted in very low yield stresses, and therefore lower plastic stresses in the chamber wall which were approximately equal to the yield stress. Stresses significantly higher than the yield point would require unrealistically high amounts of strain, which would not occur in a deflection-controlled situation such as the OTV thrust chamber. Therefore, even though the temperatures were high, the lower yield stress in the chamber wall resulted in smaller creep strains since creep is a stress-driven phenomenon.
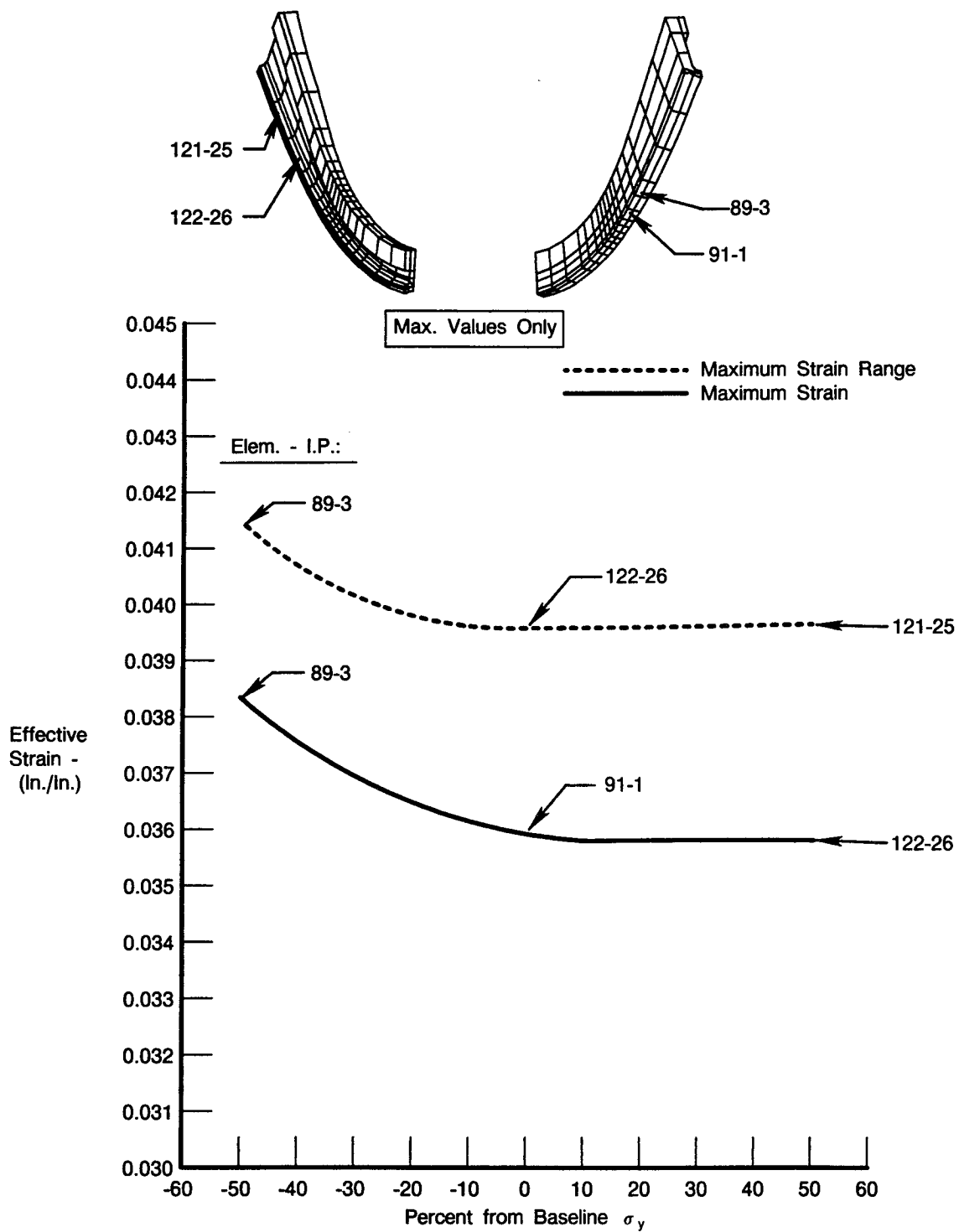
Figure 105. *Effective Strain vs Yield Stress (σ_y), Maximum Values Only*
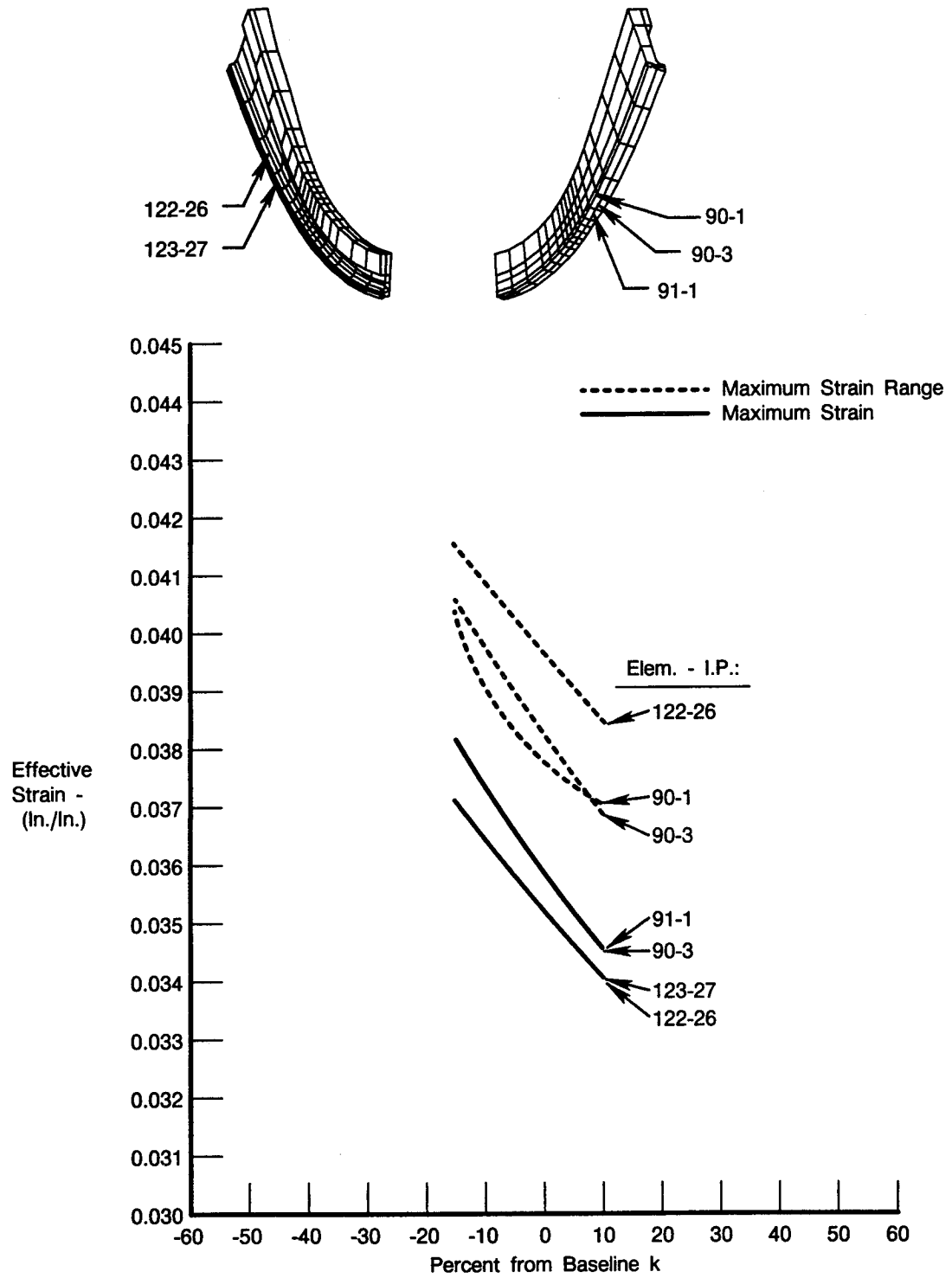
Figure 106. Effective Strain vs Thermal Conductivity (k)

174
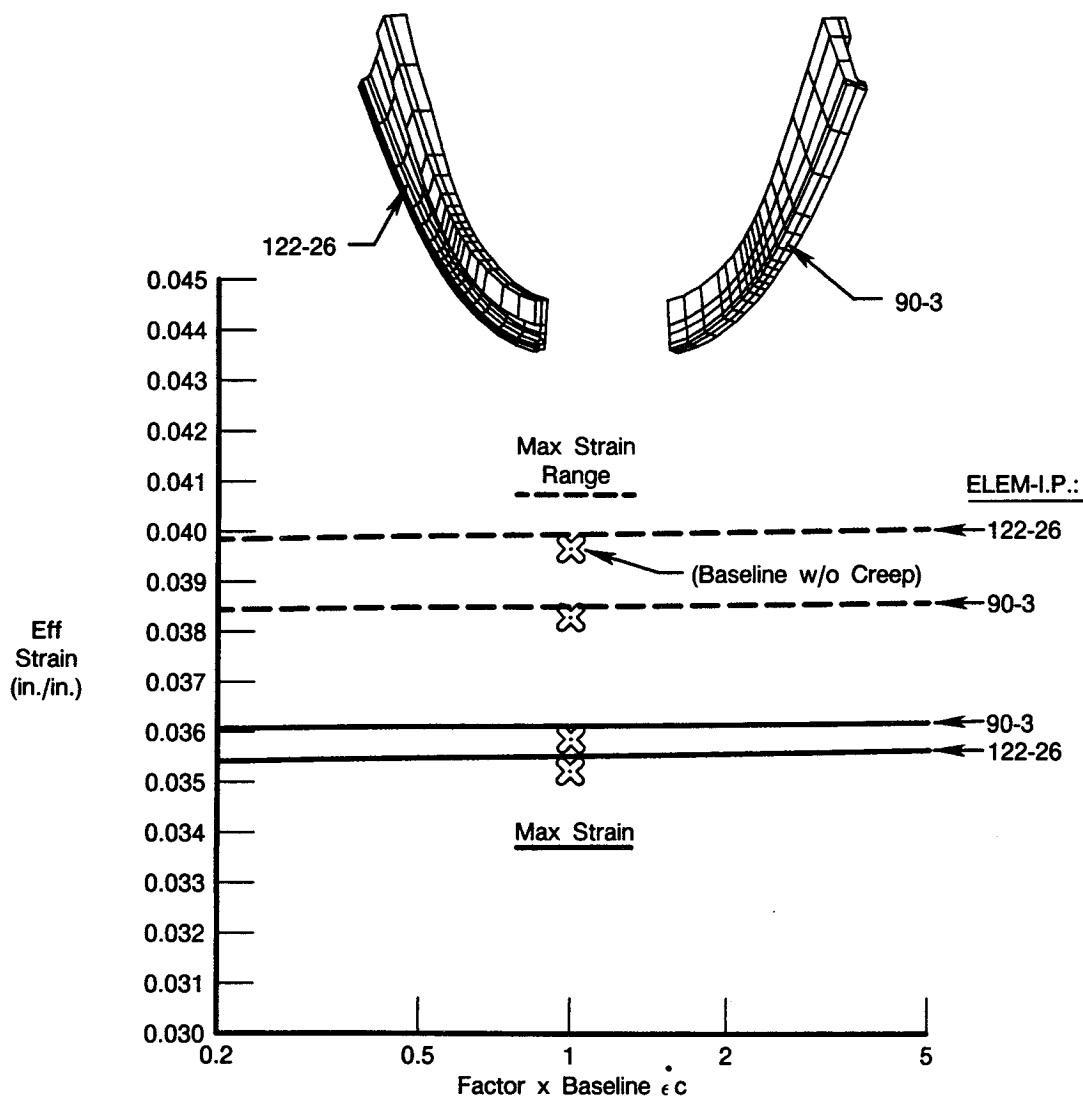
Figure 107. Total Effective Strain vs Creep Rate ($\dot{\varepsilon}_c$)

The chamber geometry used for this study was not optimized for heat transfer characteristics, although the design was felt to be adequate for the comparitive purposes of this material study. Consequently, metal temperatures were higher than would normally be allowed for a high-life design. A more optimized chamber design would have lower metal temperatures, and thus a higher yield stress. A higher yield stress would allow more stress for a given strain, and would produce more creep strain.

To test the effect of yield stress on creep strain, an additional MARC analysis was done using baseline creep characteristics with a 50 percent higher yield stress (instead of lowering the temperatures, the yield stress was increased to save the time and cost of a new thermal analysis). The results of this MARC analysis confirmed that a higher yield stress would produce more creep strain. For the baseline yield stress and creep properties, the maximum creep strain was 0.001537 in./in. But with a 50 percent higher yield stress, the creep strain increased to 0.003618 in./in., or 2.4 times that of the baseline yield stress. The overall effective strain increased 2.7 percent with creep and the increased yield stress, as indicated below in Table 29. Pertinent values from Table 27 are repeated in Table 29 for comparison.

175

Table 29. *Effect of Yield Stress on Creep Strain*

Material Property	Max. Eff. Strain	Change Relative To Baseline (%)	Max. Eff. Strain Range	Change Relative To Baseline (%)
Baseline, No Creep	0.03588	—	0.03962	—
+50% σ_y, No Creep	0.03579	−0.3	0.03965	+0.1
Baseline w/ Creep	0.03610	+0.6	0.03993	+0.8
Creep w/ +50% σ_y	0.03686	+2.7	0.04111	+3.8

The higher creep strain with higher yield stress indicates that, with an optimized chamber design, lower metal temperatures, and higher yield stress, creep strain may become a more important factor in the overall effective strain.

C.3.F.2 Effective Strain vs Variations in Creep Strain Rate

As creep strain had little impact on the overall effective strain, variations in the creep strain rate had little impact on strain as well. The effect of variations in creep strain rate was determined by increasing the rate five times and decreasing the rate to one-fifth of the baseline creep rate. The changes in creep rate were made independently, with the other properties left unchanged. Figure 107 is a plot of the values of maximum effective strain and strain range as a function of the creep strain rate. Also shown is the baseline strain without creep for comparison, marked as points "x" in Figure 107. Again, with an optimized chamber design with lower metal temperatures and a higher yield stress, creep strain may become a more important factor.

C.3.G Estimated LCF Lives

LCF life estimates for the material property variations studied in this analysis are presented in Table 30. The effective strain range values summarized in Table 27 were used to determine the LCF lives from Figure 108. Figure 108 is a plot of strain range vs. cycles for NARloy-Z and NASA-Z, based on the various sources of data described in Ref. 37 (NASA-Z is the same composition as NARloy-Z, but procured by NASA from an outside vendor). The life estimates given in Table 30 are based on material specimen tests by J. B. Conway et al at Mar-Test, Inc., indicated in Figure 108 and discussed in more detail in Ref. 37. These lives should be used only for comparison with one another, since the amount of LCF data for NARloy-Z is very limited and sometimes inconclusive.

The property with the greatest effect on LCF life was the coefficient of thermal expansion (α), for the reasons explained in Section C.3.C. The property with the least effect on LCF life was creep strain rate (except when the yield stress was increased 50 percent, as discussed in Section C.3.F.1).

176

Table 30. *Estimated LCF Lives Based on Effective Strain Range of Material Property Variations*

Material Property	Max. Eff. Strain Range (from Table III-1)	Max. Temp. (°F)	Cyclic Life (from Fig III-16)	Change Relative To Baseline (%)
Baseline (NARloy-Z)	0.03962	1059	87	—
+35% E	0.04029	1059	84	−3.4
−20% E	0.03883	1051	91	+4.6
+10% α	0.04454	1059	68	−21.8
−10% α	0.03493	1044	114	+31.0
+50% σ_y	0.03965	1019	87	0.0
−50% σ_y	0.04148	1153	79	−9.2
+10% k	0.03847	1036	92	+5.7
−15% k	0.04154	1100	78	−10.3
Baseline w/ Creep	0.03993	1059	85	−2.3
5.0× $\dot{\varepsilon}_c$	0.04003	1059	85	−2.3
0.2× $\dot{\varepsilon}_c$	0.03983	1059	86	−1.1
Baseline Creep w/+50% σ_y	0.04111*	1019	80	−8.0

*From Table III-3.

The LCF data in Figure 108 was for NARloy-Z and NASA-Z at 1000°F. The locations of maximum effective strain range in the MARC analysis occurred inside the coolant passage where the temperatures were near 1000°F, as listed in Table 30 (with the exceptions of the −50 percent σ_y run, in which the maximum effective strain range occurred on the combustion side of the liner, and the −15 percent k run, which produced higher temperatures due to slower heat conduction). Although the maximum overall temperature in the MARC analysis was over 1300°F (Figure 93), this temperature occurred on the combustion side surface of the liner away from the maximum strain range location. Test data indicated that temperature had little effect on LCF life at higher strain ranges. But at lower strain ranges, temperature became more significant, with lower temperatures resulting in higher lives.

Conway's data was based on cycles to failure. Test data from D. Fulton (Figure 108) was based on cycles to initiation of failure, but gave higher life predictions than Conway's data. However, Fulton's data was for a faster cyclic strain rate (0.1/sec), whereas Conway's data used in Table 30 was for a slower cyclic strain rate (0.002/sec). Other test data from Conway also indicated that faster cyclic strain rates resulted in higher LCF lives (Figure 108). While the life estimates quoted in Table 30 are based on a cyclic strain rate of 0.002/sec, the actual thrust chamber strain rate during OTV operation may be faster. In the baseline analysis, the effective strain approached 0.03559 in approximately one second, which is a significantly faster rate than 0.002/sec. (approximately six seconds more were required for the strain to reach 0.03588 as the temperatures approached steady state).

Used for LCF Life Estimate (Table 30):

⊙ NARloy-Z, Continuous Cycle, .002/sec;
(J. B. Conway, Mar-Test, Inc., see Ref. 1)

Additional Data:

▲ NARloy-Z, Continuous Cycle, .05/sec;

△ NARloy-Z, Continuous Cycle, .01/sec;

▽ NARloy-Z, Continuous Cycle, .0004/sec;   } (J. B. Conway, Mar-Test, Inc.,
                                                           see Ref. 1).
⊡ NARloy-Z, Tensile Hold, 300 sec.;

■ NARloy-Z, Compressive Hold, 300 sec.;

● NASA-Z, Continuous Cycle, .002/sec;
(J. Kazaroff, NASA Lewis Research Center, see Ref. 1) .

━ ━ ━ NARloy-Z, Continuous Cycle, .10/sec;
(D Fulton, Rockwell International Corp., see Ref. 19.
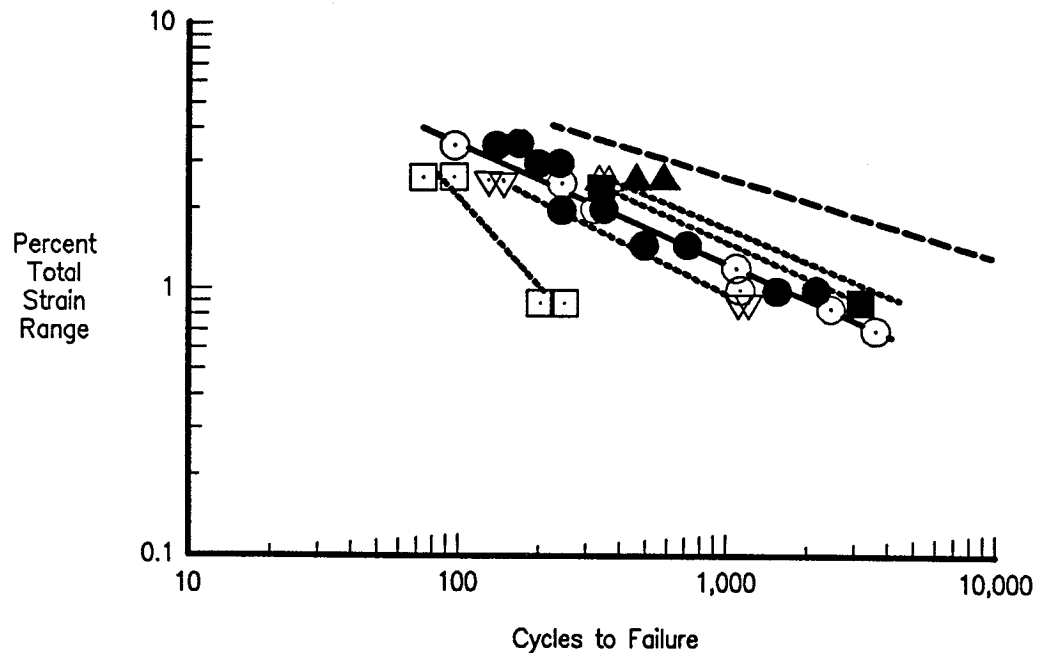
Figure 108. Low Cycle Fatigue Behavior of NARloy-Z and NASA-Z at 1000°F

Lives quoted for the creep analyses in Table 30 were based only on changes in the effective strain range resulting from creep rate variations, and did not include the effects of dwell time. However, test data indicated that cycles with compressive hold periods resulted in higher lives than those with no hold periods or those with tensile hold periods (Figure 108). The OTV thrust chamber strains that drove LCF life were mainly compressive (Section C.3.A).

Since the relationship between strain range and cycles in Figure 108 is logarithmic, the higher values of strain range produced smaller differences in LCF life for varying test conditions.

178

The strain ranges determined in this analysis (and used for the life estimates in Table 30) were relatively high, and the effects of material property changes were not as pronounced on LCF life as they would have been with lower strain ranges. A more optimized chamber design with lower temperatures and lower strain ranges may show greater differences in LCF life.

C.3.H Liner Wall Deformation

The cycling of plastic strains in the liner wall resulted in a physical thinning of material in the arch of the coolant passage at cycle shutdown. Figure 109 illustrates the thinning mechanism on the NARloy-Z baseline material. A cross-section of the liner wall near the location of the maximum effective strain range was examined. Figure 109a shows the original shape of the coolant passage before the material was cycled.
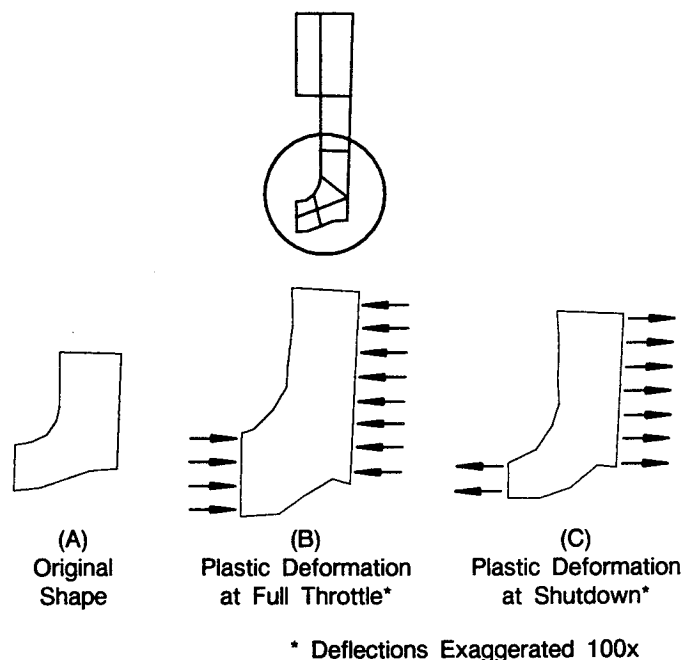

(A)	(B)	(C)
Original	Plastic Deformation	Plastic Deformation
Shape	at Full Throttle*	at Shutdown*

* Deflections Exaggerated 100x

Figure 109. Plastic Deformation of Liner Wall

At full throttle, compressive thermal loads in the hoop direction caused the arch of the liner wall to expand radially (Figure 109b). Since only the plastic strains act to permanently deform the liner wall, the deflections shown in Figure 109b include only the effect of plastic strains. The elastic and thermal strains have been subtracted out. The deflections are exaggerated for clarity.

Figure 109c shows the deformed shape at cycle shutdown. Again, the deflections shown were due to plastic strains only, since the temperature was a uniform 70°F and no external loads were applied. The material in the arch of the liner, which had yielded at full-throttle, was drawn thinner at shutdown as the surrounding material contracted.

The effects of thinning in the chamber liner have been observed in previous industry experience. Test chamber results and analytical predictions of thinning were correlated in a study done by Lockheed, Inc. (Ref. 43) for different chamber liner materials in a flat-wall configuration.

179

SECTION C.4
CONCLUSIONS

Within the ranges expected, variations in candidate material properties will not have a significant impact on thrust chamber liner strain range.

The coefficient of thermal expansion had the most significant effect, with lower values giving lower strain ranges and higher life. However, lowering the coefficient in reality requires more alloying with the copper, which reduces the thermal conductivity. And in turn, reducing the thermal conductivity results in higher strain ranges and lower life, off-setting the benefits of the lower coefficient of thermal expansion. Increasing the thermal conductivity would lower the strain range, but requires less alloying, which compromises the strengthening effects of alloying. The remaining properties did not have a significant effect on strain range.

The chamber geometry used for this study was not optimized for heat transfer characteristics, although the design was felt to be adequate for the comparitive purposes of this material study. A more optimized design may result in lower temperatures, which would reduce the thermal fight between the copper liner and the nickel closeout, and would reduce the strain range. The creep strain rate may be a more significant factor for an optimized chamber geometry, as lower temperatures result in higher yield strength and more creep strain.

Significant chamber life improvements should be sought through the following:

- An optimized chamber configuration for improved heat transfer capabilities and enhanced structural characteristics,

- Candidate materials with improved fatigue life capability, including creep/LCF interaction,

- Better fatigue life definition of candidate materials (i.e., strain range vs. cycles to failure under more applicable strain rates and loading conditions), including creep/LCF interaction.

APPENDIX D
REFERENCES

REFERENCES

1. Goalwin, D.S., *A High-Pressure Regeneratively Cooled Thrust Chamber, Vol. 1: Analysis, Test and Evaluation,* Rocketdyne, Aug. 1969 (AFRPL-TR-68-226-Vol. 1).

2. Fulton, D., *Investigation of Thermal Fatigue in Non-Tubular Regeneratively Cooled Thrust Chambers, Vol. 2,* Rockwell International Corporation, May 1973 (AFRPL-TR-73-10-Vol. 2).

3. Conway, J. B., et al., *High Temperature Low Cycle Fatigue of Copper-Base Alloys in Argon, Part 1. Preliminary Results of 12 Alloys at 1000°F (538°C),* Mar-Test, Inc., Jan. 1973 (NASA CR 121259).

4. Conway, J. B., et al., *High Temperature Low Cycle Fatigue of Copper-Base Alloys in Argon, Part 2, Zirconium Copper at 482, 538, and 593°C,* Mar-Test, Inc., August 1973 (NASA CR 121260).

5. Conway, J. B., et al., *High Temperature Low Cycle Fatigue of Copper-Base Alloys in Argon, Part 3: Zirconium Copper, Thermal-Mechanical Strain Cycling, Hold Time and Notch,* Mar-Test, Inc., Dec. 1973 (NASA CR 121261).

6. Conway, J. B. et al., *High Temperature, Low Cycle Fatigue of Advanced Copper Base Alloys for Rocket Nozzles; Part 1 — NARloy Z,* Mar-Test, Inc., May 1974 (NASA CR 134627).

7. Hannum, N.P., et al., *Experimental and Theoretical Investigation of Fatigue Life in Reusable Rocket Thrust Chambers,* AIAA Paper 76-685, Palo Alto, CA, July 1976.

8. Quentmeyer, R.J., *Experimental Fatigue Life Investigations of Cylindrical Thrust Chambers,* AIAA Paper 77-893 (AIAA Conf., Orlando, 1977).

9. Private Communications with NASA Lewis Research Center, Cleveland, OH.

10. *240 K Staged Combustion Testing,* Pratt & Whitney, 1 June 1971.

11. Newburn, F. and Romine, D., *Internal Letter PAM 2112-2014,* North American Rockwell, 22 March 1972 (From Marshall Space Flight Center).

12. Moeller, C.E. and McKown, R.D., *Internal Letter MPR 76-2304,* Rockwell International, 6 December 1976 (from Marshall Space Flight Center).

13. Andrus, J. S., and Bourdeau, R. G., *Thrust Chamber Material Exploratory Technology Program — Literature Review of Copper Base Alloys,* Pratt & Whitney, 20 May 1984 (P&W No. FR-18383-1, NASA Contract NAS3-23858).

14. Small, L., *Hardness Theory and Practice, Part 1,* 1960, Service Diamond Tool Co., Pg. 484 (Also in ASTM Standard E140, Table 4).

15. Bourdeau, R. G., *Development of Iron Aluminides*, Pratt & Whitney, May 1987, (P&W No. FR-18807, AFWAL-TR-87-4009).

16. Phillips, V. A., *Metallography*, Vol. 7, No. 2 pp 137-155, April 1974.

17. Jones, F. W., et al., *Proceedings of the Royal Society, A*, Volume 181, pp 154-168, 1942.

18 Raty, R. and Miekk-oja, H. M., *Philosophical Magazine*, Vol.18, pp 1105-1125, 1968.

19 Raty, R., *The Role of Lattice Defects in Precipitation Processes in Copper Silver Alloys*, Helsinki University of Technology, Laboratory of Physical Metallurgy, Otaniemi, Finland, 1971.

20. Saarivirta, M. J., *Metal Industry*, Vol. 103, No. 19, pp 685-688, 7 Nov. 1963.

21. Shih, C., *High Temperature Low Cycle Fatigue Mechanisms for a Nickel-Base and a Copper-Base Alloy*, University of Cincinnati, June 1982, (NASA Contractor Report 3543).

22. Nagai, T., et al., *Transactions of the Japan Institute of Metals*, Vol. 14, No. 6, pp 462-469, Nov. 1973.

23. Henmi, Z. and Nagai, T., *Transactions of the Japan Institute of Metals*, Vol 10, pp 305-313, 1969.

24. Novikov, A. I. and Rozenberg, V. M., *Physics of Metals and Metallography*, Vol. 37, No. 1, pp 192-194, 1974.

25. Hansen, M. and Anderko, J., *Constitution of Binary Alloys*, Second Edition, McGraw-Hill, New York and London, 1958.

26. Elliot, R. P., *Constitution of Binary Alloys*, First Supplement, McGraw Hill Book Co., N.Y., 1965.

27. Mandingo, F. N., and Breedis, J. F., U. S. Patent 4,198,248, 15 Apr 1980.

28 Tigeot, J., *Revue de Metallurgie (Paris)*, Vol. 69, No. 9, pp 773-784, September 1967.

29. Shunk, F. A., *Constitution of Binary Alloys, Second Supplement*, McGraw-Hill Book Co., N.Y., 1969.

30. Nishiyama, S. and Miyake, Y., *CDA-ASM Conf. on Copper*, Cleveland, OH, Oct 16-19, 1972, Copper Development Assn, N.Y. (preprints).

31. Private Communications with Drs. N. Grand and I. Vcok of Massachussets Institute of Technology, Cambridge, MA.

32. Donnay, J. D. H., et al., *Crystal Data, Determinative Tables*, 24d ed., Vol. 2 and 4, National Bureau of Standards and JCPDS, 1973 (V1) and 1978 (V2).

33. Sarin, V. K. and Grant, N. J., *Metallurgical Transactions*, Vol. 3, pp 875-878, April 1972.

34. Sarin V. K. and Grant, N. J., *Powder Metallurgy International,* Vol. 11, No. 4, pp 153-157, Nov. 1979.

35. Moffat, W. G., *The Handbook of Binary Phase Diagrams,* General Electric Co., Schenectady, N.Y., June 1980.

36. Esposito, J. J. and Zabora, R. F., *Thrust Chamber Life Predictions, Vol. 1: Mechanical and Physical Properties of High Performance Rocket Nozzle Materials,* Boeing Aerospace Company, March 1975 (NASA CR134806).

37. *Thrust Chamber Exploratory Technology Program — Literature Review of Copper Base Alloys,* prepared by Pratt & Whitney Government Products Division under Contract NAS3-23858, May 20, 1984 (FR-18383-1).

38. *3-Dimensional Thrust Chamber Life Prediction,* Boeing Aerospace Company, March 1975 (NASA CR-134979).

39. *Orbit Transfer Rocket Engine Technology Program — Monthly Technical Program Report No. 13,* 1 through 31 August 1984, prepared by Pratt & Whitney Government Products Division under Contract NAS3-23858, September 20, 1984 (FR-17808-13).

40. *Orbit Transfer Vehicle (OTV) Advanced Expander Cycle Engine Point Design Study — Final Technical Report,* prepared by Pratt & Whitney Government Products Division under Contract NAS8-33567, March 15, 1981 (FR-14615, Volume II).

41. *Thrust Chamber Life Prediction, Vol. II — Plug Nozzle Centerbody and Cylinder Life Analysis,* Boeing Aerospace Company, May 1975 (NASA CR-134822).

42. *Investigation of Thermal Fatigue in Non-Tubular Regeneratively Cooled Thrust Chambers,* Vol. 1, Rockwell International Corp., May 1973 (AFRPL-TR-73-10 — Vol. 1).

43. *Structural Analysis of Cylindrical Thrust Chambers — Final Report,* Volume I and Volume II, Lockheed Missiles and Space Company, Inc. (NASA CR-159522 and NASA CR-165241, respectively).

1. Report No. NASA CR-187206	2. Government Accession No.	3. Recipient's Catalog No.
4. Title and Subtitle Thrust Chamber Material Technology Program Final Report		5. Report Date March 1989
		6. Performing Organization Code
7. Author(s) J.S. Andrus and R.G. Bourdeau		8. Performing Organization Report No. FR-20672
		10. Work Unit No.
9. Performing Organization Name and Address United Technologies Corporation Pratt & Whitney P.O. Box 109600 West Palm Beach, FL 33410		11. Contract or Grant No. NAS3-23858, Task C-1
		13. Type of Report and Period Covered Final Report Aug 1983 - Aug 1986
12. Sponsoring Agency Name and Address National Aeronautics and Space Administration Lewis Research Center Cleveland, Ohio 44135-3191		14. Sponsoring Agency Code

15. Supplementary Notes

Task Order Mgr.: Mr. John Kazaroff, NASA Lewis Research Center

16. Abstract

This report covers work performed at Pratt & Whitney on development of copper-based materials for long-life, reuseable, regeneratively cooled rocket engine thrust chambers. The program approached the goal of enhanced cyclic life through the application of rapid solidification to alloy development, to introduce fine dispersions to strengthen and stabilize the alloys at elevated temperatures. After screening of alloy systems, copper-based alloys containing Cr, Co, Hf, Ag, Ti, and Zr were processed by rapid-solidification atomization in bulk quantities. Those bulk alloys showing the most promise were characterized by tensile testing, thermal conductivity testing, and elevated-temperature, low-cycle fatigue (LFC) testing. Characterization indicated that Cu- 1.1% Hf exhibited the greatest potential as an improved-life thrust chamber material, exhibiting LCF life about four times that of NASA-Z. Other alloys (Cu- 0.6% Zr, and Cu- 0.6% Zr- 1.0% Cr) exhibited promise for use in this application, but needed more development work to balance properties.

17. Key Words (Suggested by Author(s)) High-conductivity copper alloys, NASA-Z, thrust chamber materials, rapid solidification, powder metallurgy, dispersion strengthening, low-cycle fatigue, and thermal conductivity.	18. Distribution Statement Unclassified — Unlimited Subject Categories: 20 and 26		
19. Security Classif. (of this report) Unclassified	20. Security Classif. (of this page) Unclassified	21. No. of Pages 200	22. Price*

*For sale by the National Technical Information Service, Springfield, Virginia 22161

NASA-C-168 (Revision 10-86)